

THE STELLAR POPULATIONS AND INTERNAL REDDENING OF SPIRAL GALAXIES

by

Roger B. Rouse

A Dissertation Presented in Partial Fulfillment
of the Requirements for the Degree
Doctor of Philosophy

ARIZONA STATE UNIVERSITY

December 2002

THE STELLAR POPULATIONS AND INTERNAL REDDENING OF SPIRAL GALAXIES

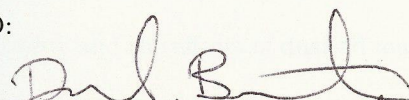
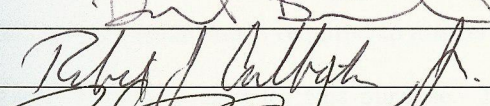
by

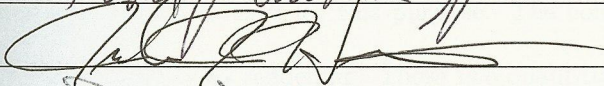
Roger B. Rouse

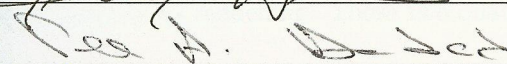
has been approved

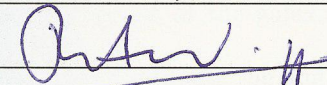
November 2002

APPROVED:


_____, Chair





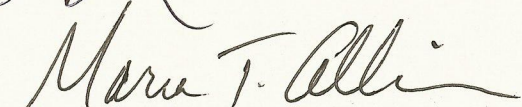




Supervisory Committee

ACCEPTED:



Department Chair


Dean, Graduate College

ABSTRACT

In this dissertation two results are presented. The first is the calibration of a data set of optical, infrared, and spectral images of ten spiral galaxies. The data set is unique because of the combination of imaging and spectroscopy. The galaxies are imaged in the optical B, V, R, I, and near-infrared J, H, and K filters. Spatially resolved, long slit spectra are obtained at two position angles and two spectral resolutions in each galaxy. This data may be used to study surface brightness and color distributions, line strength gradients, chemical compositions (metallicities), bulge-disk decomposition, galaxy models, dust models, the Tully-Fisher relation, and stellar populations.

To understand the history and current state of a galaxy's stars, gas, and dust is to understand its evolution and the evolution of galaxies in general. In this area, spiral disks are not understood as well as ellipticals or spiral bulges. In particular whether color gradients within spiral disks are due to changes in internal reddening or changes in stellar population is an open question. Because changes in age, metallicity, and the effects of dust all make the galaxy colors redder, a reddening independent measure of the population is required to answer this question. In this work, the magnesium b triplet absorption feature is used for this purpose. The color with the largest wavelength range, $B-K$, provides sensitivity to reddening. These two quantities are measured at the same locations within the disks of a subset of the galaxies. Stellar population models are used to confirm changes in population and to estimate the amount of internal reddening. This technique has the advantage of being applied to individual galaxies and to locations within galaxies, but it is not feasible to apply it to large numbers of galaxies. Also, even though models from various authors agree to within 30%, they may contain systematic effects, the discussion of which is beyond the scope of this work.

The three disks studied are reddened by dust and have color gradients that can be due to stellar population changes or changes in reddening. The field galaxy had the least reddening and a color gradient due to population changes, becoming older and/or more metal rich toward the center. In its outer disk, the color becomes bluer outward because of a decrease in the reddening. The cluster

galaxies have more reddening. One has a color gradient due mostly to an increase in reddening toward the center. Thus, the field galaxy and cluster galaxy become redder in their centers for different reasons. The internal differences between the cluster and field galaxy are likely due to their different environments. By visual inspection, the color gradients are smoother than the appearance of dust lanes in the B imagery. Comparison of the data to the models reveals that the three disks are most likely composed of a mixture of intermediate ages and metallicities. Very old metal rich populations and very metal poor populations of any age do not appear to contribute to the light observed. The technique of estimating the internal reddening by comparing data to models is successful. Thus, it will be possible to correctly interpret the colors of the unresolved disks of spiral galaxies.

Future work will include determination of the wavelength dependence of the reddening, how reddening varies from galaxy to galaxy and within a galaxy, and testing of dust models. Comparisons will also be made with the reddening in our galaxy. Distinguishing between reddening and population changes is critical to understanding the stellar content of spiral galaxies and hence the evolution of galaxies in general.

To Natasha, my loving wife.

To Mom, Dad, and Rodney.

ACKNOWLEDGEMENTS

The immediate predecessors of this work are the Ph.D. theses of Guy Worthey and Jesus Gonzalez. Thanks to Guy for providing me and the world with such a useful set of models. Thanks to Jesus for studying the ellipticals and for a productive week at UNAM.

Thank you to David Burstein for the many opportunities to go observing, to conferences, to lecture, and for the connections to Guy and Jesus. Thank you for mentoring me on the early observing runs and especially for taking me along on the MDM run. Thank you also for being patient, for encouragement, and for keeping the hounds at bay.

My appreciation goes to Gary Wegner for the opportunity to observe at MDM and answering questions about the RCA CCD, and to Bob Barr for measuring those exposure times for us. Thank you to Marcia Reike for the opportunity to observe at the 61" and for assistance at the telescope and with the data processing. Thanks again to David Burstein for the opportunity to observe at the MMT. Thank you to the MMT engineering staff for answering my questions about data processing and the spectrograph and to the excellent night assistants for their dedication and patience.

Paul Schmidtke, thank you for many conversations about photometry, variable stars, and automated telescopes. Thank you, Tony Ferro, for answering an endless stream of computer questions. Thanks to Scott Austin, Doug Mathis, Peter Hauschildt, and Lyman Neuschaefer for discussions about programming, data processing, galaxy counts, stellar atmospheres, and novae. Thank you, Seth Cohen, Rolf Jansen, Stephen Odewahn, Paul Scowen, and Carl Covatto for your comments. Thank you to Li Yong for taking over computer administration and keeping things in working order. Thank you to the department office for putting up with me especially Carmen, Denise, Martha, Dianna, Lacey, and Linda. Thank you to Tim Cook and Iwonna Rzanek for providing the equipment for my defense presentation.

Thank you to Marvin Klein for understanding that the PhD helps the company as well as the individual. Thanks to my mentors at the company John Heermans and ChungFu Chang, and to the

rest of the guys, Bob, Doug, Terri, Angelia, Steve, and Mike, for their enthusiastic support.

I would like to acknowledge those who contributed to my personal growth. Thank you, Joe West, for being the most excellent roommate and officemate one could have. Thank you, Li Yun, for your years of support especially during comprehensives. I am a better man for having known you. I thank the post docs, Peter, Paul, Simon, and Steve, for enlivening the experience over many pitchers of beer. Karen, Greg, Jason, Brian, Ravi, Catrina, Steve, Seth, Carl, and Sam, you are a great bunch of people. Thanks for the good times and good company. Thanks to Jim and Sara, Dina, and the rest of the SRC workout crew for helping me improve my self image. Thanks to Kristen and Leslie and the Hip-Hop Coalition for building my confidence through dance. Thank you to Scott and Kat and those brave souls who dared attend drop-in.

Natasha, my love, thank you for putting up with my stressed-out moods and long unfriendly hours at the computer. Thank you for being my personal cheering squad. I look forward to continuing our life together wherever it takes us. Mom, thank you for being there every step of the way, for lending me your ear, and for loving me in spite of myself. Thank you, Rodney, for looking out for me after Dad died and when I was at LSU. Dad, thank you for hanging in there as long as you could. The first three years are so important. Your love is still with me today.

This research has made use of the NASA/IPAC Extragalactic Database (NED) which is operated by the Jet Propulsion Laboratory, California Institute of Technology, under contract with the National Aeronautics and Space Administration.

This research has made use of the NASA/ IPAC Infrared Science Archive, which is operated by the Jet Propulsion Laboratory, California Institute of Technology, under contract with the National Aeronautics and Space Administration.

This research has been funded in part by the National Science Foundation and the Department of Physics and Astronomy, Arizona State University.

TABLE OF CONTENTS

	Page
LIST OF TABLES	xii
LIST OF FIGURES.	xiv
PART I: INTRODUCTION AND OBSERVATIONS	
CHAPTER	
1 INTRODUCTION	1
1.1 Stellar Populations: What are they and why study them?	1
1.2 Brief Historical Sketch	2
1.3 Stellar Population Models	5
1.4 Worthey's Evolutionary Synthesis Models	6
1.5 Lick System of Line Indices	7
1.6 Motivation and Goals	8
1.7 Overview	9
2 SAMPLE SELECTION AND OBSERVATIONS	10
2.1 The Sample	10
2.1.1 The Subsample	11
2.2 The Observations	13
2.2.1 Spectral Imaging	13
2.2.2 Optical Imaging	15
2.2.3 Infrared Imaging	15
PART II: DATA PROCESSING AND CALIBRATION	
3 CCDS AND IR ARRAY BASICS	24
3.1 CCD Basics	24

CHAPTER	Page
3.2 Basics of Infrared Arrays	30
3.3 Software	32
4 OPTICAL IMAGE PROCESSING	33
4.1 Overscan	33
4.2 Zeros	34
4.3 Darks	35
4.4 Flats	43
4.5 Star and Galaxy Images	51
4.6 Cosmic Ray Hits and Bad Pixels	51
5 SPECTRAL IMAGE PROCESSING	60
5.1 Overscan, Zeros, and Darks	60
5.2 Quartz Flats	67
5.3 Twilight Flats	68
5.4 Cosmic Ray Hits and Bad Pixels	77
5.5 Distortion Correction	77
5.6 Sky Subtraction	89
5.7 Scan Correction	89
5.8 Flux Calibration	92
5.9 Example Spectral Image	93
5.10 Hysteresis in Serial Register	99
5.11 Extraction of One Dimensional Spectra	103
6 INFRARED IMAGE PROCESSING	106
6.1 Preprocessing	106
6.2 Zeros and Darks	109
6.3 Wobble-And-Jitter Mode	112

CHAPTER	Page
6.4 Mapping Mode	121
7 OPTICAL PHOTOMETRY	125
7.1 Exposure Time Correction	125
7.2 Instrumental Magnitudes	125
7.3 Transformation to Standard System	128
8 INFRARED PHOTOMETRY	143
8.1 Stars	143
8.2 Galaxies	151
8.2.1 H–K of 2MASS Extended Sources	151
8.2.2 Measuring K Magnitudes	152
PART III: DATA ANALYSIS	
9 MGB, B-K, MODELS, AND INTERNAL REDDENING	158
9.1 Background	158
9.2 Measuring the Line Index	159
9.2.1 Measuring the Total Flux in a Band	161
9.2.2 Calculating the Continuum and the Line Index	162
9.2.3 Error Estimate and Propagation for Single Index Measurement	164
9.2.4 Reddening Independence of Mgb	165
9.2.5 Radial Velocities and Index Position Error	167
9.3 Transforming Mgb Measurements to Lick System	170
9.4 Mgb Index Profiles	175
9.5 Slit Profile Extraction and Magnitudes	178
9.5.1 B Slit Profile Extraction	178
9.5.2 Iterative Extraction Procedure	179
9.5.3 K Profile Extraction	180

CHAPTER	Page
9.5.4 Assignment of B and K Magnitudes	182
9.5.5 Galactic Extinction Correction	190
9.6 Comparing Observations and Models to Constrain Age and Metallicity	192
9.7 Combining Observations and Models to Estimate Internal Reddening	196
10 RESULTS AND CONCLUSIONS	199
10.1 Results	199
10.1.1 Color Gradients	199
10.1.2 Constraints on Stellar Population and Internal Reddening	212
10.2 Conclusions	222
10.3 Future Work	224
REFERENCES	226
APPENDIX	
A AREA OF A POLYGON	234

LIST OF TABLES

Table		Page
2.1	Data From the RC3 and $H_{-0.5}$ from [AMH82]	11
2.2	Detector Parameters	13
2.3	Data Acquisition as of December 1993	14
2.4	Observing Runs by Object	17
7.1	MDM Exposure Times	126
7.2	Instrumental Magnitudes for 26JUN92	131
7.3	Corrected Magnitudes for 26JUN92	133
7.4	UT and Airmass for 6 Observations of SA106-834	133
7.5	Combined Magnitudes for 26JUN92	134
7.6	UT Lookup Table for 26JUN92	135
7.7	UT Lookup Table for 28JUN92	135
7.8	UT Lookup Table for 29JUN92	135
7.9	Photometric Solutions for Each Night	135
8.1	Instrumental K Magnitudes for HD105601 on 20APR92	147
8.2	Instrumental Magnitudes for HD129655 on 09JUN93	147
8.3	Combined Instrumental Magnitudes for 20APR92	149
8.4	Apertures and H Magnitudes from [TB95]	154
8.5	Galaxy Instrumental K Magnitude Measurements	154
8.6	Range in UT and Airmass for Each Galaxy	154
8.7	Zero Points and Offsets for Each Galaxy in K	155
9.1	Mgb Band Values for NGC4654 Position One	166
9.2	Wavelengths and Interpolation Coefficients for the Mgb Index Bands	168

Table		Page
9.3	Instrumental MgB Values and Lick Values for each Slit Position	174
9.4	B To K Transformation Parameters.	181
9.5	Observed B and B-K for each Slit Position	191

LIST OF FIGURES

Figure		Page
2.1	The Subsample of Galaxies	12
4.1	Overscan Region in B Quartz Images for MDM	36
4.2	Example Evening Combined Zero for MDM	37
4.3	Morning Combined Zero for MDM	38
4.4	Standard Deviation of Morning Combined Zero for MDM	39
4.5	Histograms of Zeros	40
4.6	Evening Combined 900 Second Dark for MDM	41
4.7	Standard Deviation of Evening Combined Dark for MDM	42
4.8	B Response to the Quartz Lamp	45
4.9	R Response to the Quartz Lamp	46
4.10	B Twilight Response at MDM	47
4.11	R Twilight Response at MDM	48
4.12	An Individual B Twilight that has been Flat-Fielded.	49
4.13	An Individual R Twilight that has been Flat-Fielded.	50
4.14	Example of Interactively Finding Bad Pixels and Cosmic Rays	53
4.15	Graphical User Interface for Interactively Marking Cosmic Rays	54
4.16	Example of Image Section Displayed as Cosmic Rays are Removed	55
4.17	Example of Raw Galaxy Image in B	56
4.18	Example of Raw Galaxy Image in R	57
4.19	Example of Galaxy Image After Processing in B	58
4.20	Example of Galaxy Image After Processing in R	59
5.1	Example of Fitting Overscan	62

Figure		Page
5.2	Example of Residuals from Fit to Overscan	63
5.3	Example of MMT Combined Evening Zero after Bias Subtraction	64
5.4	Example of MMT Combined Dark	65
5.5	Standard Deviation of MMT Combined Dark	66
5.6	Example of MMT Combined Evening Quartz Lamp	69
5.7	Example of MMT Quartz Lamp Spectrum	70
5.8	Example MMT Response Derived from Quartz Lamp Observations	71
5.9	Example MMT Twilight After Dividing by Quartz Lamp Response	72
5.10	Example Twilight After Dividing by Median Column	73
5.11	Example Smoothed Twilight Flat	74
5.12	Example MMT Response Derived from Twilights	75
5.13	Standard Deviation MMT Response Derived from Twilights	76
5.14	Interactively Marking Bad Pixels	78
5.15	Image of MMT Comparison Lamp After Flat-Fielding and Before Distortion Correction	81
5.16	Example of How Distortion Affects Plots	82
5.17	Example Fit of Wavelengths to Pixels	83
5.18	Example Residuals of Fit in Figure 5.17	84
5.19	Example Feature Selection	85
5.20	Determining Distortion Corrections	86
5.21	Image of MMT Comparison Lamp After Distortion Correction	87
5.22	Difference of MMT Comparison Lamp Before and After Distortion Correction . . .	88
5.23	Example MMT Sky Spectrum	90
5.24	Example of Scan Correction of MMT Standards	91
5.25	Steps in Flux Calibration	94
5.26	Raw Spectral Image of Galaxy	95

Figure	Page
5.27 Processed Spectral Image of Galaxy	96
5.28 Sky-subtracted Spectral Image of Galaxy	97
5.29 Fluxed Spectral Image of Galaxy	98
5.30 The Average Column of a Galaxy Spectral Image	100
5.31 A 100th Order Fit of Cubic Splines to the Overscan Region	101
5.32 Residuals of Fit Shown in Figure 5.31	102
5.33 Example of Aperture Selection	104
5.34 Example of Extracted Spectra	105
6.1 Clipped Histograms of a Sequence of K Exposures on NGC 6384	108
6.2 Example in IR of Median Combine of Ten Bias Images	110
6.3 Example in IR of a Median Combine of Ten 30 Second Darks	111
6.4 Statistics of a K Band Sequence of NGC 6384	115
6.5 Example of IR Sequence Processing	116
6.6 Example of Average Sky Image	117
6.7 Example of Flat-Fielding IR Image of Galaxy	118
6.8 IR Sequence of Sky-Subtracted and Flat-Fielded Galaxy Images	119
6.9 IR Sequence of Combined Galaxy Images	120
6.10 Example of Sky Used in IR Mapping Mode Processing	122
6.11 Standard Deviation of IR Sky Used in IR Mapping Mode Processing	123
6.12 IR Standard Taken in Mapping Mode After Processing	124
7.1 Defocused Standard Star, SA106-834, with Nearby Star Contaminating the Aperture	127
7.2 Residuals in B of Photometric Solution for 26JUN92	136
7.3 Residuals in R of Photometric Solution for 26JUN92	137
7.4 Residuals in B of Photometric Solution for 28JUN92	138
7.5 Residuals in R of Photometric Solution for 28JUN92	139

Figure	Page
7.6 Residuals in B of Photometric Solution for 29JUN92	140
7.7 Residuals in R of Photometric Solution for 29JUN92	141
7.8 Graphical User Interface Developed for Determining Photometric Solutions	142
8.1 Defocused Standard Star, HD105601, with Aperture	145
8.2 Curve of Growth for Standard Star, HD129653, in K	146
8.3 K Magnitude Residuals and Position on IR Array	150
8.4 Relationship of H and K for Objects from the 2MASS Extended Source Catalogs	153
8.5 Predicted H Magnitudes Compared to [TB95] H Magnitudes	156
9.1 Spectral Image with Features Labeled	160
9.2 Example of Measuring Mgb in NGC 4654	163
9.3 Example of Measuring Position Error in Mgb in NGC 4654	169
9.4 Index Values as a Function of Velocity Dispersion	173
9.5 Mgb Index Profile for NGC 4654 Positions One and Two	176
9.6 Mgb Index Profile for NGC 5204 and NGC 6384 Positions One	177
9.7 Graphical User Interface for Choosing Initial Slit Position	183
9.8 Output from Iterative Extraction Procedure for Positioning the Software Slit in B Image	184
9.9 B Slit Position Transformed onto K Image	185
9.10 Software Slit with Apertures on B Image of NGC 4654	186
9.11 Software Slit with Apertures on K Image of NGC 4654	187
9.12 Example Longslit Software Apertures Displayed on the Extracted Profiles	188
9.13 The Three Profiles are Aligned in the Spatial Dimension	189
9.14 Plotting Symbols for Models and Data	194
9.15 Example of Plot used to Analyze Age, Metallicity, and Internal Reddening of a Spiral Disk	195

Figure	Page
9.16 Example of How Model Color and Range in Model Color are Determined	197
9.17 Example of How Reddening is Estimated	198
10.1 NGC 4654 Position One Mgb and B–K Profiles	203
10.2 NGC 6384 Position One Mgb and B–K Profiles	204
10.3 NGC 5204 Position One Mgb and B–K Profiles	205
10.4 NGC 4654 Position Two Mgb and B–K Profiles	206
10.5 Observed Relationship between Mgb and B–K in NGC 4654 Position One	207
10.6 Observed Relationship between Mgb and B–K in NGC 6384 Position One	208
10.7 Four Slit Positions in Three Galaxies	209
10.8 Apparent Dust Distribution, Mgb, and B–K in NGC 4654	210
10.9 Apparent Dust Distribution, Mgb, and B–K in NGC 6384	211
10.10 Summary Figure for NGC 4654 Position One	218
10.11 Summary Figure for NGC 4654 Position Two	219
10.12 Summary Figure for NGC 5204 Position One	220
10.13 Summary Figure for NGC 6384 Position One	221
A.1 Right Triangle used in Proof.	236
A.2 Example of N-sided Polygon used in Proof.	236

PART I

**INTRODUCTION AND
OBSERVATIONS**

CHAPTER 1

INTRODUCTION

In this chapter an indication of why stellar populations are important is given. This is followed by a brief history of the beginnings of the field. Then modeling techniques are discussed. Next line indices are introduced. Finally the goals are stated and an outline of the text is given.

1.1 Stellar Populations: What are they and why study them?

A stellar population is by definition a set of stars with common characteristics such as age, chemical composition, spatial distribution, and kinematics. Some stellar populations also include interstellar gas and dust [Mou82].

If our goal is to understand the detailed evolution of the universe then we must understand the evolution of galaxies which are the detectable tracers of mass. To understand the evolution of galaxies we must understand the evolution of their stars, gas, and dust, which are the sources of the radiation we observe. Even though dark matter may be the primary influence on the evolution of the universe, its existence and distribution is inferred from observations of stars and gas [Buz89]. Other important points needing explanation are late stages of stellar evolution, the origin of the Hubble sequence, the role of galaxy interactions, the effects of galaxy environment, and the properties of the first generation of stars [Sea86]. The first step is to determine the kinds of stellar populations that exist. This means determining their ages, chemical compositions (metallicities), spatial distributions, and kinematics within galaxies and how they differ from galaxy to galaxy. This is challenging because increasing the age, metallicities, or the effects of dust all make the integrated colors of a galaxy redder especially in spirals. Observing only a color gradient within a spiral does not indicate whether that gradient is due to a change in age, metallicity, or reddening of its stellar populations. The next step

is to determine what evolutionary scenarios could reproduce the observed stellar populations. Much progress has been made in this area and the resulting insights have advanced our understanding of the universe.

1.2 Brief Historical Sketch

There are numerous excellent reviews of the field [Kin71, vdB75, Mou82, San86, Fro88, Hod89, Ken98]. A brief outline of the early history is given.

In 1944 upon resolving the faint red stars in the center of the Andromeda galaxy and its elliptical companions Baade, [Baa44], confirmed his suspicion that these stars had a color-magnitude diagram (CMD) resembling a globular cluster CMD [San86]. He also made a distinction between these stars and bluer stars associated with spiral arms that have CMDs like open cluster CMDs. He called the red, globular cluster like stars Population II, and the blue spiral arm stars he called Population I. At this time it had already been determined that the Galaxy had kinematic subsystems [Str24, Str25, Lin25a, Lin25b] and rotated [Oor28]. Because the high velocity stars contained no OB stars Baade connected them with Population II. The low velocity stars he associated with Population I. Thus Population II had a globular cluster CMD, the spatial distribution of globular clusters, and included globular clusters, high velocity stars in the Galaxy, stars in spiral bulges, and stars in ellipticals. Population I had a solar neighborhood CMD and included OB stars, open clusters, the low velocity stars in the Galaxy, and stars associated with spiral arms and gas and dust clouds in the Galaxy and other galaxies. Although several characteristics were considered it appeared as though they conspired to put all stars in one of these two groups [Hod89]. Thus stellar populations were defined empirically. The connection between Galactic stars, their spatial distribution, and kinematics was made with stars in other galaxies.

The connection with stellar evolution soon followed. Before 1944 it had been determined that nuclear energy powered the sun, [vW38, Bet39], and that the sun and all stars would evolve [ŚC42,

Gam38]. Gamow apparently suggested this to Baade in 1944 [Ost94], but Russell put it in writing [Rus48]. When isochrones became available in the mid fifties, [HS55], it was found that the globular clusters were old and open clusters were young, and, hence, that Population I was young while Population II was old. This was the beginning of the theoretical explanation of stellar populations. Roman, [Rom50], determined that the high-velocity stars were weak-lined while the low-velocity stars were strong-lined. Therefore, high-velocity stars were lacking in heavy elements compared to low-velocity stars [Rom50]. Thus, Population II was old and metal poor while Population I was young and metal-rich. Age and chemical composition became part of the stellar population paradigm.

Evidence continued to mount that there were age and chemical composition variations within the two populations. For instance, the CMD of the high-velocity stars resembled the CMD of open clusters more than that of globular clusters, [KK53], and composite spectra of globulars showed a variation in composite type (F to G) [Mor56, Mor59, May46]. Both of these facts indicated a significant variation the chemical composition of Population II. At the Vatican Conference of 1957 a new set of stellar populations was defined. The new populations were an extension of Lindblad's kinematic subsystems [Lin25a, San86]. Instead of two there were five that progressed in a linear and continuous fashion from halo Population II to intermediate population II (a more flattened distribution than the halo) to disk population to older Population I (older stars in the disk) and, finally, to extreme Population I (stars forming in association with spiral arms) [Bla65, MB81].

The populations were explained in terms of galaxy formation. Theory held that the Galaxy formed via the rapid collapse of a single, isolated gas cloud [ELBS62]. The halo population formed during the initial part of the collapse, and as the collapsing gas began to flatten the intermediate population was formed. As the disk formed (through conservation of angular momentum and energy dissipation of energy by cloud-cloud interactions) another episode of star formation created the disk population. Old Population I stars formed in the completed disk, and the extreme Population I stars

formed in the spiral structure of the disk. At each stage the evolved stars enriched the surrounding gas. Thus the populations progressed from old metal poor to young metal rich as a single parameter family [Hod89]. However, observations continued to reveal variations even within the new stellar populations.

The field continued to grow rapidly through the '60s and '70s and accelerated by space missions like IUE, IRAS , and HST through the '80s and '90s. To exhaustively survey the work done during this period is beyond the scope of this thesis. Only a few important results that are relevant to this work are listed here. The Hubble sequence can be explained by the current star formation rate (SFR) in galaxies. The SFR increases from early to late types, highlighting the spiral structure [Rob63, Ken98]. This is another important parameter in defining stellar populations [Hod89]. Synthesis techniques came to the fore enabling ages and metallicities to be readily assigned to observed stellar populations. These were applied first to ellipticals [Woo66, MvdB68, Las70, ST69, Fab72, Pic85, Wor93, Gon93, TFWG00] then to spiral nuclei and bulges [Tur76, Fro85, Gre89b, Gre89a, Sil91, BdJ00, LVPB01]. Only recently have attempts been made to study the inter-arm regions of spiral disks. Chemical evolution models uncovered the G-dwarf problem [Sch63, Tin80]. Studies of the Galaxy found abundance gradients in the disk and halo [Mou82]. The rapid collapse model of galaxy formation gave way to the revelation that most galaxies are interacting (e.g. merging, accretion, infall) and that they may have formed by assembly of smaller masses [TT72, Tin80]. This, of course, brings into question the formation scheme of the stellar populations since the isolated-cloud assumption of the theory does not hold. Indeed it appeared that ellipticals, the simplest structurely, have the most complex evolution (merging of spirals) [Mou94]. So it seemed that all most every combination of age, chemical abundance, kinematics, and spatial distribution existed.

Although the Vatican scheme is inadequate nothing has arisen to replace it [Mou94]. Opinions vary from those who would abolish the populations and just quote age and metallicity distributions to those who would go back to just Population I and Population II [Mou94]. Today typing of stellar

populations is no longer a point of focus. Instead stellar populations and their physical properties are modeled. In this context a simple stellar population (SSP) is one with a single age, metallicity, and initial mass function (IMF). All other stellar populations are thought of as linear combinations of multiple SSPs.

1.3 Stellar Population Models

Even with large space based telescopes most galaxies in the universe will not be resolved into stars. Thus the integrated light of these galaxies is our only source of information about them. The integrated light contains contributions from all of the stars within a resolution cell as modified by extinction and reddening. Because of the composite nature of the integrated spectrum models are required to interpret them [O’C86]. A synthetic spectrum and colors are produced by a model with a known age, metallicity, IMF, and, perhaps, other parameters. A synthetic spectrum that matches a galaxy’s spectrum tells us which stars contribute most to the integrated light and that the age, metallicity, IMF, etc of the model correspond to the age, metallicity, IMF, etc of the galaxy. The range of models that match yields the uncertainties involved. Models also help to refute or confirm our theoretical understanding of the physics of galaxy formation and stellar evolution [Fer92].

Leitherer et al., [L⁺96], provide a summary of many synthesis models. Methods for synthesizing the integrated spectrum of a galaxy include population synthesis and chemical evolution models. The two methods of population synthesis are empirical and evolutionary synthesis [Tin80]. While Scheiner, [Sch99], appears to be the first to compare the spectrum of M31 to that of the Sun it was Whipple, [Whi35], who first suggested synthesizing integrated spectra. His was an empirical synthesis. In this case the integrated spectrum of a galaxy is matched by combining the observed spectra of stars and/or clusters. The evolutionary synthesis method can be totally theoretical or partially empirical. It requires isochrones (stellar evolution model), spectral energy distributions (SEDs) from stellar atmosphere models or spectrophotometry, and an IMF. The stellar atmospheres

can be replaced or supplemented with fitting functions that predict observed colors and line strengths in terms of effective temperature, surface gravity, and chemical composition.

Chemical evolution models divide a galaxy into spatial zones. In each zone the exchange between stars and the interstellar medium is taken into account by setting down a system of integro-differential equations. The equations involve terms such as the SFR, the death rate, yields, abundances, and the IMF. The equations are solved numerically subject to constraints such as the Fuel Consumption Theorem [RB86]. For a given time step the number of stars and their evolutionary state are known. Spectral energy distributions can be assigned so that colors and line strengths can be predicted [Tin80, AY86].

Efforts are being made to combine stellar population models or chemical evolution models with dynamic models of galaxies [CSFvA98] and to incorporate cloud evolution, star formation within clouds, and dust into chemical evolution models [Bru95, CF00].

1.4 Worthey’s Evolutionary Synthesis Models

The three main sources of models are Bruzual and Charlot [BC93], Worthey [Wor93], and the Padova group [BCF94]. These authors indicate that their model outputs agree to within 25% to 30% [CWB96]. Even so, they may contain systematic effects, the discussion of which is beyond the scope of this work.

The evolutionary synthesis models of Worthey, [Wor93, Wor94], were chosen for this work because they provide predictions of numerous observable quantities such as UBVRIJHK standard magnitudes and the Lick line indices (see Section 1.5). They provide these quantities for a range of ages and metallicities and have been used with success to study elliptical galaxies, [Gon93, CWB96, TFWG00]. The models are SSPs constructed in the following manner. For a given age, metallicity, and IMF an isochrone is selected. An SED is assigned to each point on the isochrone. Worthey used SEDs from stellar atmosphere models. The SEDs are weighted by the fraction of stars at each point on

the isochrone and summed to give the SED for the population. The observable quantities are calculated using the SED and filter functions or empirically determined fitting functions. The Worthey models use SEDs and filter functions to calculate magnitudes and use empirically determined fitting functions to calculate the line indices. The reader is referred to [Wor93] for a detailed discussion of the models and their components.

1.5 Lick System of Line Indices

There is a standard system for line indices analogous to the standard magnitude system. It is the Lick System. The Lick system is based on an extensive set of stellar line index measurements made using the Image Dissector Scanner (IDS) at the Lick Observatory. The Lick system of line indices and stellar library are discussed in [Jav93, WFGB94]. Evolutionary synthesis uses fitting functions derived from these data to estimate line indices. Therefore, observed indices are transformed to this system.

Observed spectra contain many overlapping absorption features. Because of this line-blanketing of the continuum there is no region in the observed wavelength range free of absorption. However, there are features that stand out against this background or pseudo-continuum. The Lick indices are designed to measure these features. The relative strength of such features are measured using three band passes one blue, one red, and one centered on the feature. The side bands are placed in the pseudo-continuum. Interpolation between the side bands is used to give a continuum value in the center band. The line ratio is the ratio of the center to the estimated continuum. The line depth is unity less the line ratio. Magnitudes of the line ratio are used for narrow lines and equivalent widths of the line strength are used for the broader features. The details of measuring a line index are given in Section 9.2.

1.6 Motivation and Goals

To understand the evolution of galaxies requires an understanding of the current state and history of their stars, gas, and dust. In the area of stellar populations spiral disks are not understood as well as bulges and ellipticals. In particular, whether color gradients within spiral disks are due to changes in internal reddening or changes in stellar population is an open question. Because changes in age, metallicity, and the effects of dust all make the galaxy colors redder, a reddening independent measure of the population is required to answer this question. The magnesium b triplet (Mgb) at 5177\AA is used for this purpose. The Mgb absorption feature may also contain contributions from the (1,1) band of the magnesium hydride (MgH) $A^2\Pi - X^2\Sigma^+$ system [Mou78]. Mgb is a well established indicator of stellar population [Dee60, Fab73, Mou78, Bur79, BFGK84, BBB⁺88, BEMM92]. The reddening independent nature of the Mgb measurement is discussed in Section 9.2.4. A reddening dependent quantity is also needed. The optical near-infrared color, $B-K$, is used because it covers the longest wavelength range of the available colors. Furthermore, exploring Mgb gradients requires spatial resolution in the spectroscopy. Because the galaxies are not resolved into stars it is not possible to use individual stellar spectra to separate the effects of age, metallicity, and reddening on the observations. Instead models are used to aid in the separation of the effects of reddening changes and population changes on the integrated colors. The further separation of age and metallicity will be attempted in future work. Comparison of the measurements to the models also yields an estimate of the internal reddening of each galaxy.

Thus, the main goals of this work are to: 1) image the spiral disks in BVRI and JHK, 2) to obtain longslit spectroscopy in the optical region, 3) to measure $B-K$ gradients from the imagery and Mgb gradients from the spectral images in a subset of the sample, 4) to use those measurements to investigate the cause of color gradients, 5) to put constraints on the stellar populations, and 6) to estimate the internal reddening within the subsample galaxies. The sample, subsample, observations, and data processing satisfying the first two goals are documented in Parts I and II. The calibration,

data analysis, model comparisons, and internal reddening estimate satisfying the remaining goals are documented in Parts II and III.

1.7 Overview

All necessary data has been collected on the target objects. Chapter 2 discusses the sample and observations. Optical images are the most straightforward data to reduce. They are discussed first in Chapter 4. Then it is natural that the longslit data reduction be next in Chapter 5. Finally the IR data reduction is discussed in Chapter 6. Chapter 7 discusses the optical photometry. Chapter 8 discusses the IR photometry. Chapter 9 explains how the stellar population models are used, how the spectral indices are measured and calibrated, and how the colors are obtained. It also discusses how the data and models are used to constrain the ages and metallicities of the disks and to predict the internal reddening. Chapter 10 discusses the cause of color gradients within two of the subsample galaxies, the age and metallicity constraints, the internal reddening estimates, and other results. It presents the conclusions and lists the subjects of future work. Chapters 2 to 6 apply to the full sample of ten spirals. Chapters 7 through 10 refer only to the subsample.

CHAPTER 2

SAMPLE SELECTION AND OBSERVATIONS

In this chapter the sample selection is discussed. Then the observations are detailed. The spectral, optical, and infrared observations are discussed in that order. All galaxies observed are discussed even though only NGC 4654, NGC 5204, and NGC 6384 are used in the analysis presented in later chapters.

2.1 The Sample

Ten galaxies satisfying the following criterion are selected from the Aaronson H-band Tully-Fisher data set [AMH82]. The angular size of a galaxy is chosen to be less than $7'$ so that it can be observed with a $3'$ longslit with one end at the center and the other on sky. To avoid large obscuration by dust lanes the inclination of a galaxy is required to be more face on than 56° . For each galaxy fitting these first two criteria there is another galaxy of similar $B_T - H_{-0.5}$ color that also satisfies the first two criteria (i.e. there is a pair in $B_T - H_{-0.5}$). Table 2.1 lists the morphological type, total B magnitude, B_T , logarithm of the major axis isophotal diameter at a B surface brightness of 25 in units of $0.1''$, $\text{Log}(D_{25})$, the logarithm of the axial ratio of the same isophote, the mean heliocentric velocity, and the extinction in B all from the Third Reference Catalog of Bright Galaxies, RC3. Also listed is the optical infrared color, $B_T - H_{-0.5}$, where $H_{-0.5}$ is the H magnitude inside an aperture of size $\text{Log}(D_{25}) - 0.5$. $H_{-0.5}$ is from [AMH82].

The Aaronson data set is chosen for two reasons. H aperture magnitudes have been measured for all the galaxies and some have J and K aperture magnitudes. Also these galaxies are used to establish the infrared Tully-Fisher relation. Thus the internal character of the galaxies can be related

Table 2.1: Data From the RC3 and $H_{-0.5}$ from [AMH82]

Name	Type	B_T	$\text{Log}(D_{25})$	$\text{Log}(R_{25})$	$B_T - H_{-0.5}$	$V_0(\frac{\text{km}}{\text{s}})$	A_B
NGC 772	SA(s)b	11.1	1.86	0.23	2.63	2458	0.16
NGC 949	SA(rs)b	12.6	1.38	0.27	2.37	612	0.17
NGC 2268	SA(r)bc	12.2	1.51	0.21	2.63	2222	0.21
NGC 2701	SAB(rs)dm	12.4	1.34	0.13	1.58	2326	0.05
NGC 3338	SA(s)c	10.9	1.77	0.21	1.98	1301	0.06
NGC 3782	SAB(s)cd	12.8	1.22	0.19	1.13	739	0.01
NGC 4654	SAB(rs)cd	10.7	1.69	0.24	2.01	1035	0.06
NGC 4713	SAB(rs)d	11.9	1.43	0.20	1.53	653	0.00
NGC 5204	SA(s)m	11.4	1.70	0.22	1.17	204	0.01
NGC 6384	SAB(r)bc	11.3	1.79	0.18	2.37	1663	0.41

to their Tully-Fisher residuals. However, a detailed analysis awaits future work.

2.1.1 The Subsample

Four slit positions in three galaxies are chosen for further analysis. The galaxies are selected by their $B_T - H_{-0.5}$ color. NGC 5204 is the bluest of the ten galaxies with $B_T - H_{-0.5} = 1.17$. NGC 6384 is the reddest at 2.37. NGC 4654 is intermediate with $B_T - H_{-0.5} = 2.01$. They are shown in Figure 2.1 where the grey scale represents the B image, the contours are from the K image, and the line represents the position and orientation of the longslit. NGC 4654 is in Virgo and interacts with intragalactic medium [PM95]. NGC 5204 is a member of the M101 group and has a highly warped disk [SCD96]. NGC 6384 is a field galaxy.

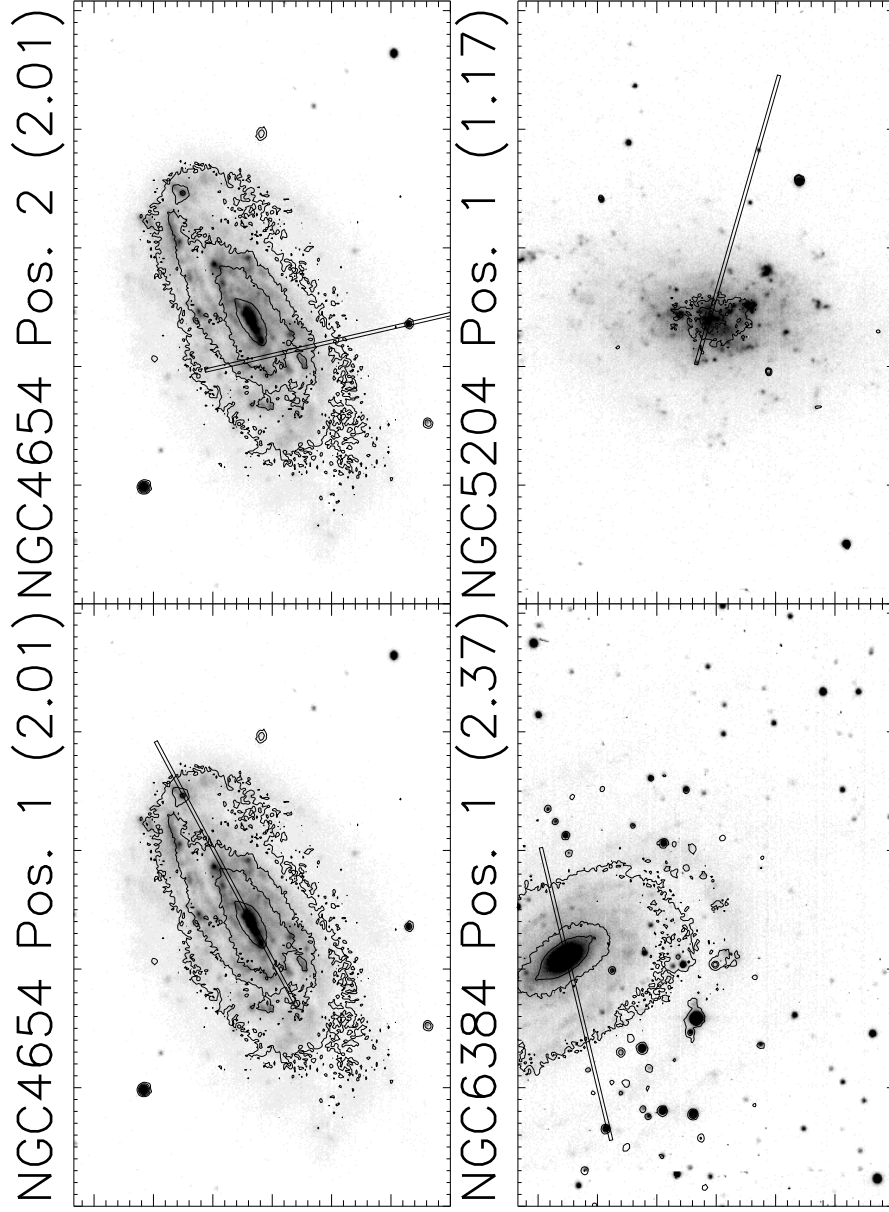


Figure 2.1: The Subsample of Galaxies: The four slit positions and three galaxies are analyzed later in this document. The galaxies were chosen by their $B_T - H_{-0.5}$ color NGC 5204 being the bluest of the full sample ($B_T - H_{-0.5} = 1.17$), NGC 6384 the reddest ($B_T - H_{-0.5} = 2.37$), and NGC 4654 intermediate ($B_T - H_{-0.5} = 2.01$). The grey scale represents the B image, the contours are from K, and the line represents the position and orientation of the longslit. NGC 4654 and NGC 5204 are cluster galaxies while NGC 6384 is in the field.

Table 2.2: Detector Parameters

Detector	Readnoise (e^-)	Dark Current	Gain (e^-/DN)
MMT Loral CCD (old)	7	$36 e^-/hr$	2.2
MMT Loral CCD (new)	6.3	$6.3 e^-/hr$	2.5
MDM RCA CCD	35	$7.2 e^-/hr$	17
NICMOS (old)	70	$40 e^-/s$	15.3
NICMOS (new)	70	$40 e^-/s$	15.3

2.2 The Observations

Observations of three kinds were taken over the period May 1991 to December 1993. Longslit spectra with spatial resolution, spectral images, give the value of Mgb at different positions within a galaxy. Optical and infra-red imaging give optical infrared colors at the same positions observed with the longslit. Table 2.2 list some critical parameters of the various detectors used. Table 2.3 indicates which exposures and how many are available for each galaxy. Observations listed by galaxy are given in Table 2.4. The three kinds of observations are discussed in turn.

2.2.1 Spectral Imaging

Each of the ten galaxies is observed using the red channel spectrograph on the Multiple Mirror Telescope (MMT). A $3'$ longslit of $2''$ width is used with both 300l and 600l gratings resulting in resolutions of 18\AA at a dispersion of $3.22\text{\AA}/\text{pixel}$ and 9\AA at a dispersion of $1.62\text{\AA}/\text{pixel}$ respectively. The low resolution spectra cover 3600\AA to 6000\AA . One grating is used for each night. Two positions in each galaxy are observed at least twice with the 300l grating and once with the 600l grating. In most cases the position of the slit is determined by two bright sources seen on the guider TV. Typically these are the galaxy's center and a foreground star or bright knot in the galaxy. Otherwise the position of the slit is not well determined. Sky is obtained at one end of the slit.

A typical MMT run consists of 2-3 program objects, 2-4 standard star exposures, and 1-4 standard galaxy exposures. Quartz lamp and twilight exposures are taken at the beginning and end of each night. Zeros are also taken at the beginning and end of each night. Dark exposures are taken at the

Table 2.3: Data Acquisition as of December 1993

Galaxy	Pos1 ^a 300l	Pos2 300l	Pos1 600l	Pos2 600l	B ^b	V	R	I	J ^c	H	K
NGC 772	2	2	2	0	2	3	3	3	4	4	4
NGC 949	2	2	1	1	1	1	1	2	5	5	8
NGC 2268	2	2	1	1	1	1	1	1	0	0	0
NGC 2701	2	2	1	1	2	2	2	2	5	4	6
NGC 3338	2	2	1	1	2	1	1	1	3	3	3
NGC 3782	2	1	2	1	2	3	2	1	3	3	7
NGC 4654	2	2	2	2	1	1	1	1	3	3	6
NGC 4713	2	1	1	1	1	1	1	1	3	3	4
NGC 5204	2	2	2	2	1	1	1	1	4	3	4
NGC 6384	2	2	3	2	2	1	3	1	9	5	9

^aColumns marked Pos1 or 2 indicate the number of exposures at that slit position.

^bColumns B, V, R, & I are the number of exposures taken in that filter.

^cColumns J, H, & K are the number of sequences of exposures taken in that filter.

end of each night. The dark exposures are 45 minutes same as the galaxies. The comparison lamps used are Helium, Neon, and Argon and sometimes Mercury and Cadmium. One comparison lamp exposure is taken before and after long exposures. A comparison lamp exposure is taken before or after short exposures.

In order to determine the sensitivity function of the charged-coupled device (CCD) spectrophotometric standard stars are observed. The stars are from the *IIDS Standard Star Manual* [Str77] which is composed of the spectral energy distributions of Oke and Stone [Oke74, Sto77]. The galaxies are spatially resolved along the slit. Therefore each point along the slit must be calibrated. So the stars are scanned along the slit at a rate of 10'' per second or 20'' per second.

Stars from the Lick stellar library [WFGB94] are also scanned along the slit. These observations serve two purposes: (1) to calibrate variations of line strength along the slit due to the instrument-telescope system and (2) to provide a transformation to the Lick system of spectral indices. Elliptical galaxies were also observed but not on every run. The four slit positions discussed later are not accompanied by elliptical data. These ellipticals have been observed previously and have line indices measured on the Lick system. They are also used to check the line strength measurements.

A galaxy is observed for 45 minutes. During this time the MMT mirrors have to be stacked at least once. Depending on seeing and position of the telescope the mirrors have to be stacked up to three times in one 45 minute exposure. Stacking consists of pausing the exposure and allowing the technical assistant to re-align the mirrors on the guide star. Pausing an exposure means stopping the clock and closing the shutter. Data reduction is discussed in Chapter 5.

2.2.2 Optical Imaging

The BVRI imaging is carried out at the Michigan-Darmouth-MIT (MDM) 51 inch McGraw Hill telescope. Each galaxy is observed at least once in each filter. Many of the nights are photometric (see Table 2.4). An RCA 330×512 CCD is used for most of the observations. There are a few taken with the WYLBUR 2048×2048 but those are not presented here. Quartz lamps and twilights are taken in each filter at the beginning and end of each night. Darks are taken at the end of the night and the afternoon of the following day. Different sets of darks were taken to match the different exposure times for the star and galaxy images. Zeros are taken at the beginning and end of each night. Landolt CCD fields are used for standard stars [Lan73, Lan92]. To get exposures of significant length the stars are taken out of focus. The amount of defocus is changed with the filter. The standards cover airmasses between 1.0 and 2.0, B−R between -0.36 and 2.34, and are taken throughout the night.

In the work discussed in the remainder of this document only the B and R data are considered because the June 1992 observing run has the highest photometric quality. The V and I data are still useful and will be discussed in future work. Presently priority is given to B and R. Data reduction is discussed in Chapter 4.

2.2.3 Infrared Imaging

The JHK work is done using the NICMOS 256×256 InSb array on the Steward Observatory's 61 inch at the Catalina site. Two IR arrays are used. Every galaxy except NGC 2268 is observed

numerous times (see Table 2.4). NGC 2268 is above the declination limit of the telescope.

The NICMOS array allows the observer to sum pixel values before readout. This is called coadding. For example, specifying an exposure time of 1 second with 2 coadds results in an image that is the sum of two 1 second exposures.

The galaxy observations are carried out in wobble-and-jitter mode. The galaxy exposures are shifted by random amounts so that array artifacts and cosmic rays can be filtered out during data processing. This mode consists of specifying a sky offset and random offset. The size of sky offsets ranges between 30 and 350 arcminutes. The first exposure is on sky. Then the galaxy is positioned within the detector array with a random offset. The random offset is specified for each sequence. It is chosen to move the galaxy significantly yet keep it within the field of view.

Elias [EFMN82] standard stars are observed in mapping mode. The stars are taken out of focus otherwise they saturate the detector even for the shortest exposure time. The amount of defocus is changed with the filter. Darks are taken at the end of the night. One set of darks is taken for each set of exposure times and coadds. Zeros are taken at the beginning and end of each night. Data reduction is discussed in Chapter 6.

The work in the remainder of this document makes use of only the K images. The J and H images will be used in future work. Only one infrared magnitude is required for the present work.

Table 2.4: Continued

NGC	Pos/Exp	Telescope	Instrument	Grating/Filters	Dectector	Date	Weather
6384	1a	MMT	Red Channel	3001	TI 800×800	09 JUN 1993	clear
	1a					10 JUN 1993	clear
	1b						
	2a					13 MAY 1991	clear
	2b					14 MAY 1991	clear
	1b						clear
	2a					03 SEP 1991	partly cloudy
	2b						partly cloudy
	1b					06 MAY 1992	clear
	2a					12 JUN 1993	clear
	2b						clear
	1c					13 JUN 1993	clear
772		MDM 1.5m	CCD Camera	B,R	RCA 330×512	25 JUN 1992	photometric
						26 JUN 1992	photometric
						01 JUL 1992	photometric
						02 JUL 1992	clear
						20 APR 1992	clear
						21 APR 1992	partly cloudy
						22 APR 1992	mostly clear
						23 APR 1992	mostly clear
						05 SEP 1992	partly cloudy
						07 JUN 1993	clear
						08 JUN 1993	clear
						09 JUN 1993	clear
		Steward 61"	NICMOS	K	InSb 256×256		
		MMT	Red Channel	3001	TI 800×800		
						03 SEP 1991	partly cloudy
						04 SEP 1991	mostly cloudy
							mostly cloudy
							mostly cloudy
						19 NOV 1992	partly cloudy
							partly cloudy
						12 OCT 1993	partly cloudy
						13 OCT 1993	partly cloudy

Table 2.4: Continued

NGC	Pos/Exp	Telescope	Instrument	Grating/Filters	Dectector	Date	Weather
		MDM 1.5m	CCD Camera	B,V,R,I	RCA 330×512	14 DEC 1992 15 DEC 1992	partly cloudy partly cloudy
949	2a	MMT	Red Channel	300l	TI 800×800 Lorel 1200×800 ^a	03 SEP 1991 18 NOV 1992	partly cloudy clear clear clear
	1a						
	1b						
	2b						
	1a			600l		12 OCT 1993	partly cloudy partly cloudy
	2a	MDM 1.5m Steward 61"	WYLBUR NICMOS	B,V,R,I K J J,H,K	Lorel 2048×2048 InSb 256×256	05 DEC 1992 23 JAN 1992 26 JAN 1992	partly cloudy partly cloudy clear clear
						02 SEP 1992	partly cloudy
						04 SEP 1992	partly cloudy
						05 SEP 1992	partly cloudy
						05 DEC 1993	clear
						06 DEC 1993	partly cloudy
						07 DEC 1993	partly cloudy
4713	1a	MMT	Red Channel	300l	TI 800×800	05 MAY 1992	clear
	1b						clear
	2a				Lorel 1200×800	28 JAN 1993	partly cloudy
	1a			600l		13 JUN 1993	clear
	2a	MDM 1.5m	CCD Camera	B,R	RCA 330×512	30 JUN 1992	clear
		Steward 61"	NICMOS	B,V,R,I J,K H	InSb 256×256 InSb 256×256	01 JUL 1992 22 APR 1992 23 APR 1992	photometric photometric mostly clear mostly clear
3338	1a	MMT	Red Channel	300l	TI 800×800	06 MAY 1992	clear
	1b						clear
	2a						clear
	2b				Lorel 1200×800	28 JAN 1993	partly cloudy

Table 2.4: Continued

NGC	Pos/Exp	Telescope	Instrument	Grating/Filters	Dectector	Date	Weather
	1c						partly cloudy
	1d						partly cloudy
	1a			600l		30 JAN 1993	partly cloudy
	2a						partly cloudy
	1b					12 JUN 1993	clear
		MDM 1.5m	WYLBUR	B,V,R,I	Lorel 2048×2048	05 DEC 1992	partly cloudy
		Steward 61"	NICMOS	K	InSb 256×256	20 APR 1992	clear
				J		21 APR 1992	partly cloudy
3782	1a	MMT	Red Channel	300l	TI 800×800	06 MAY 1992	clear
	1b						clear
	2a				Lorel 1200×800	28 JAN 1993	partly cloudy
	1a			600l		30 JAN 1993	partly cloudy
	2a						partly cloudy
	1b					12 JUN 1993	clear
		MDM 1.5m	CCD Camera	B,R	RCA 330×512	29 JUN 1992	photometric
				B,V,R,I		02 JUL 1992	clear
						15 DEC 1992	partly cloudy
		Steward 61"	NICMOS	K	InSb 256×256	23 JAN 1992	clear
				J		26 JAN 1992	clear
				K		20 APR 1992	clear
				J		21 APR 1992	partly cloudy
				J,K		22 APR 1992	mostly clear
				H		23 APR 1992	mostly clear
				J,H,K	New array	10 JUN 1993	clear
						06 DEC 1993	partly cloudy
2268	1a	MMT	Red Channel	300l	Lorel 1200×800 ^a	18 NOV 1992	clear
	1b						clear
	2a					19 NOV 1992	partly cloudy
	2b						partly cloudy
	1a			600l		13 JUN 1993	clear
	2a					12 OCT 1993	partly cloudy

Table 2.4: Continued

NGC	Pos/Exp	Telescope	Instrument	Grating/Filters	Dectector	Date	Weather
		MDM 1.5m	CCD Camera	B,V,R,I	RCA 330×512	14 DEC 1992	
2300	1a	MMT	Red Channel	300l	Lorel 1200×800 ^a	18 NOV 1992	clear
	1b						clear
	1c					28 JAN 1993	partly cloudy
	1d			600l		30 JAN 1993	partly cloudy
2681	1a	MMT	Red Channel	300l	Lorel 1200×800 ^a	18 NOV 1992	clear
2634	1a	MMT	Red Channel	300l	Lorel 1200×800 ^a	19 NOV 1992	partly cloudy
221	1a-g	MMT	Red Channel	300l	Lorel 1200×800 ^a	19 NOV 1992	partly cloudy
	1h-l			600l	Lorel 1200×800	12 OCT 1993	partly cloudy
224	1a-g	MMT	Red Channel	300l	Lorel 1200×800 ^a	19 NOV 1992	partly cloudy
	1h-m			600l	Lorel 1200×800	12 OCT 1993	partly cloudy
2701	1a	MMT	Red Channel	300l	Lorel 1200×800 ^a	19 NOV 1992	partly cloudy
	1b						partly cloudy
	2a					28 JAN 1993	partly cloudy
	2b						partly cloudy
	1a			600l		30 JAN 1993	partly cloudy
	2a						partly cloudy
		MDM 1.5m	WYLBUR	B,V,R,I	Lorel 2048×2048	05 DEC 1992	partly cloudy
		Steward 61"	NICMOS	K	InSb 256×256	23 JAN 1992	clear
				J		24 JAN 1992	mostly cloudy
						26 JAN 1992	clear
				K		20 APR 1992	clear
				J		21 APR 1992	partly cloudy
				H		23 APR 1992	mostly clear
				J,H,K	New array	05 DEC 1993	clear
						06 DEC 1993	partly cloudy
						07 DEC 1993	partly cloudy

Table 2.4: Continued

NGC	Pos/Exp	Telescope	Instrument	Grating/Filters	Dectector	Date	Weather
7626	1a	MMT	Red Channel	600l	Lorel 1200×800	12 JUN 1993	clear
	1b					12 OCT 1993	partly cloudy
	1c					13 OCT 1993	partly cloudy
7332	1a	MMT	Red Channel	600l	Lorel 1200×800	12 OCT 1993	partly cloudy
	1b					13 OCT 1993	partly cloudy
5846	1a	MMT	Red Channel	600l	Lorel 1200×800	12 JUN 1993	clear
6181	1a					13 JUN 1993	clear
6411	1a						
7454	1a					13 OCT 1993	partly cloudy

^aThis CCD had a problem with the bias.

PART II

**DATA PROCESSING AND
CALIBRATION**

CHAPTER 3

CCDS AND IR ARRAY BASICS

This chapter is an introduction to CCDs and IR arrays. It explains the basic physics and why and how they are calibrated. The chapter is closed with a brief explanation of the software used in this work.

3.1 CCD Basics

A basic description of how a charge-coupled device, CCD, works is given. This will serve as a framework for terminology and concepts used in this and later chapters. A more detailed and rigorous discussion may be found in [JE92]. A CCD is a silicon wafer which has been divided electronically into a two dimensional grid of pixels. Each pixel is defined by an electronic potential. A positive potential is maintained at the position of each pixel and a smaller potential around it by the electronic circuitry attached to the silicon. The pixels are arranged in columns. The columns are isolated from one another by regions of zero potential. A photon is absorbed in the silicon by dislocating an electron from the crystal lattice. This is the photoelectric effect. The electrons now move through the silicon to the nearest and largest positive potential. Thus while the CCD is exposed to light electrons accumulate in the potential well of each pixel. Since electrons migrate to the nearest pixel any spatial information in the light (i.e. the image) is preserved. Note that the photoelectric effect in silicon occurs for photons with energies in the range 1.1eV to 10 keV. That corresponds to wavelengths from the soft x-rays to the near infrared.

The information in the CCD is transferred to a computer by a process called "readout". During readout the electronics are clocked. This means that the potentials defining the pixels are changed. They are changed such that the electrons in one pixel are shifted to the next pixel. In fact each

column in a CCD is what an electrical engineer would call a shift register. So as the electronics are clocked the electrons in a row of pixels are shifted to the next row. It is equivalent to say the electrons are shifted along the columns. At the last row the electrons are shifted into the serial register. This is just another shift register that is arranged perpendicular to the others. So each column of the CCD empties into a pixel in the serial register. When electrons are shifted into the serial register clocking of the rows stops while the serial register is readout. The electrons in the serial register are shifted along just as in the columns. The electrons in the last pixel of the serial register are shifted into an amplifier and analog-to-digital converter, A/D. The electrons are detected by converting their charge into a voltage, amplifying the voltage, and converting it to a data number. This number is stored in computer memory¹. When the serial register has been readout clocking of the rows resumes filling the serial register again. Once the charge in the last pixel has been detected and stored in memory the CCD has been readout. Once in memory a pixel is simply an element in a two-dimensional array.

There are several subtleties that must concern the observer. They are bias, dark current, read noise, response, cosmic rays, and bad pixels. Bias refers to a voltage maintained at the point where the electrons are detected. The bias value is selected to make the best use of the dynamic range of the A/D. For example, a 16 bit A/D can only output 65536 different data numbers. However, the input can range from 0 electrons to the full well which is on the order of 150,000 electrons. To cover the full range one could use a bias near zero and gain of two. So even when no electrons are present a bias voltage is may still be detected and converted to a data number. This is the minimum voltage and corresponds to a minimum data number. When electrons are present the detected voltage is the voltage due to the electrons plus the bias voltage. That is, the bias is added to the detected signal. The bias voltage varies with time. Hence it is necessary to measure its value frequently. This is accomplished by having the serial register readout more pixels than are physically present.

¹It is often referred to as a data number and is usually given units of data numbers, DN. Gain is then defined as the number of electrons required to generate one data number. Its units are usually given as e^-/DN

This is done for each row in the CCD. Essentially this samples the bias voltage when no electrons are present. In memory these extra measurements appear as columns appended to the array of data numbers. These columns are called the overscan or overscan region. During data processing these columns are used to determine the bias level. The number of extra columns is specified at the time of observation. It may be that the bias level varies during the readout of even a single row. This means each pixel has a different bias level and implies a two-dimensional pattern in the image. Hence the observer must also take calibration frames called zeros. As the name implies the observer simply takes a number of exposures with zero integration time. These images are used to subtract out the two-dimensional bias pattern. Use of the overscan and zeros will be discussed in detail in Chapters 4 and 5.

Photoelectrons are not the only electrons that move in the silicon lattice. Because the CCD is above absolute zero there is thermal motion. Electrons can be dislocated by thermal motion of the silicon atoms or previously dislocated electrons. Thus even when no light falls on the CCD electrons still collect in the potential wells of the pixels. This is a continuous process. Charge builds up over time until the CCD is readout. This is called dark current i.e. a change in charge with time when the CCD is not exposed to light. Each pixel can have a different dark current. During an exposure these thermal electrons accumulate along with the photoelectrons. Hence the detected voltage is the voltage due to the photoelectrons plus the voltage due to the thermal electrons plus the bias voltage. The observer is then required to take calibration images called darks. A dark is an exposure taken with the shutter closed. The length of a dark exposure must be equal to the exposure time used for the objects. If different integration times were used then darks should be taken for each integration time. In an emergency a long exposure dark can be scaled by the ratio of exposure times to a shorter exposure dark. However, there is no requirement that the dark be linear. This should be checked before scaling. More detail on how darks are used is discussed in Chapters 4 and 5.

Read noise is the uncertainty introduced at the amplifier. It depends on white noise, $1/f$ noise,

and the sensitivity of the amplifier. See [JE92] for more detail. The observer need not measure the read noise. It is usually provided by the manufacturer. It is required when estimating errors in aperture photometry and signal-to-noise ratio (S/N) calculations. It is usually given in units of rms electrons i.e. the read noise squared is in units of electrons.

The most important characteristic of a CCD is its linear response to changes in light intensity. A star that is twice as bright as another star will generate twice as many electrons in the CCD. The quantum efficiency, QE, of a CCD is the slope of this linear relationship. The QE is the probability that an incident photon will generate a photoelectron. If 9 electrons were generated for 10 photons then the quantum efficiency is 90%. Note that this is multiplicative. The number of detected photons is the number of incident photons reduced by a factor equal to the QE. The QE varies from pixel to pixel and with the wavelength of the incident photon. Variations from pixel to pixel impose a two dimensional pattern in the image of a light source. Comparing the brightness of objects seen in different parts of the image requires that this pattern be removed. Otherwise one source may appear brighter than another simply because its light fell on part of the CCD where pixels tended to have a higher QE. In fact the sources may have the same apparent brightness. The QE also changes with wavelength. This leads to a different two dimensional pattern in each filter. The wavelength dependence of the CCD response is called the sensitivity. Ideally the QE pattern would be revealed by illuminating the CCD uniformly at one wavelength (e.g. with a quartz lamp and integrating sphere). The intensity of light would be the same in each pixel. However, the instrument and telescope impose their own two dimensional pattern on the image. While the QE pattern varies from pixel to pixel the instrument-telescope pattern varies over sizes much larger than a pixel. All these variations together form the pattern seen in an image. This pattern will be referred to as the response pattern. Fortunately it is not necessary to separate the QE variation from the effects of the instrument and telescope. They are removed from the data together.

The process of removing the response pattern from the data is called flat-fielding. The calibration

images required are called flats. A flat is an exposure to a light source that illuminates the face of the CCD as uniformly as possible. Flats come in four basic varieties quartz lamps, dome flats, twilights, and sky flats. Quartz flats are exposures of quartz lamps. Quartz lamps are used for many short high signal exposures providing high S/N for the QE response. Dome flats are exposures taken of an illuminated white screen or spot on the dome or just the dome lights. They can serve the same purpose as the quartz flats although the illumination may not be as uniform. The pattern usually depends on the optical path taken by the light. The optical path between the quartz lamp and CCD may be different from that between a galaxy and the CCD. Therefore, the pattern in a quartz flat may be different from the pattern in a object exposure. Hence, it is necessary to take either dome flats or twilight flats (both if you are not familiar with the system). Twilight flats are exposures of the twilight sky. The disadvantage is that a statistically significant number of them is difficult to obtain given the length of twilight and number of filters in use. The advantage is that this optical path is most similar to that taken by galaxy light. Thus quartz flats and twilights are used in combination. Sky flats are exposures taken during the night of a "dark" part of the sky. These require exposures as long as the object exposures. In this case calibration is very simple because the sky flat is subtracted from the object image. However, when your exposure times are long (>15 minutes) sky flats take too much time. They are not discussed further here.

Flats must be taken in each filter or grating because of the wavelength dependence of the response pattern. For example the response pattern in a flat taken with an R filter will look softer than the pattern in a flat taken in B or V. The flats are used to create a model of the CCD's response pattern. In this work quartz flats and twilights are used in a two step process to remove the response pattern from object images. How these images are created and used are discussed in Chapters 4 and 5.

The response of a CCD is not linear over all light levels. Obviously the response will be non-linear when a pixel's potential well becomes filled with electrons. One must be careful not to over-exposure the object of interest. At the other extreme is a more subtle problem. Many older CCDs are non-

linear at very low light levels. The TI 800×800 is a good example. The response of a pixel does not become linear until a minimum light level is reached. This problem is avoided by pre-flashing the CCD. This entails illuminating the CCD with a weak light source just before the shutter is opened. This fills the potential wells of the pixels beyond the point where linear response begins. The pre-flash is not necessarily uniform. However, no extra calibration data is required because the pre-flash pattern will appear in the zeros. It will be subtracted away along with the bias pattern. For a more rigorous solution to this problem see [Gil92]. Modern CCDs should not require a pre-flash.

Besides photoelectrons and thermal electrons there can be electrons dislodged by charged particles i.e. a cosmic ray passing through or perhaps stopping in the silicon. When cosmic ray flux is lower e.g. on the ground or in short exposures it is possible to find and remove cosmic rays by hand. The preferred method is to take multiple exposures and filter out the cosmic ray hits via some combining operation. For example, combining 10 darks by selecting the median as the output in each pixel. For the long galaxy exposures the cosmic rays were removed by hand.

Bad pixels can be dealt with by hand also. In a modern device there will be very few deviant pixels. A bad pixel is simply one that does not respond, is dead, or is one that always has a high count. There could also be an unresponsive pixel that produces a perfectly reasonable number of electrons. Such a bad pixel is likely to go unrecognized.

A formula useful for reference in data processing is

$$I_{out} [DN] = g^{-1} [DN/e^-] \times (R [e^-/photon] \times I_{in} [photon] + B [e^-] + D [e^-]) \quad (3.1)$$

for each pixel in an image. I_{in} is the number of photons incident on the pixel. R is the response of the pixel to those photons. B is the bias level for that pixel. D is the electrons from dark current accumulated during the exposure in that pixel. g is the gain (electron to DN conversion). I_{out} is the data numbers readout for that pixel.

The error in the mean flux measured in a given aperture is determined by four quantities the

number of counts in the target, the number of counts in the background, the read noise, and the dark current. In the case where read noise and dark current are negligible the error is given by the square root of the number of counts. To give an accurate error estimate however the read noise and dark current must be taken into account. The S/N ratio for CCD image data is given by

$$S/N = \frac{N_s}{\sqrt{N_s + N_b + N_{\text{pix}}(1 + \frac{N_{\text{pix}}}{N_{\text{sky}}})(td + r^2)}}$$

where N_s is the strength of the object signal, N_b is the total background signal, N_{pix} is the number of pixels that contributed signal to the object, N_{sky} is the number of pixels that contributed signal to the background, t is the exposure time, d is the dark current, and r is the read noise [How92].

3.2 Basics of Infrared Arrays

For a detailed discussion of infrared arrays see [Joy92]. An infrared array works on the same physical principle, the photoelectric effect, as a CCD. The pixels are arranged in a grid. A pixel is defined by a positive potential where electrons are collected. Each pixel responds linearly to changes in intensity. Each pixel has a bias level and dark count. So it is still necessary to take zeros, darks, and flats. This is as far as the similarities go. The need for high sensitivity to infrared wavelengths requires the use of different materials in the construction of the array. In this case the material is InSb. These materials are not arranged into shift registers. Instead each pixel is readout independently. There is no shifting of electrons and hence no overscan. This implies that each pixel has its own bias level. Thus a bias pattern is implicit. Also the dark current does not build up at a constant rate. These differences have consequences for the observer. One cannot scale a dark taken at one exposure to use with an image at a different exposure. The bias variation can be rapid. For example, the second NICMOS instrument used in this study has a bias pattern that varies as lines are readout. This is due to an exponential decay in the circuitry of the detector². If this pattern shifts by the slightest amount it becomes difficult to remove the bias from the object data. However,

²M. Reike, private communication

it is the intensity of the infrared sky that most concerns the observer.

Exposure times must be kept very short to prevent over-exposing the array. Also the object of interest is much fainter than the sky. Hence the equivalent of a long exposure is created by taking many short exposures and combining them during data processing. One advantage is that the sky is so bright that it can be used to take flats. To make the most of the night the observer can use one of two techniques referred to as wobble-and-jitter mode and mapping mode.

Wobble-and-jitter mode is used for extended sources. This technique facilitates removal of cosmic ray hits and deviant pixel values during data processing. It also increases the effective sampling of the point spread function although the $1''$ to $3''$ seeing disk of the near-infrared data is on the border of being under sampled. This mode involves taking a sequence of images that alternate between sky and galaxy. Sky means a nearby region with few or no detectable stars or galaxies and no part of the target galaxy. Each object frame is offset randomly from the previous object frame. The size of the offset is input by observer at the telescope. The size is chosen such that the object is still contained within the field-of-view but in a slightly different position on the detector.

The sky images bracketing a galaxy image are used for both sky subtraction and flat-fielding. The average of the two sky images is subtracted from the galaxy. This has the effect of removing dark count, bias, and sky. A normalized version of the average sky is used for flat-fielding. This assumes the sky illuminates the array uniformly. This is a good assumption because the field of view is only three arc minutes. A flat-field is created as follows. Dark is subtracted from the two adjacent sky images. The two dark-subtracted sky images are averaged. This average image is normalized. The normalized average dark-subtracted sky is the flat-field. The flat-field is divided into the sky-subtracted images removing the response pattern. This procedure is followed for each object frame in a sequence of frames taken in wobble-and-jitter mode.

The processed object frames are offset in pixel value such that each image has a zero mean, median, or mode. The offset images are then shifted so that the object falls in the same position in

each frame. Then the shifted frames are combined, using a median, into one higher S/N image. This eliminates a deviant pixel because it no longer falls in the same position in the shifted frames. It also improves the sampling of the point spread function. However, this can not be taken advantage of because even the S/N of the combined images does not warrant the use of image restoration.

Mapping mode is used for point sources. It involves taking a sequence of images in a grid. The object is shifted to the next grid position after each exposure. The observer specifies a number of steps in declination and right ascension. Then one exposure is taken before each step. The result is a series of images wherein the star's position forms a grid pattern on the array. In this mode all the images are used to create an average sky image. Otherwise the processing is the same as for wobble-and-jitter mode. Even the shifting is still done, but in this case the offsets are due to the grid steps not jitter. Both of these modes are discussed further in Chapter 6.

3.3 Software

The Image Reduction and Analysis Facility (IRAF), a software package written and maintained by the National Optical Association of Observatories and the Interactive Data Language (IDL), a product of Research Systems Incorporated, are used for processing. The IRAF task IMARITH is used to perform arithmetic operations on images. It provides a simple way to manipulate many images in batch mode. Another task that is performed frequently is that of combining many images into a single image. The values in the output image are determined from the input values using some rule or filter like the mean or median for example. The IRAF task IMCOMBINE is used for this operation. It also produces a sigma image. The values in the sigma image are the standard deviations relative to the values in the output image. The reader may assume that IMARITH is used when images are added or multiplied and that IMCOMBINE is used when images are combined. IDL procedures are used for interactive cosmic ray removal, determining photometric transformations, and the like. Images are stored in Flexible Image Transport (FITS) format.

CHAPTER 4

OPTICAL IMAGE PROCESSING

This chapter describes the optical image processing performed to put the data in an exploitable form. A quirk in the bias level of MDM's RCA 330×512 CCD is describe first. Then an explanation of how the zeros and darks are processed and used is given. A discussion of flat-field processing using lamp and twilight images follows. Galaxy and star image calibration is explained. Finally the process of cosmic ray and bad pixel removal is detailed.

4.1 Overscan

The RCA 330×512 has a known problem with its bias level¹. After detecting a packet of electrons a residual voltage remains at the amplifier. This residual appears in the overscan region. After the last pixel of a row is readout the residual voltage decays slowly back to the true bias level. This occurs during the overscan. Figure 4.1 reveals this decay. In panel a) is a cross section of the overscan region. Each line in the plot represents the average row from different B images of the quartz lamp. Upon closer inspection in panel b) it is clear that the true bias level has not been reached. The overscan is only eight columns wide. This is obviously not enough to reach the true bias level². In this particular example the last column is 360 DN which is still four data numbers above the value from the zeros, 356 (see histogram in Figure 4.2). That is about 1.1%. The change over these eight columns is about 7%. The overscan region is not used to determine a bias level.

The distinct gradient evident in the zeros in Figures 4.2 and 4.3 is likely due to this same problem. Imposed on the gradient is a pattern of high and low columns. The pattern is the same in every row of an image but changes from image to image. The gradient does not change from image to image.

¹private communication G. Wegner

²private communication G. Wegner

Since an independent bias level is not available the zeros serve a dual purpose. They provide the bias level and the bias pattern. This carries with it the assumption that the bias level in the zero is the same as in the other images. That is, the bias level does not change significantly with time. However, panels c) and d) of Figure 4.1 show an increase of 2 DN over the night as do the histograms in Figures 4.2 and 4.3. A correction is made by using the morning and evening zero independently. When processing an image the zero which is closer in universal time (UT) to the observation is used. Getting the bias correct is critical to flat-fielding. If there is a significant residual bias the image cannot be flat-fielded. Instead the inverse of the response will appear in the image. In the future the decay of the bias level will be modeled. This will provide a prediction of the true bias level for each image.

4.2 Zeros

The zeros taken at the beginning of the night are combined into one median zero. The zeros at the end of each night are combined into one median zero image. The output image is called a combined zero and should not be confused with the individual input images. A median is used to select the value of each output pixel. A median is used to avoid contamination by cosmic ray hits. Even though the exposure time is zero, over the time it takes to readout 30 images it is likely that some of the frames have a cosmic ray hit. Example combined zeros are given in Figures 4.2 and 4.3.

This type of figure is used frequently. It has four panels. The left panel is a grey scale representation of the image under discussion. Darker means higher values. The axes are pixel positions. The top right panel is a histogram of the pixel values in the image. The mean, median, mode, sigma, and bin size are given. The mode is the value of the bin with the largest count for the shown bin size. The sigma is the standard deviation. The middle right panel is the average row from the image. The bottom panel is the average column.

The zero changes over the course of a night. Slight differences are apparent between the two

images and an offset is seen between the histograms. Figure 4.2 is from the beginning of the night while Figure 4.3 is from the end of the night. Hence over the night a shift of about 2 DN has occurred in the bias level. However, over a short time the bias does not change. This is evidenced in Figure 4.4. Shown there is the sigma image for the combined zero in Figure 4.2. It is clear from the histogram and grey scale that there is no significant variation between zeros taken at nearly the same time. Figure 4.5 illustrates that the variation in Figure 4.4 is not systematic and that the shift between the combined zeros is also in the individual zeros. In this figure the solid lines are the histograms of the individual zeros taken at the end of the night while the dotted lines are the histograms of the individual zeros taken at the beginning of the night. Each histogram has a bin size of 1 DN and has 1024 bins. The solid histograms are clearly shifted relative to the dotted ones. So, over the course of a night the bias level and pattern does change. This is taken into account by keeping morning and evening calibrations (zeros,darks,flats) separate. When an image is processed the zero closest to it in UT will be used for the zero correction.

4.3 Darks

Four five minute and four fifteen minute darks are taken at the end of each night. The evening combined zero is subtracted from each dark. Recall that this also removes the bias level. The zero-subtracted five minute darks are combined using a median. The same is done for the fifteen minute darks. The output images are called combined darks. Figure 4.6 shows a sample fifteen minute dark. Note that there is a gradient in the average row and column. This is likely due to a slight difference in the bias pattern in the zero and bias in the darks. Otherwise the dark is uniform. Figure 4.7 shows the sigma image for the fifteen minute dark. Note the high values in the pixels affected by cosmic rays. The histogram in Figure 4.6 shows 1.5 data numbers in 900 seconds. 0.0016 counts per second is a small rate. The CCD is read noise dominated. This is not surprising for older CCDs.

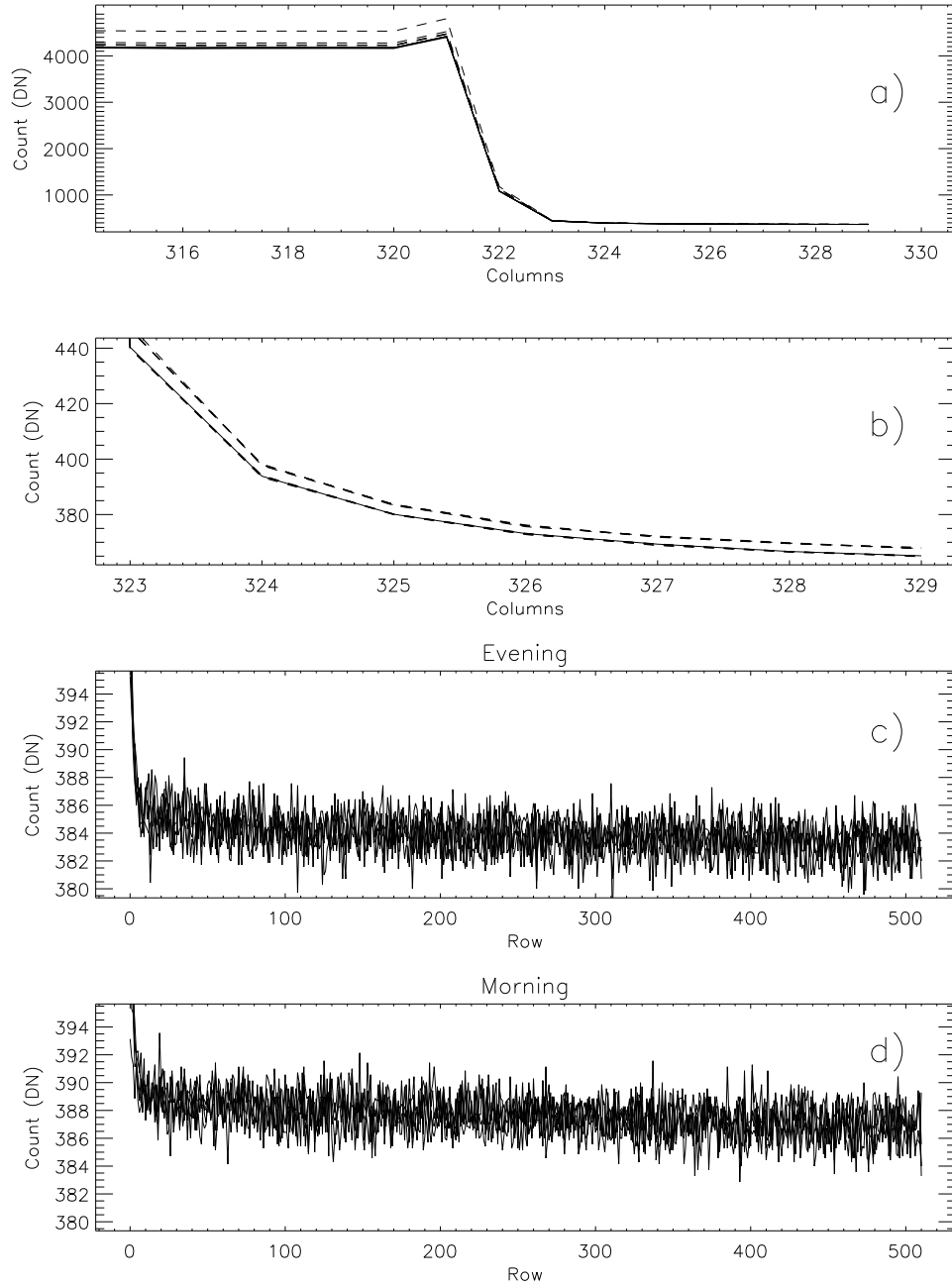


Figure 4.1: This is an illustration of the overscan region in images of the quartz lamp in B. a) This panel shows the average row for each zero image for one night. Each line represents a different image. b) This panel is a blowup of the overscan from panel a) showing that the bias level has not been reached. c) This shows the average overscan for all the evening lamp flats. Each line is from a different image. d) Same as c) for morning lamp flats. There is a difference of 2 DN.

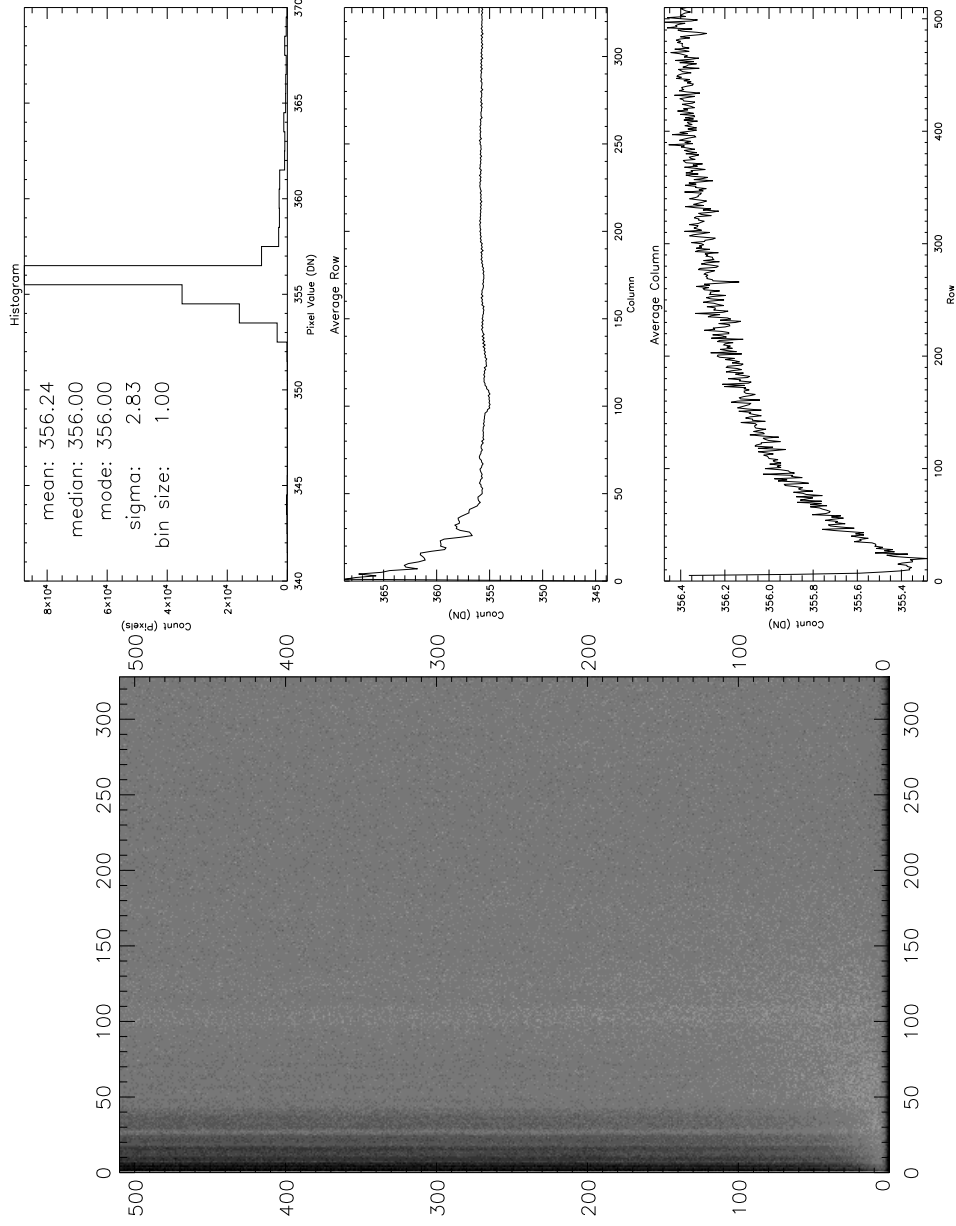


Figure 4.2: Example Evening Combined Zero for MDM: On the left is a grey scale representation of the image. On the right are three panels. The top panel is a histogram of the image displayed at left. The mean, median, mode, standard deviation, and bin size of the histogram are displayed. The average of all the rows in the image is displayed in the middle panel. The average of all the columns in the image is drawn in the bottom panel.

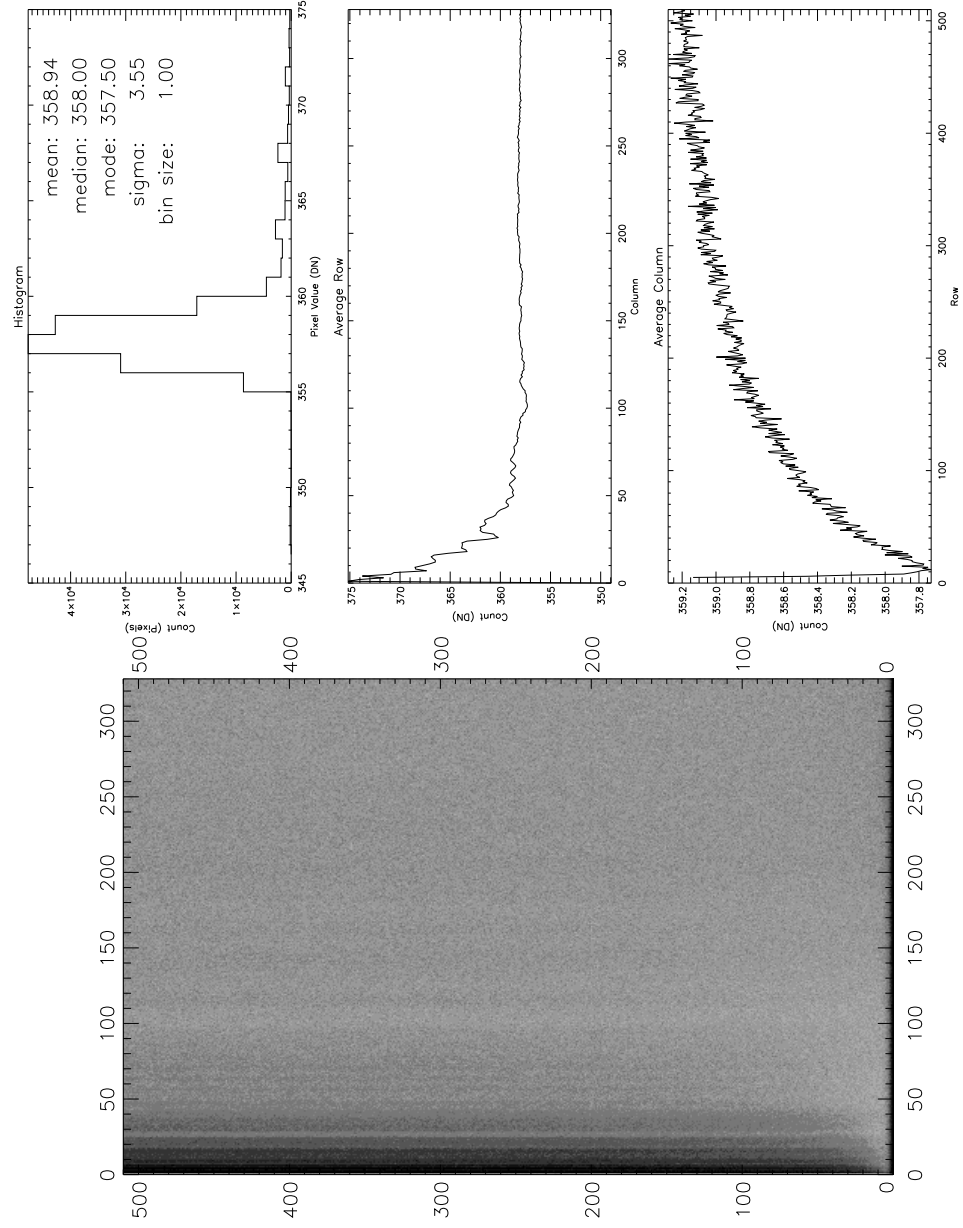


Figure 4.3: Morning Combined Zero for MDM: See Figure 4.2 for explanation of panels.

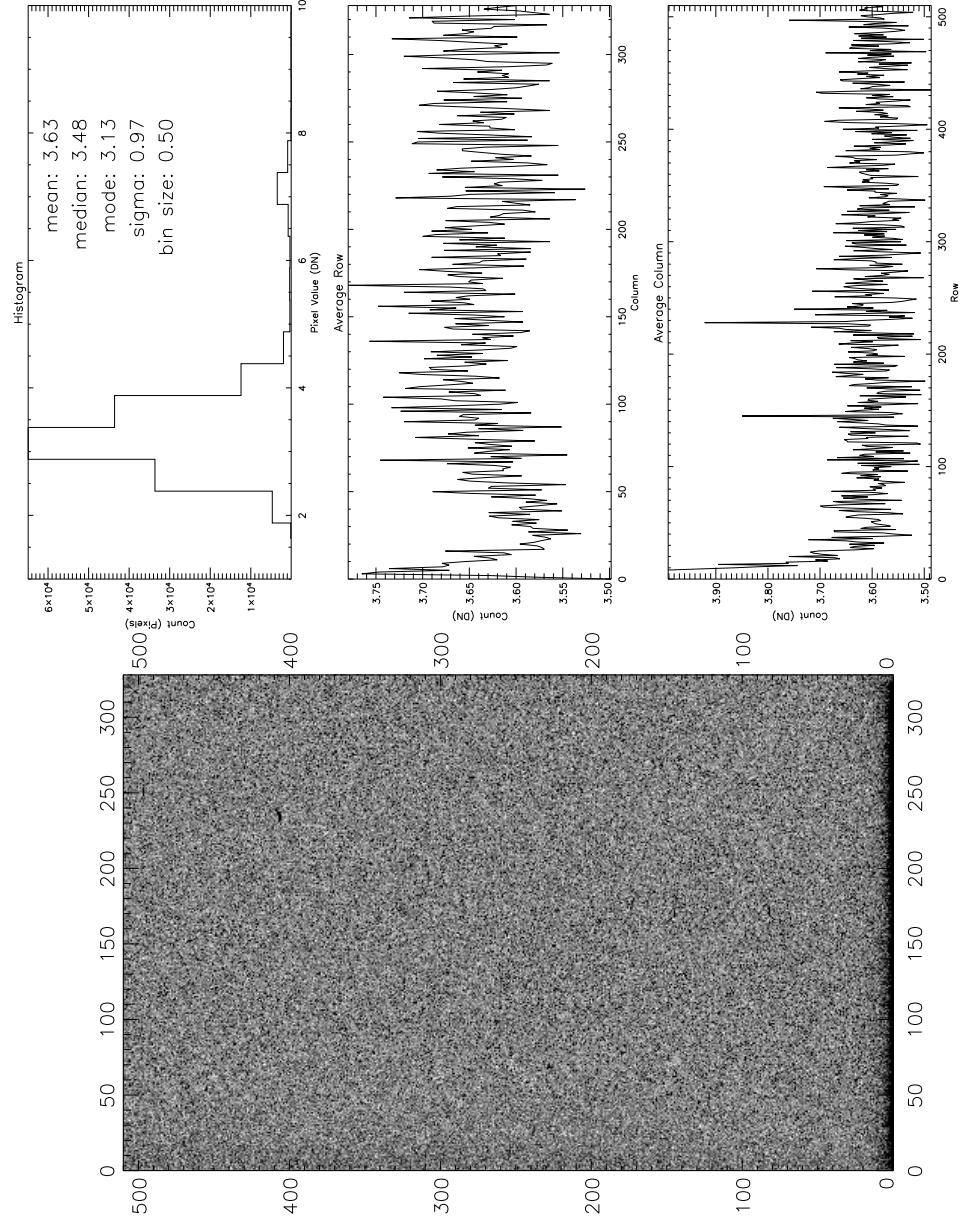


Figure 4.4: Standard Deviation of Morning Combined Zero for MDM: See Figure 4.2 for explanation of panels.

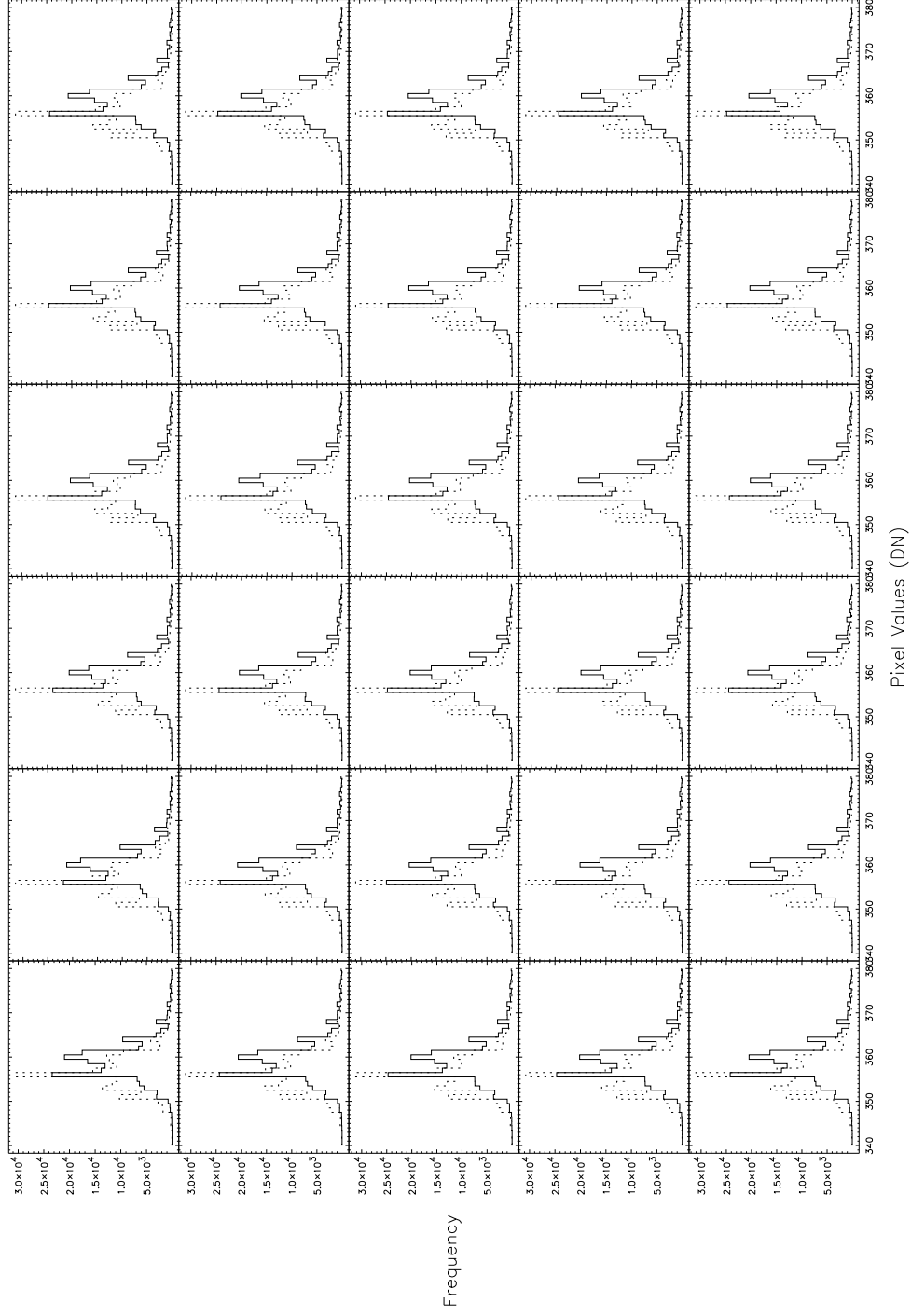


Figure 4.5: Histograms of Zeros: The bias varies slowly over the night. It does not vary significantly over a short time. The dotted lines are from the morning zeros. The solid lines are from the evening zeros for that night. All the morning zeros are shifted from all the evening zeros. Morning and evening zeros are kept separate. Each histogram has a bin size of 1 DN and has 1024 bins.

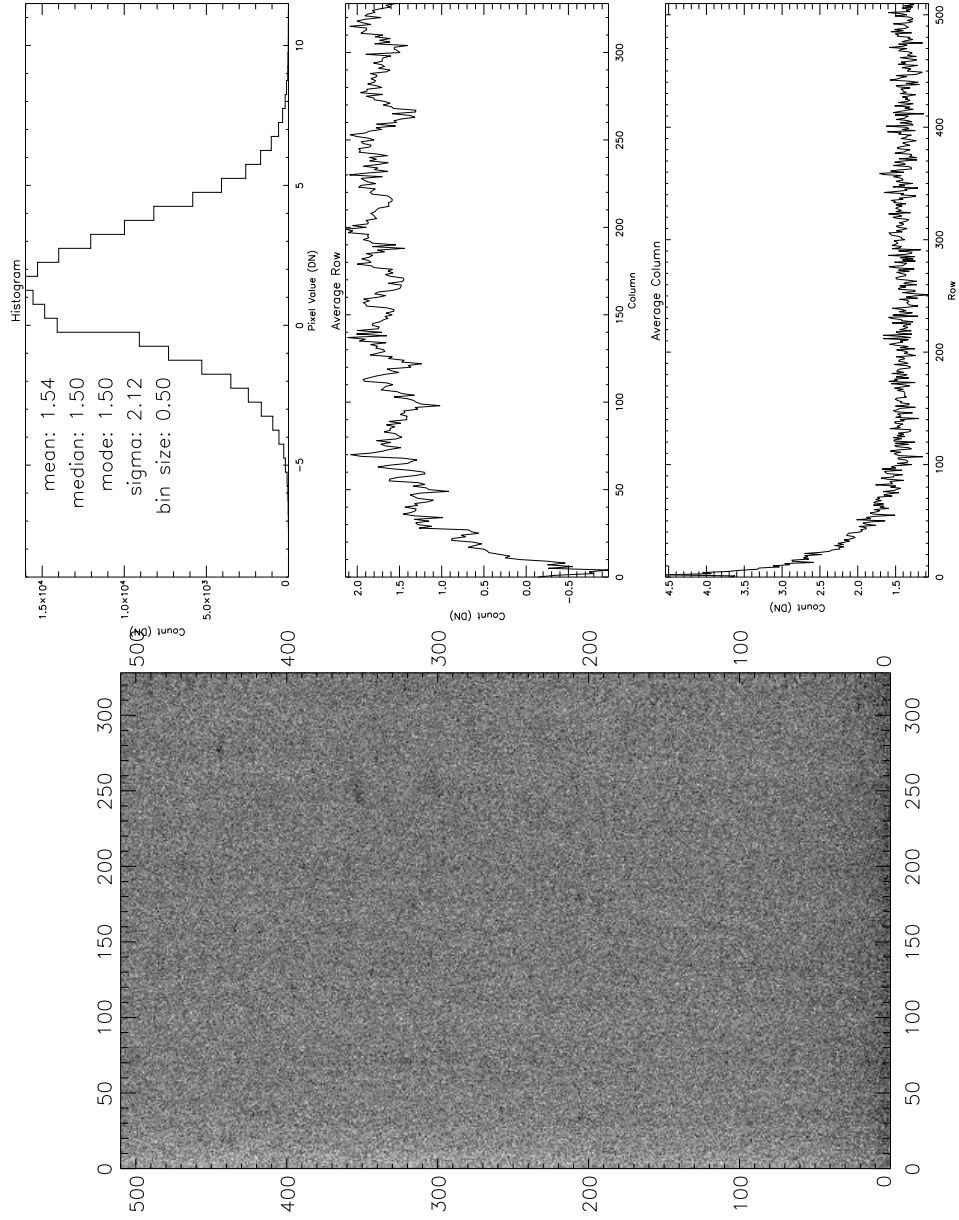


Figure 4.6: Evening Combined 900 Second Dark for MDM: The individual darks are zero subtracted before being combined using the median. (See Figure 4.2 for explanation of panels.)

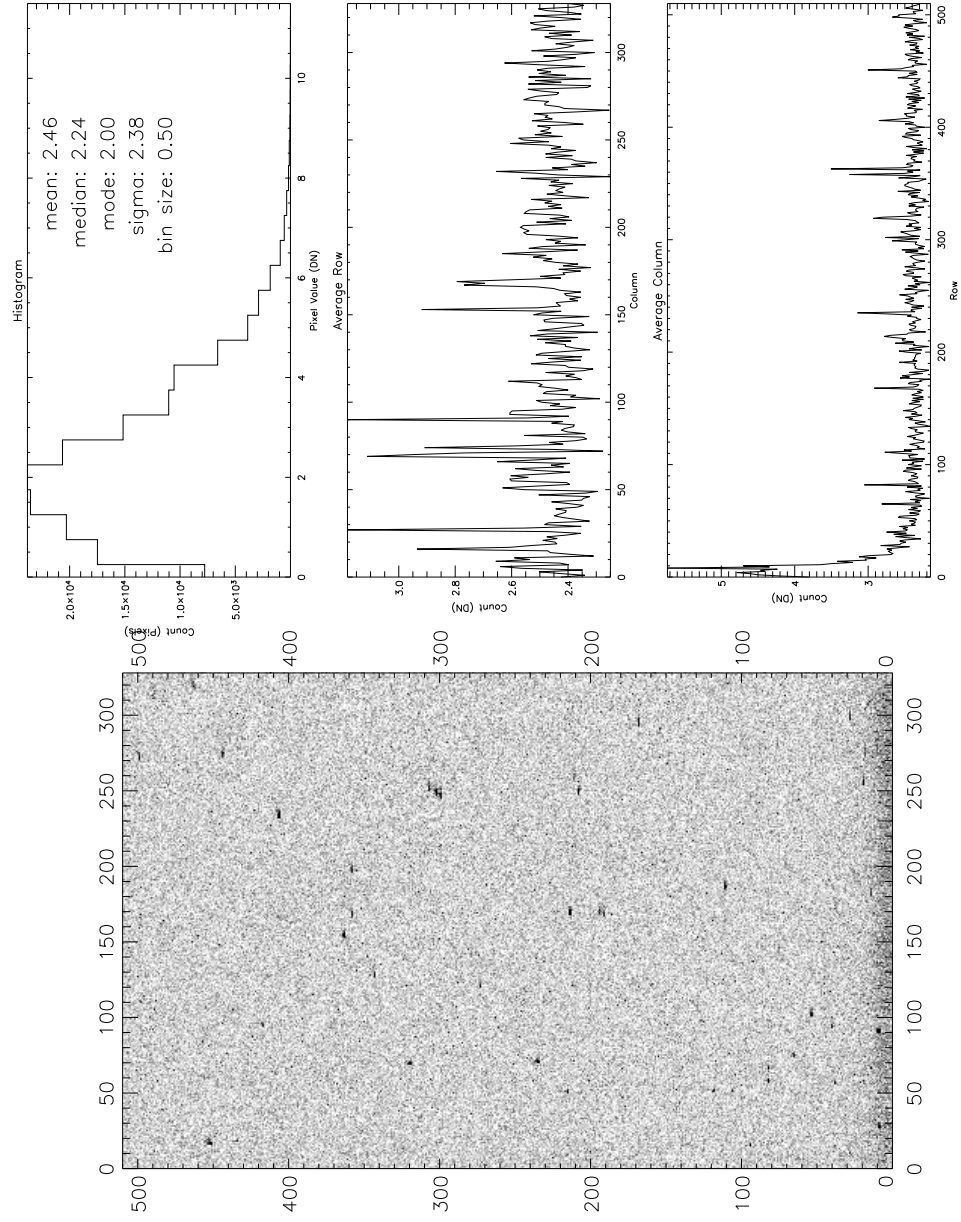


Figure 4.7: Standard Deviation of Evening Combined Dark for MDM: (See Figure 4.2 for explanation of panels.)

4.4 Flats

Five lamp flats are taken in B and R at the beginning and end of each night. The evening zero is subtracted from each lamp flat taken in the evening and the morning zero from the morning lamp flats. The zero-subtracted lamp flats are combined using a median in the same way as the zeros and darks were combined. The resulting images are normalized. This means that the image is divided by its average pixel value. The normalized image is called a lamp response. This is done separately for the B morning, R morning, B evening, and R evening lamp flats resulting in four different lamp responses. A sample morning B lamp response is shown in Figure 4.8, and a sample morning R lamp response is shown in Figure 4.9.

Five to eight twilight images are taken in B and R at the beginning and end of each night. The morning zero is subtracted from the morning twilights and the evening zero from the evening twilights. The morning B lamp response is divided into the zero-subtracted morning B twilights and the morning R lamp response into the zero-subtracted morning R twilights. The same is done for the evening twilights. The resultant images are examined for flatness. If they are uniform then the lamp response images are sufficient for flat-fielding. However, Figures 4.10 and 4.11 reveal that there is a residual pattern in the twilights. This is due to differences between the optical path taken by light from the lamp and the optical path taken by light from the twilight sky. This is especially important at MDM because the lamps are off axis. They are mounted around the aperture of the telescope. The twilights in each filter are combined using the median. However, the twilight sky brightness changes rapidly during the observations. Hence it is necessary to compensate for the different light levels and exposure times when combining the twilights. This is done by scaling each image by its exposure time and shifting its pixel values to a common mode. The combined images are normalized in the same way as the lamp flats. Thus B and R twilight responses are created for evening and morning. Figures 4.10 and 4.11 show examples of twilight response images. As a check the individual twilight images are processed and examined for flatness. Figure 4.12 is an

example individual morning twilight in B processed through flat-fielding. The frame is very flat. The remaining small gradients amount to less than 0.2% of the count in the average row or column. Figure 4.13 shows the same for an individual morning twilight in R. The image is not as flat as the B example. However, the gradients are less than 0.3% of the count in the average row or column.

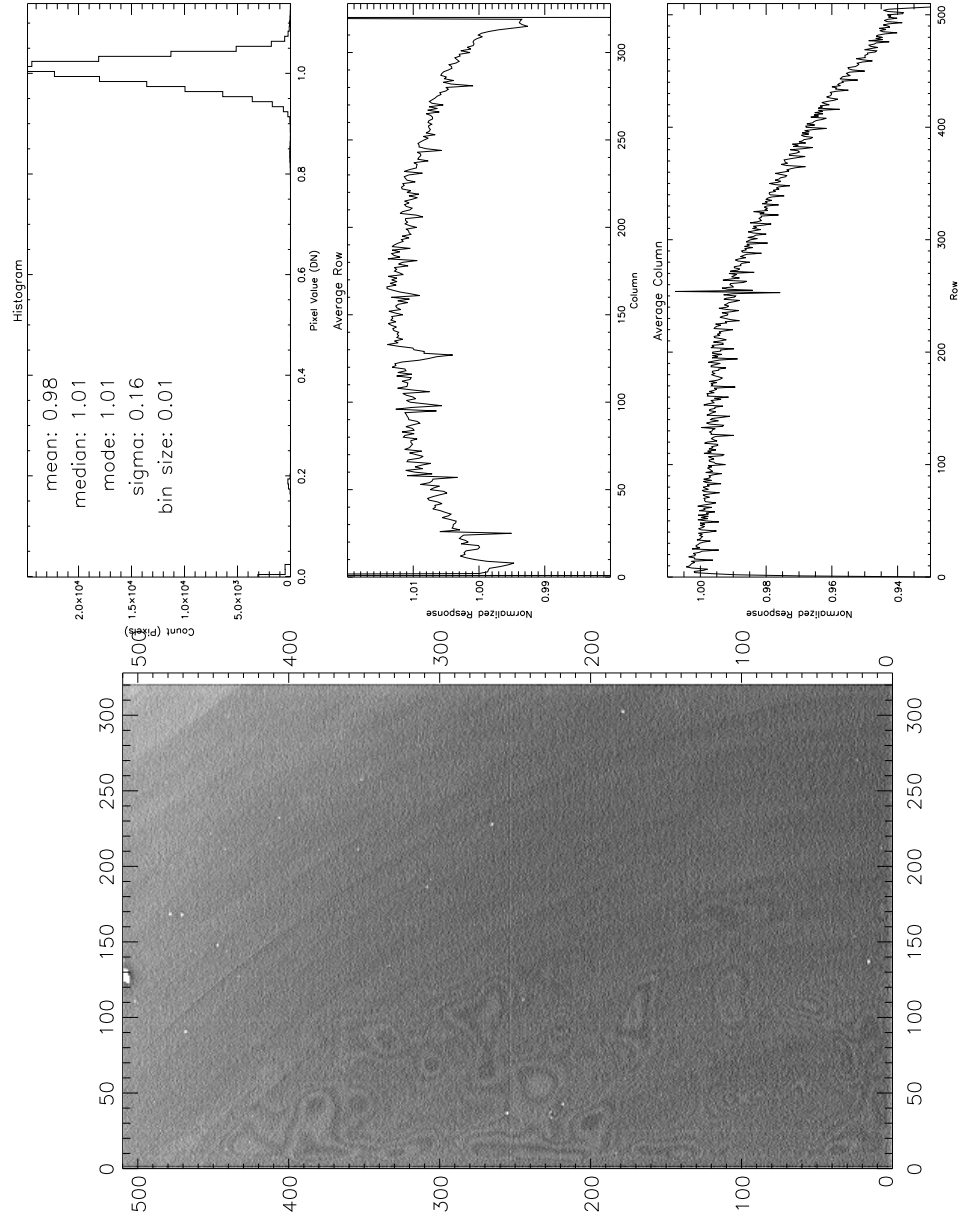


Figure 4.8: B Response to the Quartz Lamp: The B lamp images are zero subtracted then combined using a median. The combined image is divided by its mean resulting in the B response. (See Figure 4.2 for explanation of panels.)

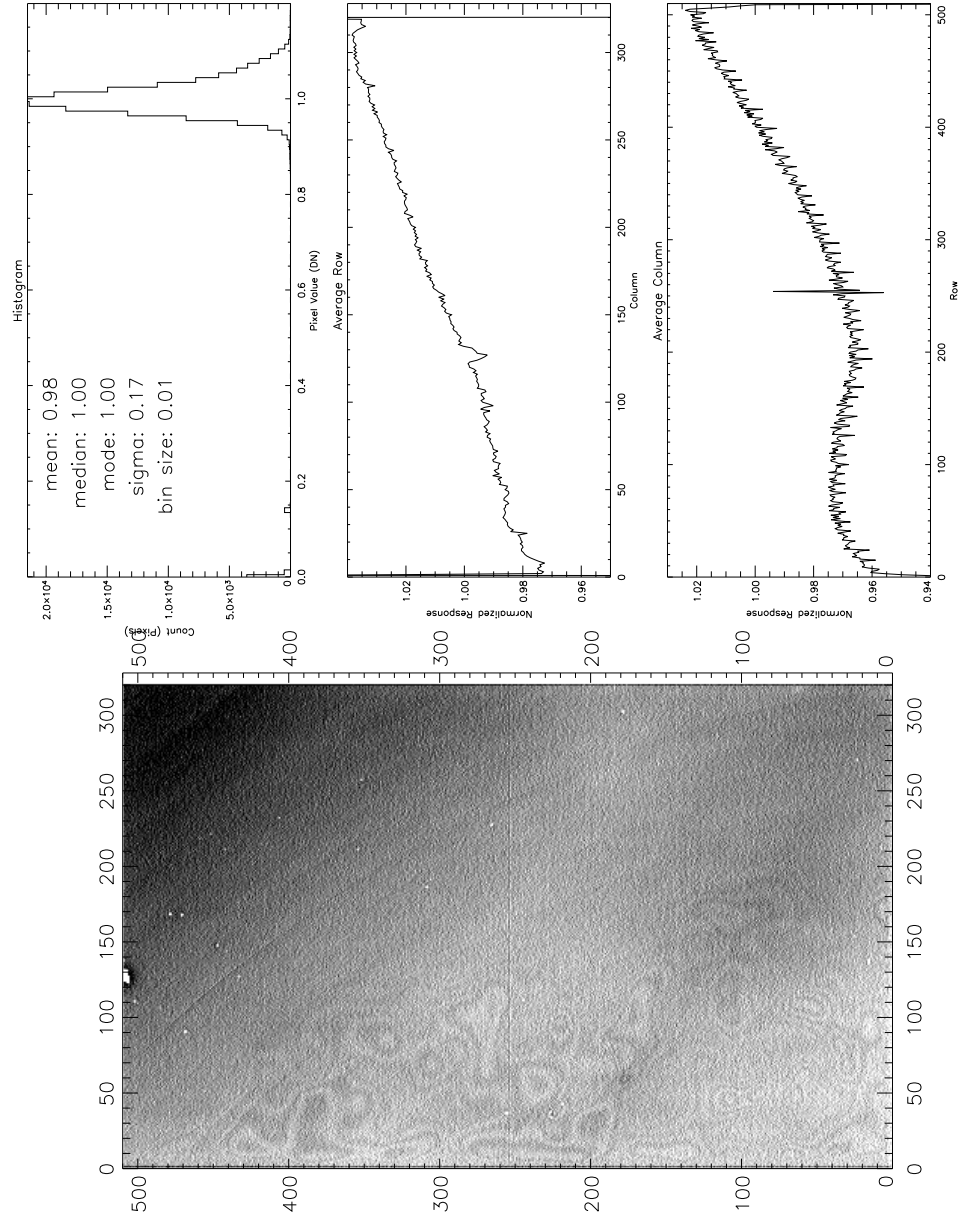


Figure 4.9: R Response to the Quartz Lamp: The R lamp images are zero subtracted then combined using a median. The combined image is divided by its mean resulting in the R response. (See Figure 4.2 for explanation of panels.)

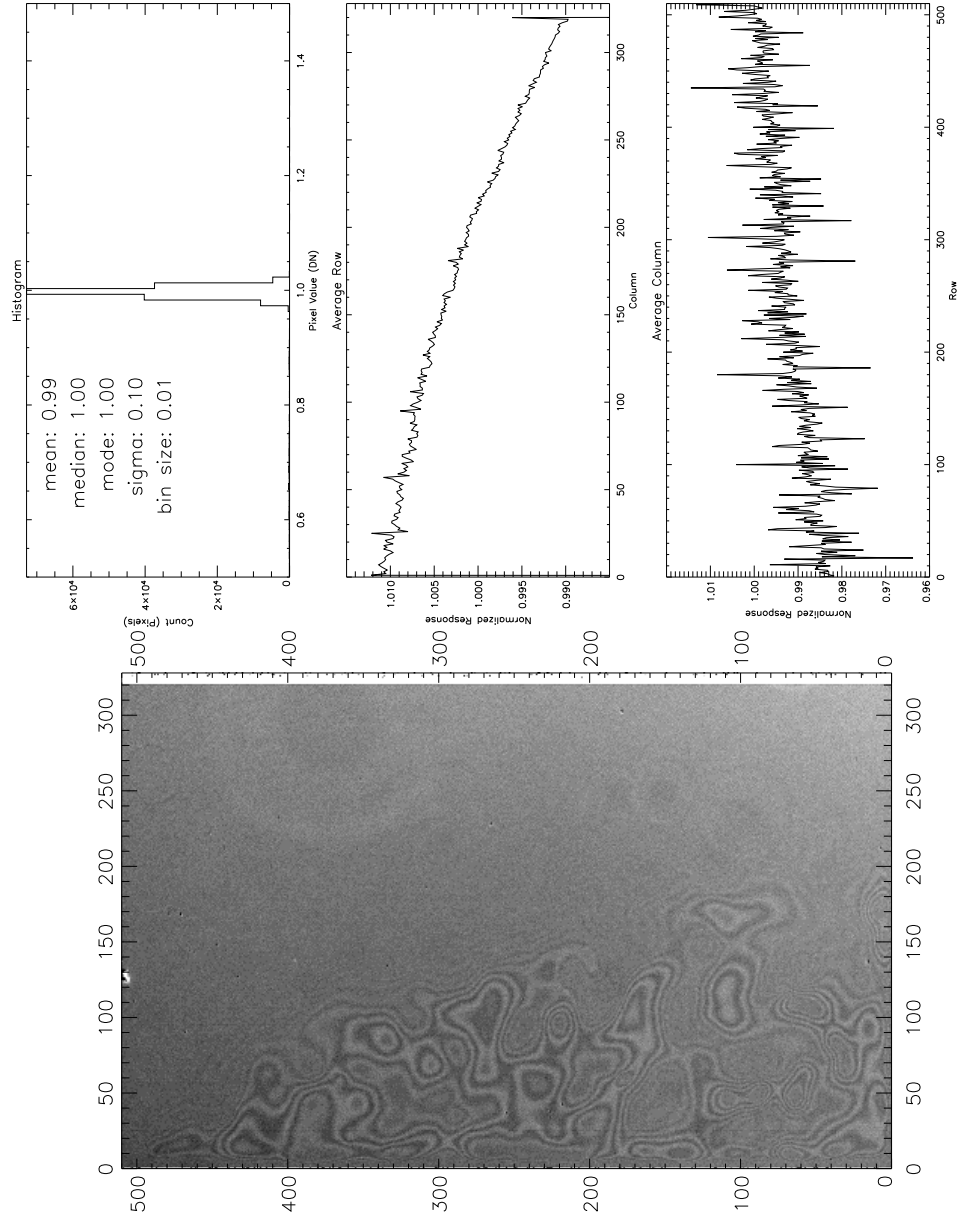


Figure 4.10: B Twilight Response at MDM: The twilight images are zero subtracted and divided by a lamp response. The resulting images are combined taking into account differences in exposure time and sky brightness. The combined image is normalized to obtain the twilight response. (See Figure 4.2 for explanation of panels.)

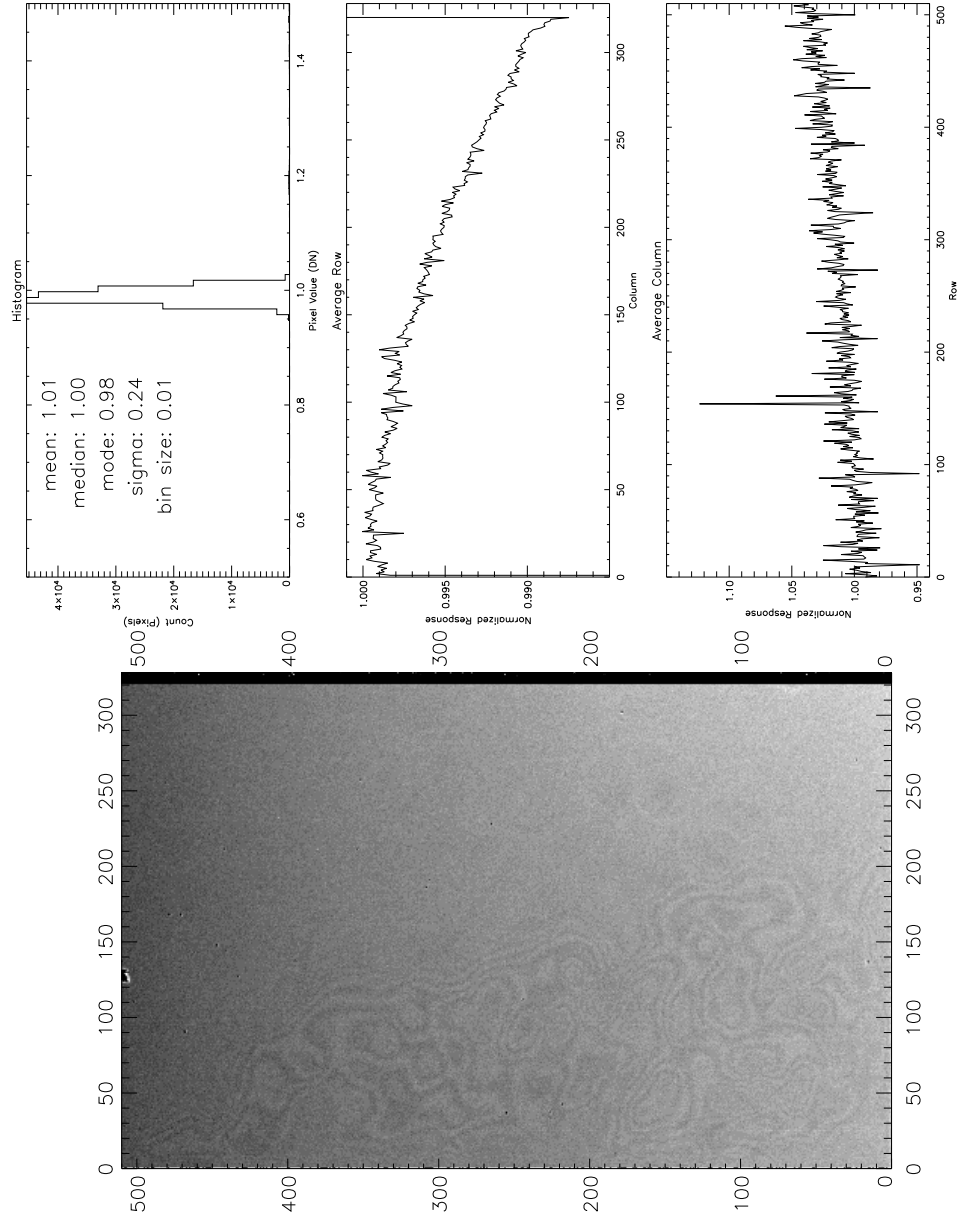


Figure 4.11: R Twilight Response at MDM: The twilight images are zero subtracted and divided by a lamp response. The resulting images are combined taking into account differences in exposure time and sky brightness. The combined image is normalized to obtain the twilight response. (See Figure 4.2 for explanation of panels.)

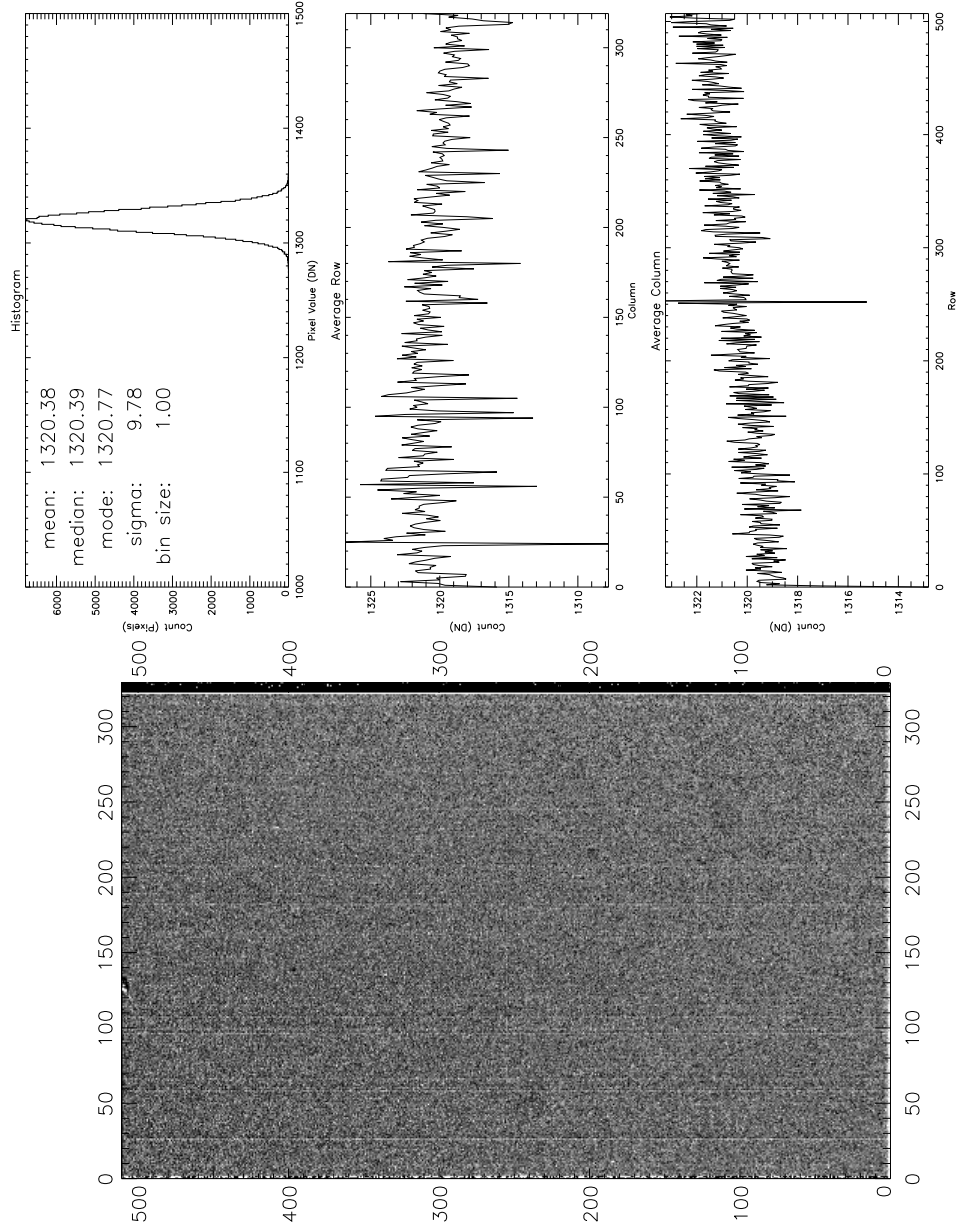


Figure 4.12: An Individual B Twilight that has been Flat-Fielded: The B lamp and twilight responses were used to flat-field this image. The remaining gradient across rows is 0.2%. (See Figure 4.2 for explanation of panels.)

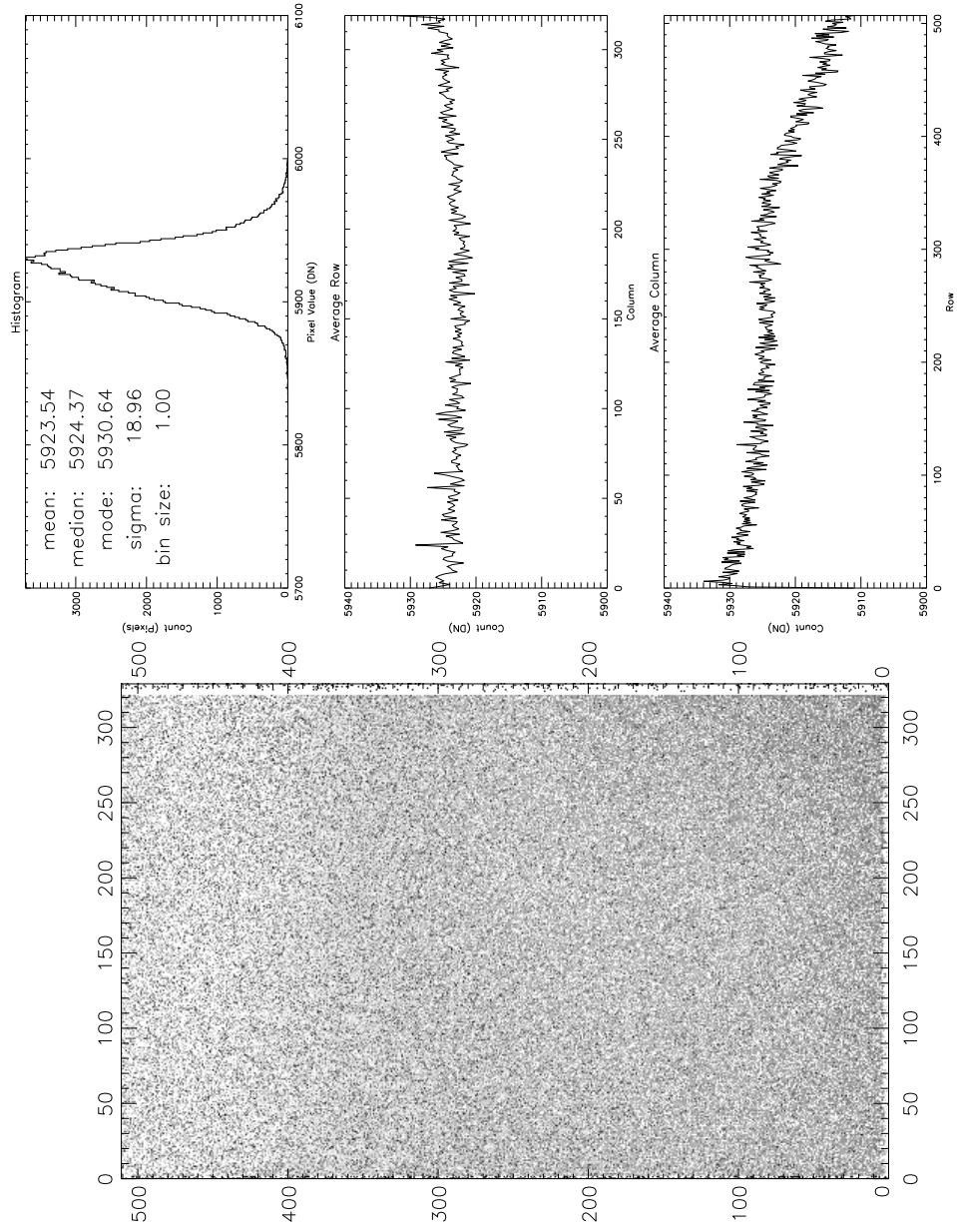


Figure 4.13: An Individual R Twilight that has been Flat-Fielded: The R lamp and twilight responses were used to flat-field this image. The remaining gradient across rows is 0.3%. (See Figure 4.2 for explanation of panels.)

4.5 Star and Galaxy Images

The processing of the remaining star and galaxy images is straight forward. A combined zero is subtracted from each image. The combined zero is chosen by the time of observation. The zero nearest the observation in UT is used for that observation. Then a five and fifteen minute combined dark is subtracted from all the exposures of five and fifteen minutes respectively. The galaxy images are five minutes in R and fifteen minutes in B for example. No dark is subtracted from the standard star images because they are never exposed longer than 200 seconds. It would only increase the noise. The resultant images are divided by a lamp response. This time the appropriate response image is selected by both the filter and UT of the observation. The output images of this operation are then divided by a twilight response selected in the same way as the lamp response. The only processing left is to remove cosmic ray hits and bad pixels.

4.6 Cosmic Ray Hits and Bad Pixels

Cosmic ray hits and bad pixels are removed by hand. This is done in a three step process. The first step is to get an initial guess at the location of offending pixels. This is done in the following manner. The image is searched pixel by pixel. A small 5×5 box is centered on the candidate pixel. If the candidate has not the largest pixel value in the box it is not considered a cosmic ray hit. If the candidate does have the largest pixel value in the box the process continues. The second largest pixel value is found. Then the mean inside the box is calculated excluding these two pixel values. If the difference between the candidate pixel value and the mean is less than a specified threshold it is dropped as a candidate. If it is greater the process continues. A plane is fit to the edge pixels of the box excluding the second largest pixel value if it happens to fall on the edge. The plane is subtracted from the box. Then the mean is recalculated. The new mean is divided by the plane-subtracted value of the candidate pixel giving the flux ratio for the candidate pixel. The larger the candidate pixel value the smaller the flux ratio. This mean and flux ratio scaled by one hundred are plotted

in an interactive mode. Then a second threshold is set on the flux ratio. An example is shown in panel a) of Figure 4.14. Candidates that fall below the second threshold are kept as cosmic ray hits. Each point in the graph can be checked using a surface plot like the one shown in panel b). Panel c) shows where the second threshold might be set. Individual points can also be undeleted when below the threshold or deleted when above it. A list of the deleted pixel positions is created and saved.

In the second step the neighborhood around each deleted pixel is displayed as a grey scale and examined visually. If a neighboring pixel is part of the cosmic ray hit it is added to the list of deleted pixels. If there is a pixel on the list which is not part of a cosmic ray hit it is removed from the list. An example session is shown in Figure 4.15.

The last step is removal of the flagged pixels. The following procedure is used to remove them. Begin with the nearest neighbors of a flagged pixel (eight pixels forming a square centered on the pixel in question). If any of these pixels are also flagged they are ignored. Go out one pixel to the next set of neighbors. This would be 16 pixels in a square around the first eight. Any of these that are flagged are ignored. Progress outward until more than ten good pixels are accumulated. The mean of these pixels is used to replace the value of the center pixel. A small section of the image is displayed during this automated process. An example is shown in Figure 4.16.

All the galaxies and standard star images are processed in this way. Now the images are ready for photometry. Figures 4.17 and 4.18 show an unprocessed galaxy image in B and R respectively. Figures 4.19 and 4.20 show the same galaxy image after processing in B and R respectively.

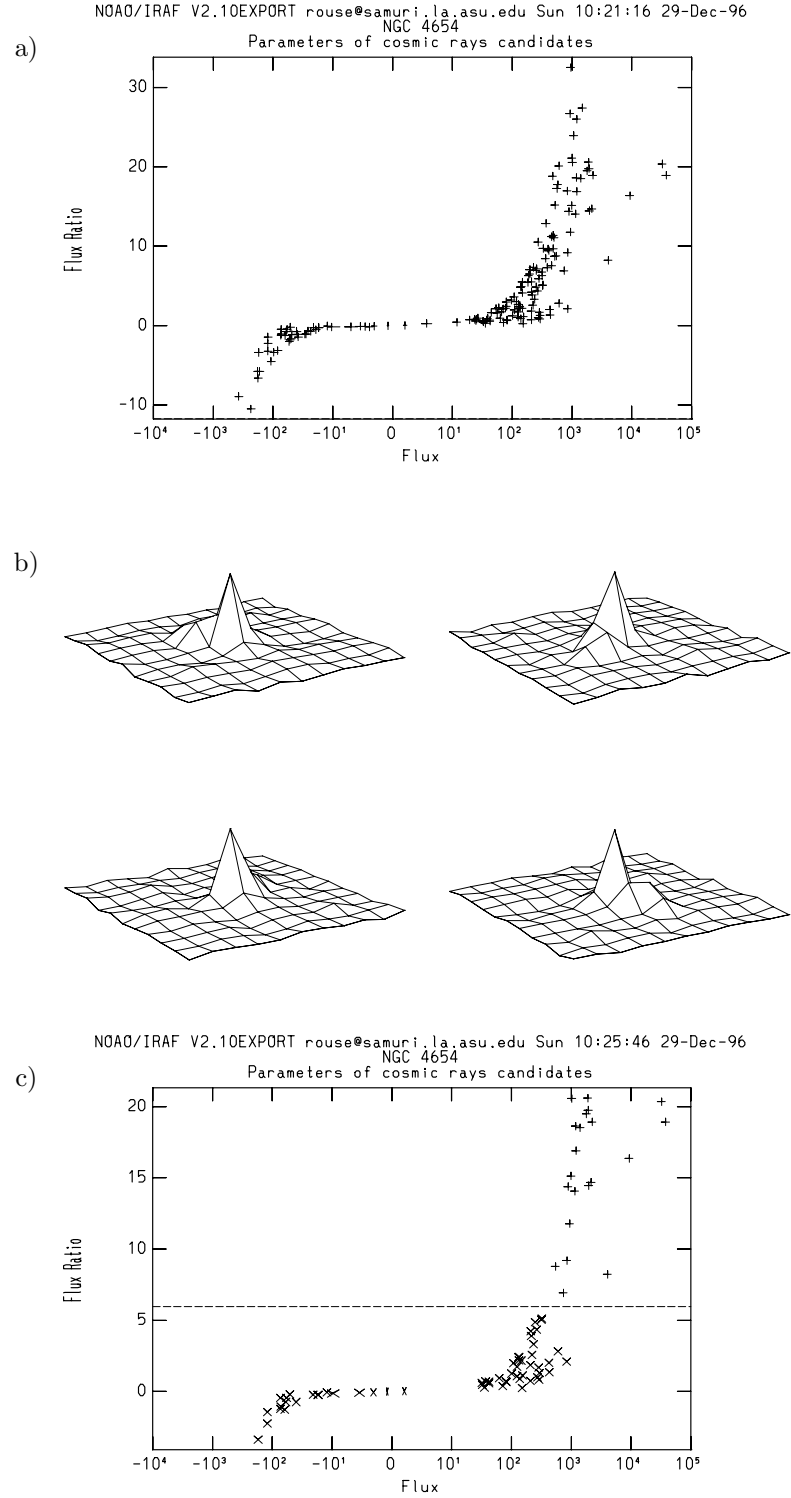


Figure 4.14: Example of Interactively Finding Bad Pixels and Cosmic Rays: a) Flux ratio plotted against flux b) Surface plot of a candidate pixel c) Example threshold. See Section 4.6 for detailed explanation.

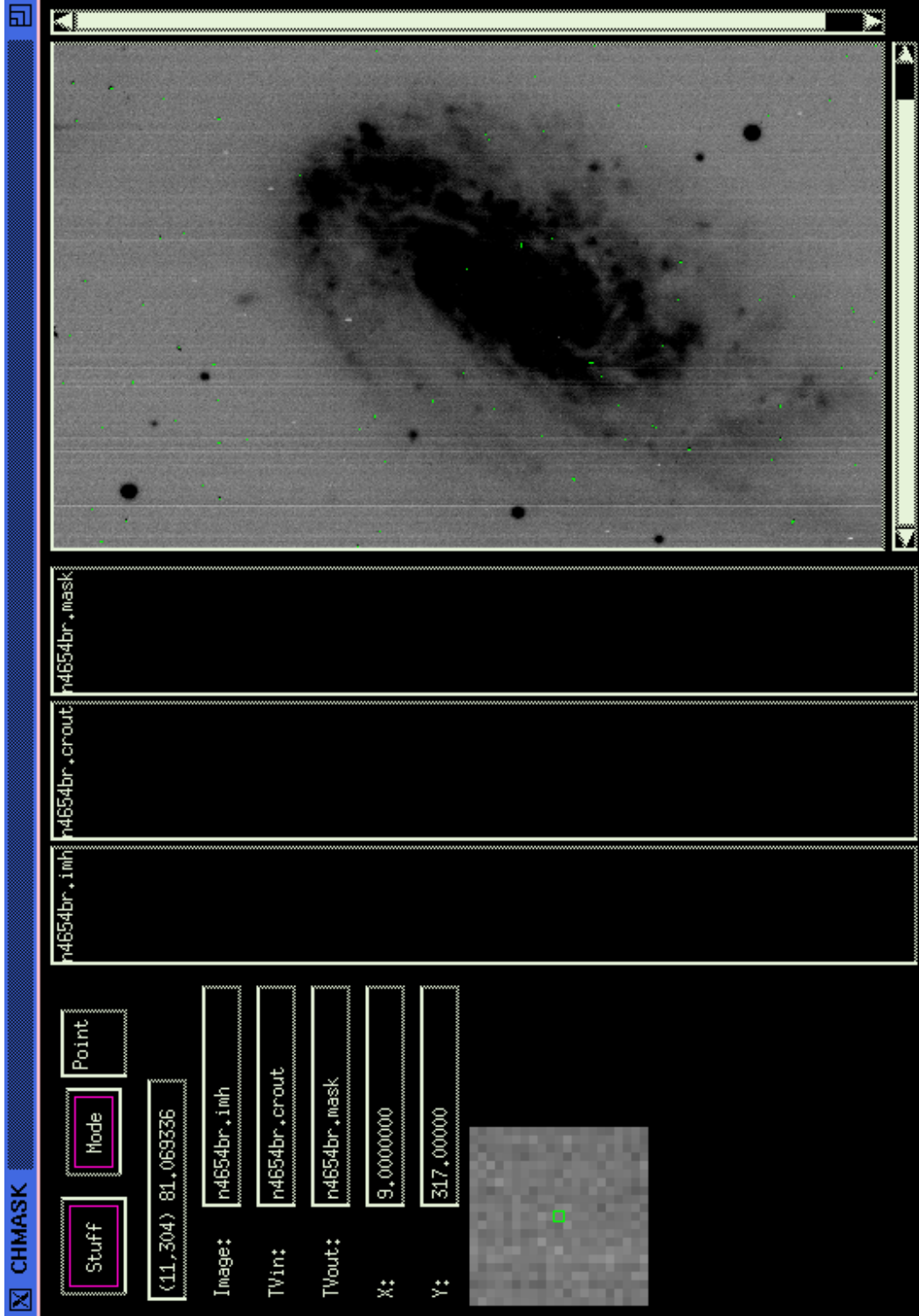


Figure 4.15: Graphical User Interface for Interactively Marking Cosmic Rays: This GUI was developed by the author to increase the efficiency and accuracy of updating the cosmic ray lists.

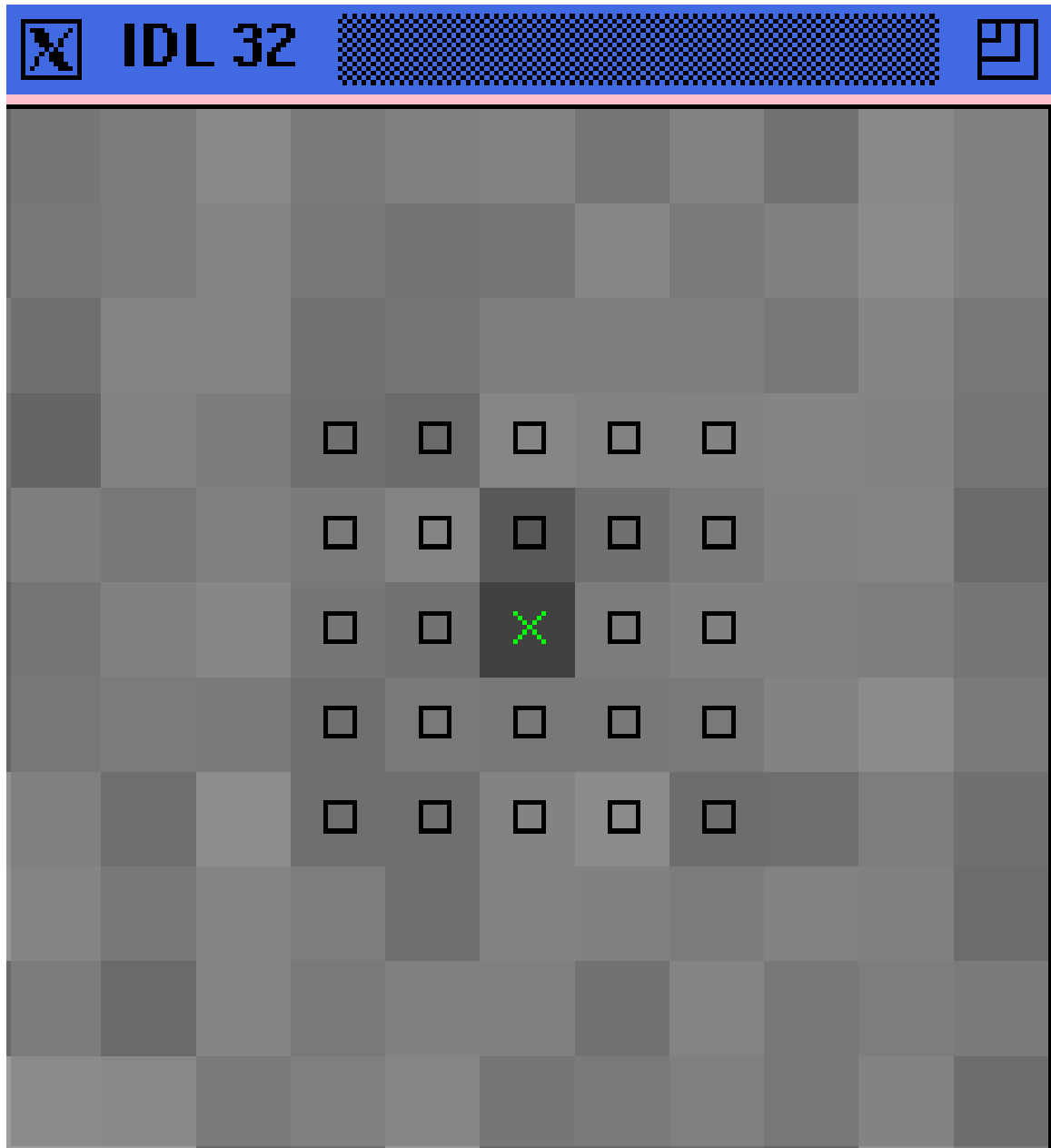


Figure 4.16: Example of Image Section Displayed as Cosmic Rays are Removed

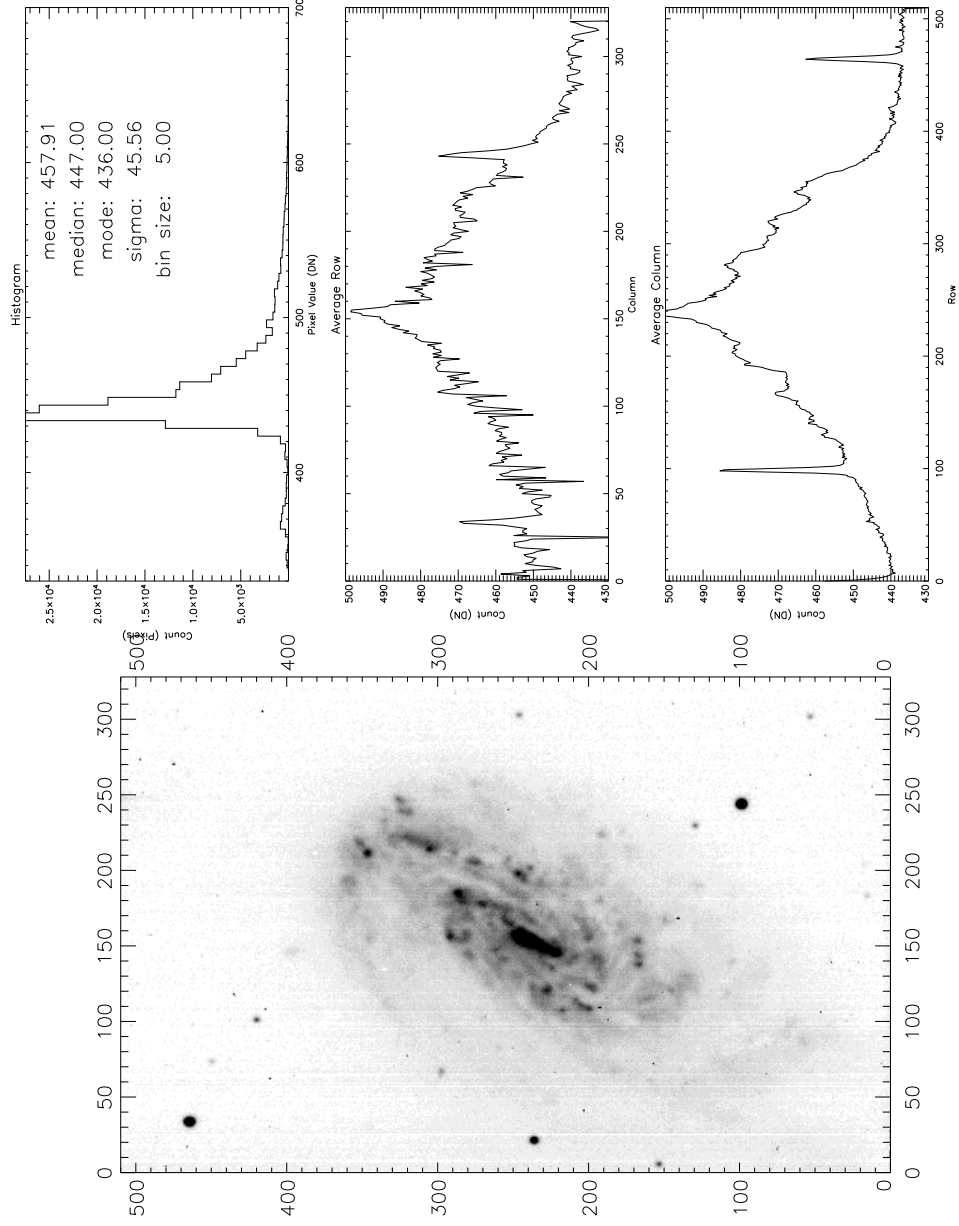


Figure 4.17: Example of Raw Galaxy Image in B: Compare this figure to the processed image in Figure 4.19. (See Figure 4.2 for explanation of panels.)

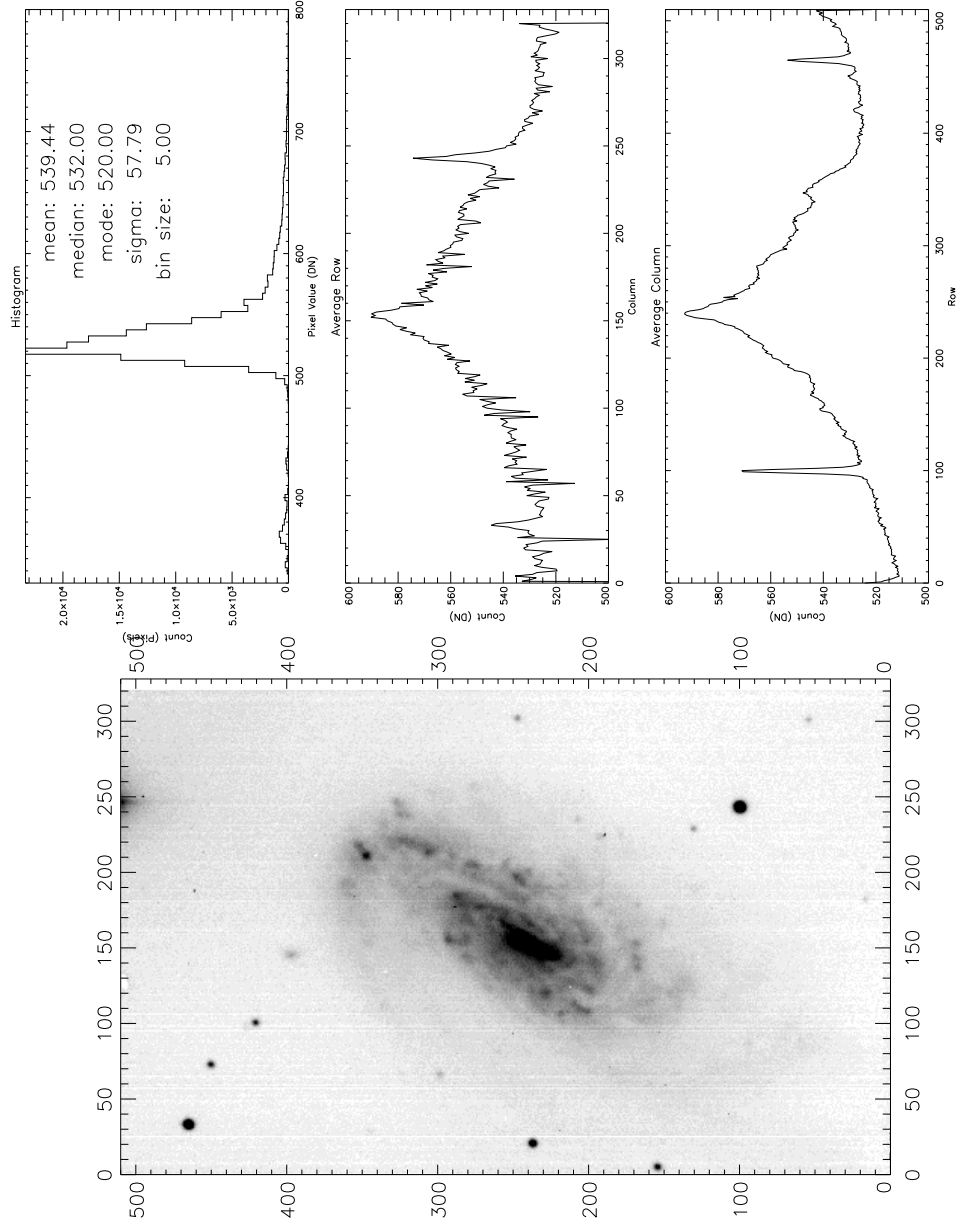


Figure 4.18: Example of Raw Galaxy Image in R: Compare this figure to the processed image in Figure 4.20. (See Figure 4.2 for explanation of panels.)

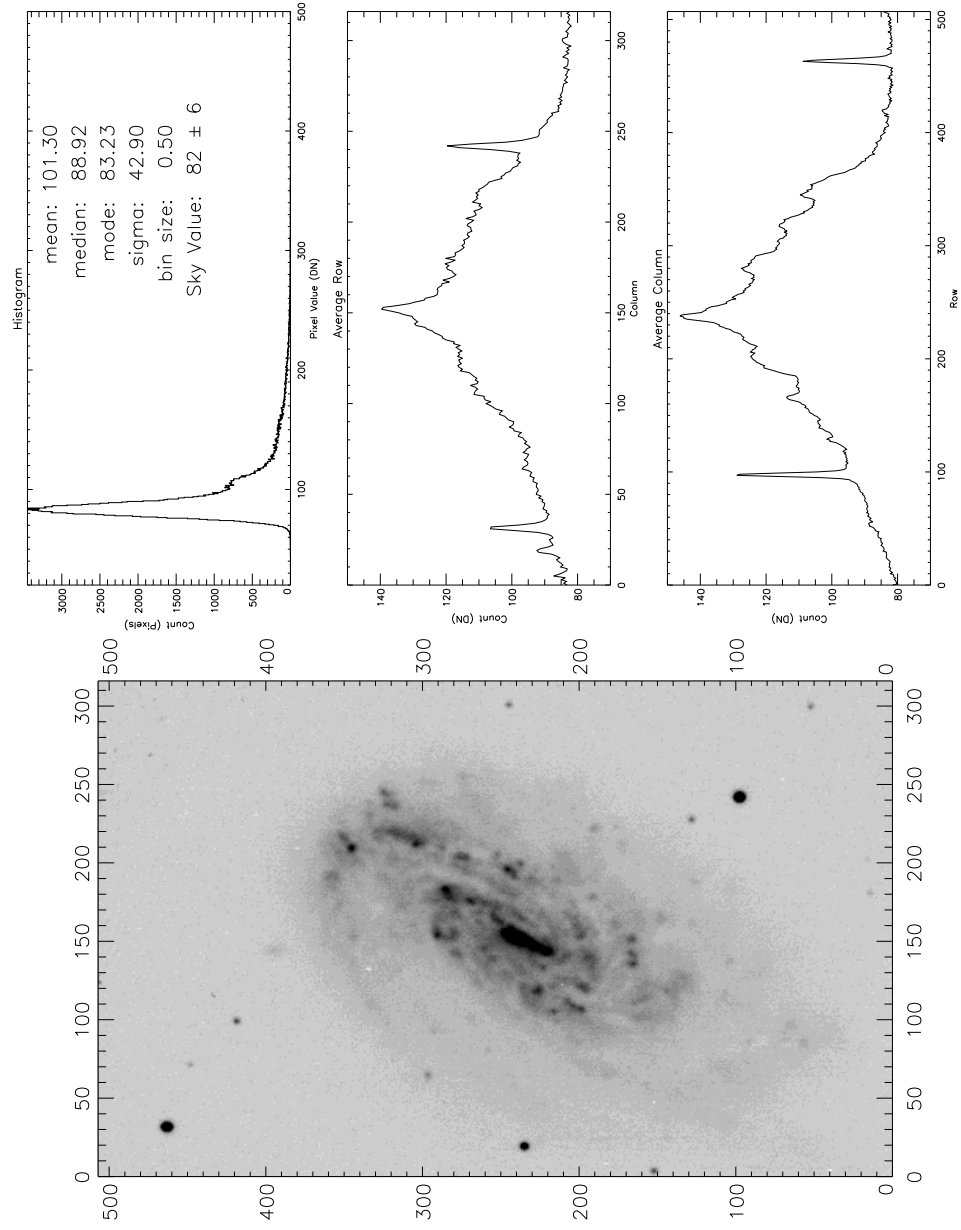


Figure 4.19: Example of Galaxy Image After Processing in B: (See Figure 4.2 for explanation of panels.)

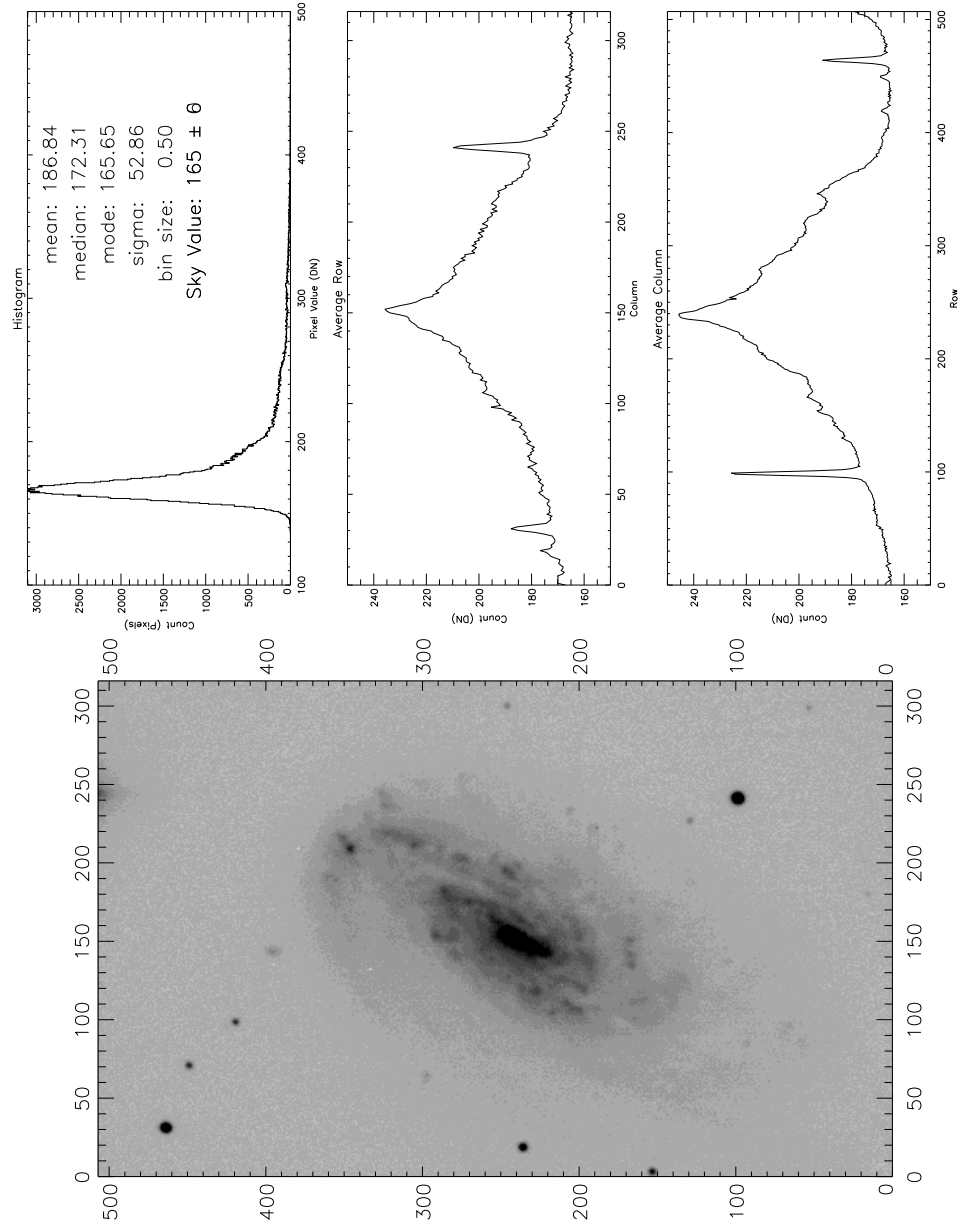


Figure 4.20: Example of Galaxy Image After Processing in R: (See Figure 4.2 for explanation of panels.)

CHAPTER 5

SPECTRAL IMAGE PROCESSING

This chapter describes how the spectral imagery is processed. Processing steps are presented in the order they are performed. All the calibration exposures taken for optical imaging are also taken for spectral imaging. Darks, zeros, and the overscan are essentially unaffected by the fact a spectrograph is used. However, all other images now contain the dispersed light of the source along one axis. In addition to the normal image processing steps there is a wavelength calibration (also called distortion correction) and a flux calibration (also called sensitivity correction).

5.1 Overscan, Zeros, and Darks

The TI 800×800 has a normal overscan region. There is a slight gradient of approximately .3% across the overscan. The variation along this overscan is about 7%. The first step in spectral image processing is to remove the bias level using the overscan region. This is done in the following manner. The overscan region is averaged over rows (spatial axis) to form an average column (spectral axis). A low order Chebyshev polynomial is fit to the average column. The fitted function is subtracted from the other columns in the image. Figure 5.1 shows an example fit. Figure 5.2 shows residuals from that fit. This is done to every image.

The 30 zeros taken each evening and morning were combined at the telescope using a median. An example bias-subtracted combined zero is shown in Figure 5.3. The TI 800×800 requires a pre-flash. Any illumination pattern in the pre-flash is present in the zeros. Hence it will be removed when the combined zero is subtracted from the star and galaxy images. A combined zero is subtracted from all the remaining images. Which combined zero is used is determined by the UT of the observation. The combined zero closest in UT is subtracted from the image just as during optical processing.

Next the zero-subtracted darks are combined using the median. An example combined dark is shown in Figure 5.4. The histogram in the top right panel shows that a dark count of 31 data numbers accumulated in a 45 minute exposure. This corresponds to a dark current of 0.01 DN/s. Note that there is a distinct pattern in the dark image. Hence one number can not characterize the dark current in this CCD. The sigma image is shown in Figure 5.5. The dark image is subtracted from every exposure of 45 minutes.

```

NGAO/IRAF V2.10EXPORT rouse@samuri.la.asu.edu Sun 11:37:53 17-Aug-97
func=spline3, order=3, low_rej=3, high_rej=3, niterate=0, grow=0
total=800, sample=800, rejected=0, deleted=0, RMS= 0.906
colbias rra0020

```

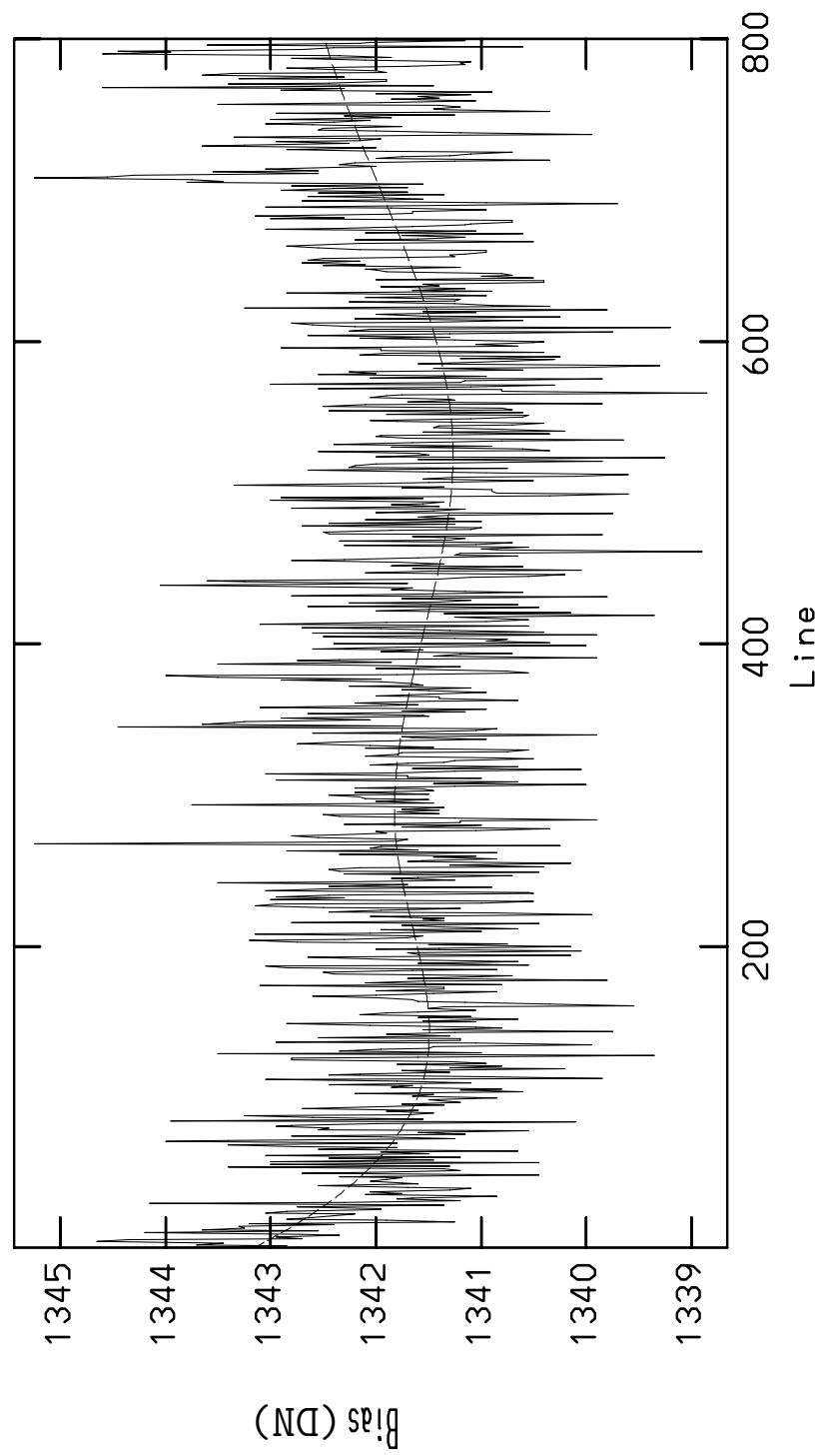


Figure 5.1: Example of Fitting Overscan: A third order cubic plane with 3σ clipping is fit to the average overscan column.

```

NQA0/IRAF V2.10EXPORT rouse@samuri.la.asu.edu Sun 11:40:23 17-Aug-97
func=spline3, order=3, low_rej=3, high_rej=3, niterate=0, grow=0
total=800, sample=800, rejected=0, deleted=0, RMS= 0.906
colbias rra0020

```

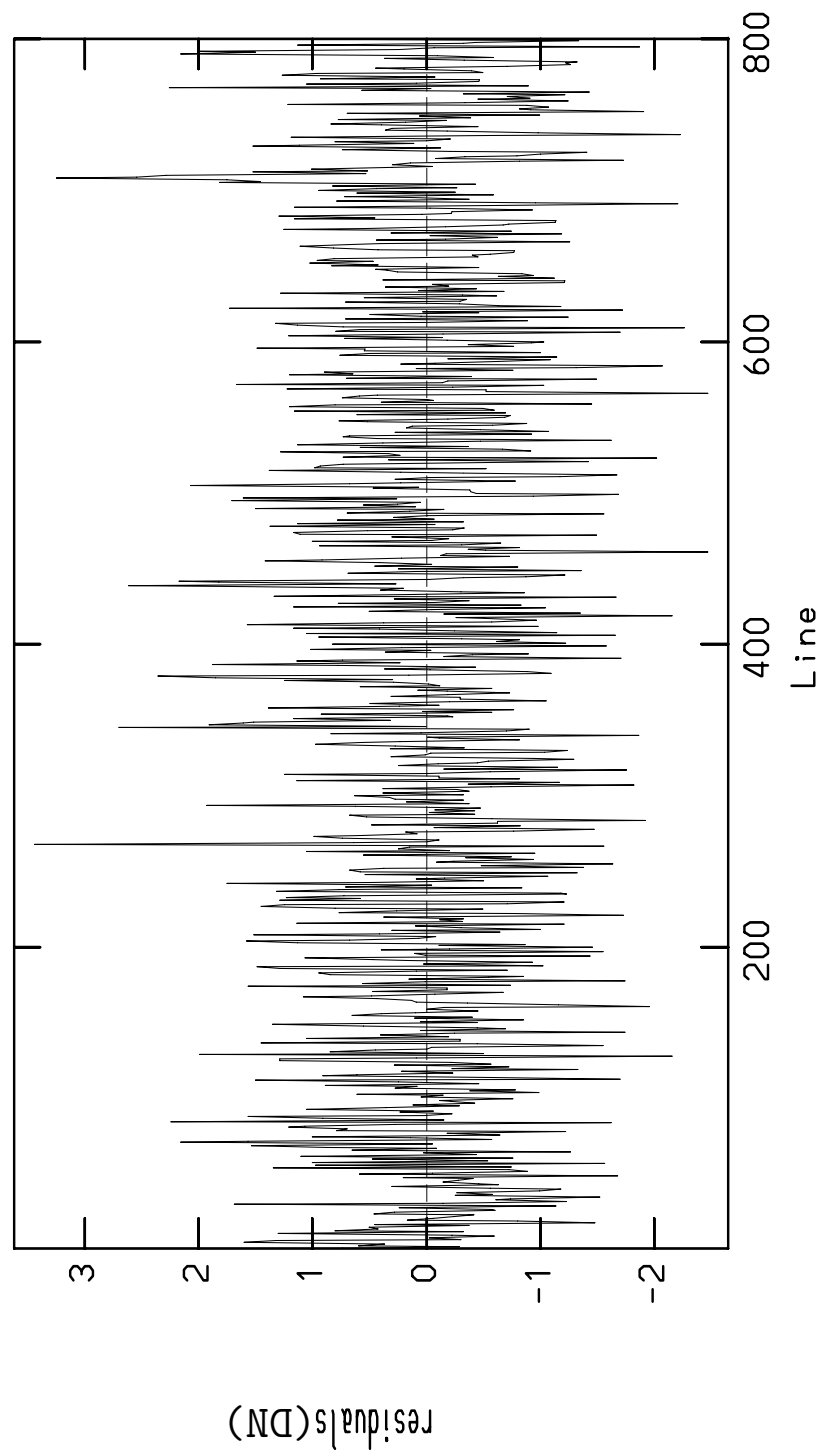


Figure 5.2: Example of Residuals from Fit to Overscan

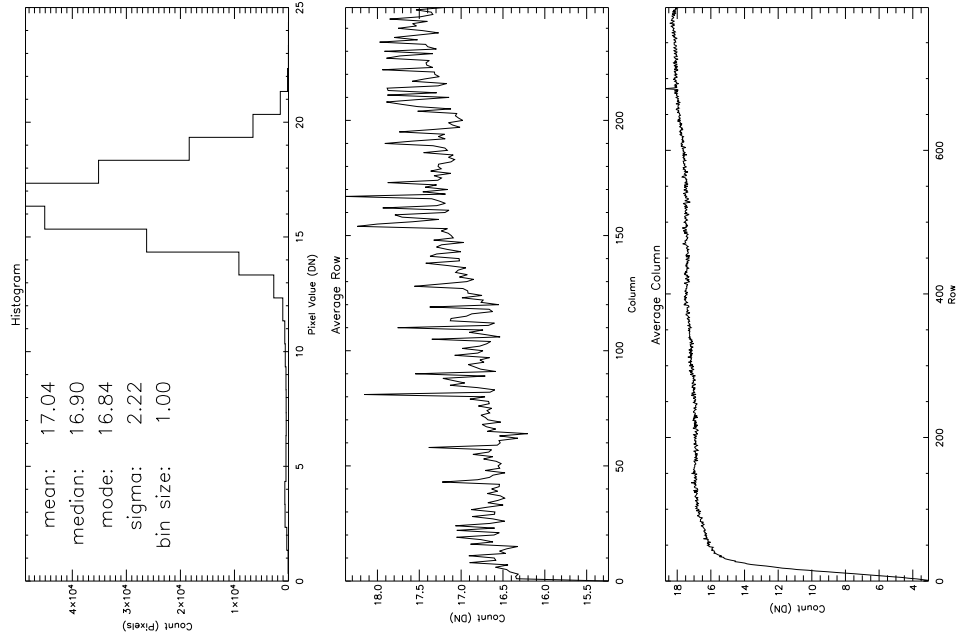
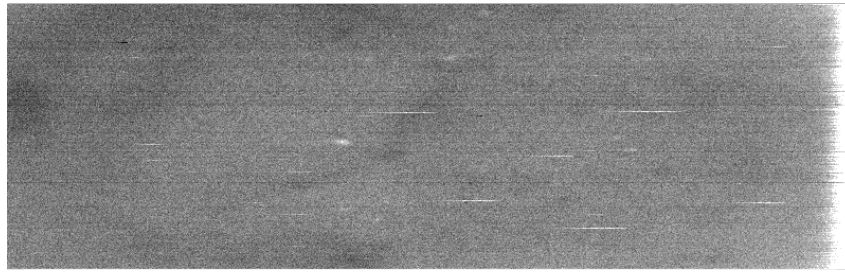


Figure 5.3: Example of MMT Combined Evening Zero after Bias Subtraction: The individual zeros were combined at the telescope. The bias level was removed from the combined zero using the overscan region. (See Figure 4.2 for explanation of panels.)

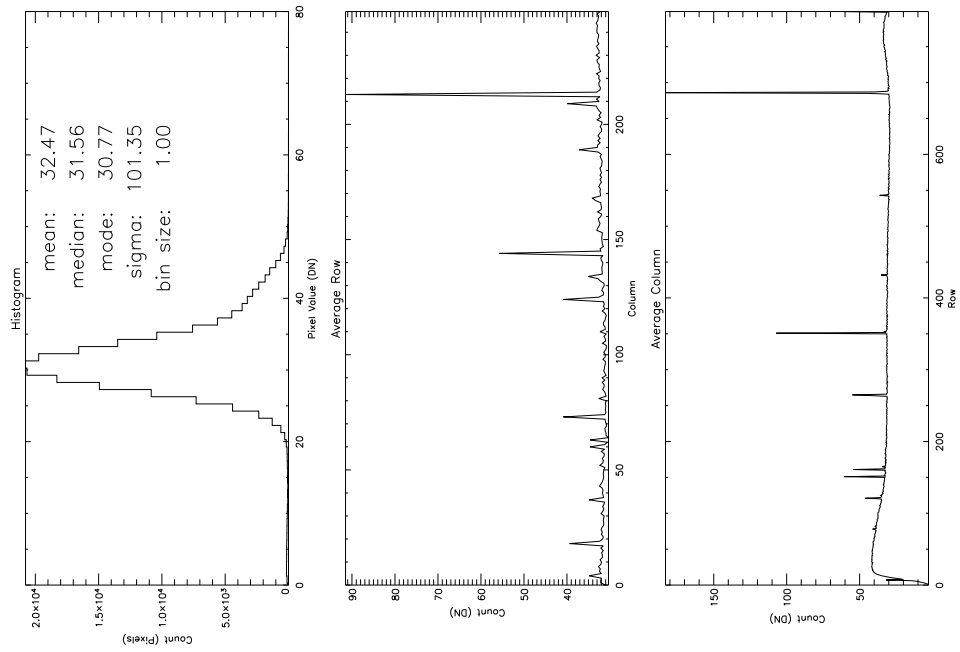
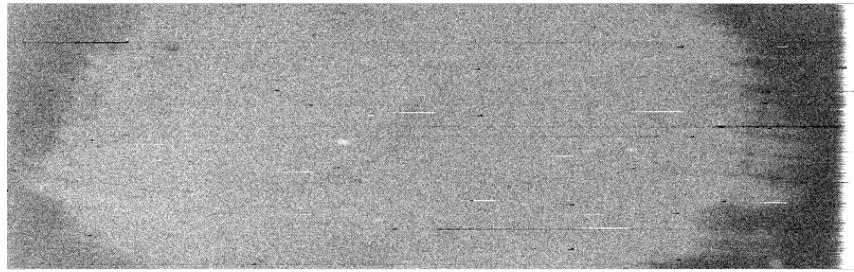


Figure 5.4: Example of MMT Combined Dark: The individual darks are bias and zero subtracted then combined using the median. (See Figure 4.2 for explanation of panels.)

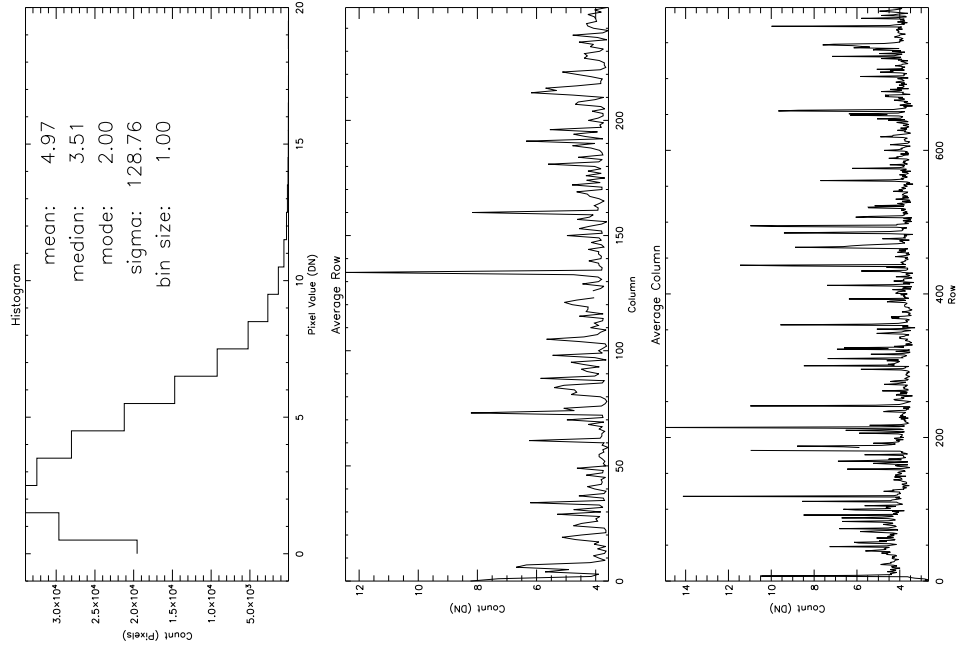
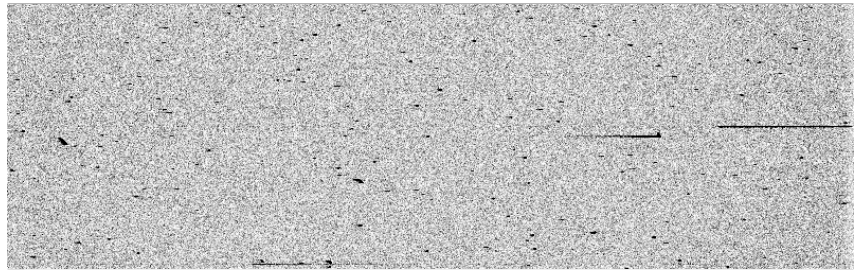


Figure 5.5: Standard Deviation of MMT Combined Dark: Note the numerous pixels affected by cosmic ray hits. A cosmic ray hit increases the standard deviation in a pixel. (See Figure 4.2 for explanation of panels.)

5.2 Quartz Flats

From this point on the spectral image processing diverges from the optical image processing. The fact that the light is dispersed along the columns of the CCD comes into play.

The 30 quartz flats taken each evening and morning were combined at the telescope. The quartz flat contains the spectrum of the lamp dispersed along the columns. For example see Figure 5.6. The variation along the columns is due mostly to spectrum of the quartz lamp. Note that the quartz lamp spectrum should vary smoothly over the wavelength range of interest to facilitate its removal. Because the quartz lamp spectrum is unknown it is not possible to distinguish between a change in the lamp spectrum and a change in the CCD response. The quartz spectrum does not appear in any other exposure and is not part of the system response. Therefore, its spectrum must be removed before the quartz flat can be used as a response image. This is done by taking the median column of the quartz flat and dividing it into every other column. The median column is formed by taking the median of each row in the image. The median of each row is one pixel in the output column. An example of the mean quartz spectrum is shown in Figure 5.7 in panel a). Panel b) shows the standard deviation in the mean quartz spectrum. The output image is the quartz response. An example is shown in Figure 5.8. The grey-scale in the left panel indicates why a median is used for creating the quartz spectrum. The bright and dark spots tend to bias other methods such as fitting a function to the average column. Each of the remaining images is divided by a quartz response. The response used is the one closest in UT to the observation.

This response does not completely remove the effect of the white spot located just above and to the left of the center of the CCD. This spot can be seen in the grey scale of Figure 5.8. This can affect the measurement of the Mgb feature in stars because the blue side band falls on the location of this spot. The quartz response over corrects this area artificially increasing the side band flux. This makes the index stronger than it really is causing an outlier in the Mgb profile. Fortunately, this only affects one small aperture in one stellar profile. The galaxy measurements are not affected

because they are red shifted such that Mgb falls in a different location on the CCD. However, other line indices may be affected, and this will be taken into account in future work. This is discussed again in Section 9.4 and Figure 9.5.

5.3 Twilight Flats

The spectrum of the twilight sky varies greatly over the optical region. Special steps must be taken to prevent this from spoiling the flat-field.

Now each of the twilight images is examined. If the image appears flat then the quartz response has done the job. However, this is not the case. There is some gradient remaining in the twilight images. It is shown in the average row plot in Figure 5.9. This is due to the fact that the light from the quartz lamp travels a different optical path than the light from the sky. Each of these quartz-divided twilight flats is treated in the same way as the quartz flats. The median twilight spectrum is divided into each column of the image. This is done for each twilight. Because of distortion a spectral feature will not fall in the same pixel in every column (see Section 5.5). It will not be aligned with the rows. Furthermore the twilight spectrum varies greatly over the optical region. Hence when the columns are divided by the median twilight spectrum there are large deviations especially for narrow spectral features. See Figure 5.10 for an example. The net result being that the latter division does not remove the twilight spectrum perfectly at each point on the CCD. Therefore, the median-divided twilight is smoothed using a $100 \text{ pixel} \times 50 \text{ pixel}$ window. The 100 pixels are in the dispersion direction and the 50 in the slit direction. See Figure 5.11 for an example.

All the twilight images are processed in this way. Then the resultant images are combined using a median. Morning and evening twilight responses are created in this way. An example is shown in Figure 5.12. Figure 5.13 shows the associated image standard deviation. Now each of the remaining images is divided by a twilight response. Once again the response used is the one closest in time to the star or galaxy observation.

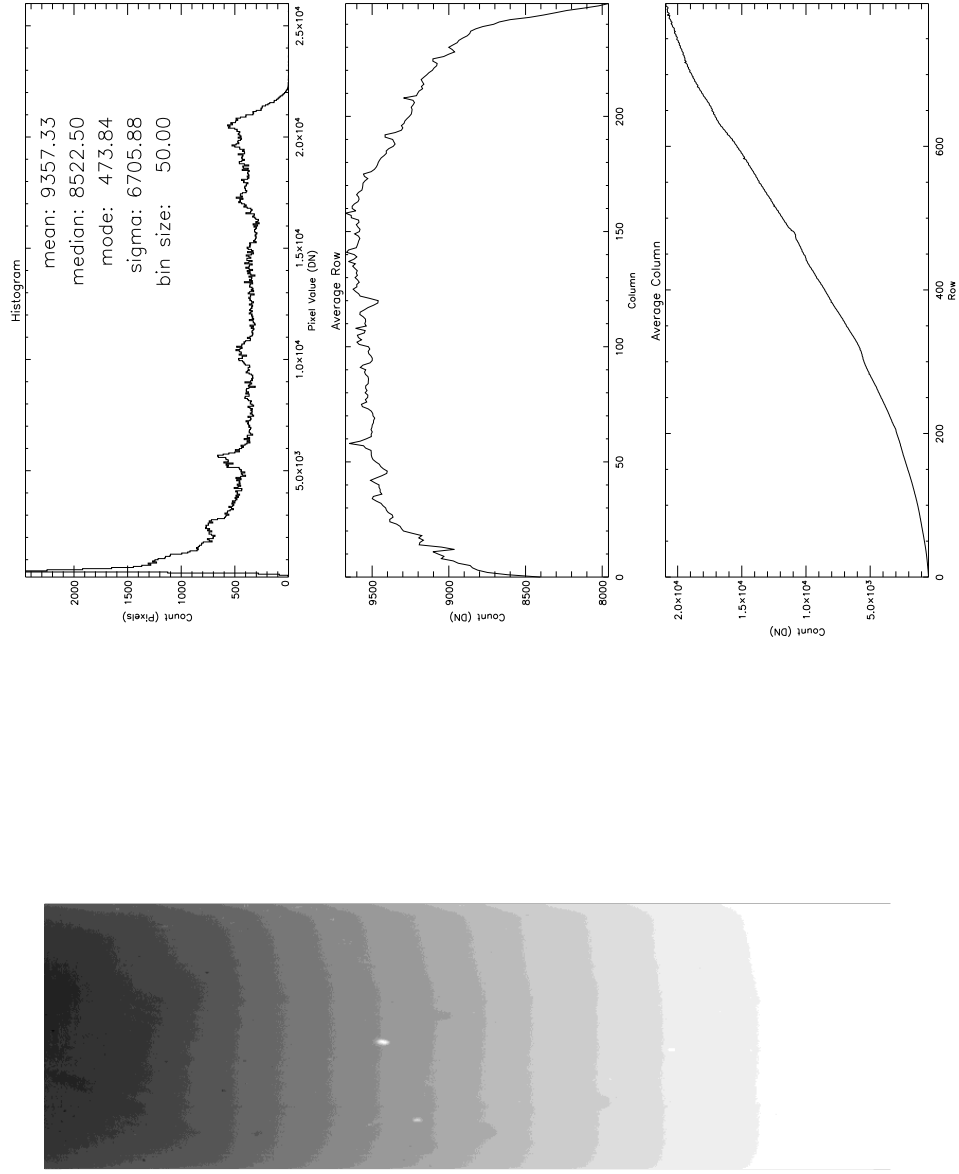


Figure 5.6: Example of MMT Combined Evening Quartz Lamp: The individual flats were combined at the telescope. The combined flat was bias subtracted using the overscan and zero subtracted using the combined zero. (See Figure 4.2 for explanation of panels.)

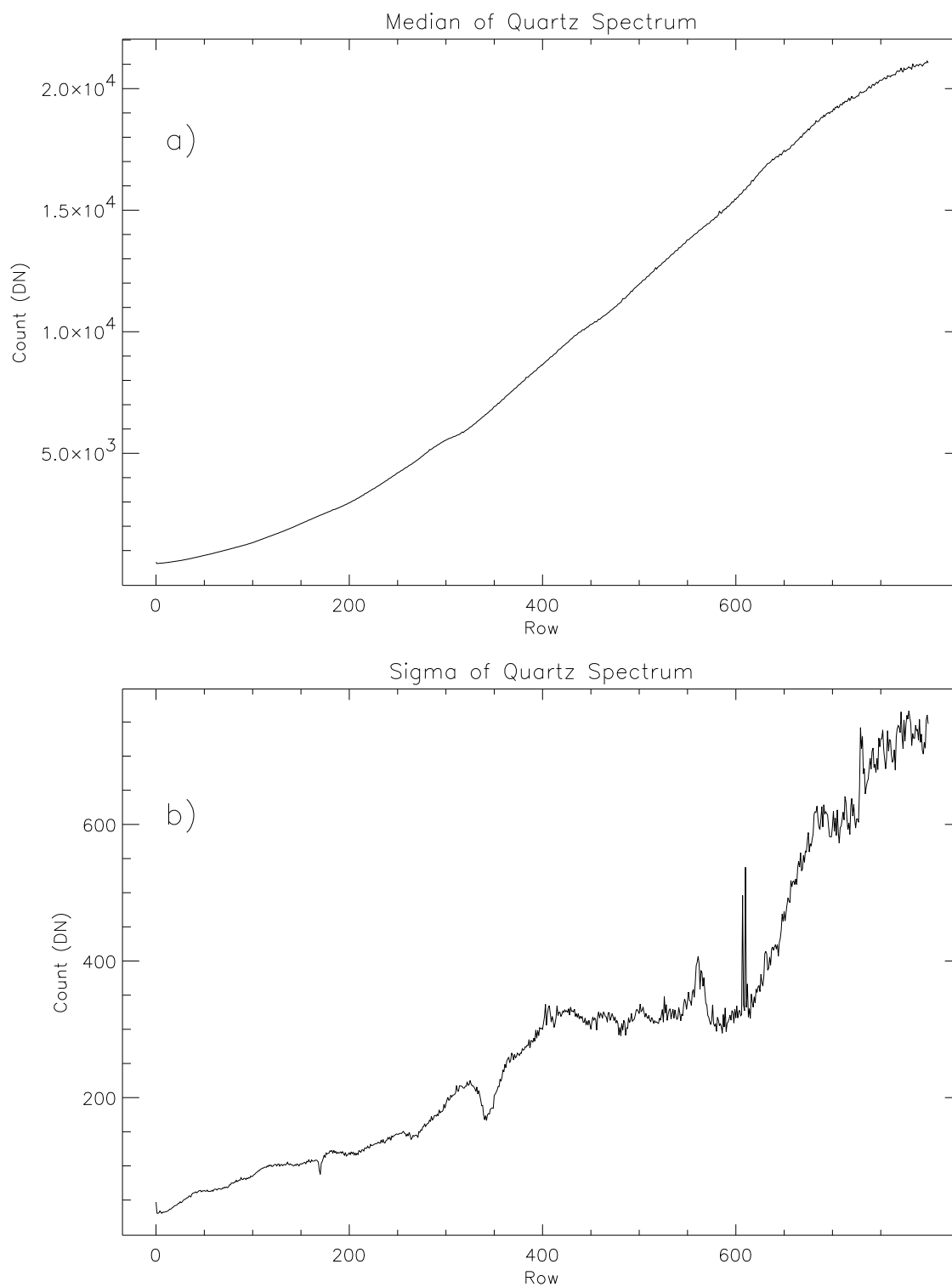


Figure 5.7: Example of MMT Quartz Lamp Spectrum: a) The quartz spectrum is the median column of the image. b) This is the standard deviation of the quartz spectrum.

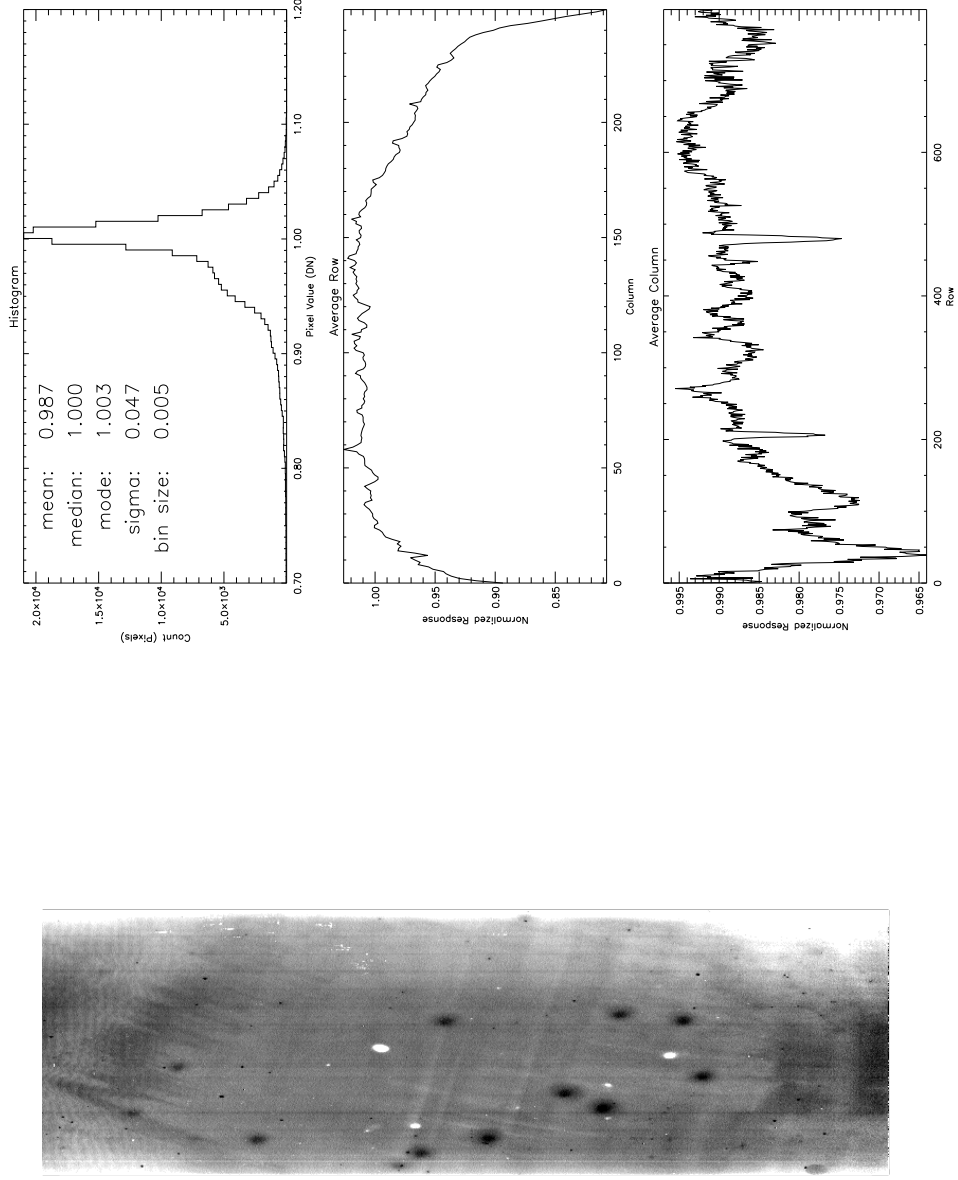


Figure 5.8: Example MMT Response Derived from Quartz Lamp Observations: The combined and calibrated flat is divided by its median column to form the lamp response. The white spot located just above and to the left of center in the grey scale is over corrected in the flat-fielded images. In one small aperture in one star measurement this cases the Mgb index to be anomalously large as shown in Figure 9.5. See Sections 5.2 and 9.4 for discussions. (See Figure 4.2 for explanation of panels.)

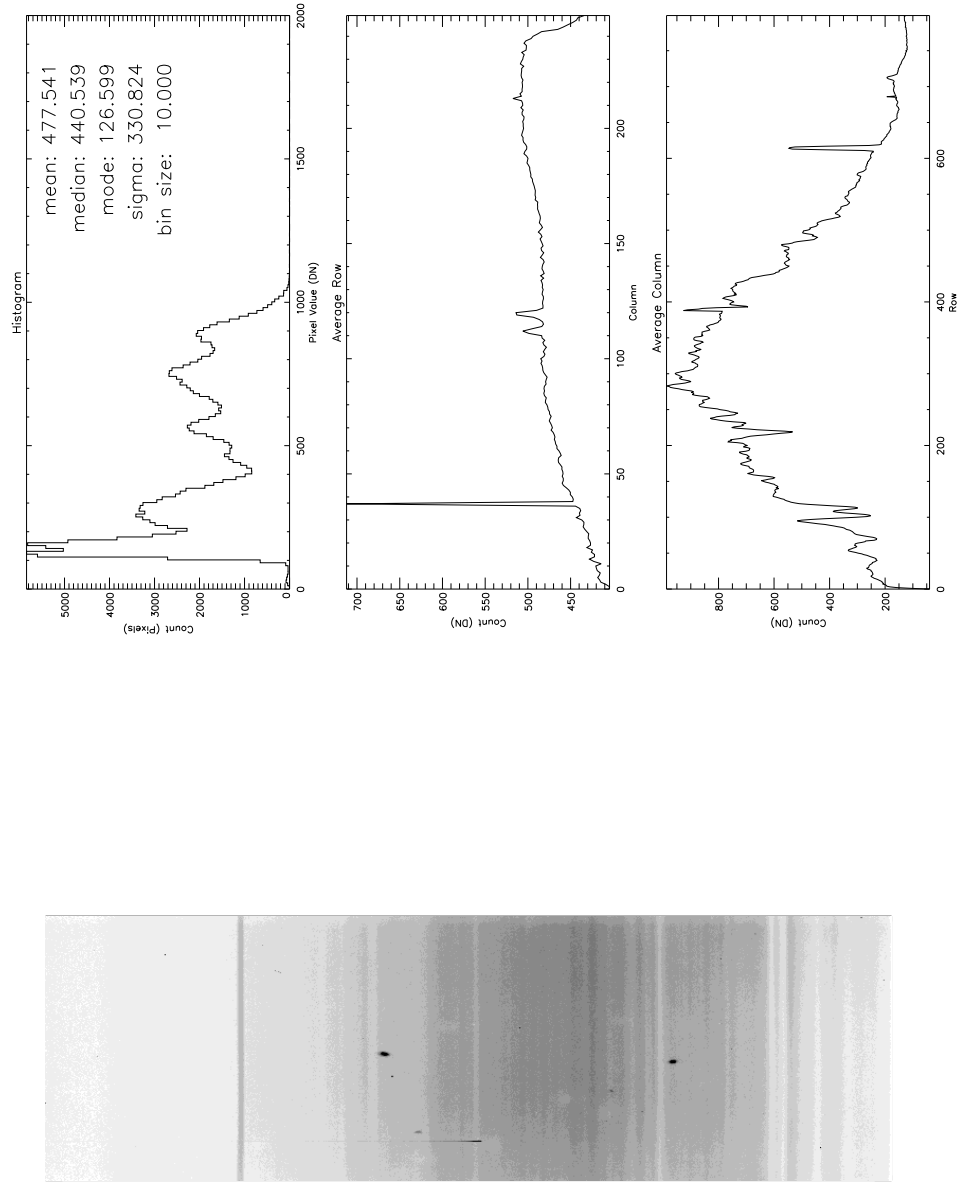


Figure 5.9: Example MMT Twilight After Dividing by Quartz Lamp Response: Each twilight image is bias and zero subtracted then divided by the lamp response. The average row in the middle panel shows that there is a significant residual gradient. (See Figure 4.2 for explanation of panels.)

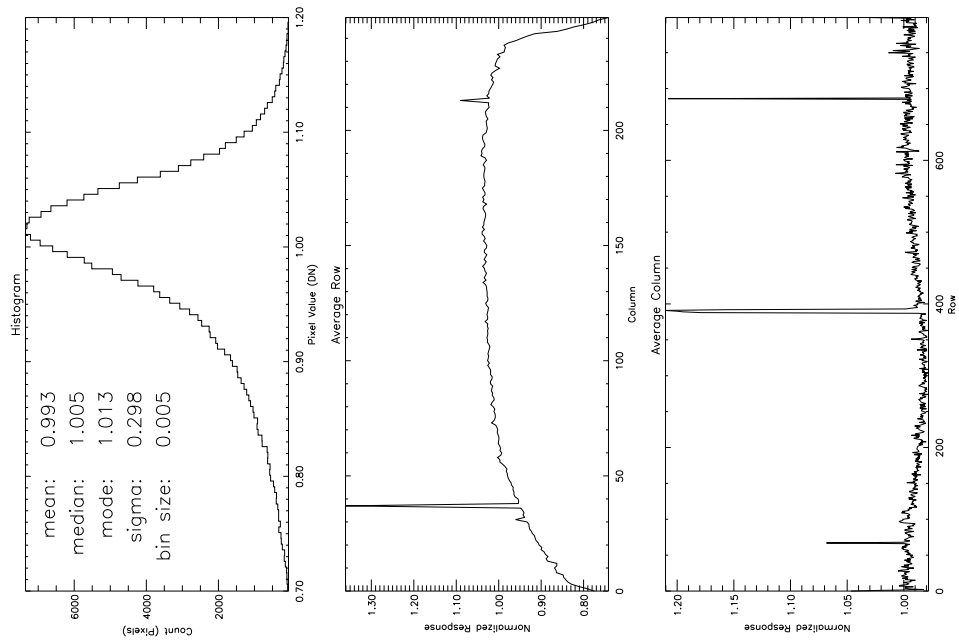
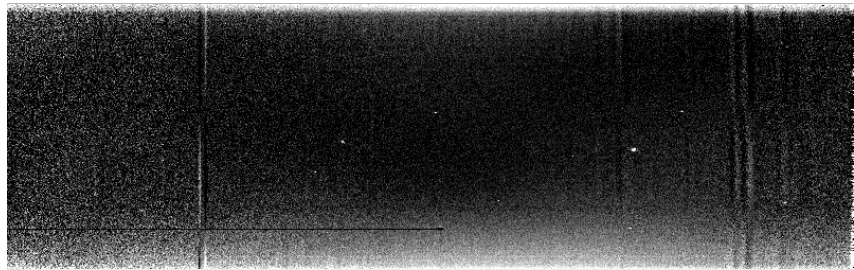


Figure 5.10: Example Twilight After Dividing by Median Column: The first step in isolating the residual gradient in the twilight image is to divide by the median column. There are large residuals around the strong sky lines. (See Figure 4.2 for explanation of panels.)

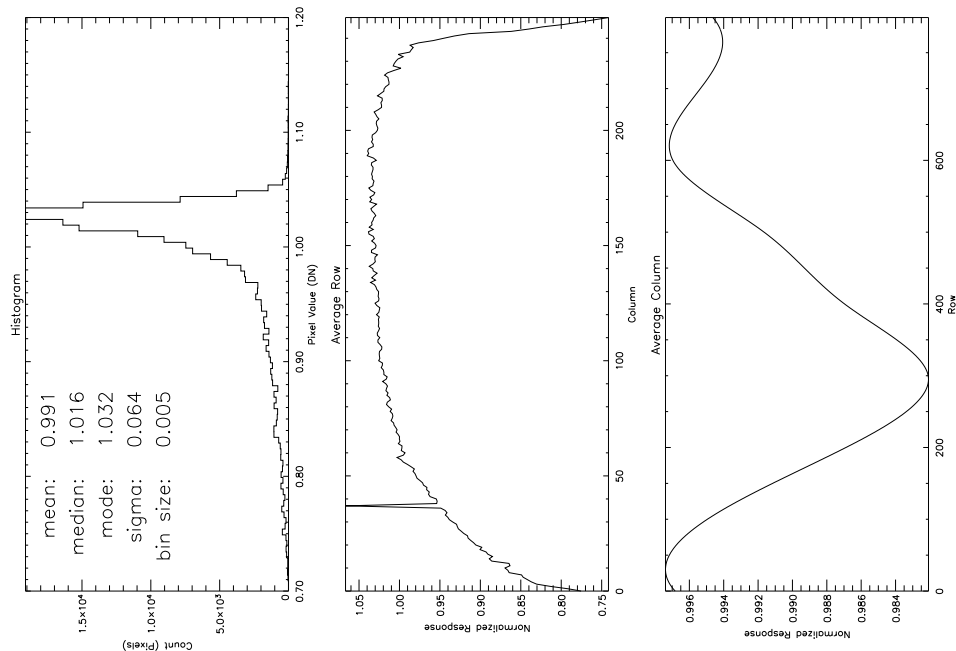
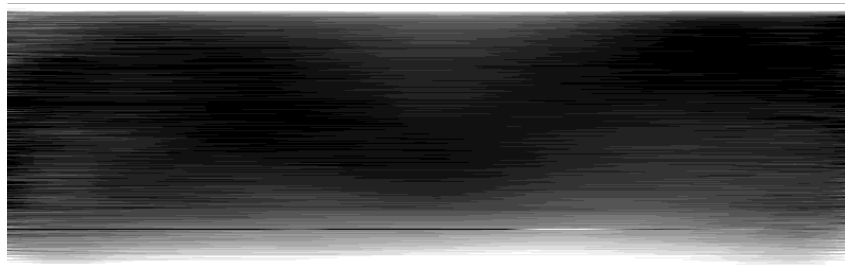


Figure 5.11: Example Smoothed Twilight Flat: The second step in isolating the residual gradient in the twilight images is to smooth each image heavily (after dividing by the median column). (See (Figure 4.2 for explanation of panels.)

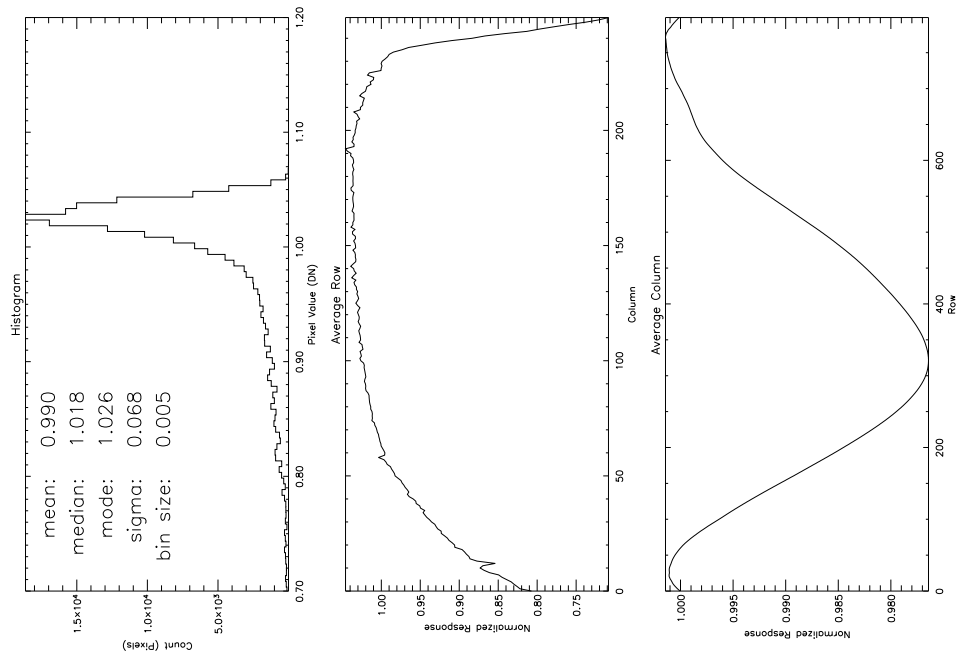
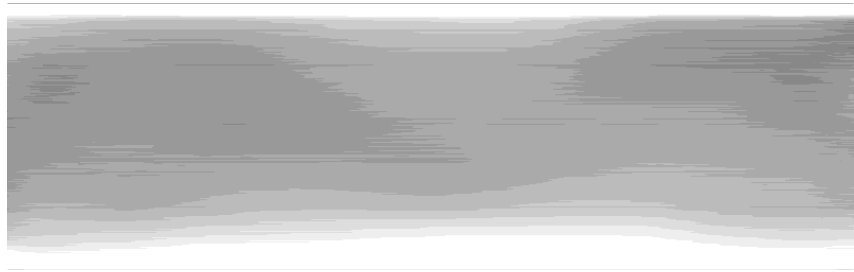


Figure 5.12: Example MMT Response Derived from Twilights: The final step in isolating the residual twilight response is to combine the heavily smoothed twilight images. (See Figure 4.2 for explanation of panels.)

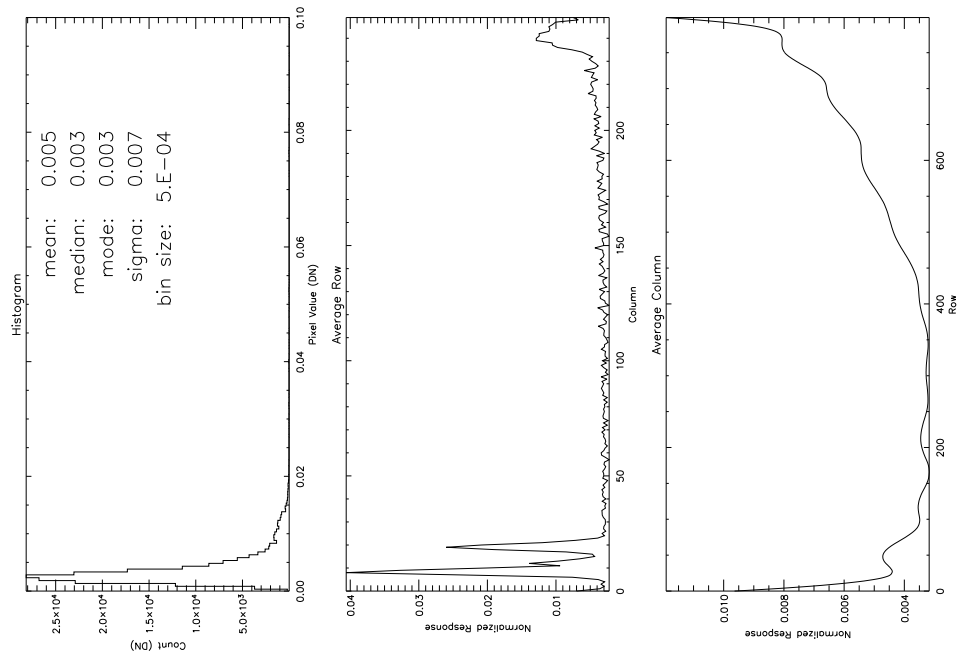
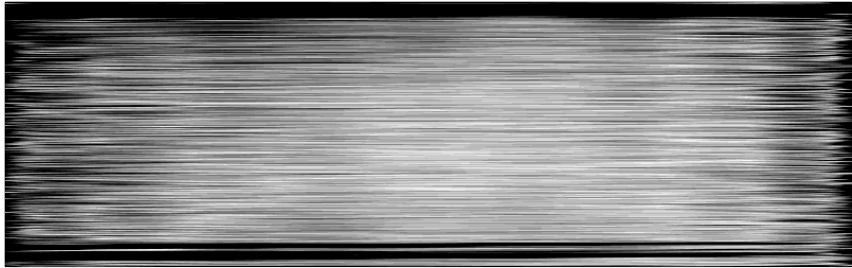


Figure 5.13: Standard Deviation MMT Response Derived from Twilights; See Figure 4.2 for explanation of panels.

5.4 Cosmic Ray Hits and Bad Pixels

Now the images are cleaned. This means the cosmic ray hits and bad pixels are removed. This must be done before the images are corrected for distortions because that transformation will cause adjacent good pixels to be contaminated. That is, a bad pixel will get smeared into the surrounding pixels. The cleaning technique is the same as in the optical image processing described in Section 4.6. An example is given in Figure 5.14 to show how cosmic ray hits are detected even when they are atop a spectral feature.

5.5 Distortion Correction

This section describes how a wavelength is assigned to each row in the spectral image. Distortions are critical in spectral imaging because of the large gradients that exist in spectra. There are several sources of distortion including curvature in the CCD, flexure in the telescope-spectrograph system, misalignment between the CCD and dispersion axis of the spectrograph, and aberrations introduced by the optics. Because of this a spectral feature does not fall on the same row of pixels all the way across the CCD. The comparison lamp images are used to remove these distortions.

Figure 5.15 shows a comparison lamp image. Only with close inspection is it possible to discern any distortion in this image. However, even a slight bend or misalignment can have dramatic consequences especially for narrow spectral features. If a narrow spectral feature does not fall along a row then one cannot simply plot the row and expect to see the true variation in the line along the slit. Plotting along a row near the center of an emission line demonstrates this. The variation seen is simply the spectral line entering then leaving the row. Figure 5.16 shows an example of this.

Another consequence is that a fixed step in pixels does not correspond to the same step in wavelength everywhere along a column i.e. the wavelength solution is not necessarily linear. Along the dispersion axis the spectrum can be stretched and/or compressed. Hence one cannot assume that one step in pixels always corresponds to the same step in Angstroms. This can be shown by

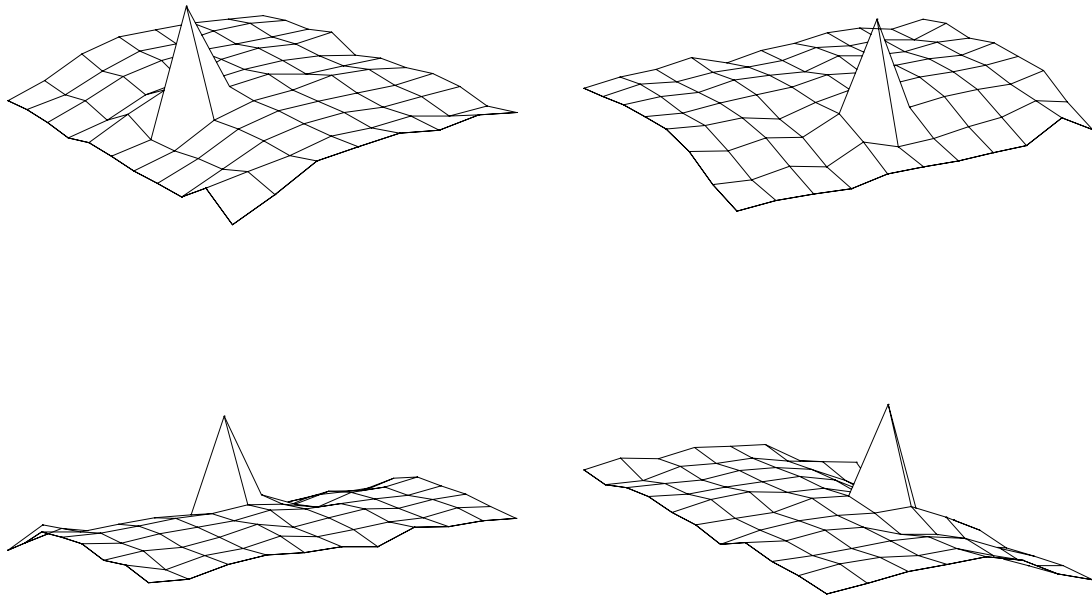
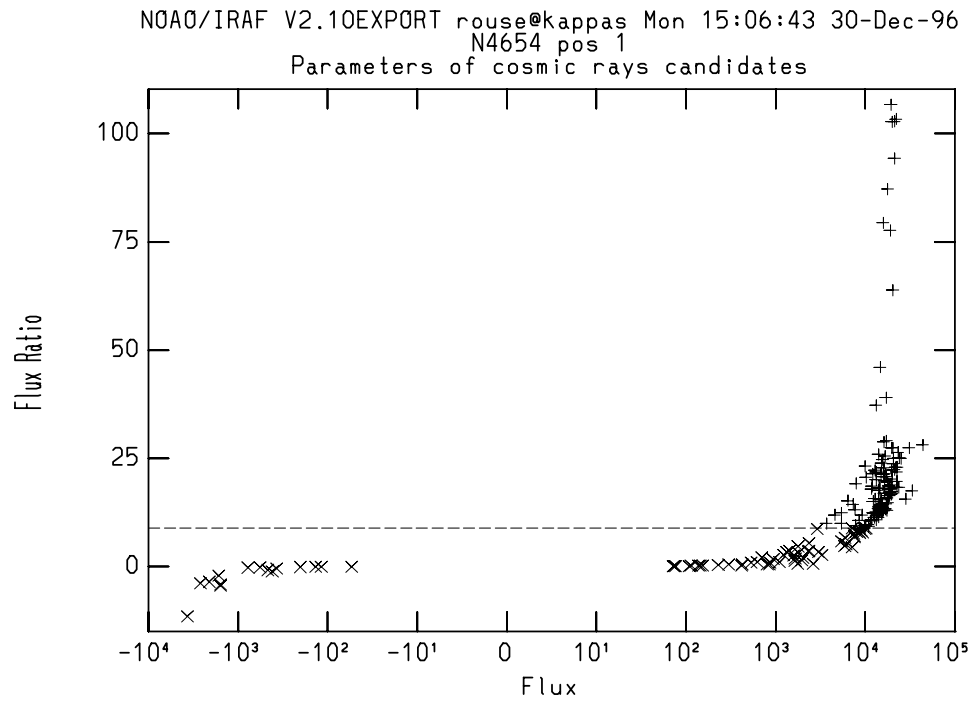


Figure 5.14: Interactively Marking Bad Pixels: See Figure 4.14 for explanation of panels.

plotting wavelength against pixel position along a row. Figure 5.17 shows an example and a fit to the wavelength-pixel relationship. Figure 5.18 shows residuals of this fit.

Because distortions vary with temperature and telescope position it is necessary to take comparison lamps at every exposure. If the exposures are long then a comparison lamp exposure is taken before and after. The comparison lamps provide a known grid of spectral features in the wavelength dimension and along the slit. The procedure is this. Identify the known features in the comparison lamp image. Then follow the peaks of those features across the CCD (along the slit direction). The result is a mapping of wavelength onto pixel position. So for each row and column there corresponds a wavelength. A fit is made that results in a function that maps wavelengths into pixel positions. The inverse of this function is used to remove distortions from the images. A sanity check is provided by transforming the calibration lamp image itself. After distortion correction a step in pixels along a column will always correspond to the same step in wavelength, and a spectral feature will be centered on a row. The dispersion axis and columns will be aligned.

The distortion correction is carried out as follows. Using a hard copy figure and database provided by MMT the He, Ne, Ar, Hg, and Cd lines in the center column of a comparison lamp image are identified. An example is shown in Figure 5.19. A function that transforms pixels to wavelength is determined. The same lines are automatically identified in the other columns. This is done using the fitting function and a peak finding algorithm. The function is refit at each column. It is important to avoid blended features. Otherwise the peak tracing algorithm will be fooled. For example, it could jump from one peak in the blend to another yet label it with the same wavelength. The wavelength-pixel pairs are used to determine a two-dimensional fit. Sixth order Chebyshev polynomials are used. Figure 5.20 shows an example. The top left panel shows the residuals of the fit along each row. The top right panel shows the residuals along the columns (i.e. for each identified line). The left bottom panel shows the points plotted as they fall on the CCD. X is columns and Y is rows. The bottom right panel is the same except that the wavelength replaces row number on the vertical

axis. A fit is determined for each comparison lamp. The inverse of the fitted function is used to transform the corresponding spectral images. The transformation removes the distortions. A cubic spline is used for interpolation during the transformation.

This procedure is followed for all comparison images that accompany short exposures. The long galaxy exposures have a comparison image before and after. These comparison images are treated the same until the fitting step. In this case the line identifications of both comparisons are combined and fit together by one two-dimensional function. The fitting procedure itself is unchanged. Figure 5.21 shows a comparison image after distortion correction. Figure 5.22 shows the difference between the before and after comparison images. This helps reveal the distortions in the input image. Note that most of the distortion is along the columns. All remaining images are distortion corrected.

There is one type of distortion that is not removed by this method. If there is a stretch or compression parallel to the rows it will remain in the distortion corrected image. There is no calibration data available to check for this type of distortion. It would be the same scale factor for each row. This type of distortion can be detected by placing a standard star in even steps along the slit during an exposure. Given that the steps are the same number of arc seconds apart any stretch along the slit is revealed by uneven steps in the image. The unevenness can be measured in the same way as for the comparison lamps. Then it can be removed. This is not done here because the appropriate calibration data is not available.

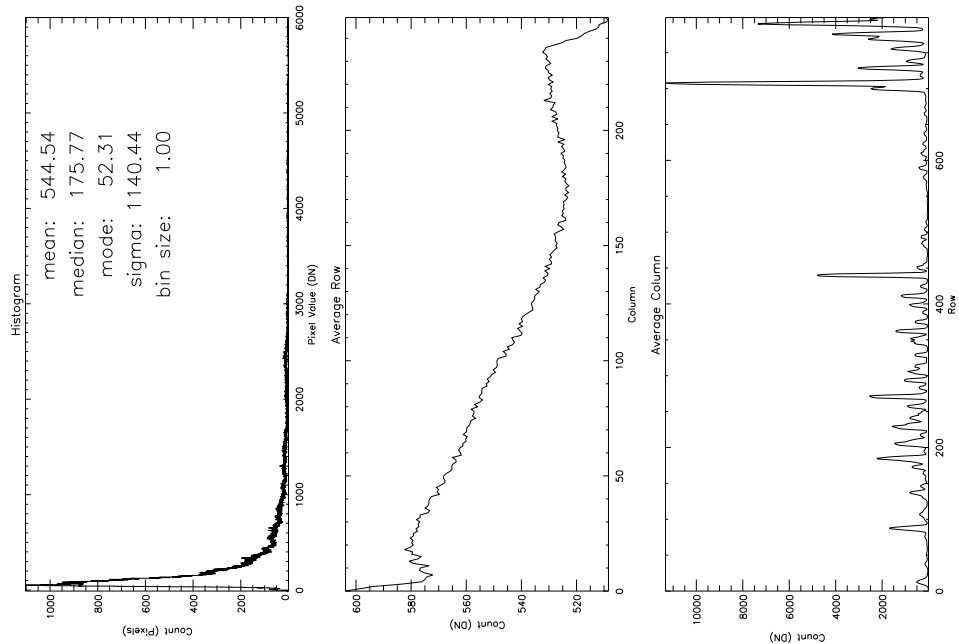
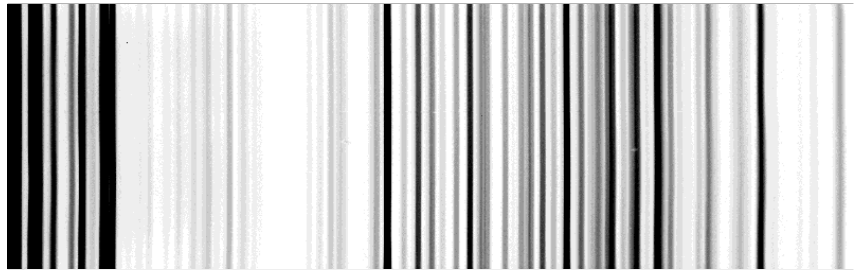


Figure 5.15: Image of MMT Comparison Lamp After Flat-Fielding and Before Distortion Correction: Distortions are difficult to see in the gray scale but are clearly affecting average row shown in the middle panel. (See Figure 4.2 for explanation of panels.)

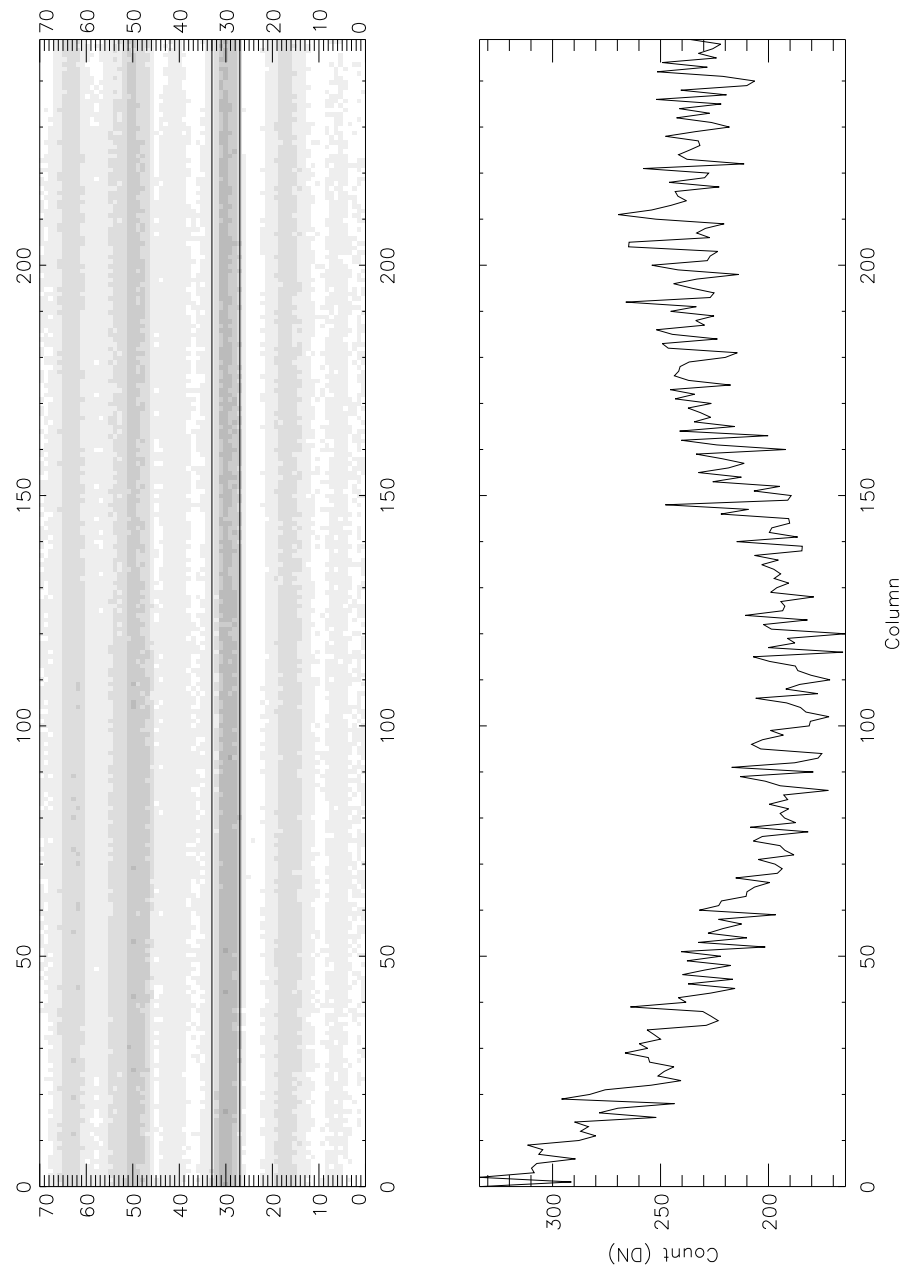


Figure 5.16: Example of How Distortion Affects Plots: The plot in the bottom panel is the row centered between the lines in the top panel: The variation seen in this plot is due to the emission line moving in and out of the row. (See Figure 4.2 for explanation of panels.)

```

NOAO/IRAF V2.10EXPORT rouse@kappas.la.asu.edu Sun 16:21:38 17-Aug-97
func=spline3, order=1, low_rej=3, high_rej=3, niterate=0, grow=0
total=41, sample=41, rejected=0, deleted=0, RMS= 2.213

```

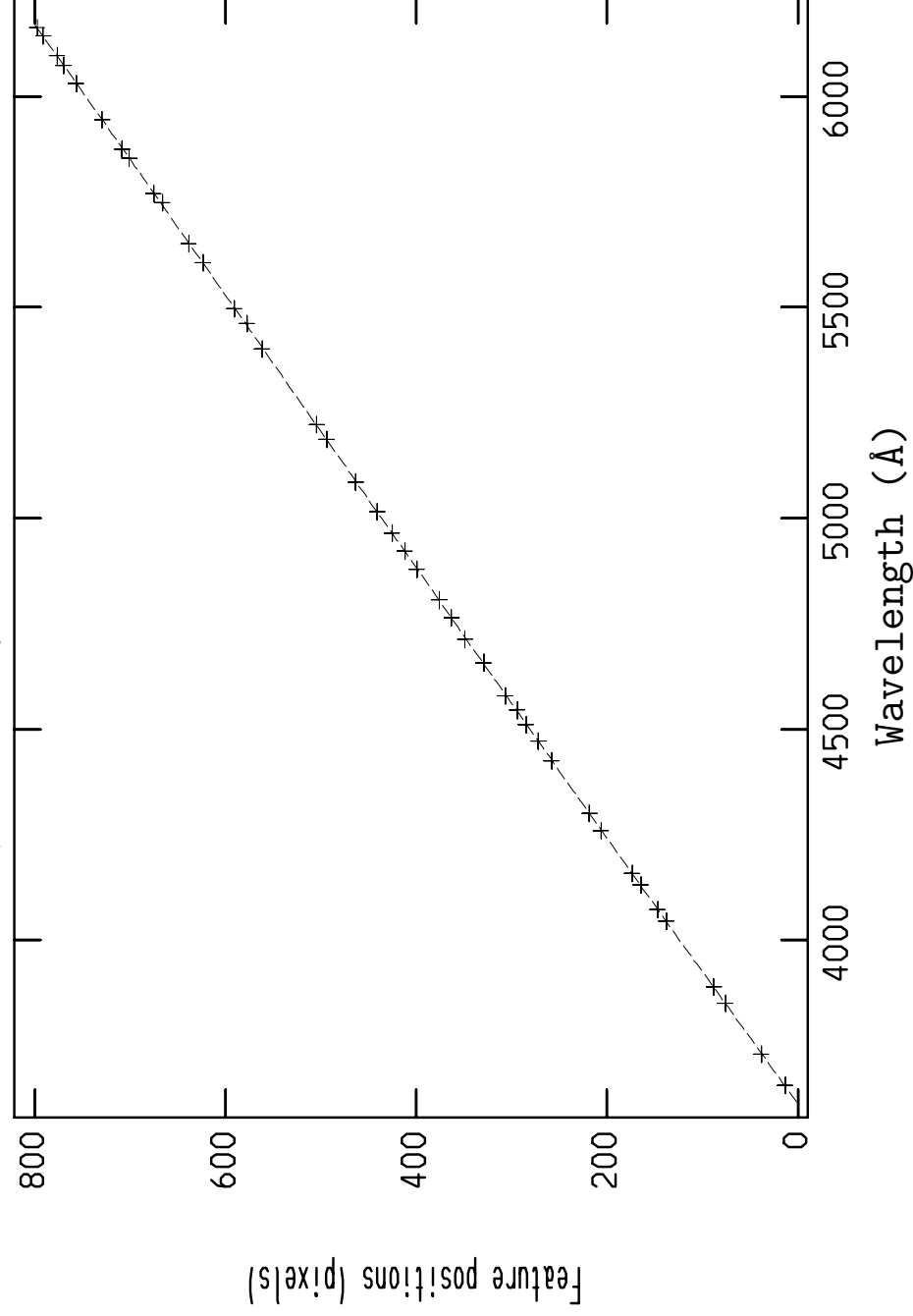


Figure 5.17: Example Fit of Wavelengths to Pixels: The fit is a first order cubic spline with 3σ clipping. The mapping of wavelength to pixels is not linear.

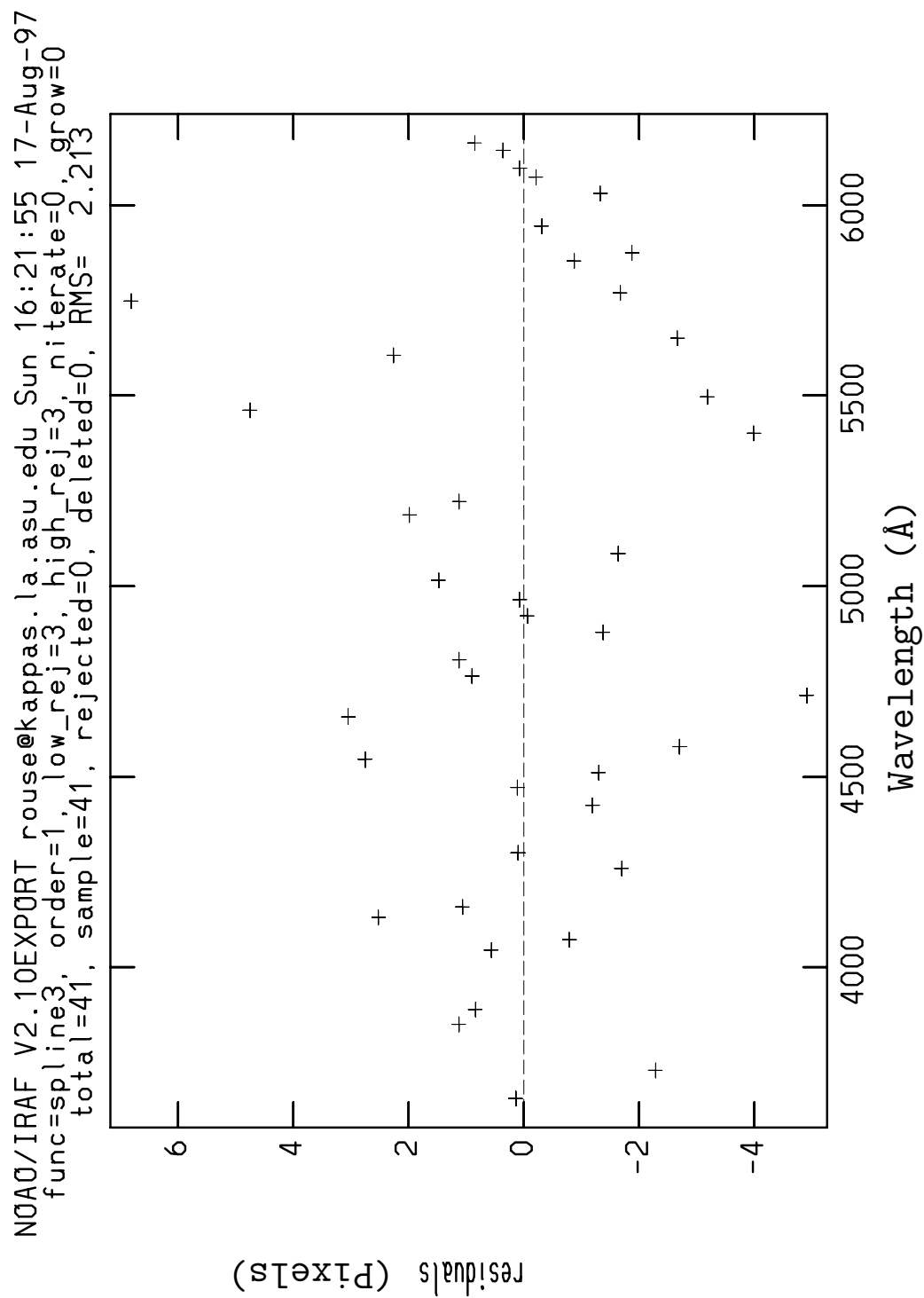


Figure 5.18: Example Residuals of Fit in Figure 5.17


```

N0A0/IRAF V2.10EXPORT rouse@kappas.la.asu.edu Sun 16:19:06 17-Aug-97
identify comp0025[125,*]
comp

```

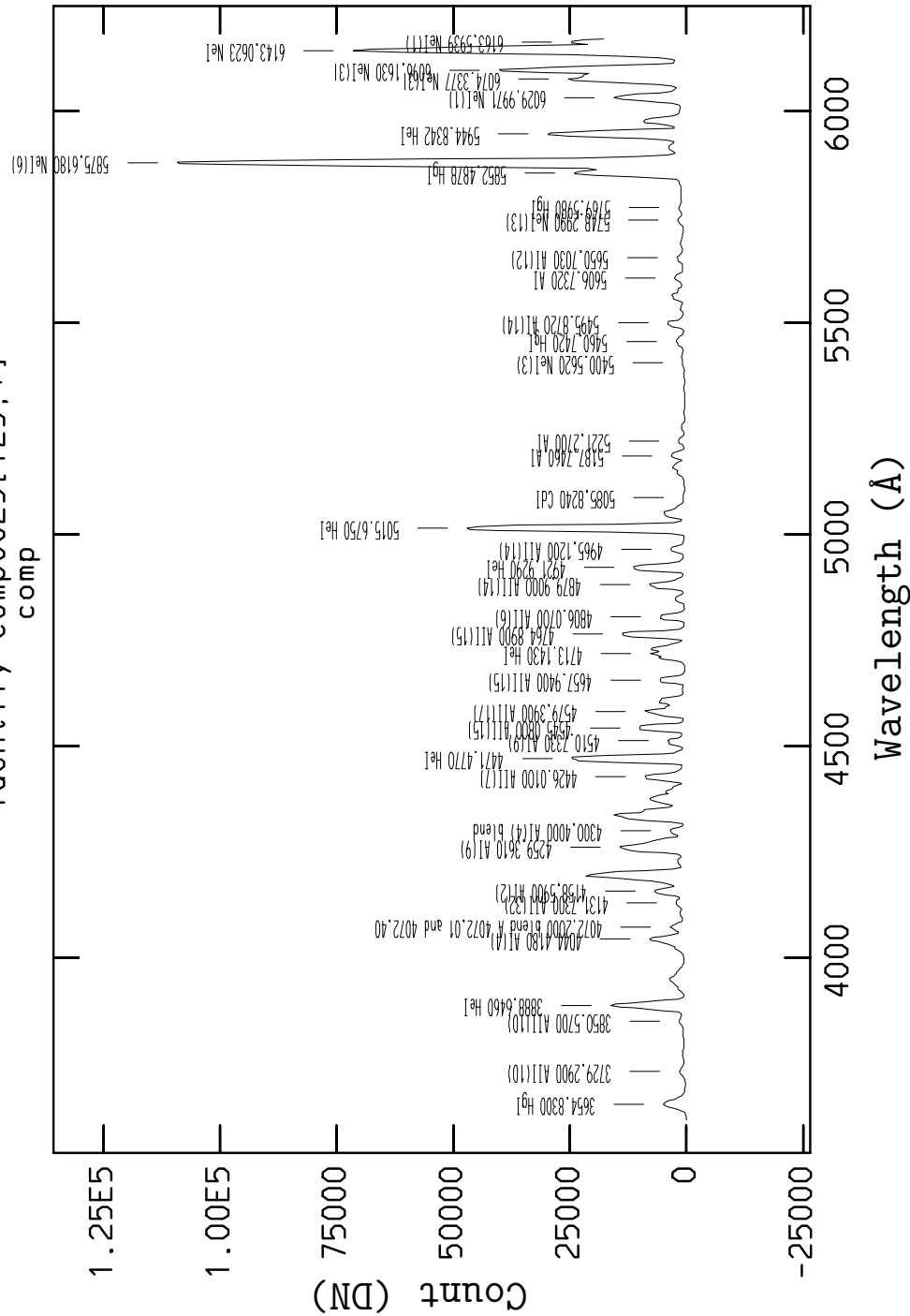


Figure 5.19: Example Feature Selection: The fitting procedure is initialized by interactively assigning wavelengths to known emission features.

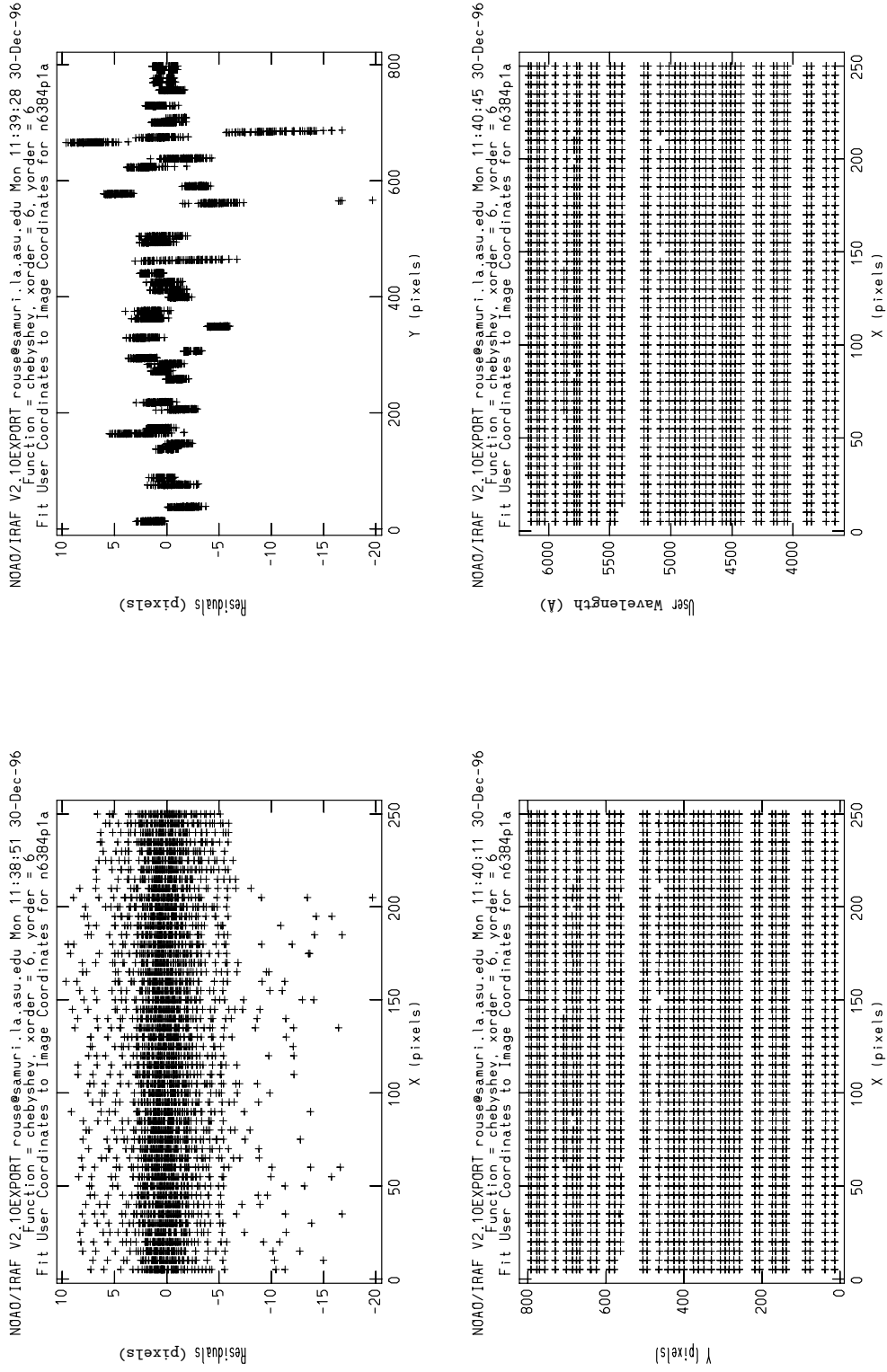


Figure 5.20: Determining Distortion Corrections: The lower left panel shows the feature traces in pixel coordinates. The upper left shows the residuals of the two dimensional sixth order fit along the spatial axis. The upper right shows the residuals along the dispersion axis. The lower right panel shows the corrected traces.

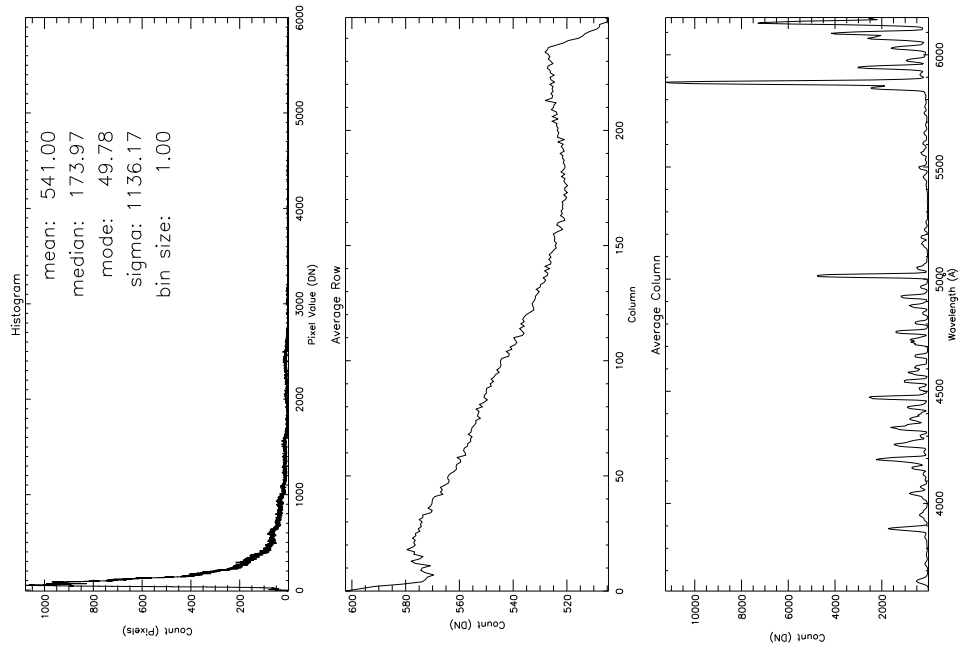
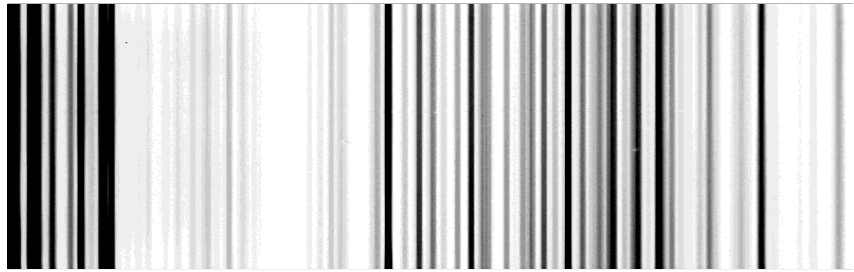


Figure 5.21: Image of MMT Comparison Lamp After Distortion Correction: The inverse of the wavelength-to-pixel transformation is used to remove distortions from input images. (See Figure 4.2 for explanation of panels.)

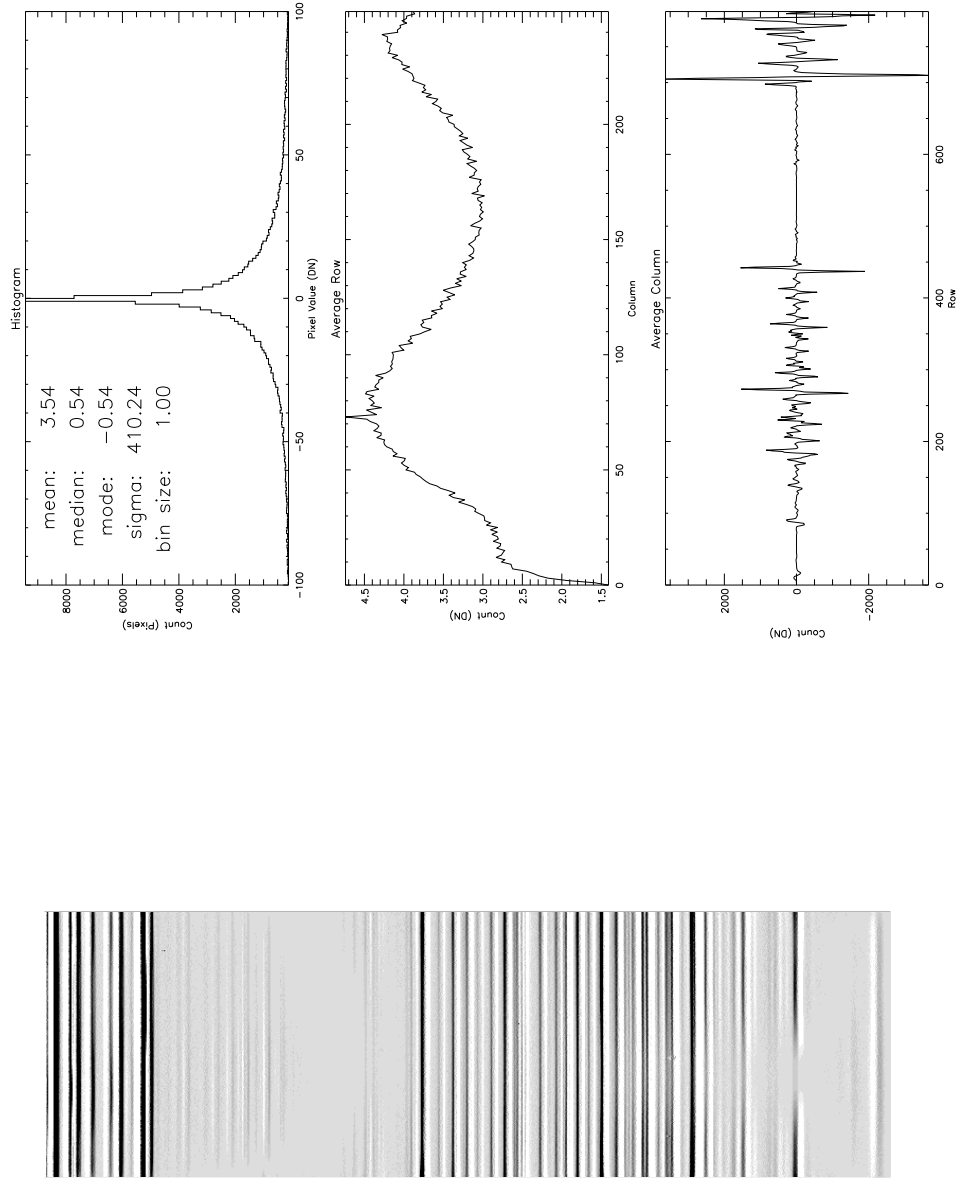


Figure 5.22: Difference of MMT Comparison Lamp Before and After Distortion Correction: This reveals clearly the distortions present in uncorrected images. (See Figure 4.2 for explanation of panels.)

5.6 Sky Subtraction

Sky subtraction must take place after distortion correction because the wavelengths in the sky spectrum must fall in the same rows as in the object spectrum. A range of columns is selected in each image that is not contaminated by object light. Then a software mask is created with ones for sky and zeros for everything else including cosmic ray hits or bad pixels. The unmasked columns and pixels are combined spatially to form a one dimensional sky spectrum. A mean is used to select the output pixel values. The mean is unbiased because deviant pixels have been masked. Figure 5.23 shows a sample sky spectrum with its sigma image. This spectrum is then subtracted from each column in the associated image. This is done for all the star and galaxy images.

5.7 Scan Correction

Because the galaxies are spatially resolved each part of the longslit must be calibrated. Therefore, the standard stars are scanned along the slit during the exposure. However, it is not possible to align the slit perfectly with the direction of motion. So, the star does not usually remain centered in the slit as it is scanned. Also the star spends more time at the slit ends because the telescope must decelerate and accelerate when the scan changes direction. Hence an artificial gradient along the slit is introduced. Figure 5.24 shows a particularly nasty case.

This artificial gradient must be removed or else it will appear as a change in the CCD sensitivity along the slit. This is accomplished by dividing the middle row of the image into all the rows. The top panels in the figure show the middle row and another row. The bottom panels show the same two rows after the correction. The corrected image is used to determine the sensitivity function for flux calibration.

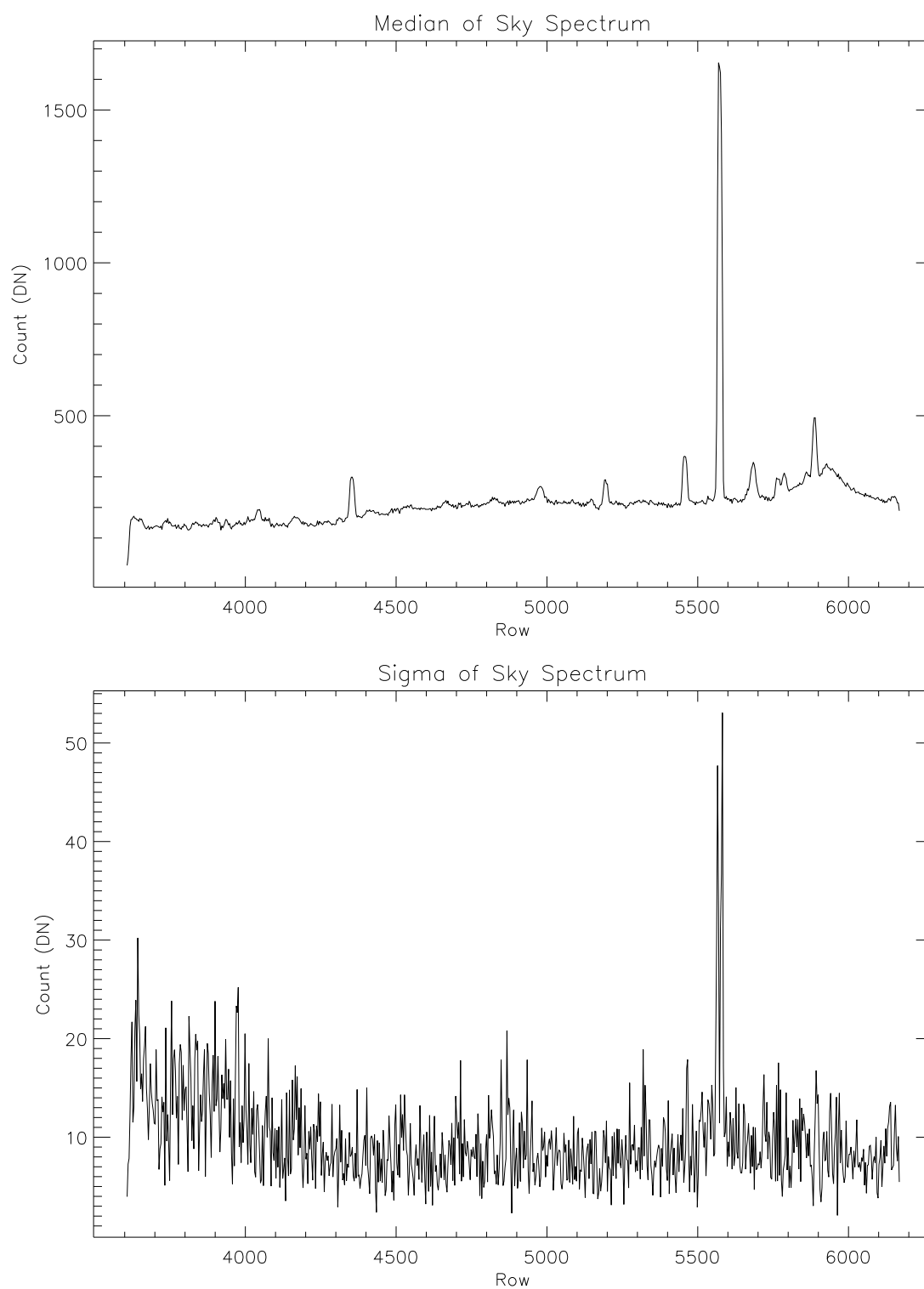


Figure 5.23: Example MMT Sky Spectrum: The top panel is the mean sky spectrum created from an image wherein the non-sky pixels were masked. The bottom panel is its standard deviation.

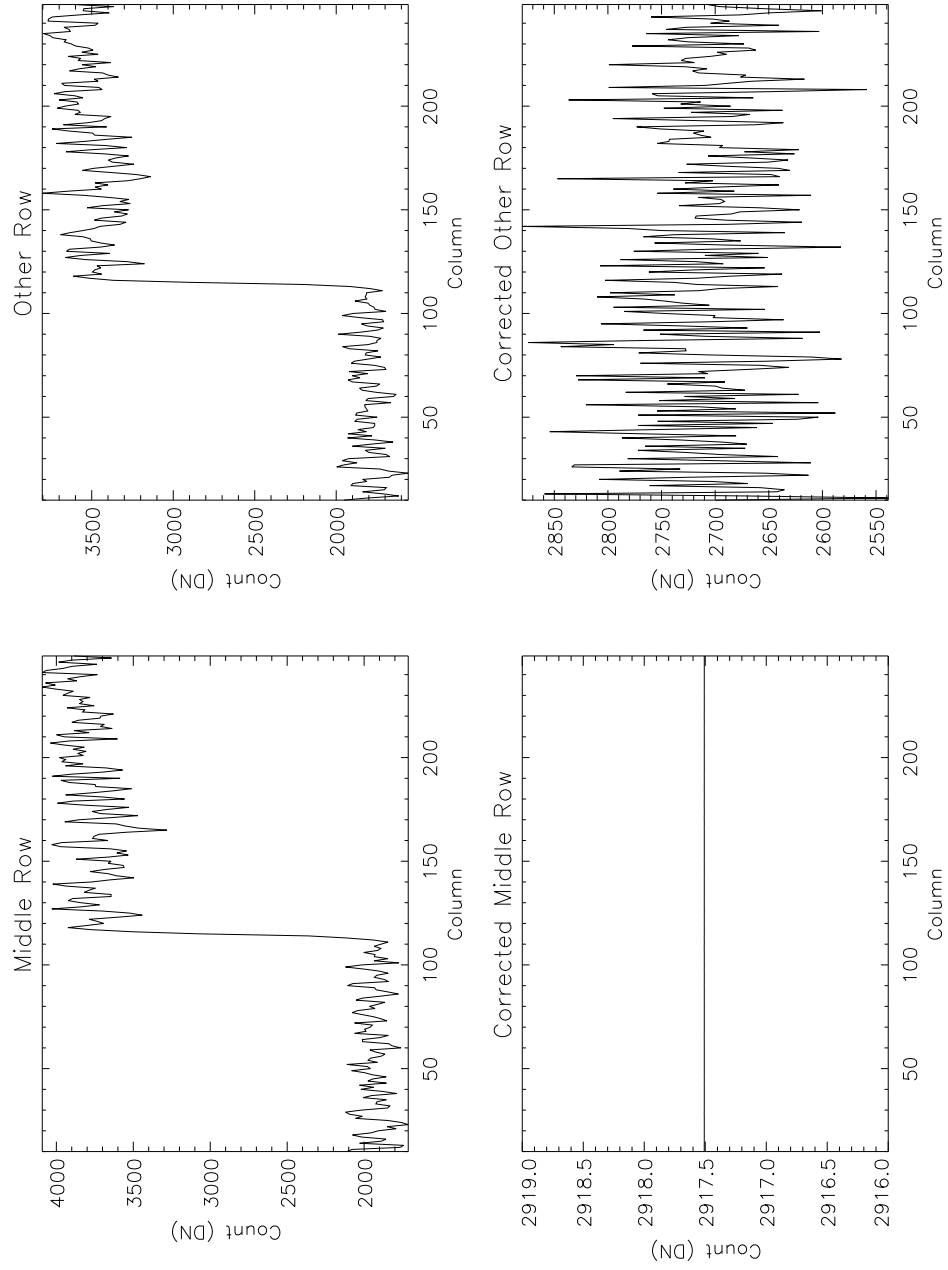


Figure 5.24: Example of Scan Correction of MMT Standards: The middle row shown on the left top is divided into all the rows. An example is shown on the right. The results are in the bottom panels.

5.8 Flux Calibration

Since the quartz lamp spectrum nor twilight spectrum are absolutely calibrated they reveal no information about the response of the CCD along the dispersion axis (Section 3.1). The sensitivity is the response of the CCD as function of wavelength. It must be determined from observations of spectrophotometric standard stars. Standards from the *IIDS Standard Star Manual* [Str77] are used for this purpose. It is composed of the spectral energy distributions from Oke and Stone [Oke74, Sto77]. The flux of a spectrophotometric standard is known in many well defined band passes in the optical region. This is based on Vega having a flux of 3.52×10^{-20} ergs/cm²/s/Hz at 5556Å. The standard band passes are placed on the observed spectrum of the standard. The total flux in each band is determined. Comparing the known flux to the observed flux gives the sensitivity.

Figure 5.25 shows the three steps involved. Panel a) of the figure shows the location of the standard band passes in the observed spectrum. The spectrum is from one column of the standard star image. The boxes in this plot have the same widths as the bands. Some of the bands (not shown) are ignored because they fall close to a strong absorption feature. Some bands are added to fill in gaps in the standard. The flux in an added band is determined by interpolating between the standard bands. The observed flux in these band passes is determined and compared to the known or interpolated flux of the standard star.

Panel b) shows the negative magnitude of the ratio of the known flux to the observed flux. This quantity is also called the sensitivity. In each band there is one measurement from each column of the spectral image. The plotting symbols at a given wavelength represent these measurements. The tight grouping of these points indicates that the sensitivity varies insignificantly along the slit. A one dimensional function, a third order cubic spline, is fit to the sensitivity. The sensitivity function facilitates the flux calibration of the galaxy spectra. The fit is shown in panel b). The residuals are shown in panel c). The residuals range from -0.1 to 0.1 magnitudes which is about 20% on the linear scale.

When evaluated at a given wavelength the sensitivity function provides the scale factor in the flux calibration equation:

$$F_g = \frac{G_{obs}}{t_g \delta \lambda} \frac{t_s \Delta \lambda F_s}{S_{obs}} 10^{-0.4ae} \quad (5.1)$$

where G_{obs} is the observed galaxy count in the band, t_g is the galaxy exposure time, $\delta \lambda$ is the dispersion, t_s is the standard exposure time, $\Delta \lambda$ is the standard band width, F_s is the known flux of the standard, S_{obs} is the observed standard count, a is airmass, e is extinction, and F_g is the galaxy flux in the band. All remaining images are fluxed using the sensitivity function.

5.9 Example Spectral Image

This section provides spectral images of one galaxy at various stages of processing. Figure 5.26 shows a raw galaxy spectral image. Figure 5.27 shows the same spectral image processed through distortion corrections. Figure 5.28 shows the galaxy after sky subtraction. Figure 5.29 shows the sky-subtracted galaxy spectral image after fluxing. The spectral image is ready for aperture selection and index measurements. All galaxies are processed in the same way.

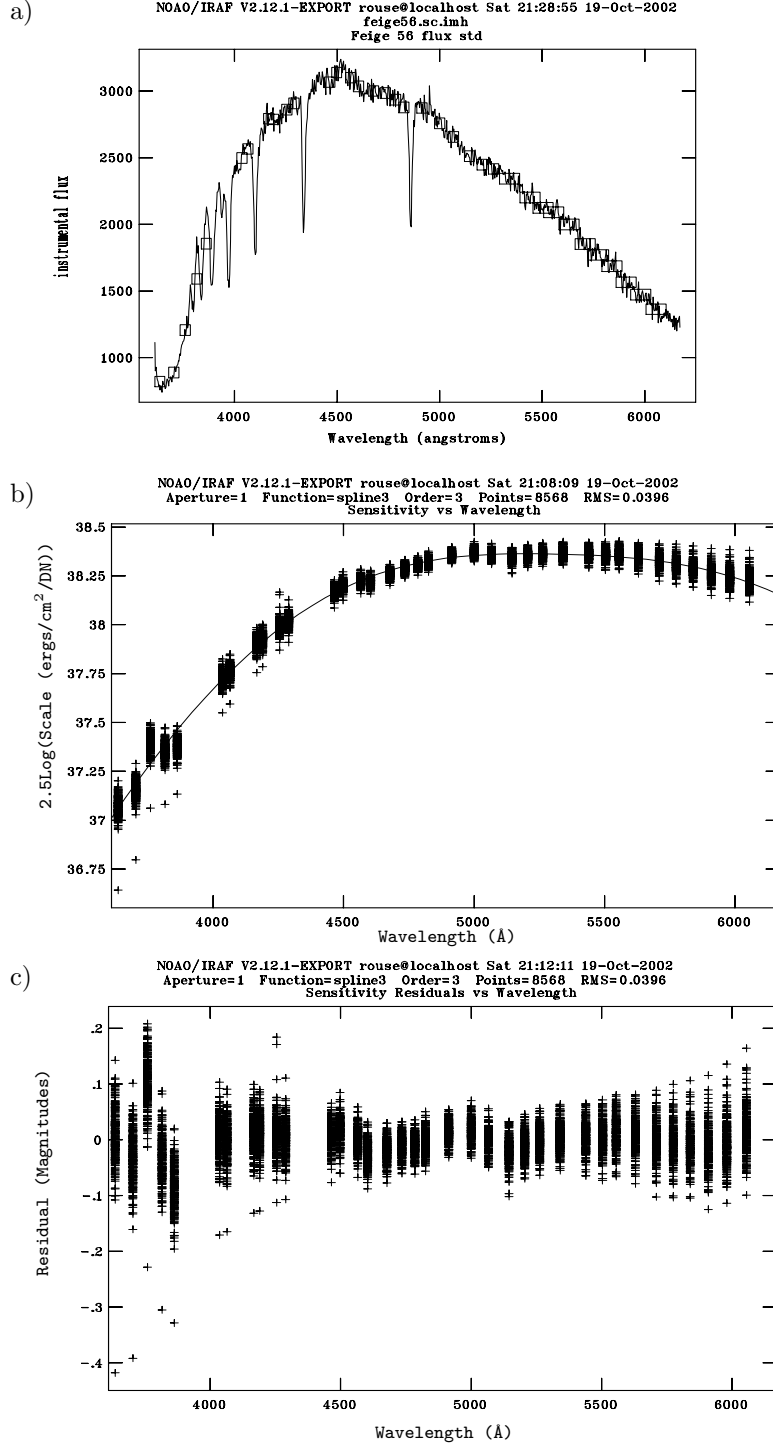
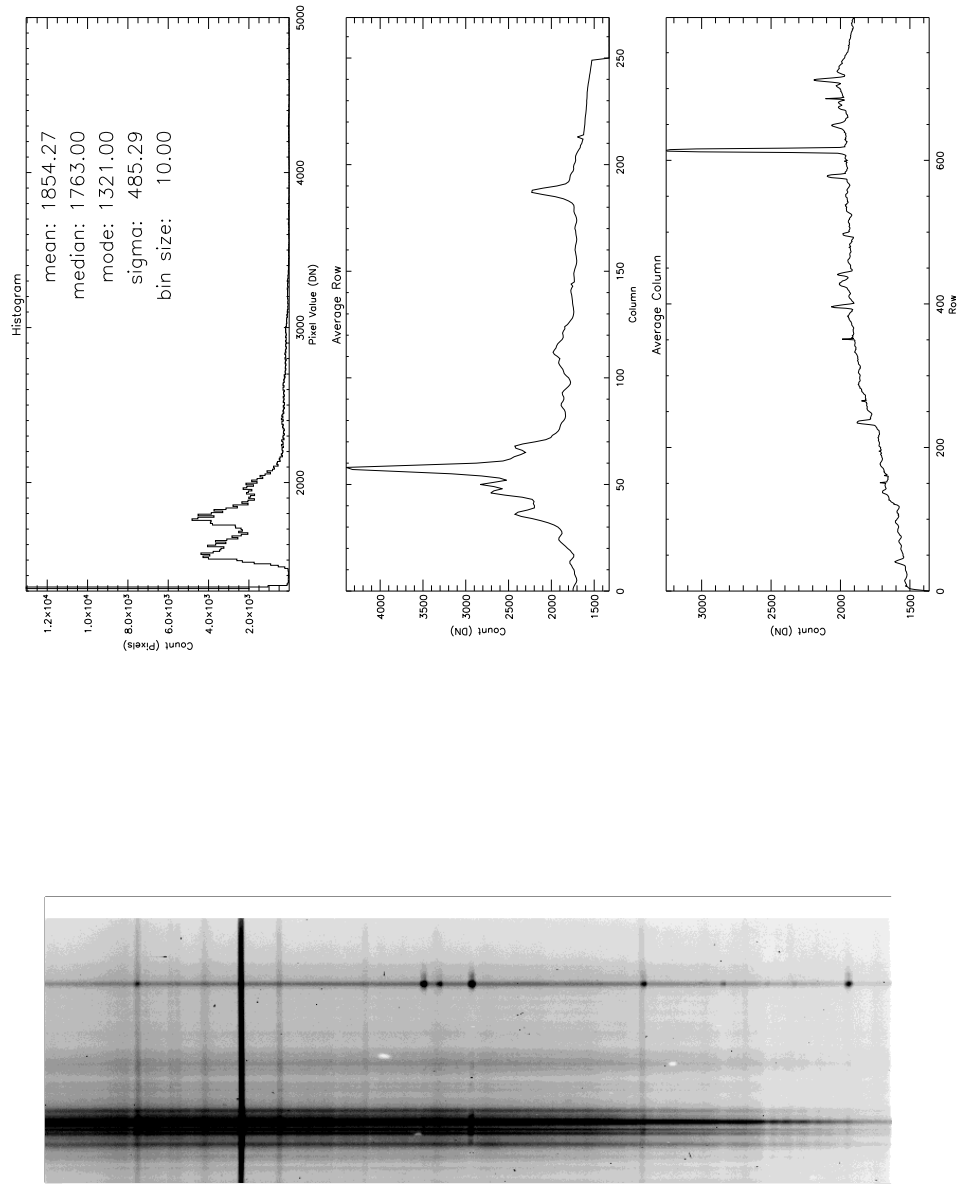


Figure 5.25: Steps in Flux Calibration: a) The boxes represent the location and width of the spectrophotometric band passes. The spectrum is one column from the standard star spectral image. b) The negative magnitudes of the ratios of the observed flux to the known flux are plotted as crosses. In each band there are measurements from each column in the standard star image. The line is a third order cubic spline fit to the measurements. c) Residuals of the fit shown in b).



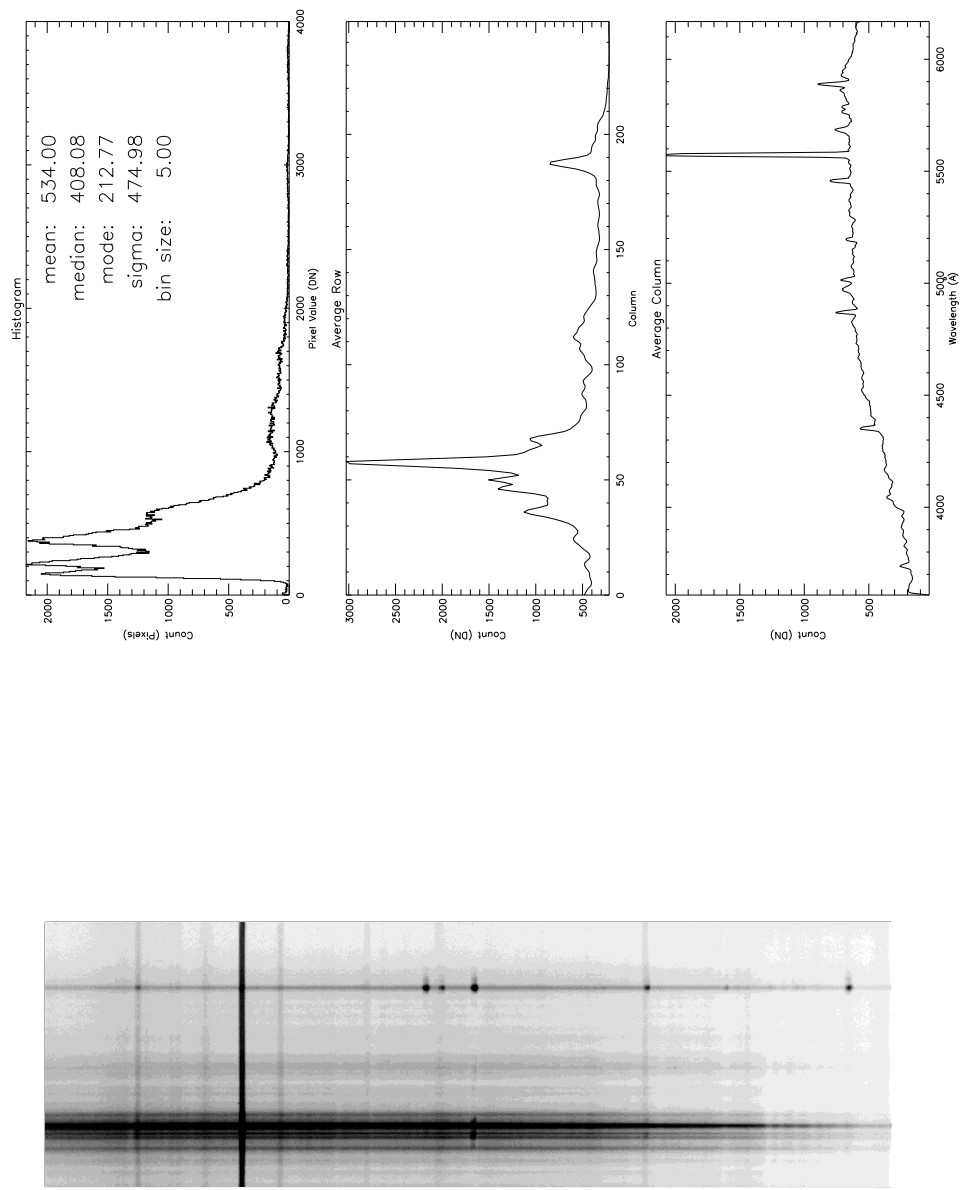


Figure 5.27: Processed Spectral Image of Galaxy: See Figure 4.2 for explanation of panels.

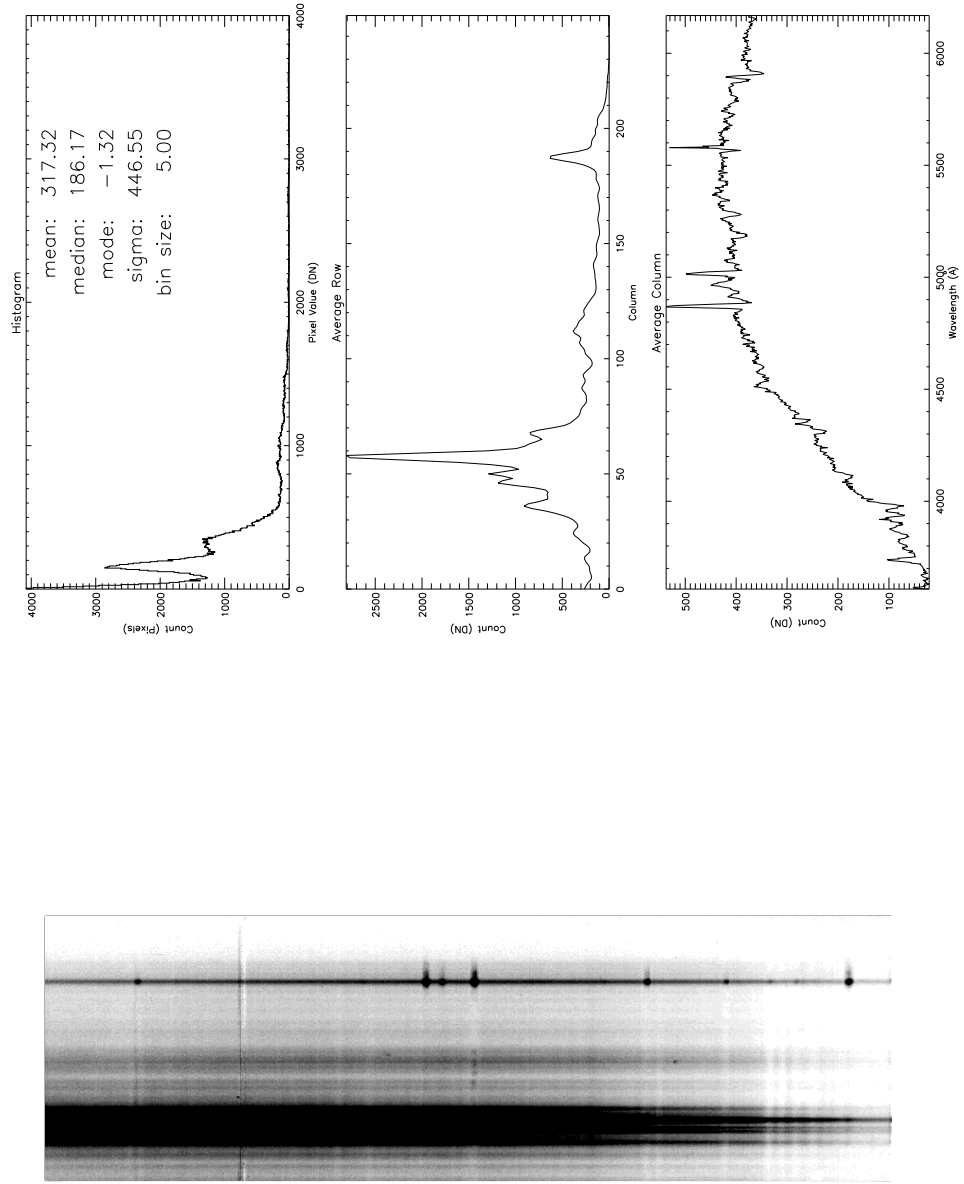


Figure 5.28: Sky-subtracted Spectral Image of Galaxy: See Figure 4.2 for explanation of panels.

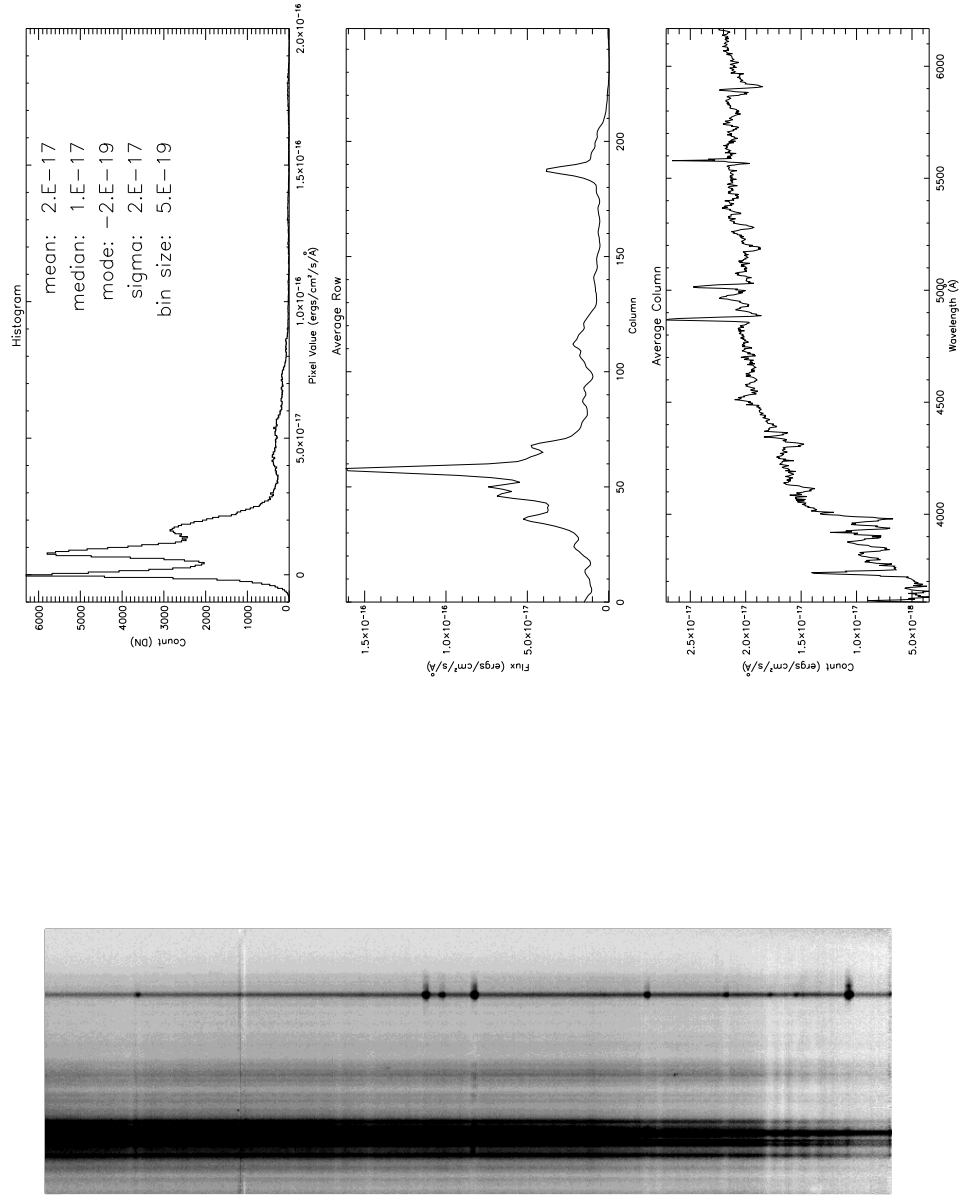


Figure 5.29: Fluxed Spectral Image of Galaxy: See Figure 4.2 for explanation of panels.

5.10 Hysteresis in Serial Register

This concerns the second Lorel 1200×800 CCD used at the MMT. Only the 27JAN93 observing run is affected. The serial register of this CCD suffers from a *hysteresis*¹ which causes regions with higher exposure to have a higher bias level. This can be seen by comparing Figure 5.30 and Figure 5.31. Figure 5.30 shows the average column of this image. Figure 5.31 shows a fit to the overscan of the same image. Note that both plots have the same profile. Thus images with significant peaks in luminosity require a high order fit to remove the bias. The largest residuals in such a fit are of order 5 DN. Figure 5.32 shows the residuals of a typical fit. This is acceptable considering that the weakest signal in the image is at least 40 times this amount and that these residuals occur in pixels with a significantly higher number of counts. Otherwise the image processing is unchanged. This does not affect the galaxy data discussed in later chapters of this work.

¹M. Lesser, private communication

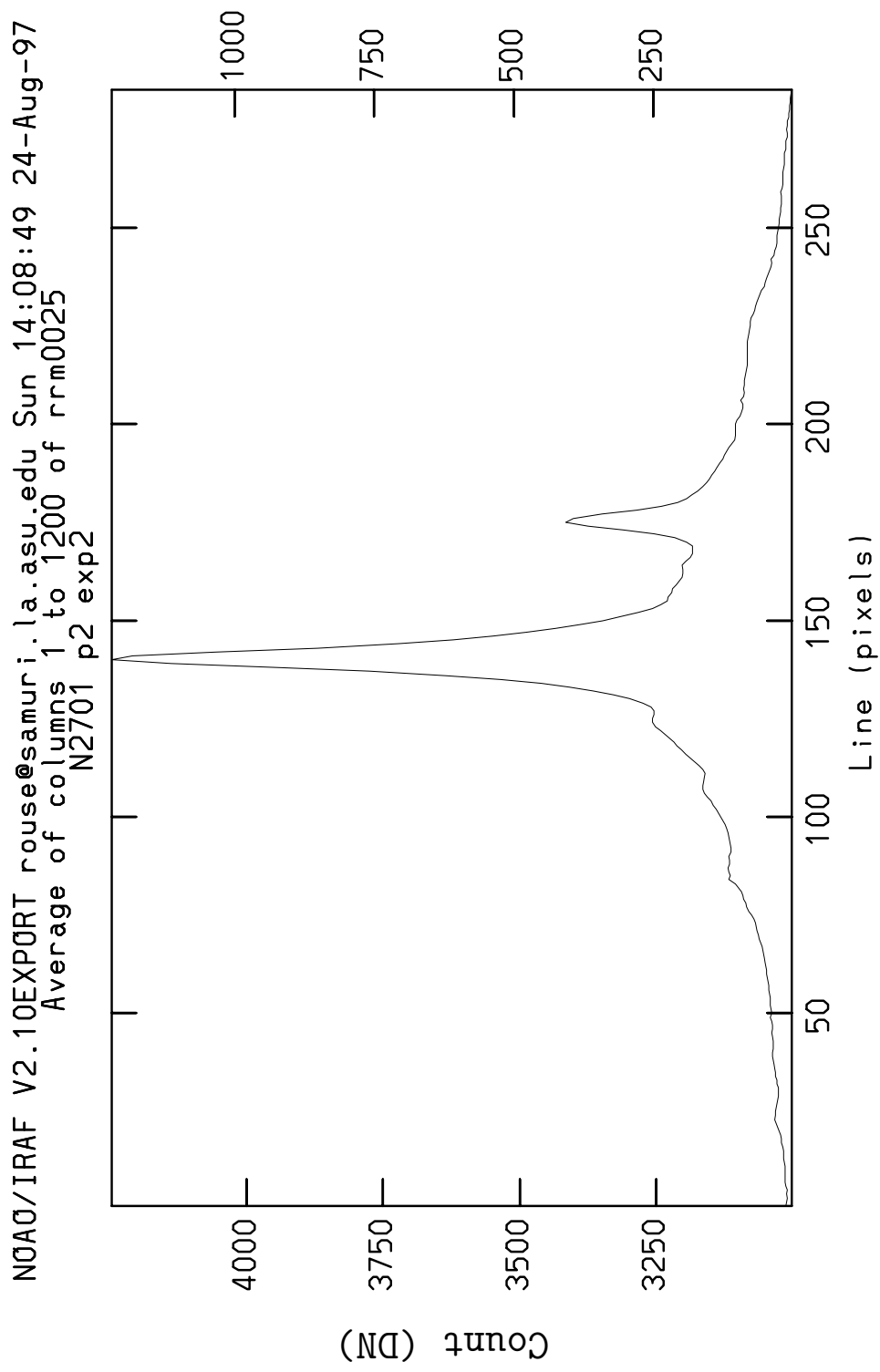


Figure 5.30: The Average Column of a Galaxy Spectral Image: Compare this figure to Figure 5.31 which is the average overscan from this image.

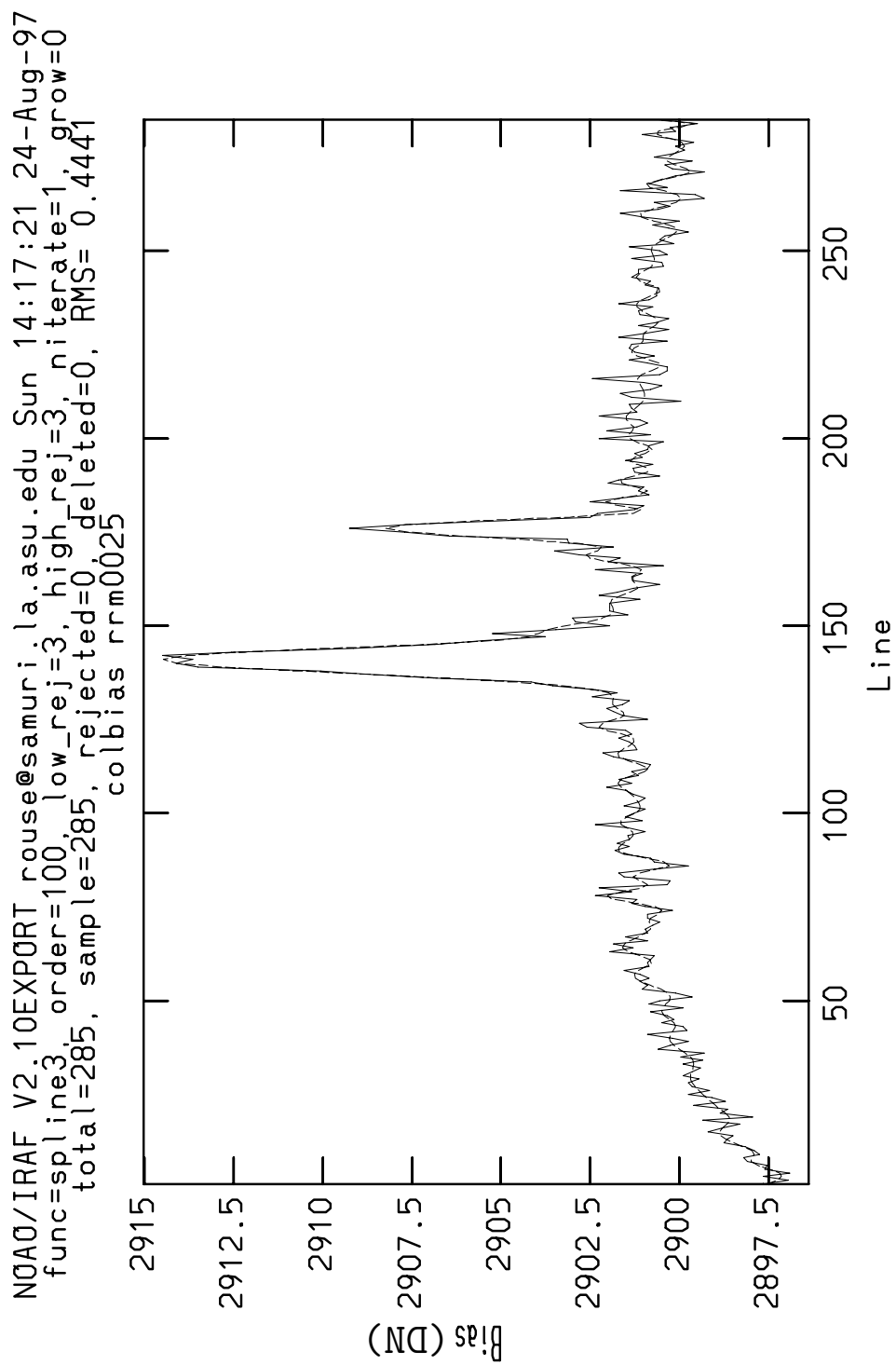


Figure 5.31: A 100th Order Fit of Cubic Splines to the Overscan Region: Compare this figure to Figure 5.30. Note that the count in the overscan resembles the galaxy profile. This is the hysteresis discussed in Section 5.10.

```

NOAO/IRAF V2.10EXPORT rouse@samuri.la.asu.edu Sun 14:17:38 24-Aug-97
func=spline3, order=100, low_rej=3, high_rej=3, niterate=1, grow=0
total=285, sample=285, rejected=0, deleted=0, RMS= 0.4441
colbias rrm0025

```

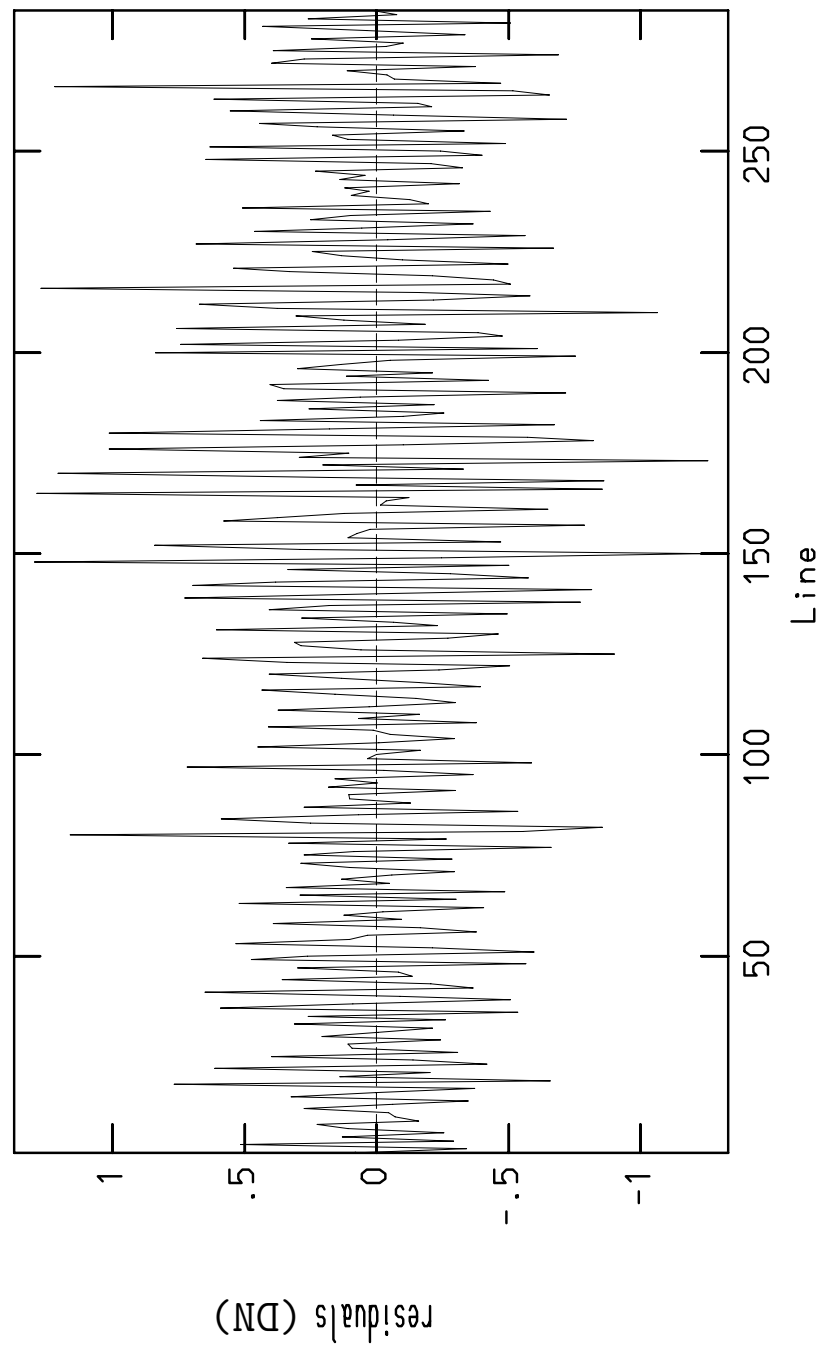


Figure 5.32: Residuals of Fit Shown in Figure 5.31

5.11 Extraction of One Dimensional Spectra

The extractions are made following two criterion the shape of the image along the slit and the count in the resulting spectra. The morphology of the image along the slit determines the placement of the first few apertures. For example, the center of a galaxy is peaked. So an aperture is centered on this peak. Spiral arms also show up as peaks of smaller amplitude. An aperture is centered on these as well. Figure 5.33 shows an example galaxy profile with apertures labeled with numbers and marked with vertical bars. Aperture 11 is the center of the galaxy. Aperture 22 is an HII region.

After the first few apertures are positioned their widths are increased so that a count of 1500 to 2000 DN is obtained upon extraction in the region around 4500\AA . However, they are not made wider than the feature on which they are centered. Figure 5.34 shows two spectra extracted from the image in Figure 5.33. The remaining apertures are positioned adjacent to the first few and their sizes are increased to obtain 1500 to 2000 counts around 4500\AA . Note that this is not always possible for faint parts of a disk. Thus, S/N is sometimes sacrificed to keep the spatial information. In this manner every part of the spectral image is included in an aperture.

The extractions are performed interactively by plotting profiles and displaying the image with the candidate aperture boundaries over plotted. For each spectral image the columns contained in an aperture are summed and stored as a one dimensional spectrum.

The extracted spectra are checked for count level at 4500\AA . If a spectrum or spectra are deemed unsatisfactory some of the apertures may be merged to increase S/N. This is not done if the apertures are from different parts of the disk (e.g. arm versus inter-arm) in order to preserve spatial information and to avoid mixing populations. In that case S/N is sacrificed and the spectrum cannot be improved. These steps are repeated until a satisfactory set of spectra is attained. This is done for each slit position. These spectra are used for measuring line indices.

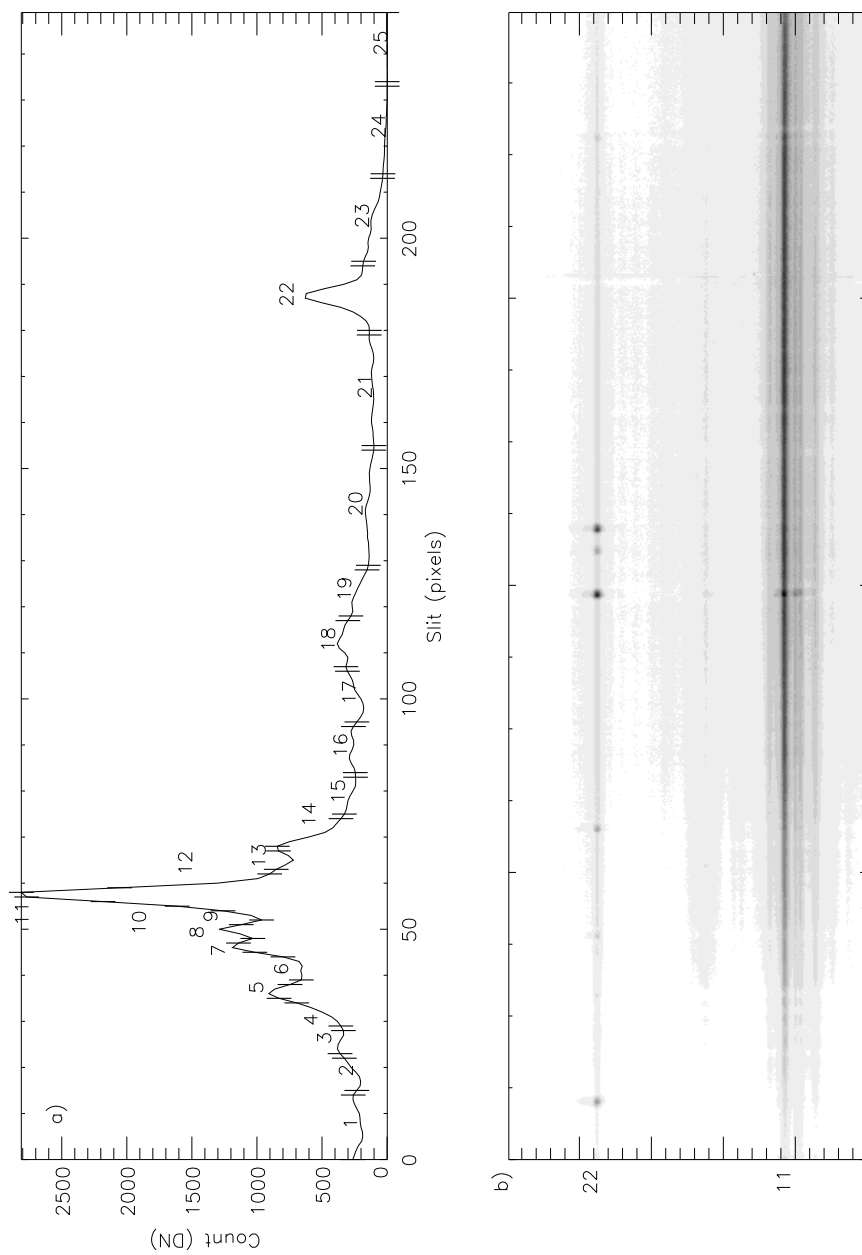


Figure 5.33: Example of Aperture Selection: a) An example slit profile with the selected apertures labeled with a number and delineated by vertical lines. The vertical lines mark the first and last pixel within the aperture. b) The slit profile in a) was created from this image. Apertures 11 and 22 are labeled. The spectra from 11 & 12 are shown in Figure 5.34

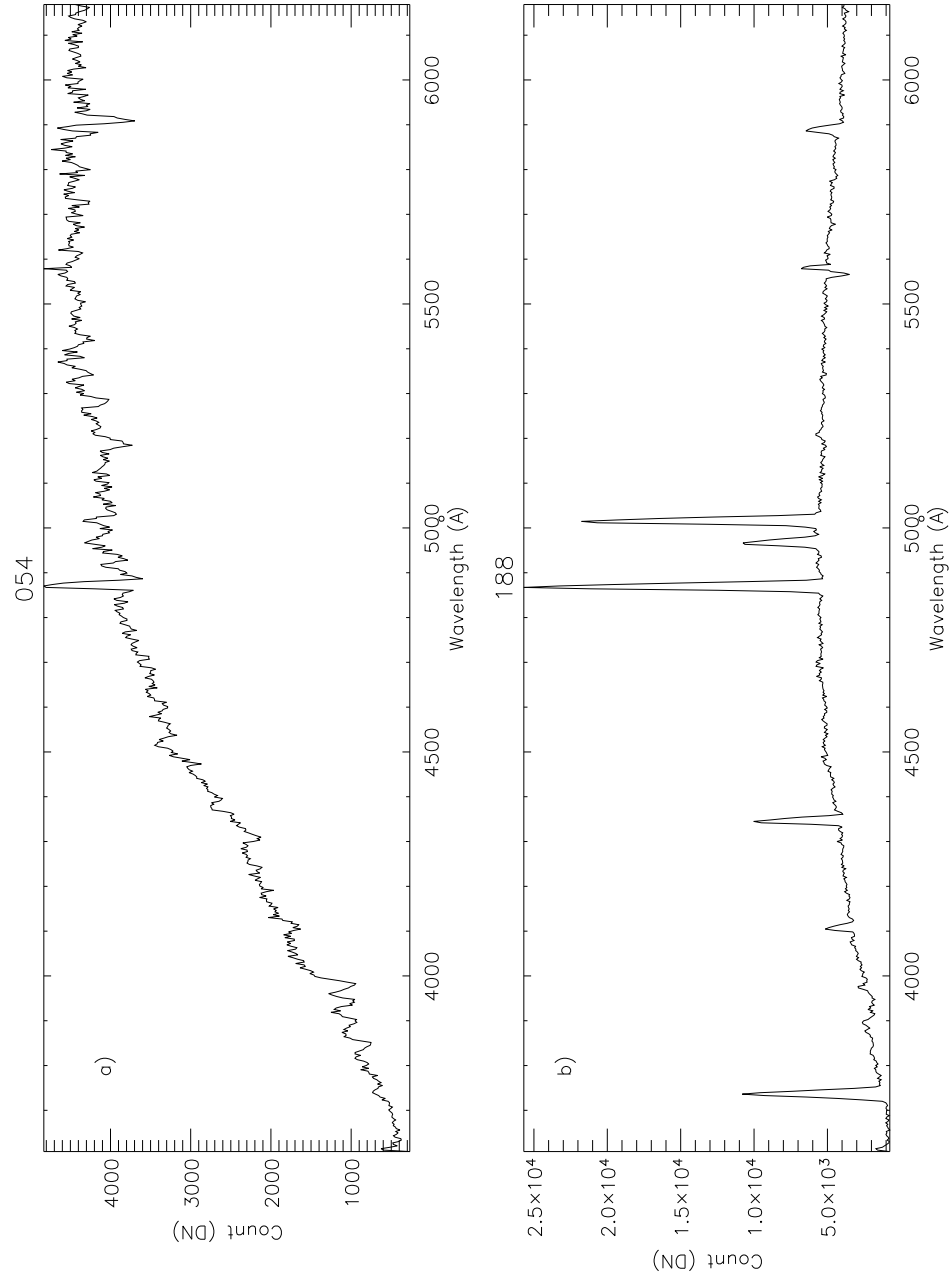


Figure 5.34: Example of Extracted Spectra: a) The spectrum in aperture 11 from Figure 5.33 b) The spectrum in aperture 22 from Figure 5.33

CHAPTER 6

INFRARED IMAGE PROCESSING

This chapter describes how the infrared imagery is processed. It is similar to the optical in that there are darks, zeros, and flat-fields. The details are very different because of the large infrared background signal. Logistical preprocessing is noted for the record. Then processing of wobble-and-jitter mode for the galaxies and mapping mode for the stars is discussed.

6.1 Preprocessing

The IR data requires some additional bookkeeping because the NICMOS headers are very terse. Hence it is necessary to add parameters such as airmass, filter, identification, and array parameters to the image headers from the observing logs. Also some of the FITS headers output by the NICMOS software do not have the correct format. They are corrected after being converted to IRAF files.

Then it is necessary to set the effective exposure time in the image headers. The effective exposure time is the exposure time times the number of coadds. For example, summing two 5 second exposures is equivalent to one 10 second exposure.

For every image in a sequence the clipped mean, median, mode, and histogram are calculated. These will be used later to help determine if all the images in a sequence are usable. Clipping is used because of the large number of bad pixels in the NICMOS arrays. The iterative clipping procedure is used to set limits on the data values that go into the histogram. The procedure is as follows. The standard deviation of the image is calculated. All points three standard deviations or more above or below the mean are clipped. The mean and standard deviation are recalculated without the clipped points. These steps are repeated until the standard deviation changes by less than .001 DN. The three sigma limits are stored. Then for a given sequence the maximum of the upper clipping

limits and the minimum of the lower clipping limits are used for all the histograms in that sequence. This gives them all the same horizontal scale. See Figure 6.1 for an example. This shows that the statistics are fairly stable over 10 to 20 minute periods. Note that the histograms do not have a Gaussian shape.

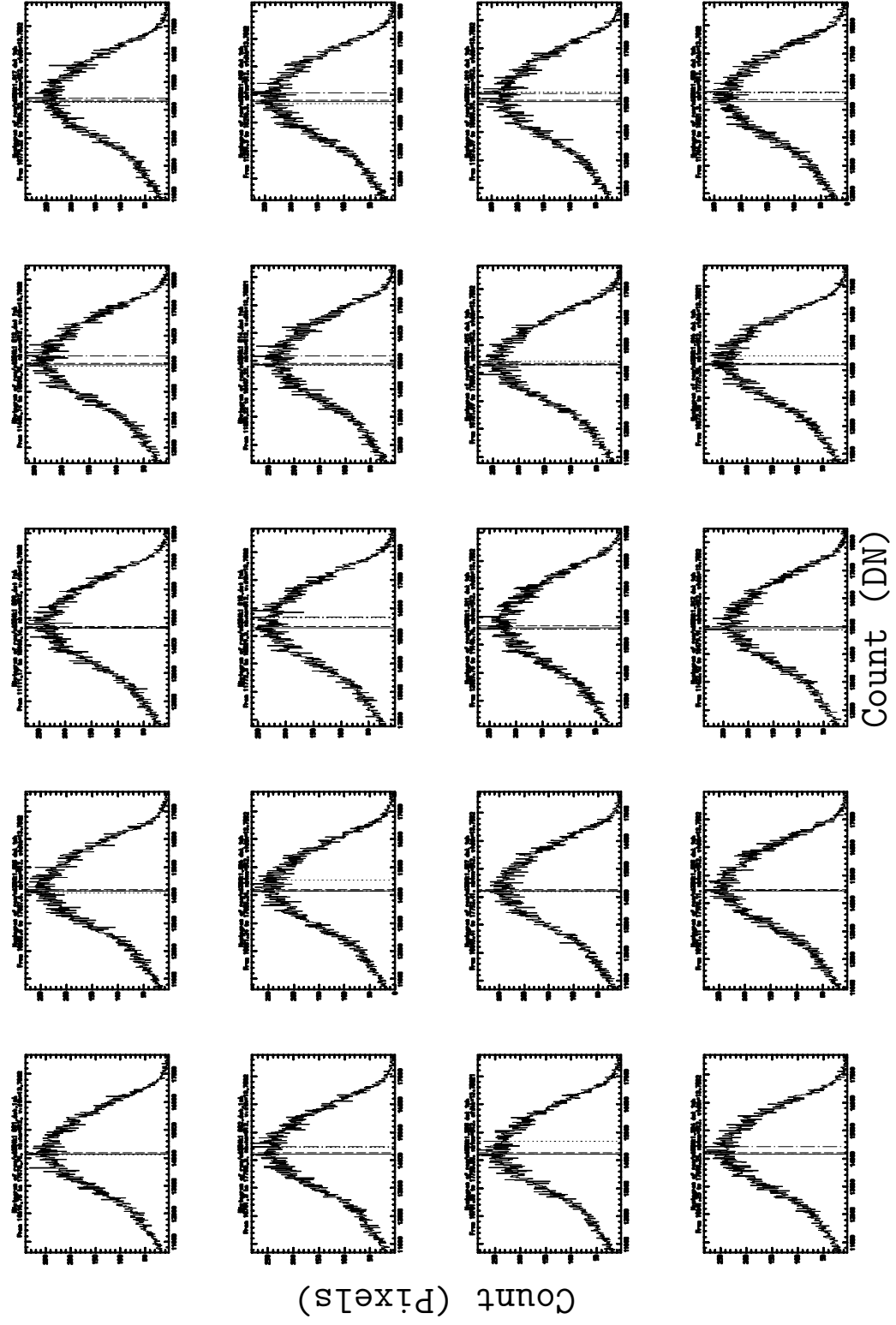


Figure 6.1: Clipped Histograms of a Sequence of K Exposures on NGC 6384: The positions of the clipped mean, median, and mode are marked by the solid, dotted, and dot-dashed lines respectively. See text for explanation of clipping procedure.

6.2 Zeros and Darks

The ten zeros taken at the beginning and end of each night are combined using the median into one combined zero image. This image is also called a bias image. An example is shown in Figure 6.2. This image is not used unless there is no other source of bias information. Darks are *not* bias subtracted. Ten darks of each exposure time and coadd are taken. Each set is combined with a median into a final dark for each set. An example of a 30 second combined dark is shown in Figure 6.3. These darks are used when creating the sky response from the average sky images.

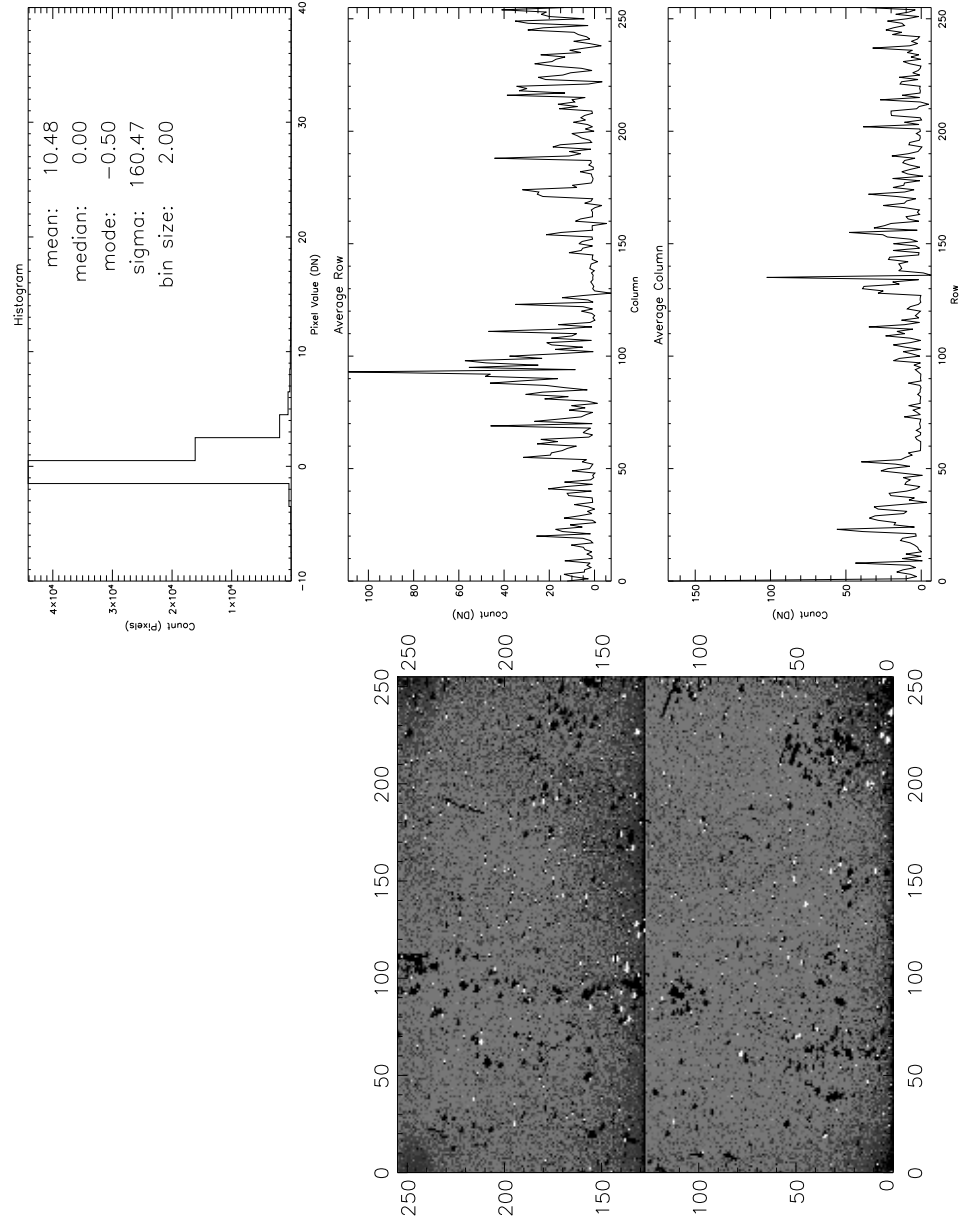


Figure 6.2: Example in IR of Median Combine of Ten Bias Images: See Figure 4.2 for explanation of panels.

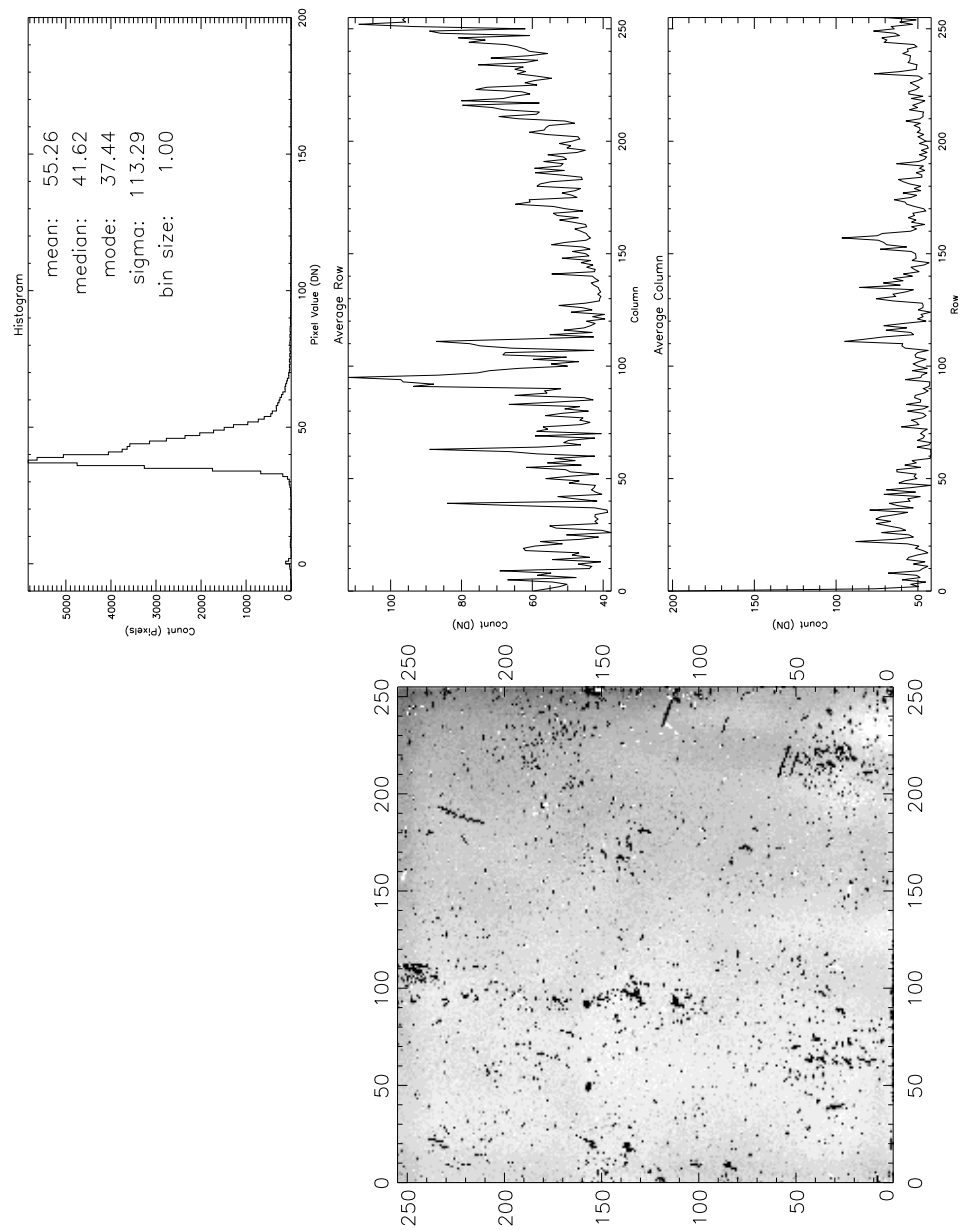


Figure 6.3: Example in IR of a Median Combine of Ten 30 Second Darks; See Figure 4.2 for explanation of panels.

6.3 Wobble-And-Jitter Mode

The details of processing a sequence of images taken in wobble-and-jitter mode is discussed. Each sequence in K typically consists of 3 sequences of 20 images starting with sky. Each sequence of exposures is reduced in the following manner. The clipped mean, mode, median, and histogram are generated for each image in the sequence. See Figures 6.1 and 6.4 for examples. The statistics vary approximately 10% over the sequence. The mode appears to vary more than the mean or median. The bottom panel in Figure 6.4 shows that it can vary from the mean by as much as three percent. This is not a significant amount. The mode is notoriously difficult to calculate. However, it is the preferred statistic when the data is not Gaussian.

The sky images before and after each galaxy image are averaged. This average sky image is subtracted from the corresponding galaxy image. In this single step the galaxy image is debiased, dark subtracted, and sky subtracted. Figure 6.5 shows the first three images in such a sequence. That figure also shows how the images are processed. In panel a) three raw images are shown. These are two sky images with the galaxy image in the middle. In panel b) the average sky is shown. In panel c) the result of subtracting the average sky from the galaxy image is shown.

Now the galaxy image is flat-fielded. Figure 6.6 shows an example average sky image. The two sky images are dark subtracted (which includes the zero) then averaged. The average dark subtracted sky it is normalized by its mode. The result of these operations is the response image. It is divided into the sky subtracted galaxy image. Figure 6.7 shows how the sky response is used to flat-field the sky-subtracted image. The left panel is the sky-subtracted image. The middle panel is the sky response. The right panel is the flat-fielded galaxy image.

Each reduced galaxy image is displayed and examined for quality of the flat-field. Figure 6.8 shows the ten processed galaxy images from a single sequence of 20 exposures. If an image is deemed substandard the statistics and histogram for the skies are consulted to determine if the image can be salvaged. An image can be salvaged only when at least one of the sky images can be used to calibrate

it. The sky image must have the same bias, dark, and response as the galaxy image. Note that in galaxy images the detector is responding mostly to the sky because it is so much brighter than the galaxy. So differences in the spectrum of the sky and galaxies does not come into play at significant level¹. However, because the nights were not photometric it is possible that the sky spectrum in the filter band pass changes between galaxy and sky exposures. When this happens the sky image will have a different flat-field pattern than the galaxy image because of the different weighting on the detector response. This is why each galaxy image must be checked by hand (although this is good practice even with photometric data). This is a likely cause of a poor quality flat-field. In this case the galaxy image is reprocessed using only the good sky images. Good sky images are ones that were used to successfully flat-field other galaxy images. If no improvement is made then it is probable that the sky spectrum in the galaxy image is anomalous relative to the rest of the sequence and that galaxy image is discarded.

After verifying the quality of each reduced galaxy image in a sequence they are combined into a single image. The histograms of the images are not all centered on the same pixel value. So, before combining, each image is offset in pixel value such that its histogram will be centered on zero. This offset is relative to the sky value for that image. Recall that the image is sky-subtracted. The sky value for the image is the offset plus the value used during sky-subtraction (i.e. mode of sky image).

Next a set of shifts in position is determined using a star common to each image. This is necessary because of the jitter (Section 3.2). Each image is shifted to be aligned with a reference image. The reference image is chosen using a centroid in position. The position of a star in the first galaxy image is determined using the centroid of the pixel values inside an aperture centered on the star. This position of the star is used to automatically find and centroid the star in the rest of the images. The position of the star is displayed and can be changed interactively for each image. Once a good position for the star in each image is available the centroid of those positions is calculated.

¹D. Burstein, private communication

The image closest to the centroid is used as the reference. This maximizes the overlap among the images giving the largest possible area for doing photometry or extracting profiles. Not shifting the reference saves a bit on smoothing the output image.

The images are now combined. The offset in DN is added to each image, centering the histograms on zero. Then each image is shifted in position using nearest neighbor interpolation. This method minimizes the smearing of bad pixels in the shifted image. Finally the offset and shifted images are combined using a median. This effectively eliminates all the bad pixels. The center region of the combined image is overlapped by all the inputs. This is the valid part of the image. The edges are ignored. The median of the sky values from each image is the sky value for the combined image. The standard deviation is taken as the error in the sky value. A background measured in the combined image should be near zero at this point.

Now there is one combined image for each sequence. Examples are shown in Figure 6.9 in panels a), b), and c). Typically there are three sequences taken on each galaxy. So there will be three combined galaxy images. The combined images from each sequence are again combined to form the final image.

The clipped statistics are calculated again in the same manner as before. The fact that the sequences are taken at different airmasses and UT is negligible (Section 8.1). The images are aligned and combined using the mean. The mean of the three input sky values is used as the sky value for the final combined image. However, a background value is determined interactively by measuring the mode in the background areas of an image. If the background value is not zero a new sky value is calculated by subtracting the background from the combined sky value. An example is shown in Figure 6.9. Panels a), b), and c) of the figure are each from a sequence of 20 exposures. The final image for this example is shown in panel d). Now the image is ready for photometry and profile extraction. This process is repeated for every set of sequences on every galaxy observed in K.

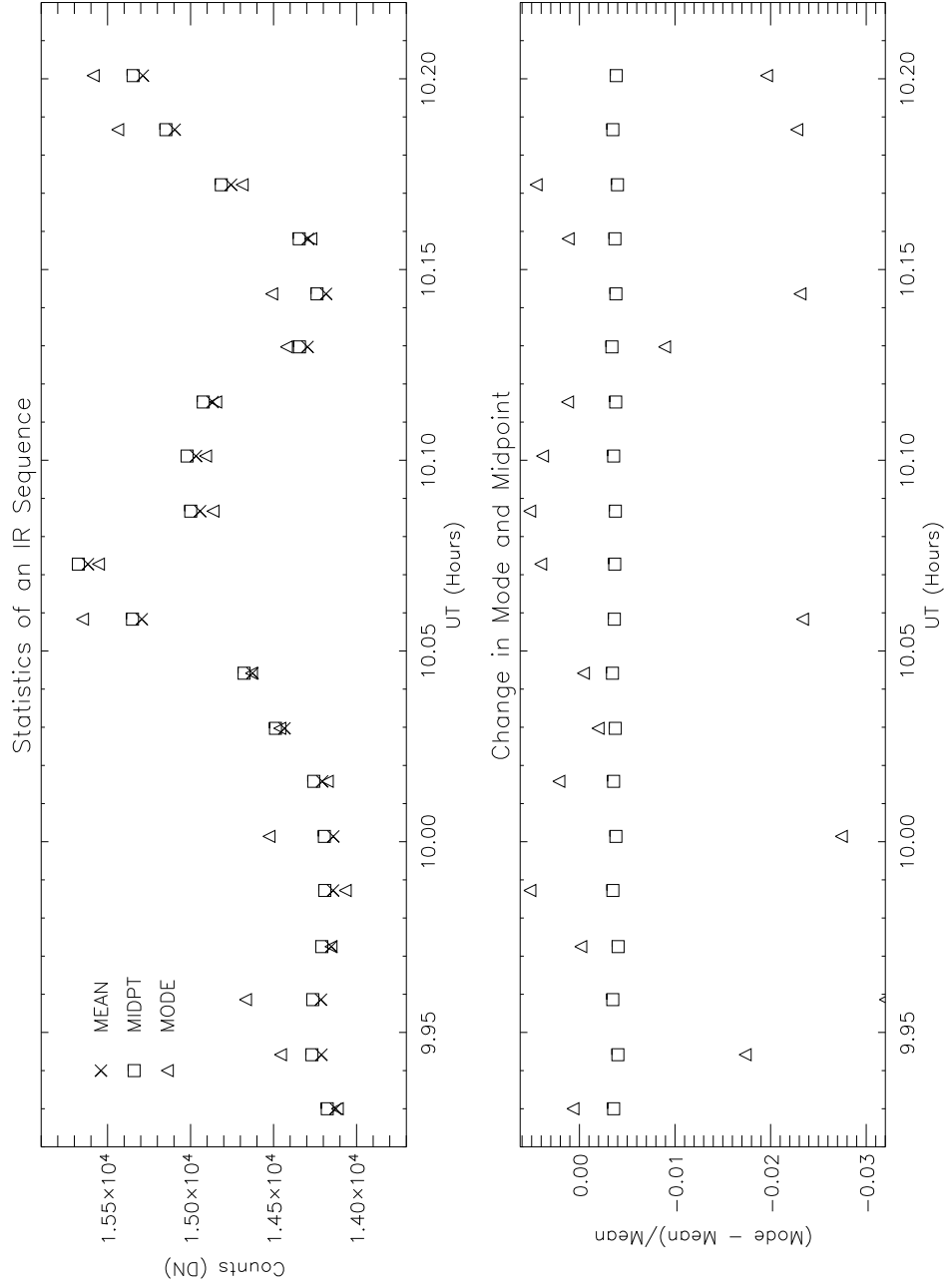


Figure 6.4: Statistics of a K Band Sequence of NGC 6384: The top panel shows the clipped mean, median, and mode. They vary about 10% over the imaging sequence. The bottom panel shows the variation in the clipped mode and median relative to the mean.

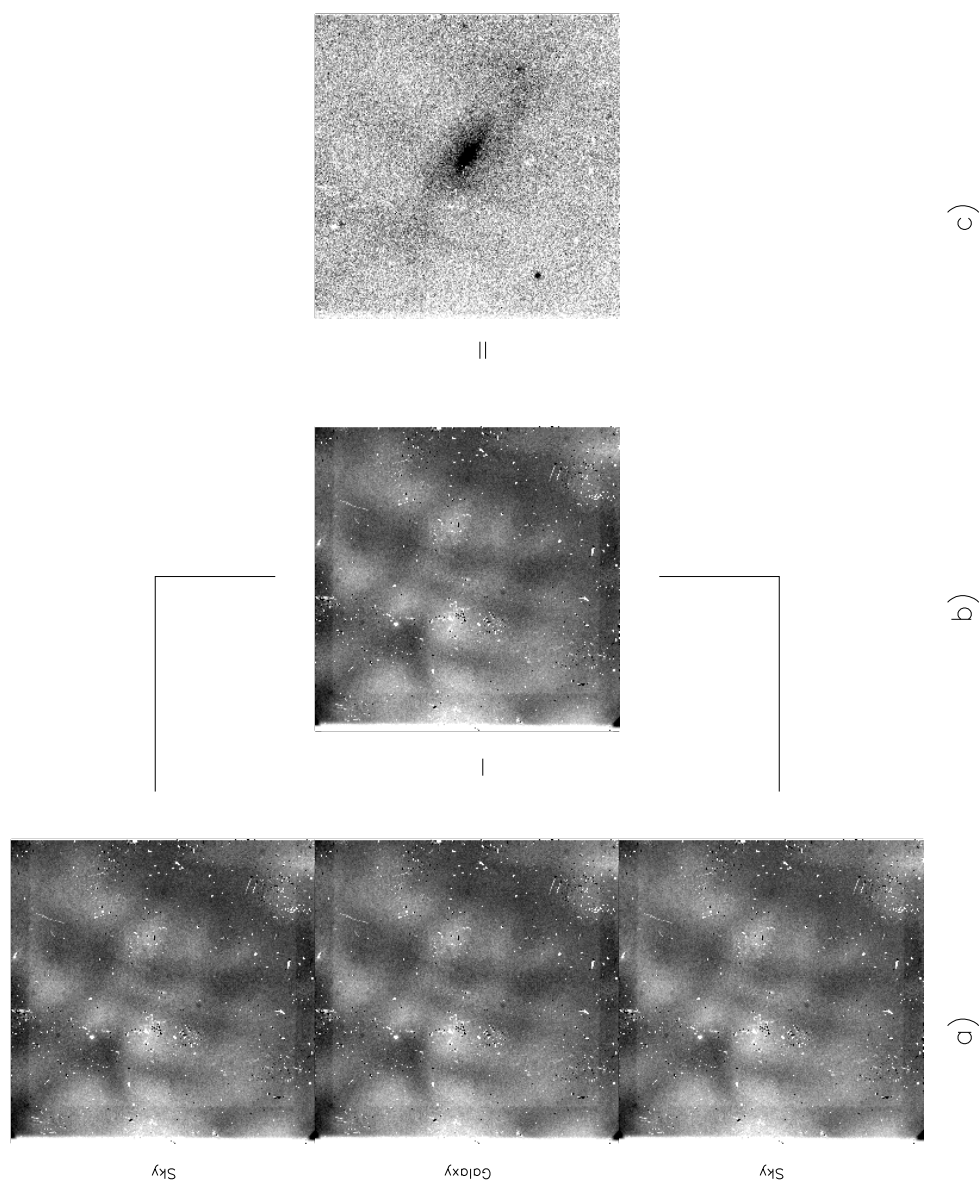


Figure 6.5: Example of IR Sequence Processing: a) Three raw images. The raw galaxy image is the middle one. b) Average sky c) The result of subtracting the average sky from the raw galaxy image. Note the response pattern.

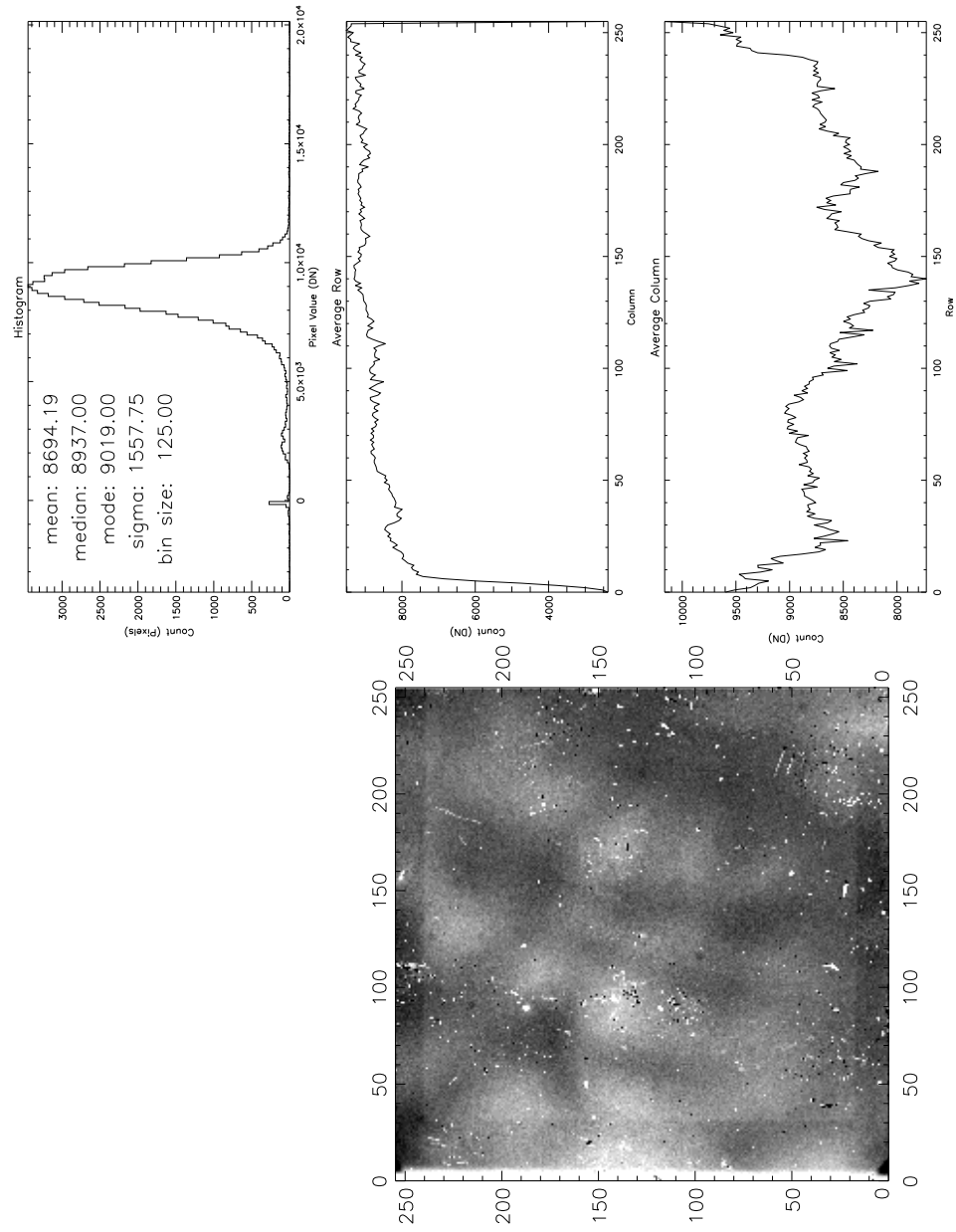


Figure 6.6: Example of Average Sky Image: See Figure 4.2 for explanation of panels.

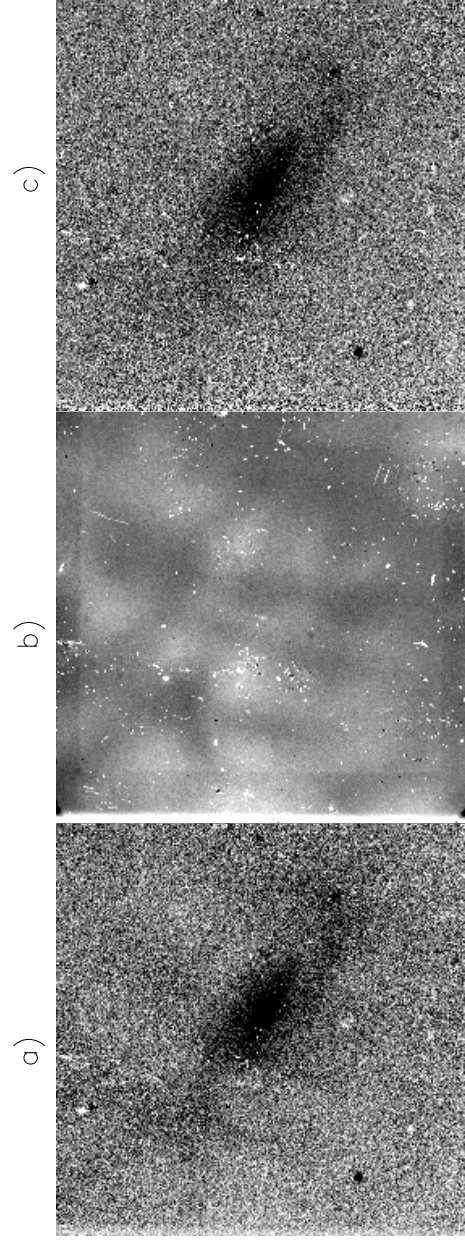


Figure 6.7: Example of Flat Fielding IR Image of Galaxy: a) Sky-subtracted galaxy image b) Flat-field/response c) Sky-subtracted flat-fielded galaxy image

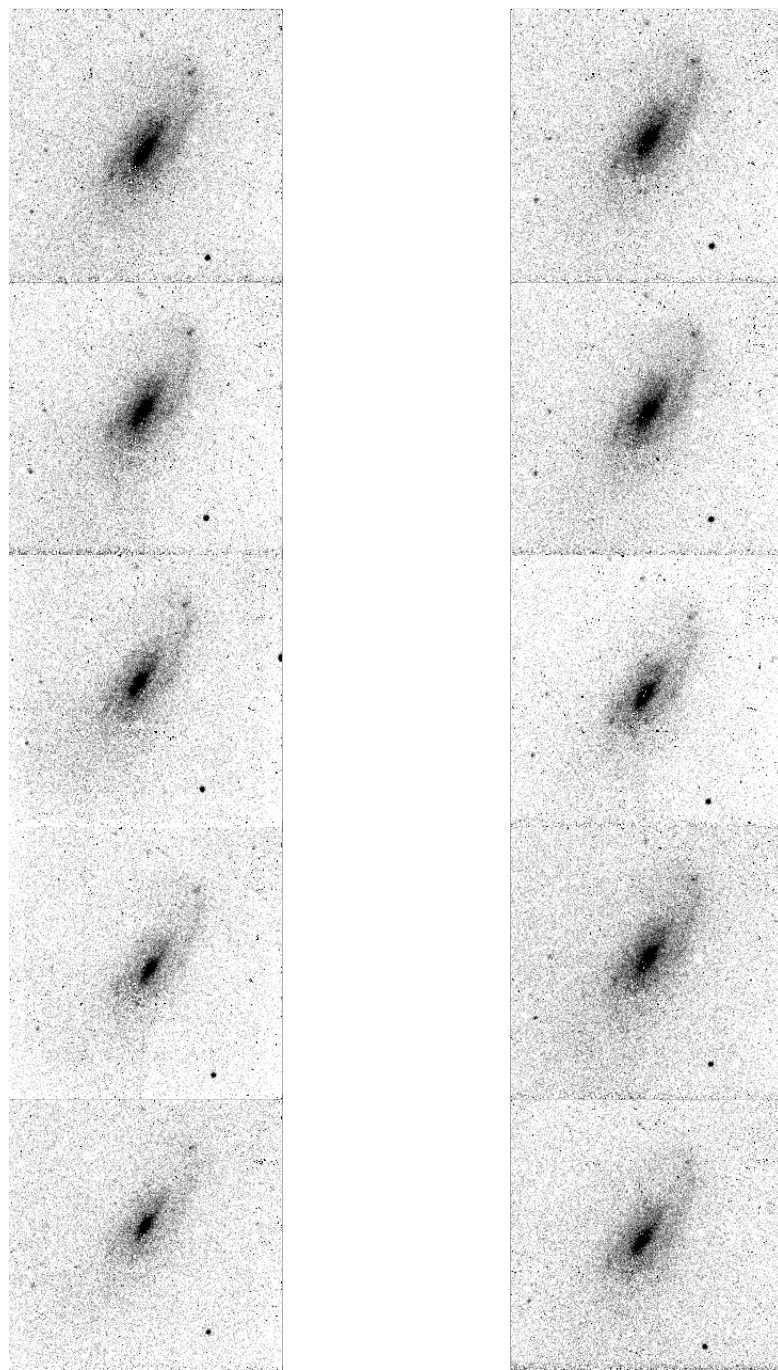
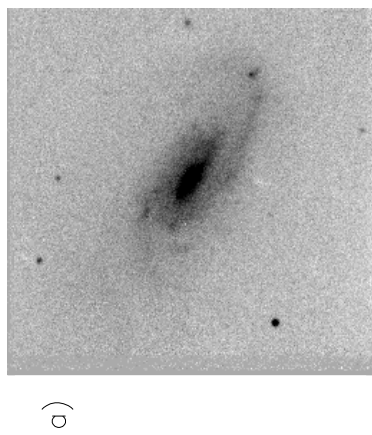
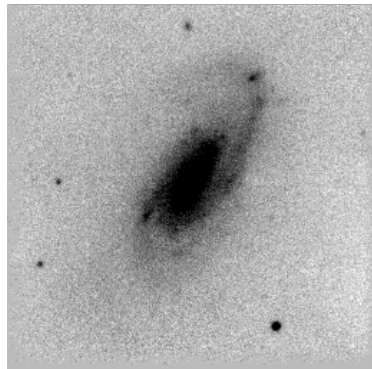


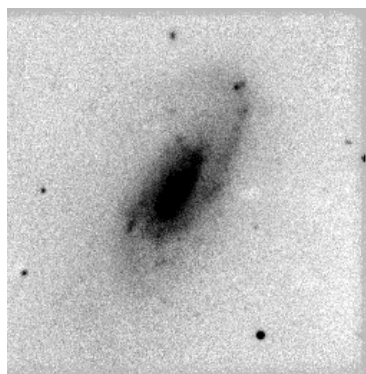
Figure 6.8: IR Sequence of Sky-Subtracted and Flat-Fielded Galaxy Images



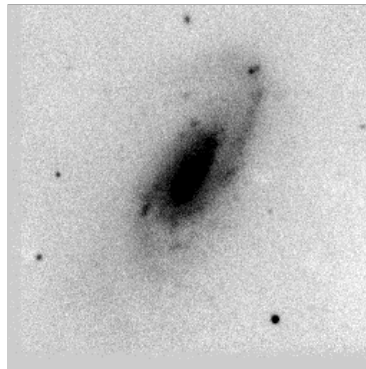
a)



b)



c)



d)

Figure 6.9: IR Sequence of Combined Galaxy Images: a), b), and c) are combined images created from three separate sequences of exposures. d) The median combine of a), b), and c).

6.4 Mapping Mode

Stars are taken in mapping mode as described in Section 3.1. The processing is very similar to wobble-and-jitter mode. The notable differences are that all the images in a mapping mode sequence are used to form the sky image and response, and separate sequences on the same star are *not* combined. They are kept separate so that correlations with airmass and UT can be investigated. Moreover, the individual images in a sequence are *not* combined either. Keeping them separate enables investigation of variation in instrumental magnitude with position on the IR array.

Since the star occupies only a small fraction of the pixels and the exposures are short we can use the star images to form a sky image and sky response. Without shifting the star images are combined into a sky image using a median. The median filters out the star very effectively. An example is given in Figure 6.10. The sigma image is shown in Figure 6.11. The pattern of the 3×3 grid used in this particular sequence is revealed in the grey scale of the sigma image. The median sky is subtracted from each of the star images. Then the median sky is used to create a sky response in the same way as for wobble-and-jitter mode. The sky response is divided into each of the sky-subtracted star images. An example of the resultant images is given in Figure 6.12. The inputs and outputs are the same as for wobble-and-jitter mode except that there is only one sky image and one response image per sequence. The explicit details are not sufficiently different from wobble-and-jitter mode to warrant repeating here.

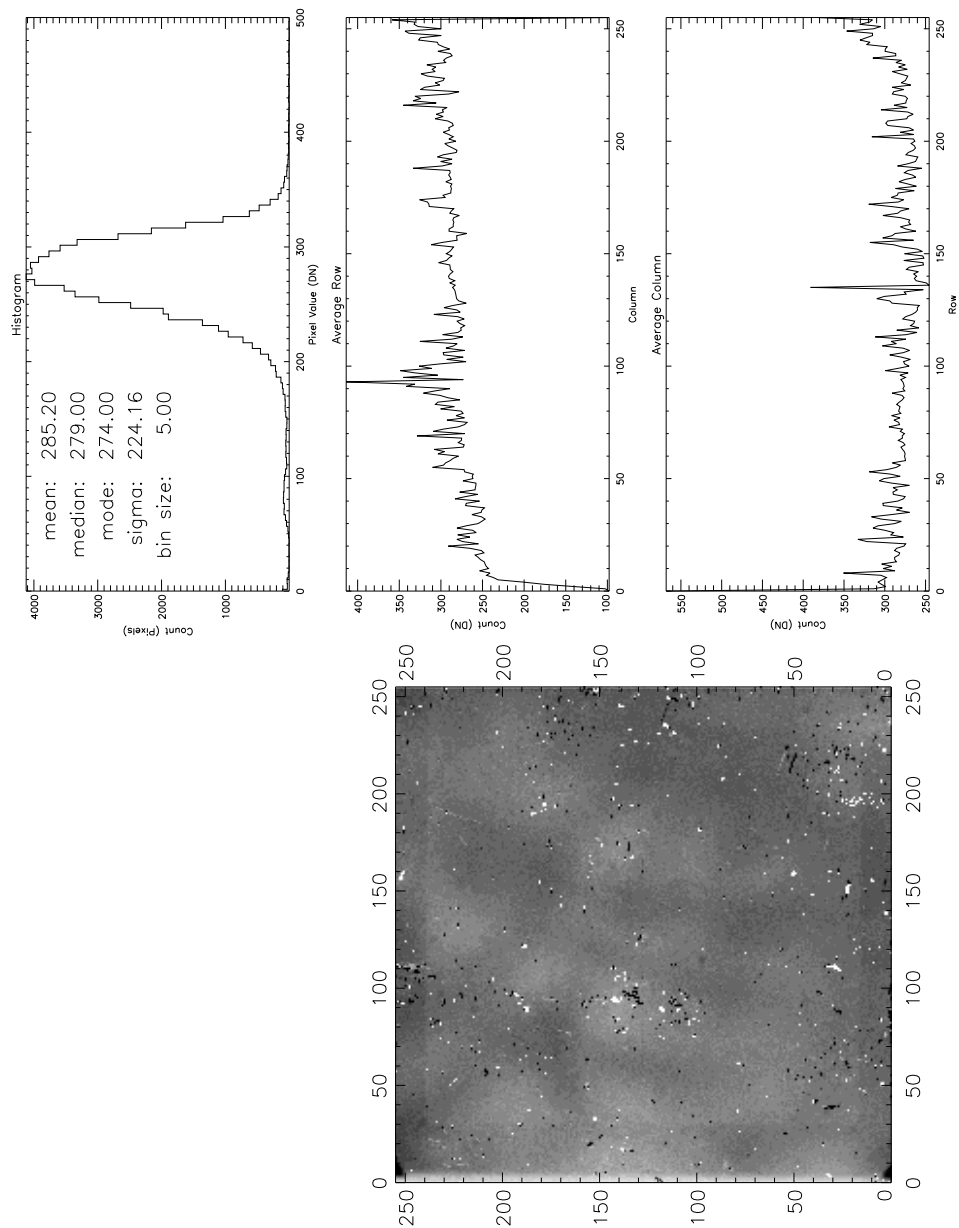


Figure 6.10: Example of Sky Used in IR Mapping Mode Processing; See Figure 4.2 for explanation of panels.

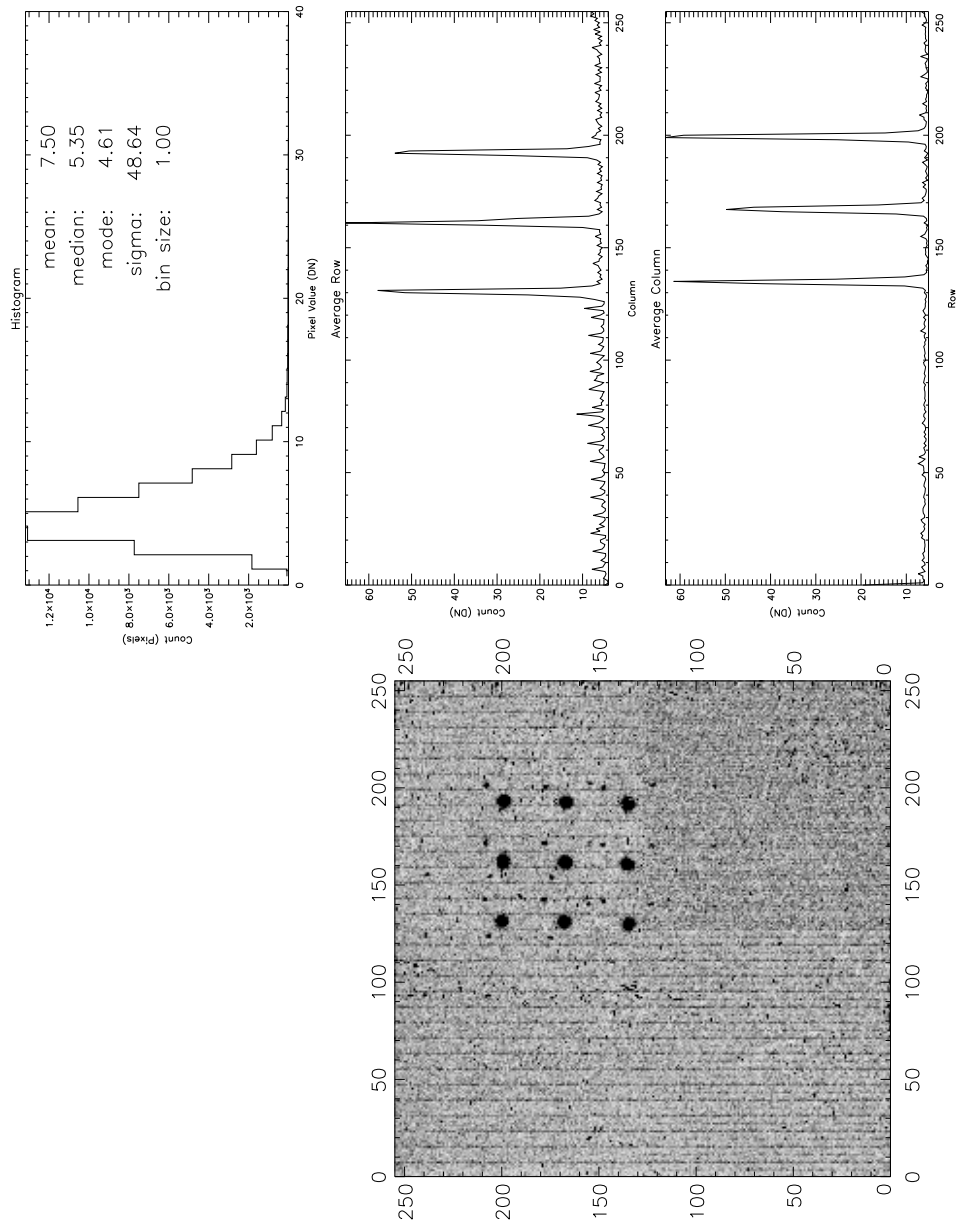


Figure 6.11: Standard Deviation of IR Sky Used in IR Mapping Mode Processing: The standard deviation is high in those pixels containing star light. In this example a 3x3 grid is used. (See Figure 4.2 for explanation of panels.)

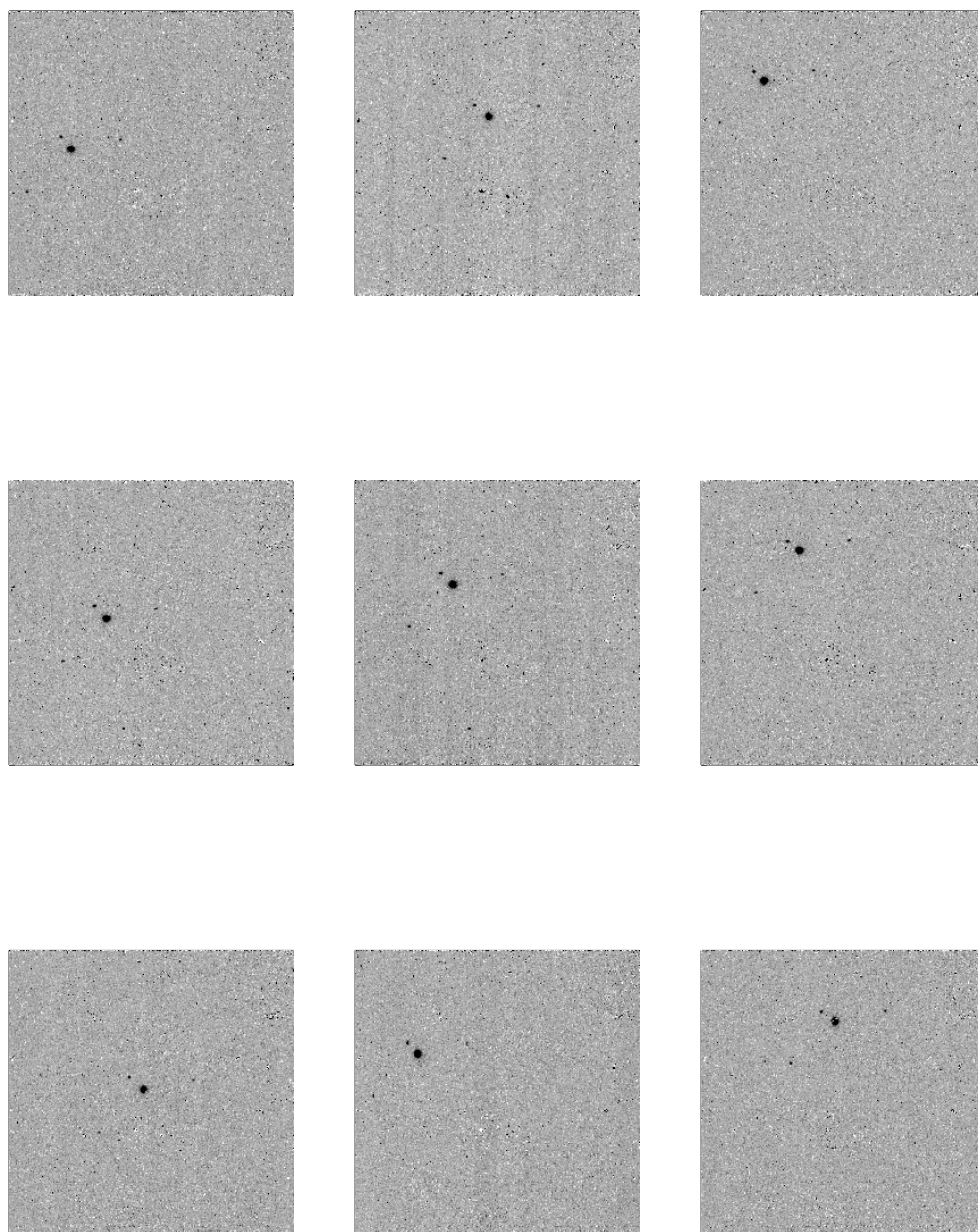


Figure 6.12: IR Standard Taken in Mapping Mode After Processing

CHAPTER 7

OPTICAL PHOTOMETRY

In order to compare to other's results, to the synthesis models, and to form the B–K color the magnitudes need to be on the standard system. This chapter describes the optical stellar photometry for the B and R data only because those nights have the highest photometric quality. The V and I photometry will be done in future work. The nights concerned were deemed photometric at the time of observation. The stars are out of focus and the exposure times require correction. This correction and measurement of the magnitudes is explained. One star is used as an example. The three nights on which optical observations of the subsample galaxies were made are discussed here: 26JUN92, 28JUN92, and 29JUN92. All three nights are processed in the same way with similar results. Atmospheric effects are reviewed and one night, 26JUN92, of measurements is presented as an example of determining the photometric solution. Landolt standards are used [Lan92].

7.1 Exposure Time Correction

The MDM exposure times are inaccurate. The MDM exposure times can vary by .02 seconds as illustrated in Table 7.1. Here are shown the times recorded in the image file header and the true exposure times as measured by Bob Barr, engineer at MDM. Recorded times equal to or longer than 20 seconds are actually longer by .3 seconds. A longer exposure time reduces the relative error. The exposure time is corrected before doing any photometry.

7.2 Instrumental Magnitudes

Stars are taken out of focus for all three nights to avoid saturating the CCD while getting a longer exposure time. This also reduces the relative error in the exposure time. Note that the defocusing precludes using Landolt's aperture sizes.

Table 7.1: MDM Exposure Times

Recorded Time	Actual Time	Error
1.0	0.88	0.02
2.0	1.80	0.02
3.0	2.70	0.01
5.0	4.50	0.02
6.0	5.40	0.03
8.0	7.20	0.02
10.0	9.10	0.02

In some cases nearby stars must be included in the aperture to avoid making the aperture too small. An example is shown in Figure 7.1. These contaminating stars are also measured albeit using a small aperture. Later their flux is subtracted from the total flux in the standard star aperture. This is a zeroth order correction.

Sky is determined from the pixels in an annulus around the aperture. The annulus abuts the aperture and is made as large as possible without including too many nearby stars. The mode of the pixel values in this annulus is as the sky value. The mode is calculated as three times the median minus two times the mean. This is approximately true for slightly skewed distributions and is true for Gaussian distributions by definition (see [Lup93]).

The aperture position and the inner and outer radii of the sky annulus are chosen interactively. The aperture radius is one pixel less than the inner sky radius. Figure 7.1 shows the standard star SA106-834 and a contaminant. The apertures are drawn as circles. A database of aperture parameters and star identifications is kept. A flag in the database indicates if the star is a standard or a contaminant. This database is used to make the aperture measurements.

The instrumental magnitude for a star is calculated using the following formula

$$M_{obs} = -2.5 \log((C - SA)/E) + 20.2 \quad (7.1)$$

where C is the count in the aperture, S is the sky value per pixel, A is the area of the aperture, E is the exposure time, and M_{obs} is the instrumental magnitude. The 20.2 magnitude offset is arbitrary.

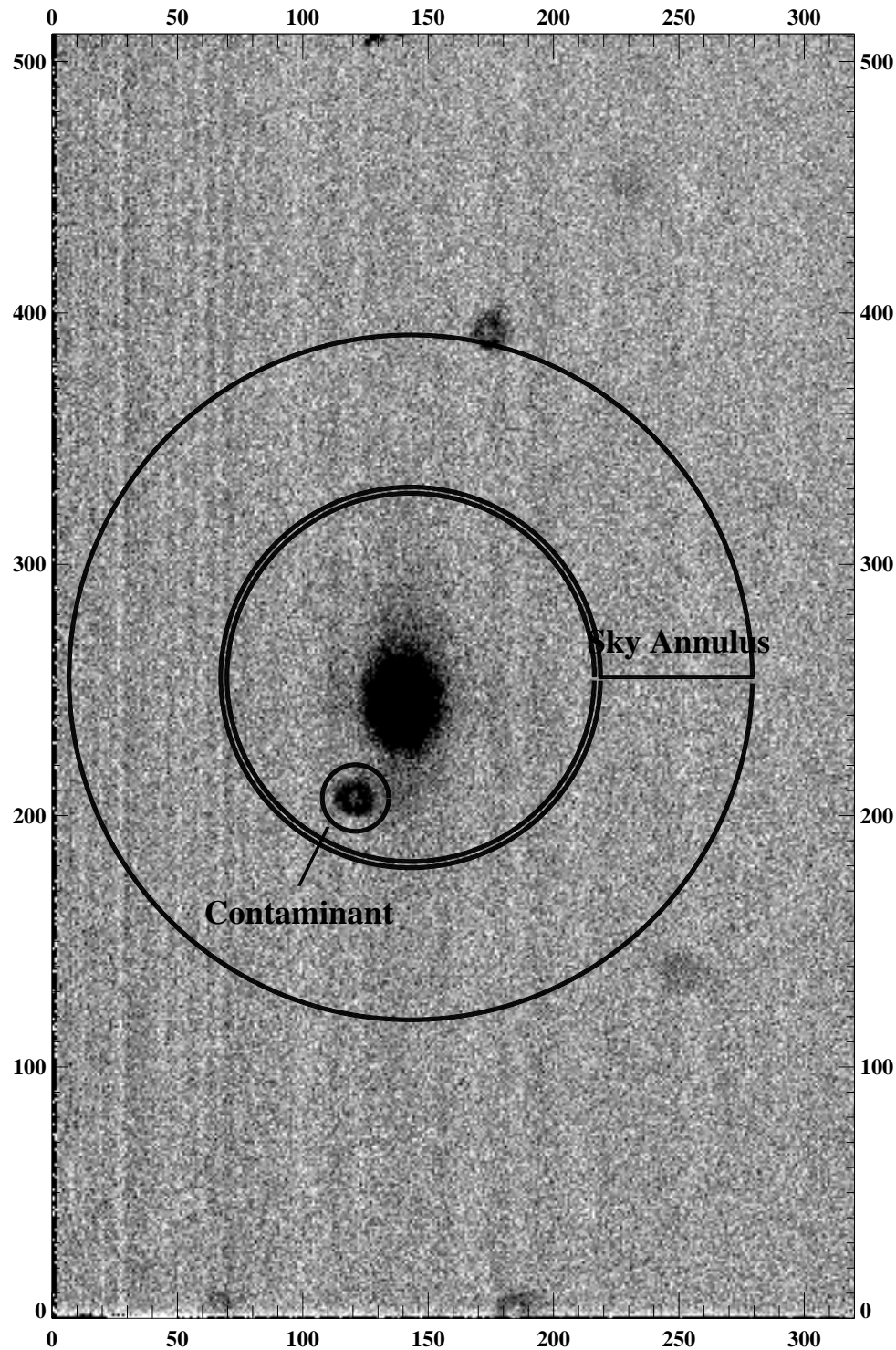


Figure 7.1: Defocused Standard Star, SA106-834, with Nearby Star Contaminating the Aperture

For SA106-834 the total count in the aperture is 960880.5 DN, the sky value is 10.232 DN/pixel, the exposure time is 15.3 seconds, and the aperture size is 74 pixels. Thus, the instrumental magnitude is 8.425. The instrumental magnitudes are added to the database along with other parameters like UT, airmass, and identification. Table 7.2 is an example database for 26JUN92. The data for the example above is on line 30 of this table.

The flux due to contaminating stars is subtracted from that in the standard stars. The sky-subtracted count in the contaminating aperture is subtracted from the sky-subtracted count in the standard star aperture. Then a corrected magnitude is calculated using

$$M_{corr} = -2.5 \log(C_{corr}/E) + 20.2 \quad (7.2)$$

where C_{corr} is the corrected aperture count. A small fraction of the standard star flux is removed along with the contaminating star's flux. For the contaminating star in Figure 7.1 the sky-subtracted count is 3707.349 DN. The corrected counts for the standard star are 78113.600. This is a change of 0.5%. Table 7.3 lists the corrected instrumental magnitudes for 26JUN92.

Many of the images are taken at nearly the same time and in the same filter. These multiple measurements are averaged into one. Multiple observations are defined to be within .8 hours in UT and .3 in airmass. To form a B-R pair the combined B and R observations have to be within .9 hours in UT. For the example star, SA106-834, there are 6 observations (3 in each of the two filters) with the UT, airmasses, and corrected magnitudes listed in Table 7.4. The combined instrumental magnitudes for this star are then 8.469 in R and 9.753 in B. The instrumental color is 1.284. Instrumental magnitudes and colors for all the standard star observations for each night are determined in this way. Table 7.5 shows the combined instrumental magnitudes for 26JUN92.

7.3 Transformation to Standard System

Through the processes of scattering and absorption the atmosphere reduces the number of photons incident on the detector. This is called extinction. The amount of extinction suffered depends

on the amount of atmosphere between the star and detector.

Scattering and absorption depend on wavelength. Absorption lines vary rapidly with wavelength. Atmospheric absorption lines are not present in the filter band passes used here. Scattering depends on wavelength. The dependency is continuous over the optical range. Shorter wavelength photons are scattered preferentially over longer wavelength photons. This is Rayleigh's law. The light incident on the detector is reddened.

Atmospheric conditions vary considerably with time and geolocation. Therefore, the effects of extinction and reddening must be taken into account when comparing independent observations. The system of standard magnitudes is devised for this purpose. The standard magnitudes give the apparent brightness of stars outside the atmosphere. Differences in independently determined standard magnitudes can be attributed to difference in the stars themselves. Stars that have well determined standard magnitudes are standard stars. The effects of the atmosphere are removed in the following manner. Standard stars of various colors, magnitudes, and locations are observed along with program objects. The observed (instrumental) magnitudes are compared with the standard magnitudes to determine a transformation from one to the other. The program objects are put on the standard system using this transformation.

Because the amount of extinction depends on the amount of atmosphere between the detector and the star the transformation depends on airmass. Because of the wavelength dependence of scattering the transformation depends on the color of the star. Because atmospheric conditions depend on temperature it is expected that the transformation will change with time of night. During the fitting process a dependence on a cross between color and airmass is also considered. The method used to determine this transformation as a function of airmass, color, and UT is now discussed.

The instrumental magnitudes are matched with Landolt's magnitudes, [Lan92]. The photometric solution for the night is determined interactively. The zero point, extinction coefficient, and color coefficient are adjusted such that residuals are minimized. Also a final correction is made by

interpolating over the diurnal variation of the residuals. Plots of residuals against Landolt's magnitude, Landolt's color, color times airmass, airmass and UT are examined. It is determined that the coefficients of the cross term and the UT are best left at zero. Some stars were deleted from the fit. Stars with large measurement errors were given less weight during the fitting process.

A typical interaction is shown in Figure 7.8. Thus a photometric solution is determined for each night. Table 7.9 shows the solutions for each night. Tables 7.6, 7.7, and 7.8 show the UT lookup table for 26JUN92, 28JUN92, and 29JUN92 respectively. The fits are good. The standard deviation of the residuals in either filter ranges from .01 to .03 magnitudes. Reviewing Figures 7.2, 7.3, 7.4, 7.5, 7.6, and 7.7 shows there are no significant systematics left in the residuals. All the plots are flat within the errors. The B photometric solution is applied using the following equation.

$$B = B_{\text{instr}} + K_a A + K_{(B-R)}(B - R) + B_z - B_{\text{UT}}$$

B_{instr} is the instrumental magnitude. K_a is the extinction coefficient. A is the airmass. $K_{(B-R)}$ is the color coefficient. B_z is the zero point. B_{UT} is the UT correction. A similar equation applies for R. The UT correction is calculated using linear interpolation in the appropriate lookup table. Thus a photometric solution is determined for each night. These solutions are used to calculate B slit magnitudes in Chapter 9.

Table 7.2: Instrumental Magnitudes for 26JUN92

ID	Name	X	Y	R	F	Count	Sky	Area	Exp	R _{sky}	Width	Mag
1	SA104-598	159	245	24	R	35805.370	3.863664	1810.358	4.5	25	129	10.684
2	SA104-598	161	252	26	R	37259.660	3.836022	2125.096	4.5	27	128	10.673
3	SA104-598	161	248	24	R	36028.540	3.817111	1810.358	4.5	25	130	10.673
4	SA104-598	162	252	23	R	35497.140	3.724981	1662.186	4.5	24	132	10.666
5	SA104-598	162	250	27	B	43301.850	5.125056	2290.304	30.3	28	129	12.656
6	SA104-598	161	248	23	B	53018.500	5.765051	1662.186	40.3	24	132	12.619
7	SA104-337	172	237	25	B	45258.000	4.167648	1962.339	20.3	26	121	12.046
8	SA104-335	275	376	25	B	34092.940	4.532696	1962.339	20.3	26	19	12.465
9	SA104-337	171	235	21	B	43386.110	3.956143	1385.783	20.3	22	127	12.022
10	SA104-335	276	376	25	B	34234.670	4.383493	1962.339	20.3	26	18	12.447
11	SA104-337	167	236	25	R	73952.880	6.797740	1962.339	9.1	26	126	10.641
12	SA104-335	269	374	25	R	48521.390	7.680139	1962.339	9.1	26	24	11.287
13	SA104-337	170	237	25	R	45902.940	4.738667	1962.339	5.4	26	123	10.622
14	SA104-335	273	375	22	R	28398.920	4.443060	1520.885	5.4	23	24	11.193
15	SA104-337	167	236	21	R	42343.290	4.984292	1385.783	5.4	22	130	10.657
16	SA104-335	270	373	23	R	28535.830	4.561451	1662.186	5.4	24	25	11.228
17	SA106-700	161	251	44	R	178076.000	3.972070	6082.293	4.5	45	111	8.865
18	SA106-700	161	259	49	R	350533.800	5.719884	7542.516	9.1	50	106	8.878
19	SA106-700	159	257	57	R	623193.000	8.574827	10207.280	15.3	58	95	8.839
20	SA106-700	162	255	28	B	153522.100	3.459270	2463.412	30.3	29	127	11.000
21	SA106-700	160	253	34	B	254882.300	5.462946	3631.753	50.3	35	120	11.026
22	SA106-700	160	254	36	B	259963.700	5.276387	4073.247	50.3	37	117	11.010
23	SA106-834	152	258	31	B	141406.200	2.863183	3020.775	9.1	32	114	9.790
24	SA106-834	151	255	32	B	318731.500	3.862983	3216.555	20.3	33	112	9.753
25	SA106-834	149	257	33	B	488755.600	4.447550	3421.421	30.3	34	110	9.715
26	SA106-834	142	247	60	R	264943.700	3.582036	11311.590	4.5	61	75	8.455
27	contaminant	127	213	16	R	4855.781	5.344634	804.319	4.5	17	105	14.968
28	SA106-834	144	252	72	R	540677.100	6.806238	16287.070	9.1	73	66	8.514
29	contaminant	124	209	14	R	6268.719	6.923320	616.655	9.1	15	104	14.345
30	SA106-834	144	256	74	R	960880.500	10.231540	17204.600	15.3	75	63	8.425
31	contaminant	122	208	14	R	10515.880	11.041070	616.655	15.3	15	102	14.239
32	SA106-700	162	255	51	R	329553.500	4.007781	8171.471	9.1	52	104	8.916
33	SA106-700	160	257	55	R	336927.600	3.732965	9504.062	9.1	56	98	8.900
34	SA106-700	168	258	40	B	245666.500	3.306787	5026.279	50.3	41	110	11.054
35	SA106-700	161	259	38	B	257722.600	5.034005	4537.167	50.3	39	117	11.027
36	SA106-834	173	234	35	B	295990.400	2.550181	3848.294	20.3	36	110	9.827
37	SA106-834	169	240	33	B	294228.800	0.203290	3421.421	20.3	34	117	9.800
38	SA106-834	164	239	66	R	478336.000	3.797525	13684.050	9.1	67	89	8.523
39	contaminant	145	195	12	R	4052.362	3.557559	452.806	9.1	13	126	14.128
40	SA106-834	165	234	55	R	369528.800	2.575181	9504.062	7.2	56	98	8.499
41	contaminant	144	197	11	R	2949.776	2.393797	380.332	7.2	12	126	14.070
42	SA109-1082	170	253	75	R	306244.700	2.241215	17671.920	4.5	76	74	8.268
43	contaminant	124	223	17	R	3492.298	2.077755	908.222	4.5	18	101	13.819
44	contaminant	209	229	18	R	20837.050	1.576041	1018.119	4.5	19	91	11.123
45	SA109-1082	164	258	84	R	511069.100	2.689034	22168.280	7.2	85	70	8.207
46	contaminant	122	220	18	R	6668.125	2.333906	1018.119	7.2	19	97	13.262
47	contaminant	209	226	22	R	35672.430	4.050212	1520.885	7.2	23	87	11.168
48	SA109-1082	167	262	32	B	136139.400	1.675250	3216.555	9.1	33	119	9.806
49	SA109-1082	162	258	34	B	316498.400	2.032428	3631.753	20.3	35	122	9.743
50	SA109-381	162	233	22	B	29621.980	2.077467	1520.885	20.3	23	133	12.412
51	SA109-381	162	225	24	B	30505.440	2.286752	1810.358	20.3	25	132	12.416
52	SA109-381	158	219	23	B	63133.980	3.616269	1662.186	40.3	24	129	12.321
53	SA109-381	155	223	34	R	126442.400	9.866566	3631.753	20.3	35	114	11.076
54	SA109-381	153	219	22	R	45507.830	3.836027	1520.885	9.1	23	125	11.101
55	SA109-381	156	221	24	R	46438.700	4.086738	1810.358	9.1	25	125	11.119
56	SA112-275	164	242	28	B	42785.550	1.617373	2463.412	9.1	29	127	11.125
57	SA112-250	197	461	25	B	10127.860	1.107669	1962.339	9.1	26	22	12.846
58	SA112-275	161	235	41	B	260405.800	5.074782	5282.336	50.3	42	114	11.033
59	SA112-250	193	452	25	B	62022.530	5.083261	1962.339	50.3	26	32	12.663
60	SA112-275	160	243	45	B	263967.300	5.049754	6361.827	50.3	46	108	11.041
61	SA112-250	193	452	25	B	61633.110	5.194058	1962.339	50.3	26	32	12.676
62	SA112-275	159	234	41	R	137769.300	1.990004	5282.336	4.5	42	111	9.071
63	SA112-250	196	453	23	R	15463.880	1.348777	1662.186	4.5	24	32	11.530
64	SA112-275	168	240	63	R	555551.000	6.777886	12468.650	15.3	64	88	8.979
65	SA112-250	189	443	30	R	64724.760	7.517701	2826.758	15.3	31	36	11.566
66	SA112-275	163	231	54	R	512046.800	6.817648	9159.896	15.3	55	101	9.030
67	SA112-250	186	439	34	R	68246.480	7.372020	3631.753	15.3	35	36	11.617
68	SA112-636	164	228	43	R	422925.700	6.892055	5810.522	15.3	44	112	9.204
69	contaminant	146	211	10	R	6308.430	6.809422	314.740	15.3	11	130	14.113
70	SA112-636	163	230	45	R	440411.500	6.818812	6361.827	15.3	46	110	9.165
71	contaminant	145	208	10	R	5981.487	6.833003	314.740	15.3	11	129	14.203

Table 7.2: Continued

ID	Name	X	Y	R	F	Count	Sky	Area	Exp	R _{sky}	Width	Mag
72	SA112-636	162	226	47	B	292226.300	2.264048	6938.846	35.3	48	109	10.465
73	contaminant	146	206	10	B	3352.464	4.185162	314.740	35.3	11	130	15.798
74	SA112-636	164	226	50	B	340074.900	3.751130	7854.524	40.3	51	105	10.483
75	contaminant	145	205	10	B	4206.005	3.522041	314.740	40.3	11	129	15.486
76	SA114-670	179	238	49	R	194188.800	5.781242	7542.516	15.3	50	90	10.217
77	SA114-670	180	233	45	R	102760.200	2.916145	6361.827	9.1	46	93	10.284
78	SA114-670	180	238	34	B	106809.400	5.066251	3631.753	60.3	35	104	12.285
79	SA114-670	184	234	31	B	105117.600	5.003069	3020.775	60.3	32	104	12.265
80	SA114-755	162	238	38	B	135027.400	2.951817	4537.167	40.3	39	117	11.501
81	SA114-755	162	231	31	B	131440.100	2.717071	3020.775	40.3	32	124	11.486
82	SA114-755	160	231	49	R	182887.300	5.644801	7542.516	15.3	50	104	10.294
83	SA114-755	162	226	31	R	84915.770	2.435579	3020.775	9.1	32	124	10.374
84	SA115-516	151	232	32	R	79822.350	1.310042	3216.555	4.5	33	112	9.637
85	SA115-516	150	225	37	R	164499.100	5.171343	4299.853	9.1	38	107	9.715
86	SA115-516	150	222	34	B	189341.800	6.605831	3631.753	50.3	35	110	11.408
87	SA115-516	152	219	37	B	197070.200	8.054794	4299.853	50.3	38	109	11.427
88	SA115-271	165	232	40	B	252593.300	3.252812	5026.279	25.3	41	114	10.274
89	SA115-271	168	228	46	B	288555.600	4.352073	6647.822	25.3	47	104	10.172
90	SA115-271	170	226	52	R	281880.700	5.040376	8494.597	9.1	53	97	9.151
91	SA115-271	166	226	33	R	128207.200	3.386550	3421.421	4.5	34	119	9.166
92	SA115-271	165	226	31	R	127029.700	3.379714	3020.775	4.5	32	122	9.164
93	SA112-275	152	246	58	R	564711.300	9.889198	10568.980	15.3	59	87	9.004
94	SA112-250	183	453	24	R	62567.270	10.061920	1810.358	15.3	25	31	11.544
95	contaminant	173	460	6	R	2002.607	10.067520	113.242	15.3	7	42	15.822
96	SA112-275	153	240	44	R	149290.300	4.176354	6082.293	4.5	45	103	9.100
97	SA112-250	183	459	19	R	16153.090	3.808519	1135.199	4.5	20	30	11.651
98	SA112-275	151	241	39	R	145921.300	4.034484	4778.798	4.5	40	106	9.077
99	SA112-250	184	455	21	R	17306.410	3.441418	1385.783	4.5	22	33	11.588
100	SA112-275	152	234	39	B	236885.000	19.234970	4778.798	30.3	40	107	11.000
101	SA112-250	184	451	23	B	64930.520	19.467610	1662.186	30.3	24	35	12.622
102	contaminant	171	457	5	B	2016.124	19.704020	79.127	30.3	6	46	17.254
103	SA112-275	148	237	38	B	256138.000	24.825530	4537.167	30.3	39	103	11.011
104	SA112-250	181	453	24	B	77177.610	24.659600	1810.358	30.3	25	32	12.623
105	contaminant	172	458	5	B	2513.278	24.931980	79.127	30.3	6	45	17.072
106	SA112-636	167	232	36	B	409366.000	44.422510	4073.247	30.3	37	115	10.507
107	contaminant	149	213	9	B	13976.010	44.544980	254.953	30.3	10	134	15.358
108	SA112-636	164	230	37	B	492241.900	60.772190	4299.853	30.3	38	118	10.495
109	contaminant	149	212	8	B	14562.790	60.920150	200.685	30.3	9	135	15.482
110	SA112-636	166	233	36	R	167069.500	13.818110	4073.247	4.5	37	117	9.222
111	contaminant	149	215	8	R	3989.175	13.853430	200.685	4.5	9	135	14.127
112	SA112-636	162	233	31	R	163701.400	18.642580	3020.775	4.5	32	124	9.256
113	contaminant	147	215	8	R	4772.685	18.703970	200.685	4.5	9	132	14.313

Table 7.3: Corrected Magnitudes for 26JUN92

ID Standard	ID(s)	Corrected Count	Exp	Mag
26	27	223868.1860	4.5	8.4581
28	29	427824.0055	9.1	8.5194
30	31	781143.5968	15.3	8.4299
38	39	423929.0004	9.1	8.5294
40	41	343014.7810	7.2	8.5050
42	43,44	245800.4395	4.5	8.3566
45	46,47	417653.3871	7.2	8.2913
68	69	378714.0330	15.3	9.2160
70	71	393200.5328	15.3	9.1752
72	73	274481.1952	35.3	10.4732
74	75	307514.0830	40.3	10.4936
94	95	43489.0467	15.3	11.5658
101	102	32114.7179	30.3	12.6368
104	105	31994.4089	30.3	12.6409
106	107	225803.0062	30.3	10.5192
108	109	228593.3807	30.3	10.5059
110	111	109575.9241	4.5	9.2337
112	113	106367.2797	4.5	9.2660

Table 7.4: UT and Airmass for 6 Observations of SA106-834

UT	Airmass	Mag	Filter
4:44:01	1.223	9.790	B
4:45:58	1.226	9.753	B
4:49:46	1.232	9.715	B
4:51:35	1.235	8.458	R
4:53:19	1.238	8.519	R
4:54:40	1.241	8.430	R

Table 7.5: Combined Magnitudes for 26JUN92

ID	Name	UT	Airmass	B	Sigma	N		
		UT	Airmass	R	Sigma	N	B-R	Error
1	SA104-598	4.2396	1.4665	12.6375	0.0262	2		
		4.1329	1.4370	10.6740	0.0074	4	1.9635	0.0272
2	SA104-337	4.3306	1.5140	12.0340	0.0170	2		
		4.3906	1.5330	10.6400	0.0175	3	1.3940	0.0244
3	SA104-335	4.3306	1.5140	12.4560	0.0127	2		
		4.3906	1.5330	11.2360	0.0475	3	1.2200	0.0492
4	SA106-700	4.6167	1.2140	11.0120	0.0131	3		
		4.5247	1.2080	8.8607	0.0199	3	2.1513	0.0238
5	SA106-834	4.7661	1.2260	9.7527	0.0375	3		
		4.8886	1.2380	8.4691	0.0458	3	1.2835	0.0592
6	SA106-700	5.9619	1.4160	11.0405	0.0191	2		
		5.9078	1.4035	8.9080	0.0113	2	2.1325	0.0222
7	SA106-834	6.0412	1.4395	9.8135	0.0191	2		
		6.0903	1.4525	8.5172	0.0172	2	1.2963	0.0257
8	SA109-1082	7.2439	1.1845	9.7745	0.0445	2		
		7.1954	1.1825	8.3239	0.0462	2	1.4506	0.0642
9	SA109-381	7.3394	1.1940	12.3830	0.0537	3		
		7.4281	1.1990	11.0987	0.0216	3	1.2843	0.0579
10	SA112-275	8.2111	1.2810	11.0663	0.0510	3		
		8.3011	1.2680	9.0267	0.0461	3	2.0397	0.0687
11	SA112-250	8.2111	1.2810	12.7283	0.1021	3		
		8.3011	1.2680	11.5710	0.0437	3	1.1573	0.1111
12	SA112-636	8.4485	1.2455	10.4834	0.0145	2		
		8.3915	1.2525	9.1956	0.0288	2	1.2878	0.0322
13	SA114-670	9.7806	1.3355	12.2750	0.0141	2		
		9.7139	1.3490	10.2505	0.0474	2	2.0245	0.0494
14	SA114-755	9.8633	1.3180	11.4935	0.0106	2		
		9.9192	1.3080	10.3340	0.0566	2	1.1595	0.0576
15	SA115-516	10.9940	1.3015	11.4175	0.0134	2		
		10.9321	1.3120	9.6760	0.0552	2	1.7415	0.0568
16	SA115-271	11.0717	1.2915	10.2230	0.0721	2		
		11.1375	1.2810	9.1603	0.0081	3	1.0627	0.0726
17	SA112-275	11.3382	1.2855	11.0055	0.0078	2		
		11.2747	1.2760	9.0603	0.0501	3	1.9452	0.0507
18	SA112-250	11.3382	1.2855	12.6389	0.0029	2		
		11.2747	1.2760	11.6016	0.0442	3	1.0373	0.0443
19	SA112-636	11.4368	1.3005	10.5126	0.0094	2		
		11.4801	1.3080	9.2499	0.0228	2	1.2627	0.0247

Table 7.6: UT Lookup Table for 26JUN92

UT of B	UT of R	Correction for B	Correction for R
4.3306	4.3906	-0.0045	0.0127
6.0016	5.9991	-0.0450	-0.0071
7.2916	7.3118	0.0113	0.0108
8.3298	8.3463	0.0010	-0.0348
9.8219	9.8165	0.0074	-0.0432
11.3382	11.2747	-0.0132	0.0012

Table 7.7: UT Lookup Table for 28JUN92

UT of B	UT of R	Correction for B	Correction for R
3.5974	3.6481	-0.0143	0.0367
5.9826	6.0011	-0.0095	-0.0068
7.5728	7.4158	0.0109	0.0261
8.7811	8.6556	-0.0031	0.0023
9.6219	9.4981	0.0094	0.0001
10.7992	10.6694	-0.0054	-0.0322

Table 7.8: UT Lookup Table for 29JUN92

UT of B	UT of R	Correction for B	Correction for R
3.9359	3.7959	0.0049	0.0341
5.6642	5.6814	0.0076	-0.0371
7.1146	6.9693	-0.0341	-0.0250
8.5746	8.3800	-0.0321	-0.0201
9.6367	9.4796	0.0022	-0.0110
11.1824	10.9832	0.0040	0.0112

Table 7.9: Photometric Solutions for Each Night

Night	F	Zero Point	K_a	$K_{(B-R)}$	UT LUT	Error
26JUN92	B	20.625	-0.400	0.090	Table 7.6	0.030
26JUN92	R	20.753	-0.250	-0.020	Table 7.6	0.023
28JUN92	B	20.516	-0.325	0.090	Table 7.7	0.017
28JUN92	R	20.658	-0.150	-0.020	Table 7.7	0.014
29JUN92	B	20.549	-0.320	0.090	Table 7.8	0.027
29JUN92	R	20.789	-0.250	-0.020	Table 7.8	0.015

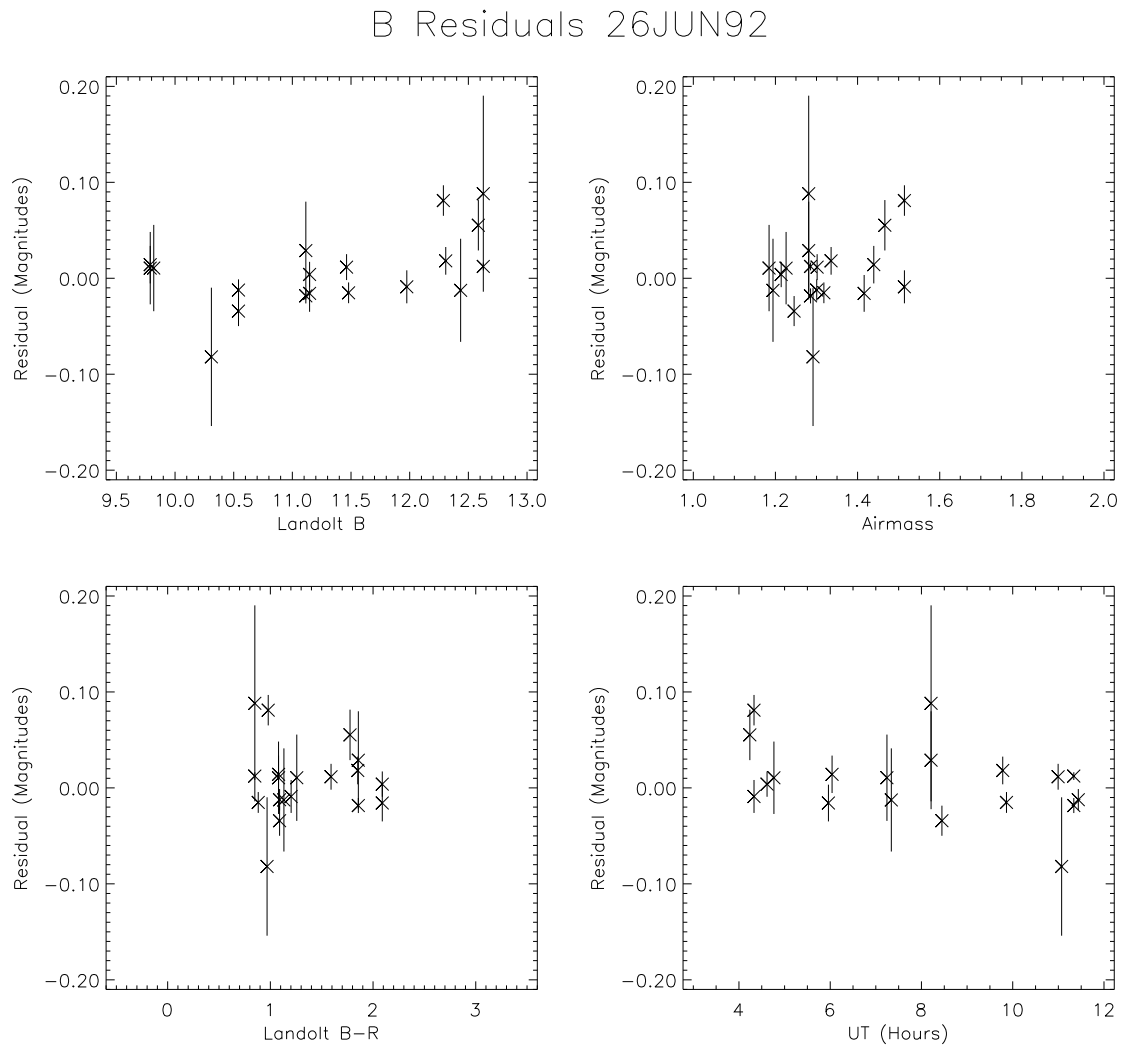


Figure 7.2: Residuals in B of Photometric Solution for 26JUN92

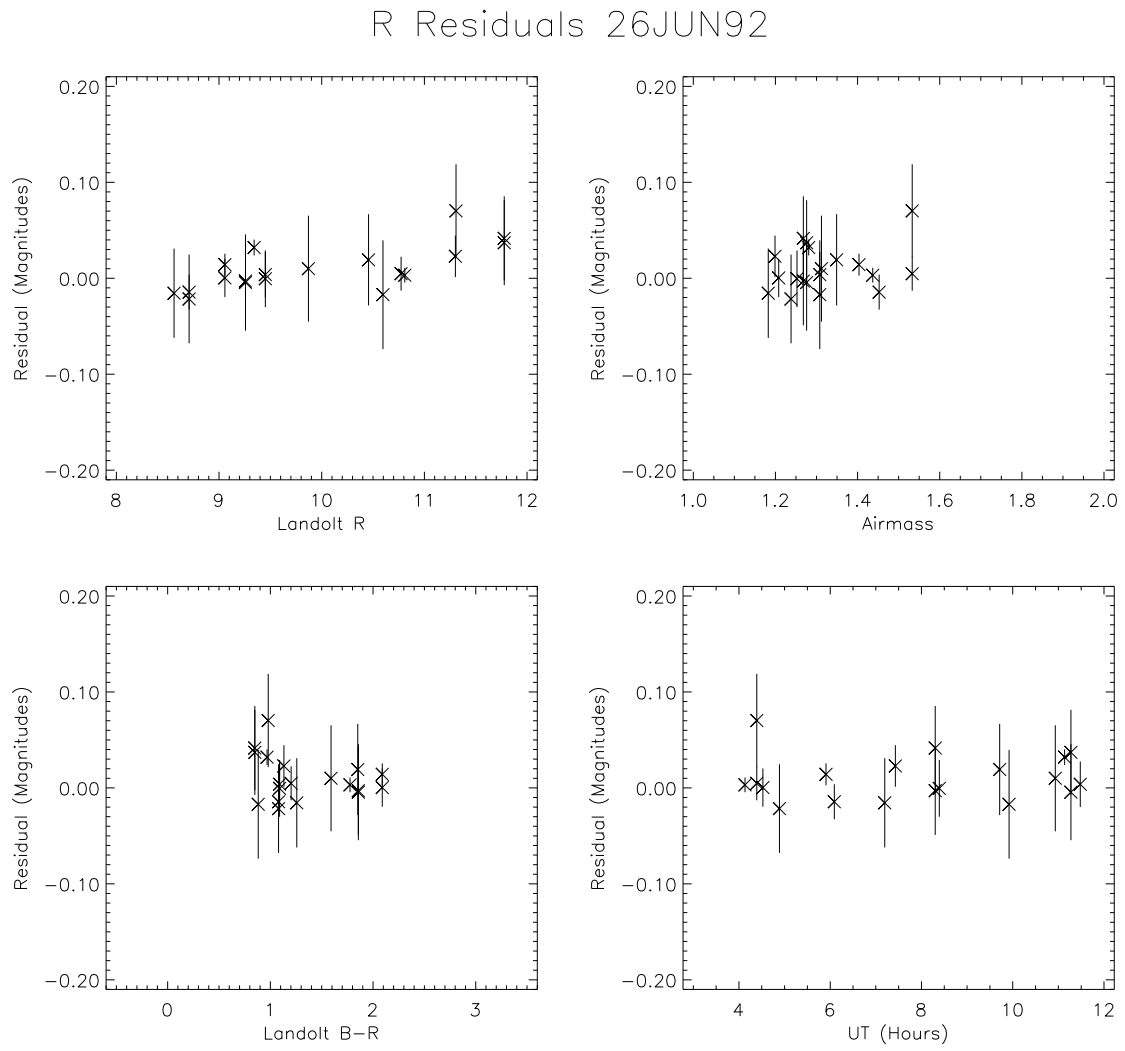


Figure 7.3: Residuals in R of Photometric Solution for 26JUN92

B Residuals 28JUN92

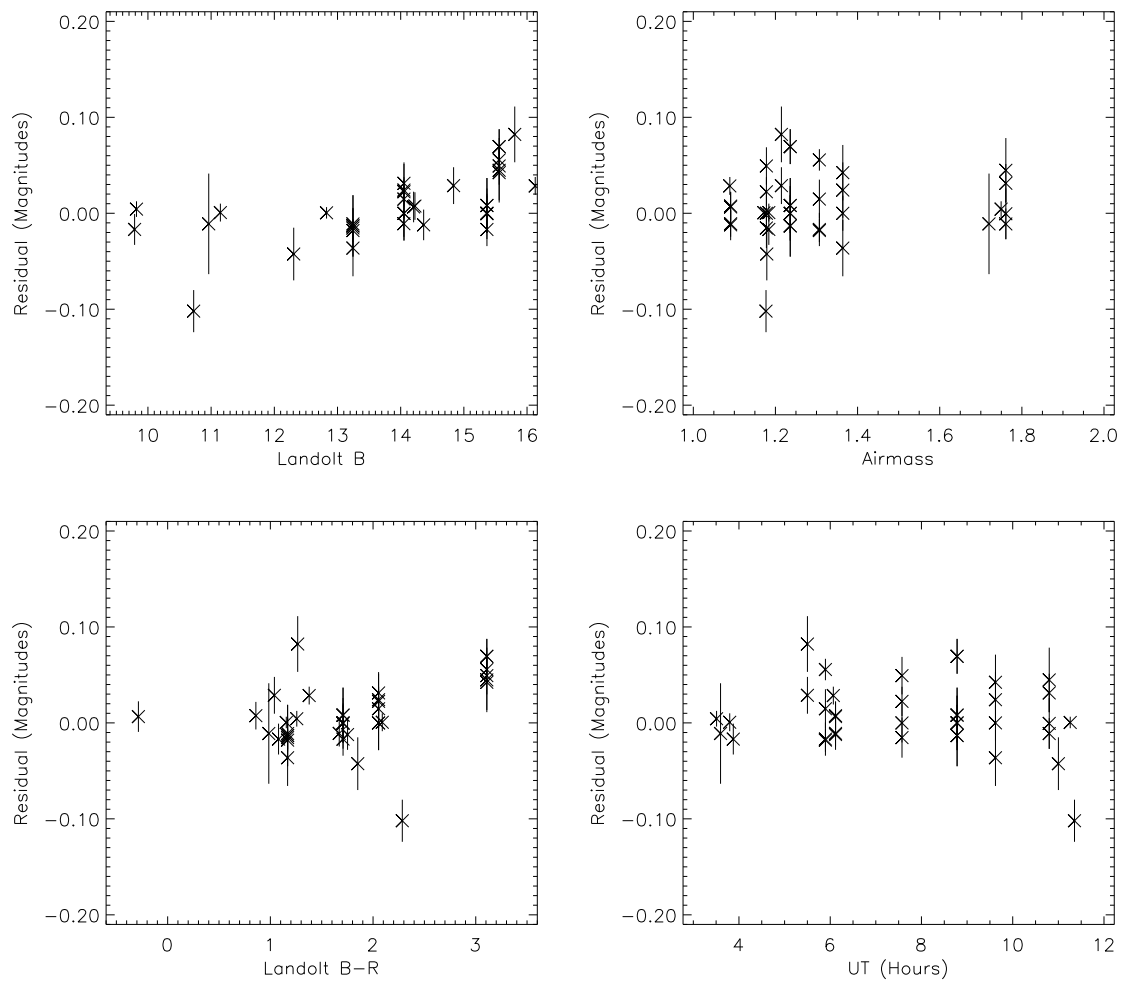


Figure 7.4: Residuals in B of Photometric Solution for 28JUN92

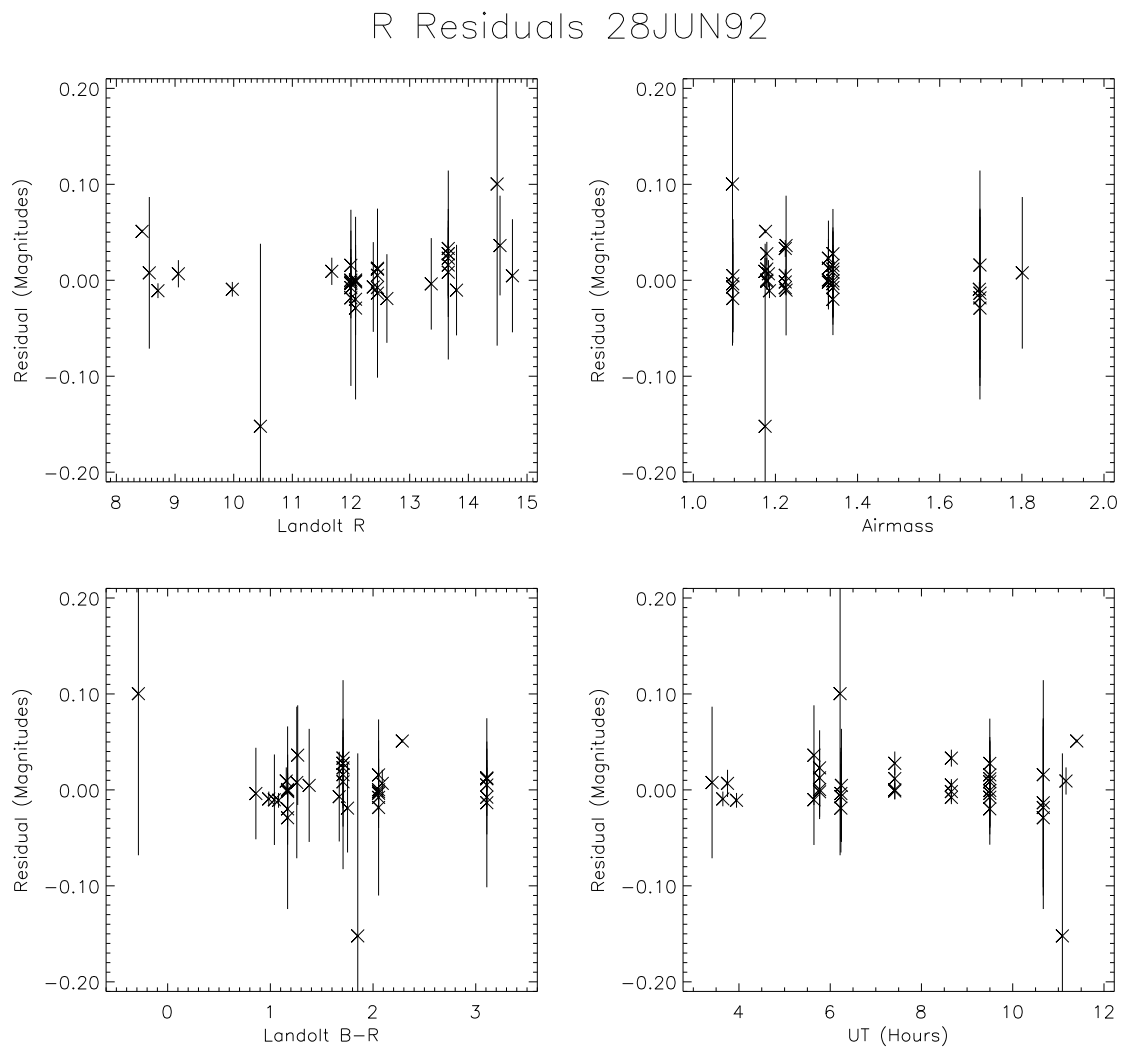


Figure 7.5: Residuals in R of Photometric Solution for 28JUN92

B Residuals 29JUN92

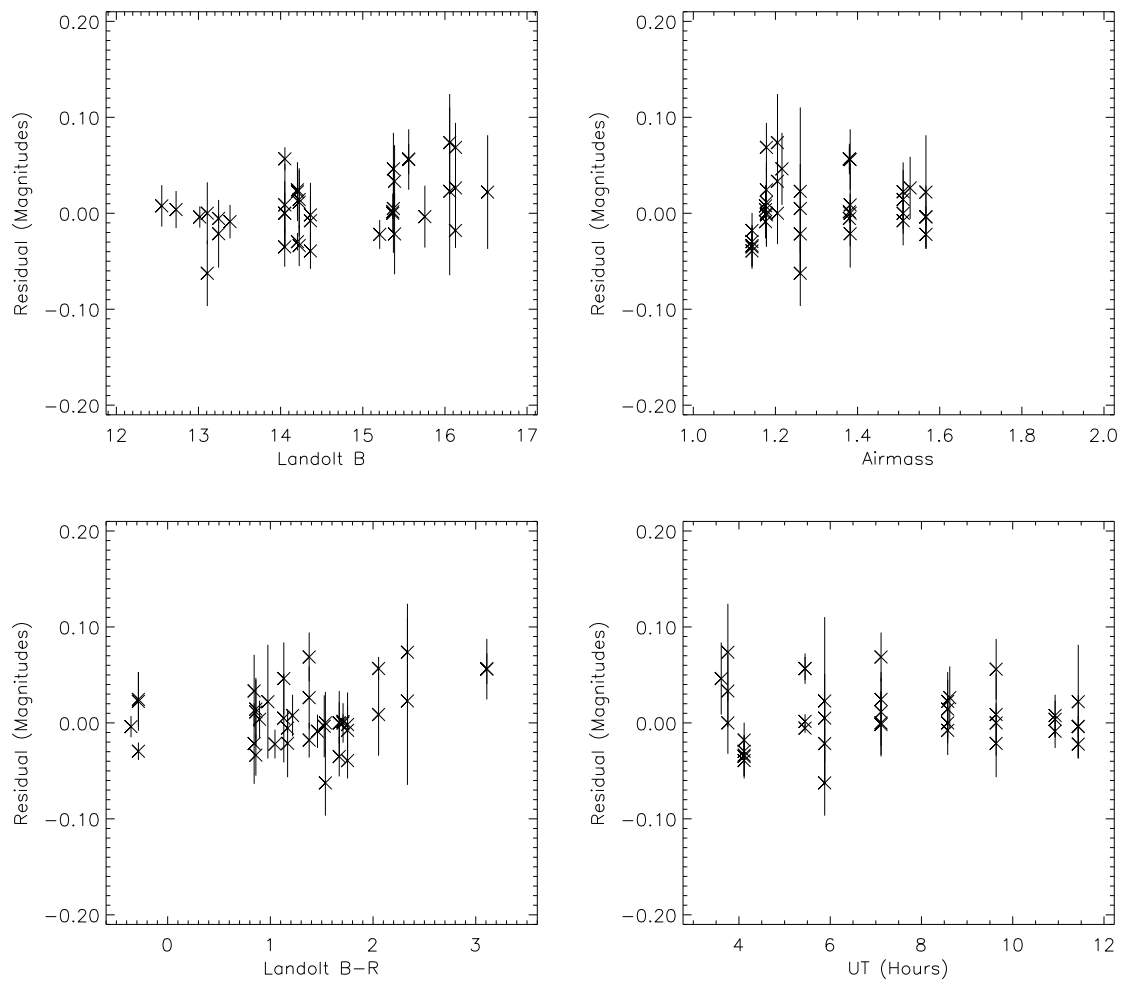


Figure 7.6: Residuals in B of Photometric Solution for 29JUN92

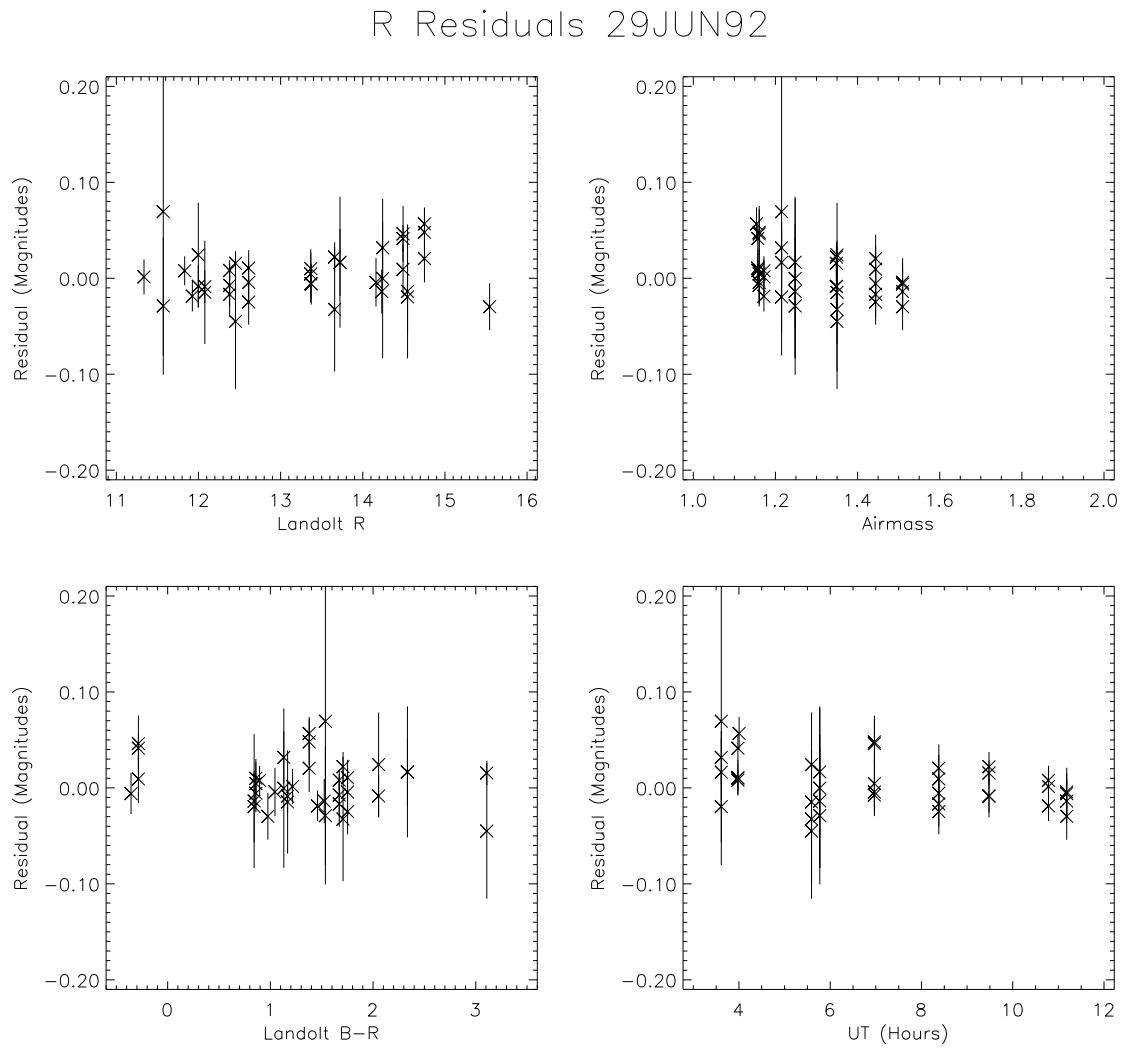


Figure 7.7: Residuals in R of Photometric Solution for 29JUN92

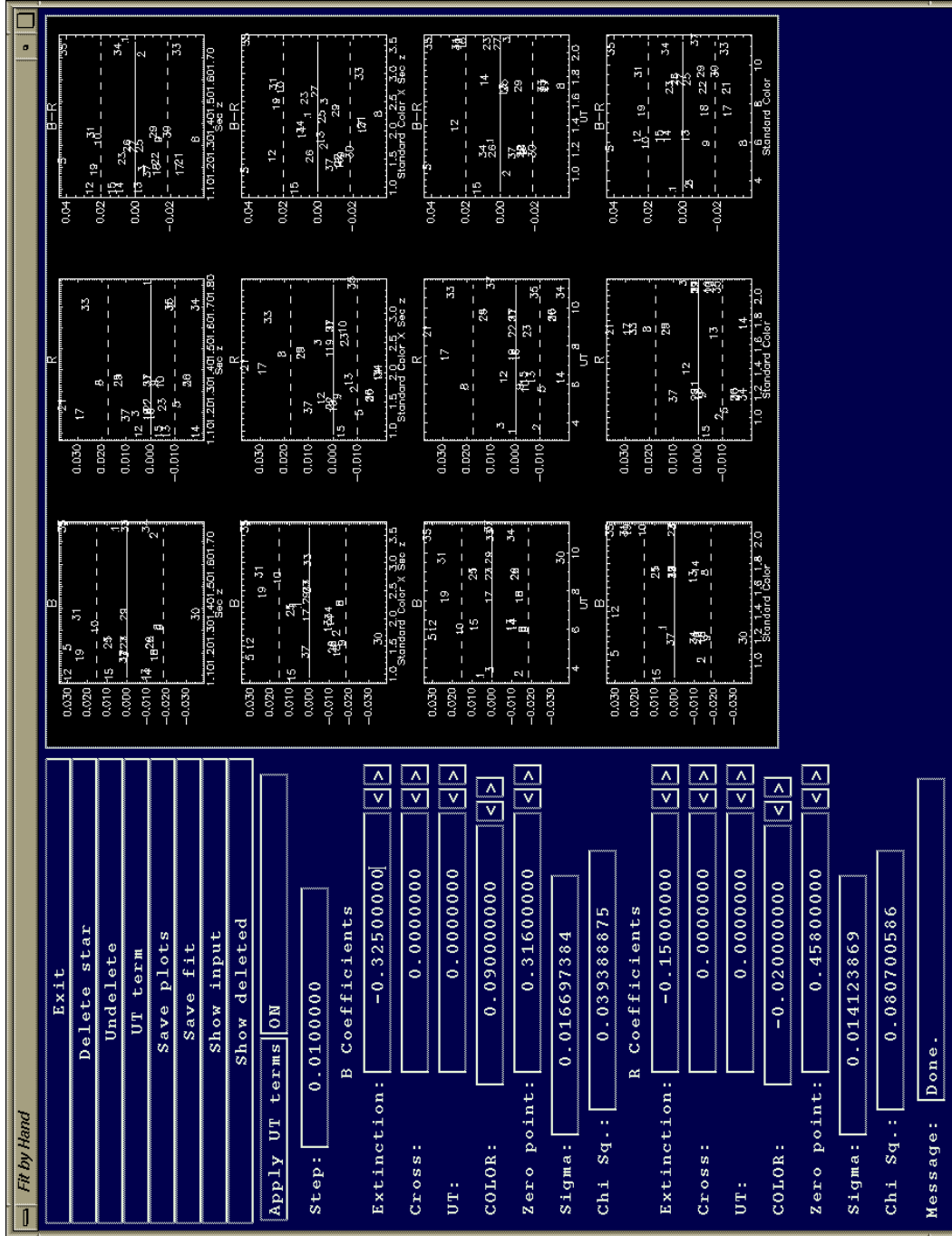


Figure 7.8: Graphical User Interface Developed for Determining Photometric Solutions: This GUI was developed by the author for the purpose of displaying residuals as coefficients were changed interactively.

CHAPTER 8

INFRARED PHOTOMETRY

To form the color $B-K$, to compare to the synthesis models, and to compare to the work of others the magnitudes must be put on the standard system. This chapter discusses how apparent K magnitudes are assigned to the galaxies. Stars are observed out of focus to avoid saturating the IR detector array. None of the nights were considered photometric at the time of observation. Hence the standard stars are used to determine a zero point only. Comparisons to previous galaxy magnitudes measured by Aaronson, [Aar77], and Tormen and Burstein, [TB95], are used to refine the zero points. The refinement requires knowledge of the $H-K$ of the galaxies. A nominal value is determined from the 2MASS extended source catalogs. Only the nights on which near infrared observations were made of the subsample galaxies are discussed here. One of those nights is treated differently as described below. It is assumed the reader is familiar with the basics of IR data collection (see Section 3.2), IR data processing (see Chapter 6), and photometry.

8.1 Stars

The analysis that follows in later chapters uses three nights of IR observations: 20APR92, 22APR92, and 09JUN93 (see 2.2.3). The instrumental magnitudes were determined via a different method for 09JUN93. When necessary that night is discussed separately.

The stars are defocused to avoid saturating the array at exposure times longer than the shortest possible exposure time, .265 seconds. Stars are observed in mapping mode. The position of the star in each image of the mapping mode grid is determined interactively by displaying the image and placing the cursor in the center of the star. Since the stars are out of focus it is not necessary to have sub pixel positions. This is done for each sequence taken in mapping mode. Figure 8.1 shows

an example aperture around the standard star HD105601.

Either a single aperture or a curve of growth is measured for each star image. For 20APR92 and 22APR92 a single aperture is used to determine the instrumental magnitudes. One example is given in Table 8.1. It is HD105601 observed on 20APR92. These sizes are chosen to include most of the star light. The fields are not crowded, but there are nearby stars that must be avoided when sizing the aperture. The clipped-mean value of the sky image determined during image processing is used for the sky value. The single-aperture instrumental magnitude is calculated using Equation 7.1.

For 09JUN93 the instrumental magnitudes are determined using curves of growth, COGs. This gives a better approximation than a single aperture that can not contain all the star's light. At each position in a mapping mode grid the COG is measured for the star. The COG is generated by calculating the instrumental magnitude in 100 apertures ranging in radius from 1 to 100 pixels using the sky value determined during image processing. Then an interactive procedure is used to refine the sky value and the instrumental magnitude simultaneously. The procedure is as follows: First adjust the sky value. Then recalculate the magnitude at each point on the curve of growth. Plot the new COG. Repeat until the COG appears as flat as possible at large apertures. Figure 8.2 shows an example COG before and after sky subtraction. For each COG the sky value and asymptotic magnitude are determined in this way. The results for one star, HD129655, are reproduced in Table 8.2. So now for all three nights there is one instrumental magnitude for each image in the mapping grid. No significant variation of instrumental magnitude is seen within the mapping mode grids. This implies there is no correlation between instrumental magnitude and position on the detector. For each sequence the mean is used for the instrumental magnitude.

The mean instrumental magnitudes are matched with the corresponding Elias magnitudes. The differences between the Elias magnitudes and the instrumental magnitudes are calculated. The results are shown for one night in Table 8.3. An attempt was made to determine the photometric parameters. It was not successful confirming that the nights were not photometric. Therefore, only

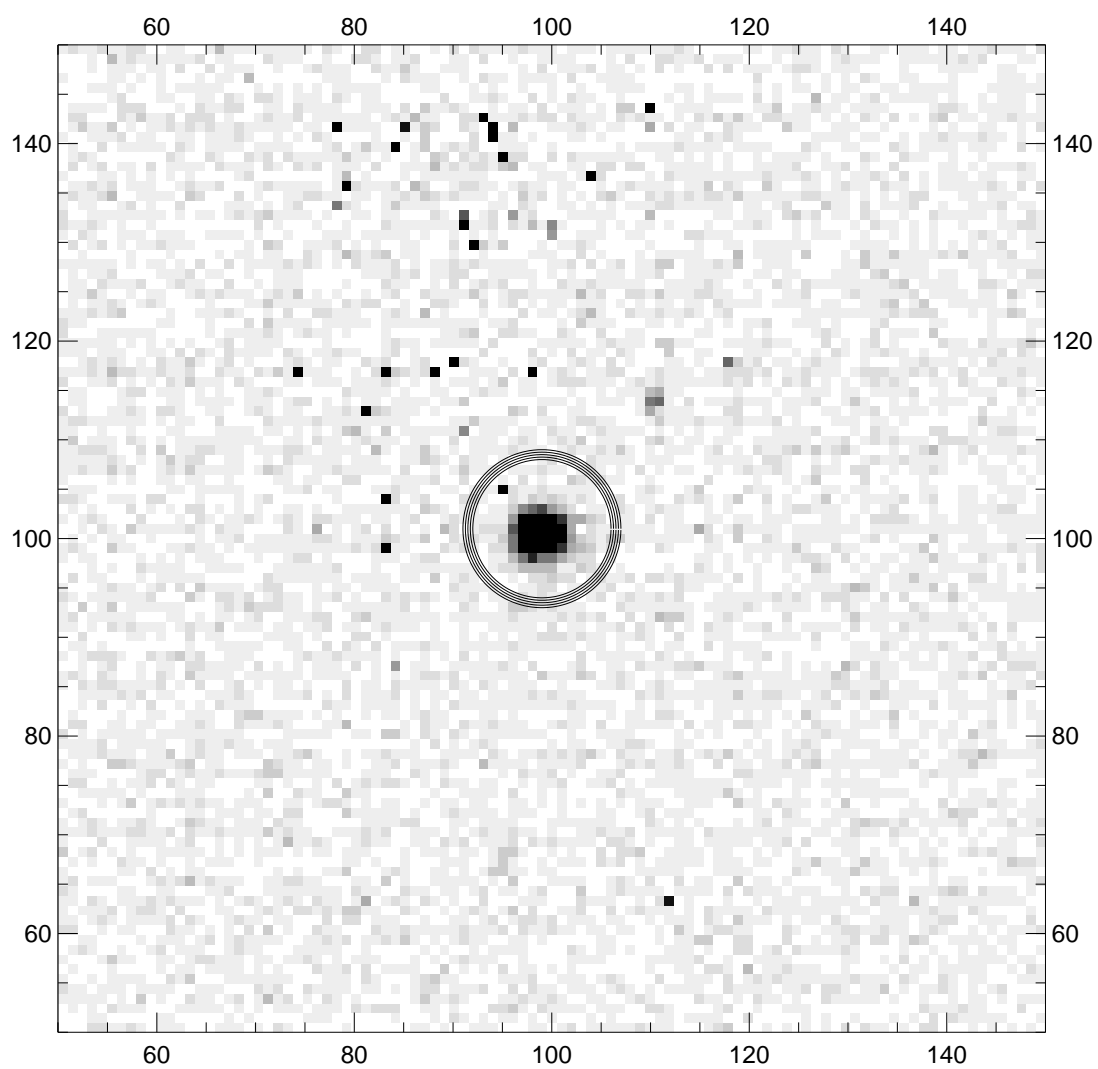


Figure 8.1: Defocused Standard Star, HD105601, with Aperture

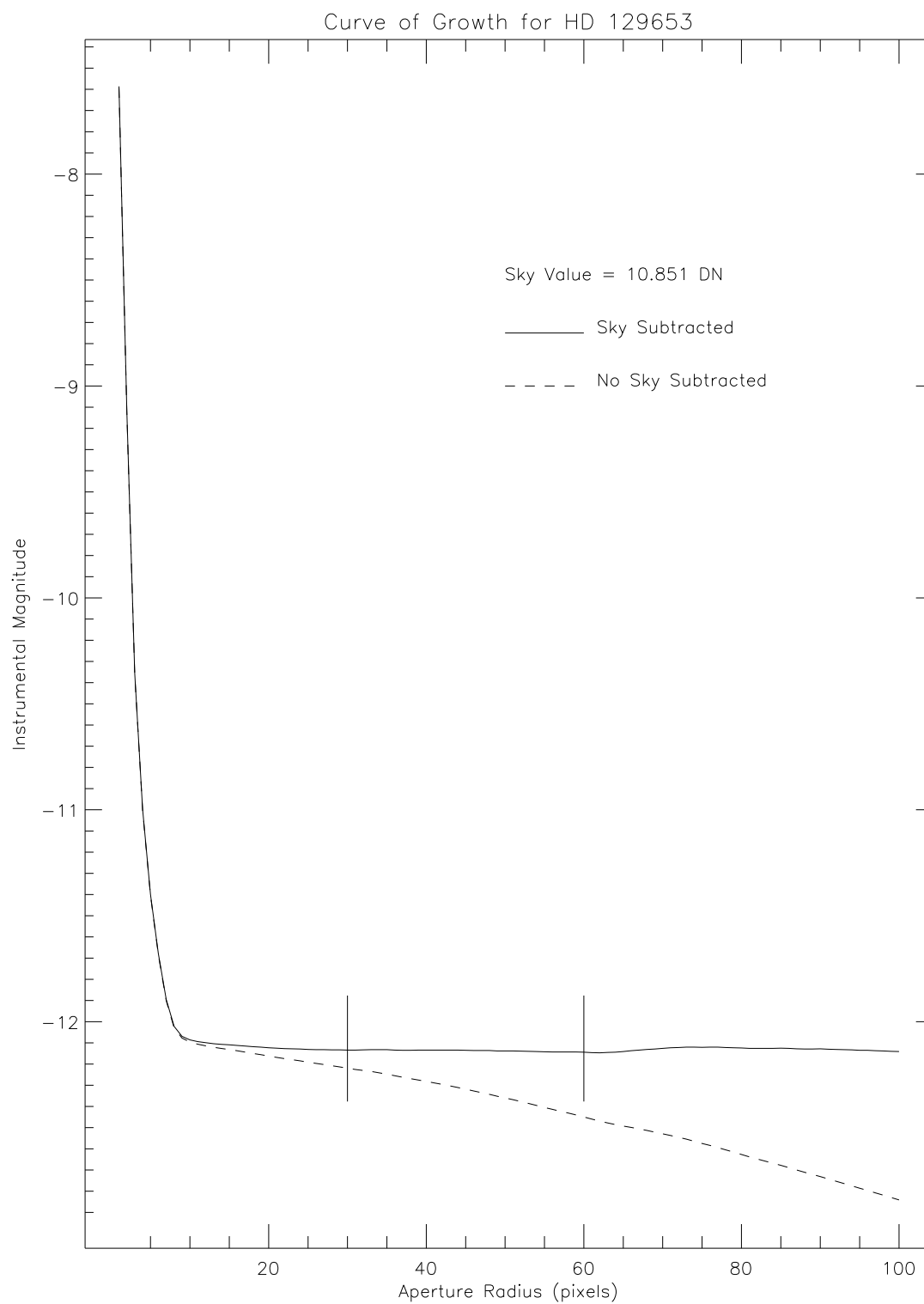


Figure 8.2: Curve of Growth for Standard Star, HD129653, in K: The sky value is adjusted until the tail of the curve is flat. The vertical lines enclose the region emphasized during adjustment.

Table 8.1: Instrumental K Magnitudes for HD105601 on 20APR92

Star ID	X	Y	R	Count	Area	Exp.	Flux	Sky	Mag
HD105601	127	131	8	39444.53	200.6849	1.0	39556.50	-0.55795840	-11.493
HD105601	128	146	8	65359.77	200.6849	1.0	65314.41	0.22597790	-12.038
HD105601	129	163	8	64919.38	200.6849	1.0	64720.74	0.98979030	-12.028
HD105601	145	163	8	63092.48	200.6849	1.0	62929.45	0.81236390	-11.997
HD105601	145	146	8	61485.92	200.6849	1.0	61382.09	0.51738330	-11.970
HD105601	144	130	8	53211.47	200.6849	1.0	53243.31	-0.15865470	-11.816
HD105601	161	128	8	59219.55	200.6849	1.0	59329.90	-0.54984480	-11.933
HD105601	161	145	8	59399.92	200.6849	1.0	59472.61	-0.36218880	-11.936
HD105601	162	162	8	66030.52	200.6849	1.0	66232.62	-1.00707400	-12.053

Table 8.2: Instrumental Magnitudes for HD129655 on 09JUN93

Star ID	Seq. No.	X	Y	Sky	Mag	R _{min}	R _{max}
HD129655	01	142.0	85.5	8.7480611801	-12.7781	50	80
HD129655	02	142.0	85.5	2.4244346619	-12.7706	50	80
HD129655	03	142.0	85.5	-0.3969567418	-12.7685	50	80
HD129655	04	142.0	85.5	1.6830490828	-12.7760	50	80
HD129655	05	142.0	85.5	7.2621736526	-12.7927	50	80
HD129655	01	144.0	83.0	-1.3176898956	-12.3948	50	80
HD129655	02	144.0	83.0	-0.7287855148	-12.4007	50	80
HD129655	03	144.0	83.0	-0.4189769030	-12.4032	50	80
HD129655	04	144.0	83.0	-0.0129670948	-12.4008	30	80
HD129655	05	144.0	83.0	-0.1837701797	-12.3951	40	80
HD129655	01	139.0	82.0	-4.0321860313	-12.2086	40	80
HD129655	02	139.0	82.0	-2.3547296524	-12.2127	50	80
HD129655	03	139.0	82.0	-3.2922916412	-12.2151	40	80
HD129655	04	139.0	82.0	0.1629231572	-12.2149	40	80
HD129655	05	139.0	82.0	-1.4166541100	-12.2016	40	80

the average differences are used as zero points for each night. In the next section, Section 8.2, previous photoelectric measurements of the galaxies are used to check these zero points.

A concern over the variation of the NICMOS K band sensitivity as a function of position on the array has arisen¹. To investigate this possibility Figure 8.3 is created. The 197 standard star observations collected in K over the three nights cover most of the 256×256 array. First a residual is calculated for each observation. The residual is the difference between an individual magnitude in a mapping mode sequence and the average for that sequence. Thus airmass, time, and night-to-night variations are removed. The figure shows a residual at each position where a star was observed except near the center where the observations are too crowded. In this region the average residual in a 3×3 grid is shown. Each cell in the grid, highlighted with dashed lines, contains the average residual with the standard deviation in parenthesis. Each cell contains between seven and twenty residuals. No systematic variation in magnitude is seen as a function of position on the array. Thus if the sensitivity is changing as a function of position on the array it is in a random fashion. If there is a systematic component it is too small to be detected with this non-photometric data. Note also that even though the nights were not photometric that the sky spectrum in K did not change in such a way as to create a systematic effect across the face of the detector in the time it took to collect a mapping mode sequence (\approx a few minutes).

Although galaxy sequences are longer (\approx tens of minutes) images with anomalous variations in the sky spectrum were sifted out by hand during flat-field processing (see Section 6.3). Moreover, any systematic effect due to the response of the detector to galaxy spectral energy distributions will be the same for all galaxies because all their spectra are nearly flat through the K band². Such an effect will be automatically included in the zero points determined in Section 8.2.

¹J. Hester, private communication

²R. Windhorst, private communication

Table 8.3: Combined Instrumental Magnitudes for 20APR92

ID	F	Mean	Median	Sig	N	Min	Max	X	UT	Exp.	NC	K	J-K	H-K	J	H	Res
HD105601	K	-11.92	-11.97	0.18	9	-12.05	-11.49	1.11	7:35:00	1.0	1	6.68	0.125	0.030	6.81	6.72	18.60
HD129653	K	-11.91	-11.92	0.06	9	-11.97	-11.83	1.03	9:11:23	1.0	1	6.92	0.060	0.020	6.98	6.94	18.83
HD136754	K	-11.62	-11.62	0.03	8	-11.65	-11.57	1.26	11:31:47	0.8	1	7.14	0.015	-0.005	7.15	7.13	18.76
HD161903	K	-11.83	-11.89	0.18	9	-11.95	-11.37	1.21	11:08:04	1.0	1	7.02	0.150	0.035	7.17	7.05	18.85
HD162208	K	-11.77	-11.78	0.07	9	-11.86	-11.61	1.01	11:20:52	1.0	1	7.11	0.105	0.035	7.22	7.14	18.88
HD44612	K	-11.63	-11.77	0.42	9	-11.81	-10.53	1.08	2:43:37	1.0	1	7.04	0.020	-0.005	7.06	7.03	18.67
HD84800	K	-11.34	-11.36	0.07	9	-11.46	-11.24	1.06	4:36:58	1.0	1	7.53	0.030	0.000	7.56	7.53	18.87

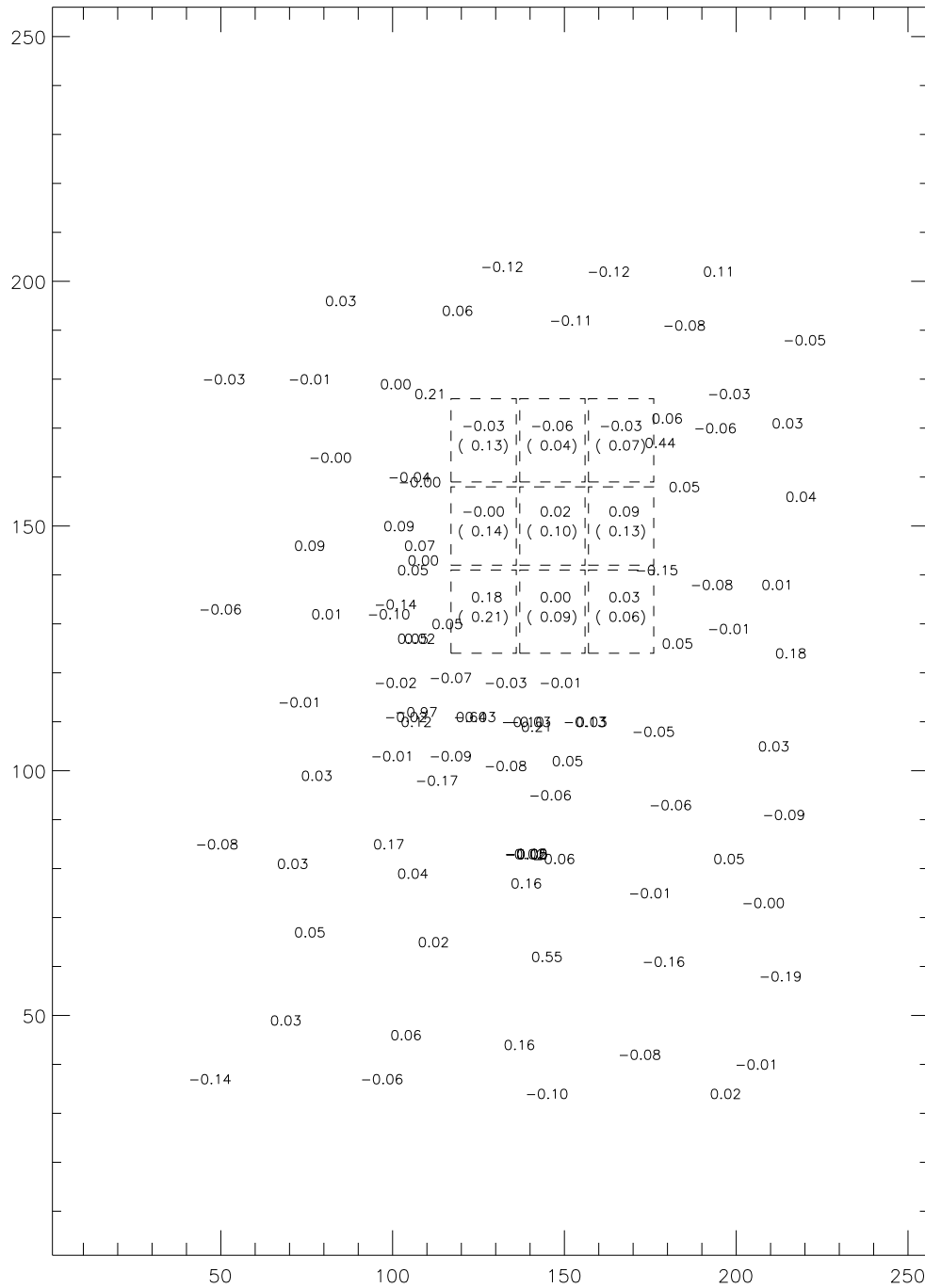


Figure 8.3: K Magnitude Residuals and Position on IR Array: Residuals are shown at positions where stars are observed. The residual is the difference between an individual magnitude in a mapping mode sequence and the average for that sequence. Thus airmass, time, and night-to-night variations are removed. Each cell in the 3×3 grid highlighted with dashed lines contains the average residual with standard deviation in parenthesis. No systematic variation in magnitude is seen as a function of position on the array.

8.2 Galaxies

Now it is possible to predict galaxy magnitudes and check them against previously measured magnitudes. For these galaxies [Aar77] and [TB95] have determined H magnitudes, H_{TB} , in one or more apertures per galaxy. Since my observations are in K a value of $H-K$ for each galaxy is required (Section 8.2.1). After $H-K$ has been determined a comparison can be made between the instrumental K magnitudes and H_{TB} . The stellar K magnitude offsets are refined such that the H_{TB} are predicted accurately. Then these zero points are used to put the instrumental K magnitudes on the standard system.

8.2.1 $H-K$ of 2MASS Extended Sources

The Two Micron All Sky Survey (2MASS) provides extended source catalogs ([JCC⁺00]). A search is made of the first and second incremental releases of the 2MASS extended source catalogs. The subset of objects with a galaxy score less than 1.4 is 95% complete and 98% reliable³. To reduce the subset to a manageable size and to minimize contamination by Galactic objects only objects with a galaxy score of one are used here. This reduced the number by 20%. All objects in the extended catalogs with a galaxy score of 1, contamination flag of zero, H magnitude, J magnitude, and K magnitude are selected. The magnitudes are within circular apertures corresponding to the 20th or 21st magnitude per square arc second isophote. They have an error of approximately 0.1 magnitudes. A histogram of the nearly 500,000 $H-K$ measurements of the extended objects is plotted in panel a) of Figure 8.4. The histogram has a bin size of 0.025 magnitudes. The mode occurs at an $H-K$ of 0.35 magnitudes. The full width half maximum (FWHM) of the histogram is 0.34 magnitudes. A similar value, 0.34 ± 0.15 , is given by [SMR⁺95]. The histogram of $H-K$ from [AMH82] is shown in the inset. This histogram of 200 spiral galaxies (the three considered here were not measured) peaks at $H-K = 0.21$. It has a bin size of 0.045 and a FWHM of 0.14 magnitudes. The difference between the two histograms is that the 2MASS catalog contains galaxies of all types

³Tom Jarrett, private communication

while the [AMH82] galaxies are all spirals. This indicates that if the histogram of 2MASS spirals were available it may peak at a bluer $H-K$. On the other hand, if more spirals were added to the [AMH82] sample its histogram may peak at a redder $H-K$. Thus, because of its statistical significance the 2MASS value is used as the fiducial $H-K$. Panel b) of the same figure shows K plotted against H . The [AMH82] H and K data are also shown as they fill in the bright end of the relationship. The line has a slope of one and an intercept of -0.35 . This shows a bias in the data not represented by the line. The relationship broadens with increasing magnitude. There is a preference for objects to scatter below and to the right of the line. This occurs at all magnitudes but only becomes significant for faint objects. Thus, $H-K$ is 0.35 ± 0.17 for the brighter extended sources and may be at most 0.14 magnitudes too red for spiral galaxies. This value is used to determine K magnitudes in Section 8.2.2.

8.2.2 Measuring K Magnitudes

Table 8.4 shows the aperture sizes and H_{TB} magnitudes for the galaxies. The [TB95] apertures are used to measure instrumental K magnitudes in the galaxies. Equation 7.1 is used to calculate the magnitudes. The sky value for a galaxy is determined by looking at the average count in background regions in the galaxy's image. The inputs and results are shown in Table 8.5. Note that each combined galaxy image is composed of images taken over a range of airmass and UT. These ranges are listed in Table 8.6 and are small. So, it is not necessary to make any corrections. In panel a) of Figure 8.5 H_{TB} is plotted as a function of aperture size for the galaxies. For each galaxy the H_{TB} points are joined by a solid line. Also shown on this plot is the instrumental H magnitude, H_{instr} , of each aperture joined by dashed lines. H_{instr} is determined from the instrumental K magnitudes, K_{instr} , using the zero point, K_{zero} , determined from the stellar data in Section 8.1 and $H-K = .35$ as discussed in Section 8.2.1.

$$H_{instr} = K_{instr} + K_{zero} + (H-K)$$

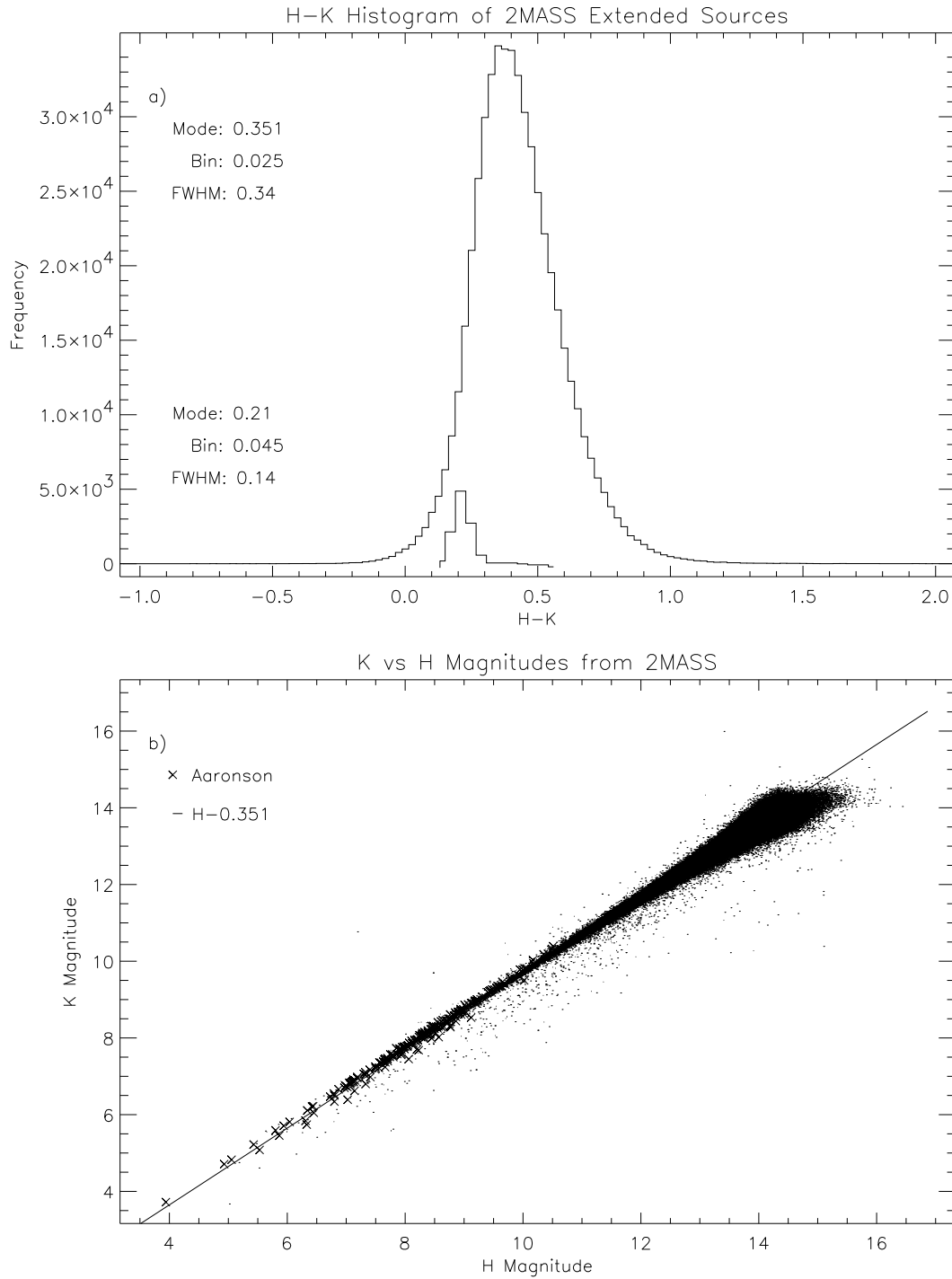


Figure 8.4: Relationship of H and K for Objects from the 2MASS Extended Source Catalogs: a) The large histogram contains nearly 500,000 2MASS H-K measurements of all galaxy types. The mode occurs at 0.35. The inset histogram contains 200 H-K [AMH82] measurements (current galaxies not included) of spirals only. Its mode is at 0.21 indicating the fiducial H-K may be overestimated by 0.14 magnitudes. (See Section 8.2.1) b) The line has a slope of one and intercept of -0.35. The [AMH82] observations (diagonal crosses) fill out the bright end of the relationship.

Table 8.4: Apertures and H Magnitudes from [TB95]

ID	H	Error	log(A/D)	Aperture
NGC4654	9.31	0.03	-0.76	26.13
	8.78	0.03	-0.56	41.41
	8.60	0.03	-0.47	50.95
NGC5204	10.90	0.04	-0.76	26.13
	10.91	0.04	-0.76	26.13
	10.25	0.03	-0.57	40.47
	10.33	0.03	-0.56	41.41
	10.34	0.03	-0.56	41.41
	10.09	0.03	-0.47	50.95
	10.12	0.04	-0.47	50.95
NGC6384	9.78	0.04	-1.19	13.71
	9.12	0.03	-0.90	26.74
	8.64	0.03	-0.72	40.47
	8.49	0.03	-0.61	52.13
	8.47	0.03	-0.59	54.59

Table 8.5: Galaxy Instrumental K Magnitude Measurements

Galaxy	Sky	Exp	R _{ap}	K _{instr}	Counts	A _{ap}	Galaxy
Galaxy	($\frac{DN}{pixel}$)	(s)	($''$)		(DN)	(Pixels)	(DN)
NGC4654	-3.0	30	26.130	-10.035	303777.100	2042.11900	309903.457
			41.410	-10.571	492221.700	5128.40700	507606.921
			50.950	-10.758	579791.600	7761.50600	603076.118
NGC5204	0.0	60	26.130	-7.054	39784.850	2042.11900	39784.850
			26.130	-7.054	39784.850	2042.11900	39784.850
			40.470	-7.566	63773.010	4898.85800	63773.010
			41.410	-7.588	65095.020	5128.40700	65095.020
			41.410	-7.588	65095.020	5128.40700	65095.020
			50.950	-7.807	79615.800	7761.50600	79615.800
			50.950	-7.807	79615.800	7761.50600	79615.800
NGC6384	-7.0	45	13.710	-9.310	234306.100	562.39150	238242.840
			26.740	-9.950	414938.100	2139.36200	429913.634
			40.470	-10.364	594843.600	4898.85800	629135.606
			52.130	-10.584	713744.700	8127.06700	770634.169
			54.590	-10.618	732532.900	8909.87200	794902.004

Table 8.6: Range in UT and Airmass for Each Galaxy

ID	Range in UT	Range in Airmass
NGC4654	08:01:25-08:41:32	1.18-1.18
NGC6384	10:09:02-10:45:29	1.11-1.13
NGC5204	05:38:36-06:03:08	1.19-1.22

Table 8.7: Zero Points and Offsets for Each Galaxy in K

ID	Obs. Date	K_{zero}	σ	$\langle H_{\text{TB}} - H_{\text{instr}} \rangle$	σ
NGC4654	20APR92	18.8	0.1	0.201	0.007
NGC6384	20APR92	18.8	0.1	0.090	0.040
NGC5204	09JUN93	18.9	0.2	-1.340	0.050

From the figure it is seen that the stellar zero points do not predict H_{TB} for NGC 5204. This galaxy was observed on 09JUN93. On this night the stellar zero point does not match the galaxy. The other galaxies were observed on 20APR92 or 22APR92. They have much smaller shifts relative to H_{TB} just .1 or .2 magnitudes. The average difference between H_{TB} and H_{instr} , $\langle H_{\text{TB}} - H_{\text{instr}} \rangle$, is used as an offset between K_{instr} and H_{TB} . Table 8.7 lists the offsets determined for each galaxy. Taking $H-K$ into account, the following is used to predict K magnitudes from the instrumental K magnitudes.

$$K_{\text{predicted}} = K_{\text{instr}} + K_{\text{zero}} + \langle H_{\text{TB}} - H_{\text{instr}} \rangle$$

Thus, given a K instrumental magnitude the appropriate zero point and offset from Table 8.7 are added to it to give a K magnitude. This formula is used below when calculating slit magnitudes (Section 9.5).

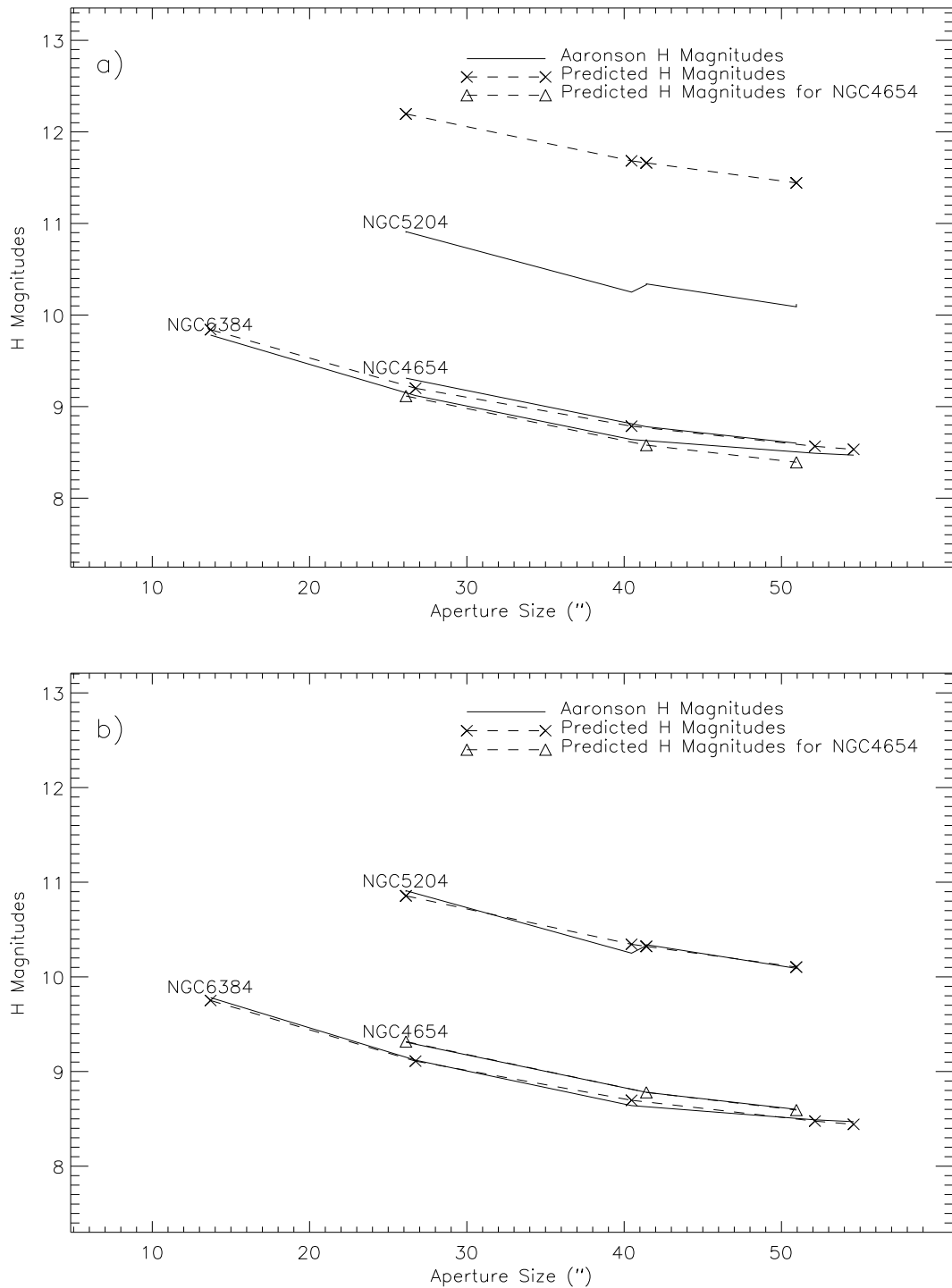


Figure 8.5: Predicted H Magnitudes Compared to [TB95] H Magnitudes: a) This plot shows the H_{TB} magnitudes joined by a solid line for each galaxy. The predicted magnitudes are joined by dashed lines for each galaxy. For each galaxy the average difference between the two defines the offset. b) The same plot but after applying the offsets to the predicted magnitudes.

PART III

DATA ANALYSIS

CHAPTER 9

MGB, B-K, MODELS, AND INTERNAL REDDENING

In this chapter the colocated measurements of Mgb, B, and K are described, including how the line index, which is an equivalent width ($EW(Mgb)$), is measured in the spectra and how B and K slit profiles are extracted from the images. Then the diagram used to investigate the cause of color gradients and to compare the observed B–K and $EW(Mgb)$ to the model B–K and $EW(Mgb)$ is described. The comparisons result in constraints on the ages and metallicities of the disk populations and are discussed in the next chapter. The comparisons also lead to a technique for estimating the internal reddening of a galaxy.

The four slit positions in the three galaxies, NGC 4654, NGC 5204, NGC 6384, described in Section 2.1.1 are analyzed in this chapter although the techniques used will be applied to the full sample in future work.

9.1 Background

Gonzalez [Gon93] was the first to compare observed Lick line indices (Section 1.5) with Worthey’s stellar population models [Wor93, Wor94]. He did so by plotting the observations on a model grid in which each point represented an SSP. The grid is formed by the values of two line indices at each age and metallicity. See Section 9.6 for more details. This type of plot is used to estimate the age and metallicity of elliptical galaxies. This work uses a model grid of line index and color to constrain the internal reddening, age, and metallicity the subsample of spiral disks. The equivalent width of a spectral feature, Mgb, and a color, B–K, are measured at the same positions within a galaxy. Comparing the observed Mgb index to the model grid confirms deductions made from the

observations alone and reveals limits on the stellar populations. The stellar population models are used to predict what the $B-K$ color should be. The observed Mgb is matched with a model value. The modeled Mgb corresponds to a model color. The difference between the predicted color and the observed color is explained by internal reddening. This is analogous to determining the reddening of a star by knowing its spectral type, although a screen model would be a very crude approximation.

There are three assumptions that justify the above interpretation. The first is that the strength of a spectral line in the optical region measured relative to a nearby pseudo-continuum is not affected significantly by the presence of dust. The second is that the stellar population models accurately represent real stellar populations as demonstrated by [Gon93] and [TFWG00]. The third assumption is that mixed stellar populations have properties that fall within the ranges of the properties of its constituent SSPs. This assumption has been tested by using the Worthey models to combine SSPs into mixed populations and producing model grids for the mixed populations.

9.2 Measuring the Line Index

Figure 9.1 shows an example spectral image, NGC 4654 position one, with the absorption and emission features labeled. The calibration (Chapter 5) and extraction of one dimensional spectra (Section 5.11) have been discussed previously in this document. The purpose of this figure is to show all the spectral features for reference, to note the emission that contaminates the hydrogen absorption lines, to note the weakness of the iron lines, and to show the location of Mgb. Gonzalez [Gon93] used an emission-corrected $H\beta$ index and a mean iron index to separate age and metallicity effects in ellipticals. The emission contaminating $H\beta$ in late type systems is much stronger than in the ellipticals. Gonzalez's technique is not necessarily applicable. The separation of emission from absorption and measurement of the iron lines will be pursued in future work.

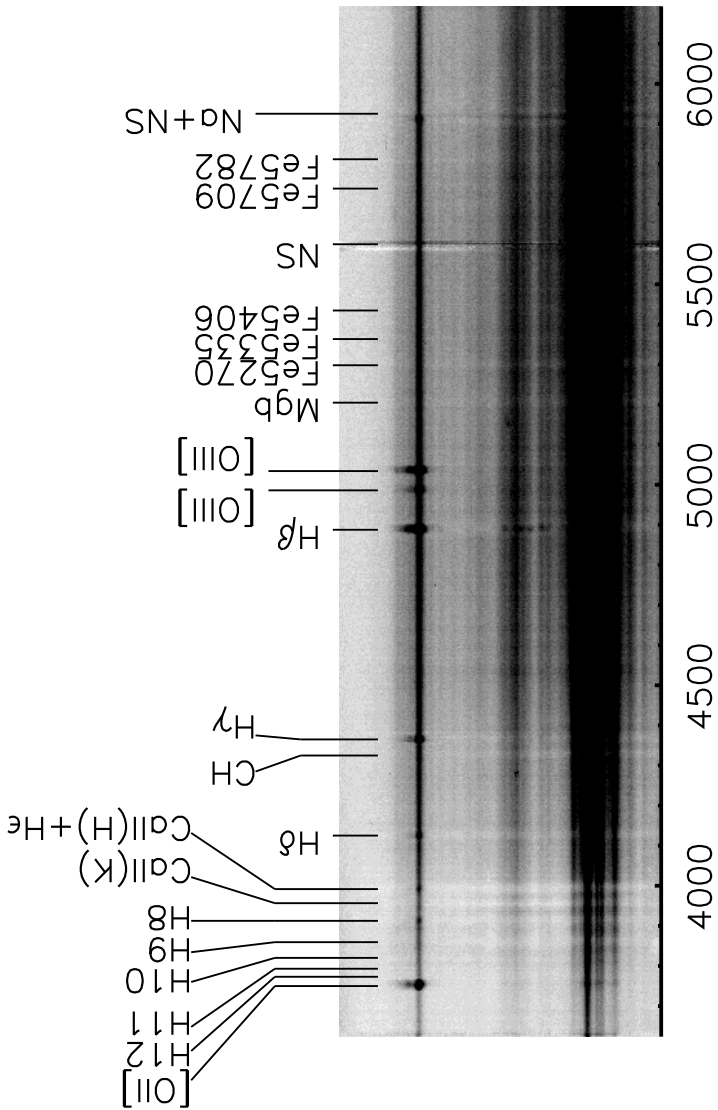


Figure 9.1: Spectral Image with Features Labeled: This figure is provided for reference. The main spectral features are labeled. The emission prevents the use of hydrogen as a population indicator. The emission and the weak iron lines will be studied in future work.

This section describes how the Lick line indices are measured and how an error is estimated for each measurement. Recall the description of line indices given in Section 1.5. First the measurement of a single band is described. Second the measurement of the continuum and line index is described. Then the error estimation process is explained. Then the Doppler shift due to a galaxy's radial velocity is taken into account. Finally the error in the index due to uncertainty in the wavelength position is described and estimated.

9.2.1 Measuring the Total Flux in a Band

Figure 9.2 shows an example of the bands for Mgb. A box in this figure is centered on a band and has the same width as the band. The line between the two side bands represents the linear interpolation used to calculate the continuum value in the center band. The vertical line is the continuum value at the center of the center band.

The total flux in a band is determined by summing all the counts in bins wholly contained within the wavelength limits of the band. Then at the ends where only a fraction of a bin is included the same fraction of the associated flux is included in the sum. The mean flux density is given by the total flux divided by the width of the band:

$$I_b = \frac{1}{\Delta w} \sum_{i_1}^{i_2} \alpha_i I_i \quad (9.1)$$

where

$$\Delta w = w_2 - w_1 \quad (9.2)$$

$$w_1 = (\lambda_1 - \lambda_0) / \Delta \lambda \quad (9.3)$$

$$w_2 = (\lambda_2 - \lambda_0) / \Delta \lambda \quad (9.4)$$

$$i_1 = \text{int}(\text{round}(w_1)) \quad (9.5)$$

$$i_2 = \text{int}(\text{round}(w_2)) \quad (9.6)$$

$$\alpha_i = \begin{cases} i_1 + 0.5 - w_1 & \text{if } i = i_1, \\ w_2 + 0.5 - i_2 & \text{if } i = i_2, \\ 1 & \text{otherwise.} \end{cases} \quad (9.7)$$

and $\Delta\lambda$ is the number of wavelengths per bin, λ_0 is the starting wavelength, λ_1 is as the center of the first bin, and λ_2 is at the center of the last bin.

9.2.2 Calculating the Continuum and the Line Index

The blue and red bands are placed such that they measure the pseudo-continuum. The mean flux density in the blue and red side bands is determined. Using the centers of the band passes and the mean flux densities linear interpolation is performed to get a mean flux density for the pseudo-continuum centered on the feature of interest. The line ratio is then given by the ratio of mean flux density in the center band to the mean flux density of the pseudo-continuum in the center band. The line depth is one less the line ratio. The equivalent width of the line is calculated by multiplying the line depth by the width of the center band. The corresponding magnitude is also determined. The following equations are used:

$$I_{continuum} = I_{blue} \frac{\lambda_{red} - \lambda_{center}}{\lambda_{red} - \lambda_{blue}} + I_{red} \frac{\lambda_{center} - \lambda_{blue}}{\lambda_{red} - \lambda_{blue}} \quad (9.8)$$

$$R = \frac{I_{center}}{I_{continuum}} \quad (9.9)$$

$$M = -2.5 \log(R) \quad (9.10)$$

$$EW = \Delta\lambda_{center}(1 - R) \quad (9.11)$$

The equivalent width is used for the narrow features like Mgb while the magnitude is used for the broader molecular bands.

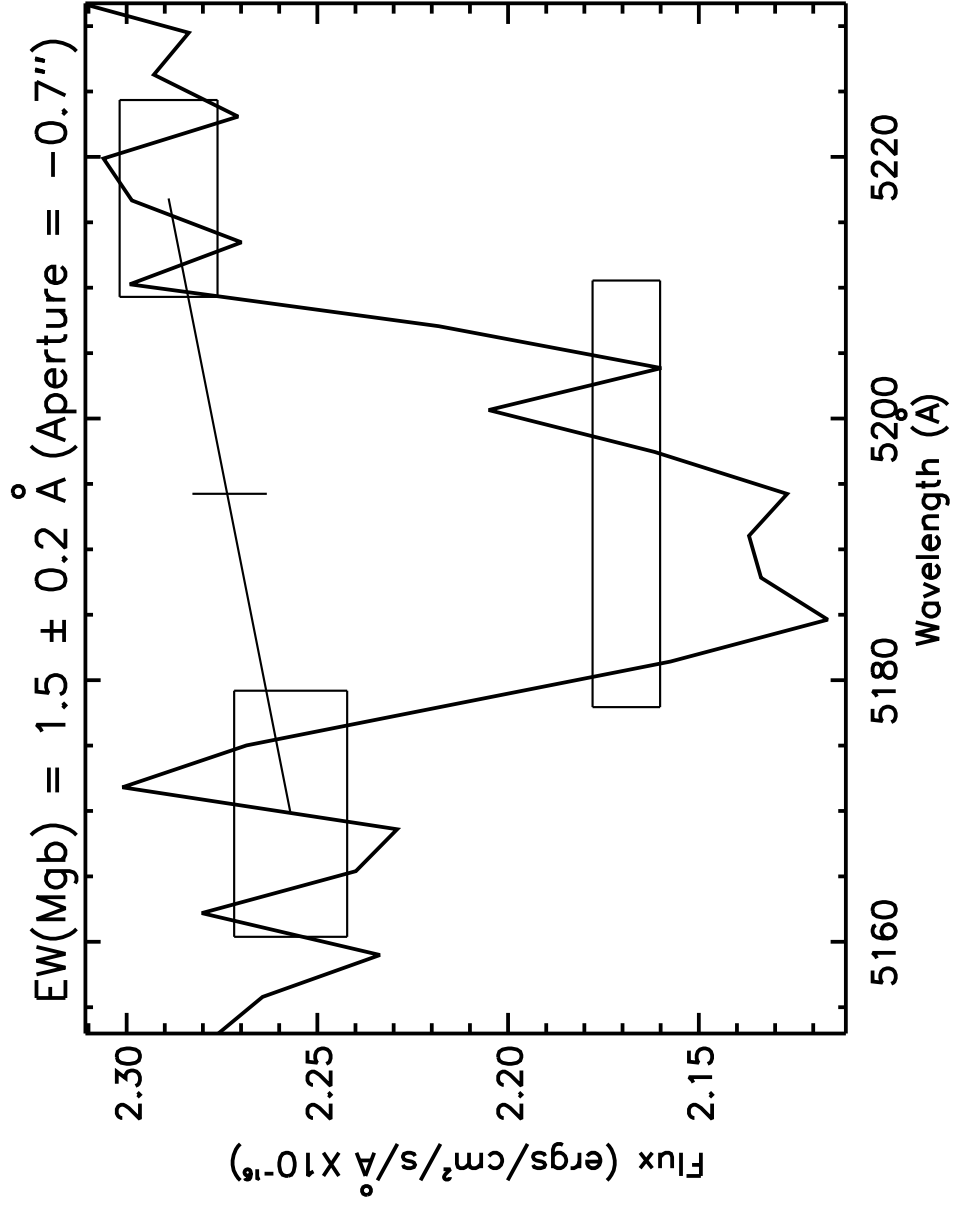


Figure 9.2: Example of Measuring Mg b in NGC 4654: The boxes represent the location and width of the red, center, and blue bands. The line between the side bands represents the linear interpolation used to calculate a continuum value. The vertical line is the continuum value and is centered on the index.

9.2.3 Error Estimate and Propagation for Single Index Measurement

The error associated with an index value is calculated using error propagation. The inputs to the error propagation are error estimates made in the total flux or counts in each band, I_b . The error estimate in a band is made in two ways. The first method uses an estimate of the noise made from the fluxed spectra. The second method uses the CCD equation to estimate the noise in each band. This method uses the unfluxed spectra.

In the first method the variance is estimated in a fluxed spectrum by smoothing it with a five pixel window and squaring the difference between the spectrum and the smoothed spectrum. Then the variance in a band is simply the sum of the variances. Thus the variance in a band is measured in exactly the same way as the total flux.

In the second method the CCD equation is used to estimate the error in a band. Each index measurement can be thought of as an approximately rectangular aperture centered on the wavelength and position of interest in the spectral image (as opposed to a window on a one dimensional spectrum). The variance in a band is given by the following equation.

$$V_b = I_b + I_{sky} + N(1 + \frac{N}{N_{sky}})(R^2 + td). \quad (9.12)$$

I_{sky} is the sky flux in the band. N is the number of pixels in the band which is the number of columns from the spectral image used to form the spectrum times the number wavelength bins in the band. N_{sky} is the number of pixels in the sky which is the number of columns used to form the sky spectrum times the number of wavelength bins in the band. R is the read noise, t is the integration time, and d is the dark current.

Error propagation is used separately on the two variance estimates to calculate the error associated with each spectral index. Thus there are two error estimates for each index. The two estimates are approximately equal implying that fluxing the spectra had little affect on the noise content. The

errors quoted in this work are based on the first method. The error propagation equations are

$$\delta I_{continuum} = \left[\left(\delta I_{blue} \frac{\lambda_{red} - \lambda_{center}}{\lambda_{red} - \lambda_{blue}} \right)^2 + \left(\delta I_{red} \frac{\lambda_{center} - \lambda_{blue}}{\lambda_{red} - \lambda_{blue}} \right)^2 \right]^{\frac{1}{2}} \quad (9.13)$$

$$\frac{\delta R}{R} = \left[\left(\frac{\delta I_{center}}{I_{center}} \right)^2 + \left(\frac{\delta I_{continuum}}{I_{continuum}} \right)^2 \right]^{\frac{1}{2}} \quad (9.14)$$

$$\delta EW = \Delta \lambda_{center} \delta R \quad (9.15)$$

$$\delta M = 2.5 \frac{\delta R}{R}. \quad (9.16)$$

δI_{center} is determined as described above. Table 9.1 is included here has an example of the band values, error values, and continuum values obtained for one slit position.

9.2.4 Reddening Independence of Mgb

While examining Figure 9.2 note the following. Extinction curves vary smoothly and slowly in the optical region and can be approximated by low order polynomials over short wavelength ranges. The side bands of Mgb are only 45Å apart, and the linear interpolation removes continuum variation to first order. Therefore, EW(Mgb) is not reddened. Any narrow optical feature measured in this fashion is independent of reddening.

Table 9.1: Mgb Band Values for NGC4654 Position One

Position (")	Width (")	Blue($\times 10^{-16}$)			Center($\times 10^{-16}$)			Red($\times 10^{-16}$)			Continuum	Error
		Total	Flux Density	Error	Total	Flux Density	Error	Total	Flux Density	Error		
-32.67	9.90	12.300	2.095	0.017	20.490	2.014	0.015	9.986	2.126	0.011	2.111	0.010
-25.08	5.28	7.479	1.274	0.017	12.370	1.215	0.008	5.952	1.267	0.006	1.270	0.009
-20.46	3.96	7.894	1.344	0.014	13.130	1.290	0.010	6.376	1.358	0.017	1.351	0.011
-16.50	3.96	10.920	1.859	0.011	17.800	1.749	0.007	8.682	1.848	0.006	1.854	0.006
-13.20	2.64	12.220	2.082	0.014	20.220	1.987	0.010	9.779	2.082	0.008	2.082	0.008
-9.90	3.96	15.070	2.566	0.015	24.900	2.447	0.011	12.030	2.562	0.018	2.564	0.012
-6.93	1.98	12.100	2.061	0.013	20.070	1.972	0.007	9.766	2.079	0.010	2.070	0.008
-4.62	2.64	16.580	2.823	0.016	28.140	2.765	0.011	13.620	2.901	0.016	2.863	0.011
-2.31	1.98	11.820	2.014	0.012	19.720	1.938	0.008	9.746	2.075	0.009	2.046	0.008
-0.66	1.32	13.250	2.257	0.015	22.070	2.169	0.009	10.750	2.289	0.013	2.273	0.010
0.66	1.32	20.180	3.438	0.012	33.960	3.337	0.010	16.330	3.477	0.021	3.458	0.012
2.64	2.64	19.810	3.373	0.012	33.130	3.256	0.011	16.190	3.446	0.010	3.411	0.008
5.61	3.30	14.650	2.495	0.017	24.170	2.375	0.008	11.820	2.517	0.013	2.506	0.010
9.57	4.62	14.530	2.474	0.011	23.710	2.330	0.012	11.770	2.505	0.010	2.490	0.007
14.85	5.94	9.526	1.623	0.009	15.860	1.558	0.008	7.855	1.672	0.010	1.648	0.007
21.45	7.26	10.980	1.870	0.014	18.390	1.807	0.010	9.104	1.938	0.018	1.905	0.012
29.04	7.92	10.360	1.764	0.019	17.440	1.713	0.012	8.498	1.809	0.017	1.788	0.013
36.63	7.26	13.540	2.307	0.010	22.520	2.213	0.012	10.910	2.323	0.009	2.315	0.007
43.89	7.26	9.530	1.623	0.012	15.730	1.546	0.009	7.641	1.627	0.014	1.625	0.009
56.10	17.16	14.310	2.436	0.024	23.670	2.326	0.017	11.560	2.462	0.013	2.450	0.013
72.93	16.50	11.300	1.924	0.041	18.820	1.850	0.022	9.035	1.924	0.029	1.924	0.025
86.13	9.90	15.480	2.636	0.021	26.640	2.618	0.018	13.030	2.774	0.026	2.708	0.017
97.35	12.54	7.570	1.289	0.023	12.830	1.261	0.016	6.292	1.340	0.026	1.316	0.017

9.2.5 Radial Velocities and Index Position Error

The galaxies have significant radial velocities (Table 2.1). Therefore the position of the bands are shifted and stretched to match the galaxy spectra. Table 9.2 shows the Doppler shifted wavelengths and interpolation coefficients for the index bands measured in each galaxy. It also shows the unshifted wavelengths and interpolation coefficients for the index bands measured in the star SA103-095.

The galaxies also have rotational velocities. Radial velocity profiles are not measured in this thesis. However to account for this slight variation in line position, which also has contributions from residuals in the wavelength solution, the following estimate is made. Each index is measured at five positions that are one pixel shifts centered on the nominal line position. Figure 9.3 shows an example of these multiple measurements for Mgb. The large crosses mark the position and mean value in each band. The width of horizontal lines show the total range covered by the five measurements. The height of the vertical line is the standard deviation of the five measurements. The points are the individual measurements. The variation in the resulting spectral index is then compared to the error estimated from error propagation. The larger is quoted as the error. This method is used for all spectra and line indices measured.

Table 9.2: Wavelengths and Interpolation Coefficients for the Mgb Index Bands

Object	Blue			Center			Red			C^a	C^b			
	Blue	Center	Red	N_p	Blue	Center	Red	N_p	Blue			Center	Red	N_p
SA103-095	5142.625	5152.000	5161.375	5.850	5160.125	5176.375	5192.625	10.140	5191.375	5198.875	5206.375	4.680	0.480	0.520
NGC4654	5160.379	5169.787	5179.194	5.871	5177.940	5194.246	5210.552	10.180	5209.298	5216.824	5224.349	4.697	0.480	0.520
NGC5204	5146.124	5155.506	5164.887	5.863	5163.636	5179.897	5196.158	10.160	5194.908	5202.413	5209.918	4.691	0.480	0.520
NGC6384	5171.152	5180.579	5190.006	5.892	5188.749	5205.089	5221.429	10.210	5220.172	5227.714	5235.256	4.714	0.480	0.480

$${}^a C_1 = (\lambda_{\text{red}} - \lambda_{\text{center}}) / (\lambda_{\text{red}} - \lambda_{\text{blue}})$$

$${}^b C_2 = (\lambda_{\text{center}} - \lambda_{\text{blue}}) / (\lambda_{\text{red}} - \lambda_{\text{blue}})$$

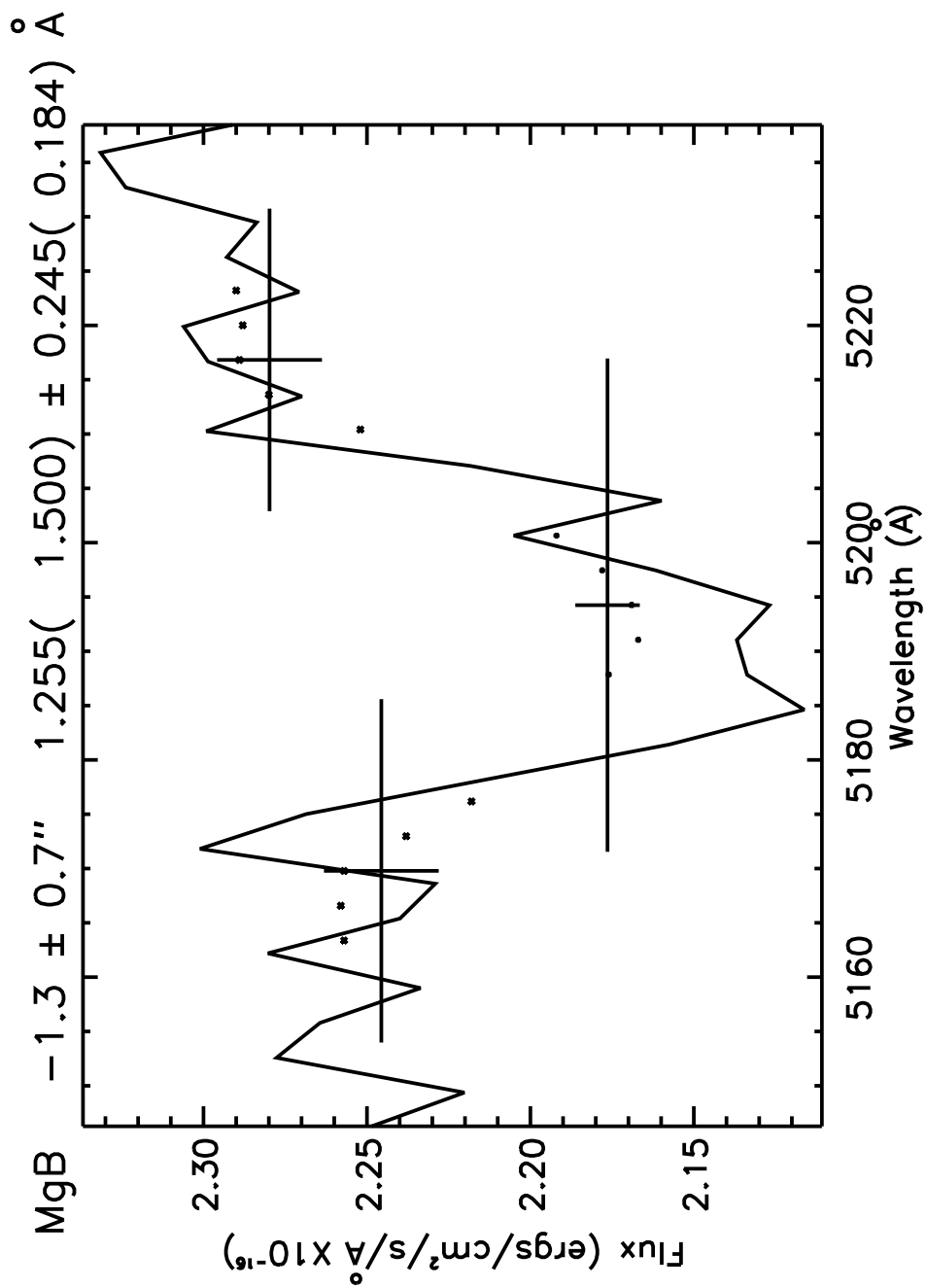


Figure 9.3: Example of Measuring Position Error in MgB in NGC 4654: The horizontal lines show the total range covered by the five measurements. The height of the vertical line is the standard deviation of the five measurements. The points are the individual band measurements.

9.3 Transforming Mgb Measurements to Lick System

To compare the Mgb index measurements to the models and to B–K they must be on the Lick System (see Section 1.5). Two steps are taken to transform the instrumental values of the Mgb index to the Lick system. The first step compensates for resolution differences between the MMT spectra and the IDS spectra. The second step is a check to determine if an offset should be applied to take into account the fact that the MMT spectra were fluxed while the IDS spectra were fit with a fifth order Chebyshev polynomial.

The value of the index depends on the resolution of the instrument used to record the spectrum. The main difference between the instrumental index values and the Lick index values are due to resolution differences. Previous methods of transforming to the Lick system considered spectra with a higher resolution than the IDS and involved smoothing the spectra to match the IDS resolution *before* measuring the indices [Gon93]. The resolution of the MMT data is coarser than the IDS resolution. So, previous methods do not apply.

The method presented here assumes that the differences in observed velocity dispersion are dominated by resolution differences. Then the relationship between velocity dispersion and index value is used to estimate a resolution correction. This relationship was determined by Gonzalez [Gon93]. It is reproduced in Figure 9.4. The individual points in this plot are index values measured in broadened template spectra of elliptical galaxies. See [Gon93] for details on how the templates are created and broadened. The lines are polynomial fits to the data. The fits are used to extrapolate the data to the MMT velocity dispersion. Extrapolation is always a dangerous process. There is not guarantee that the fits follow the true relationship beyond the range of the data. However, the small scatter leads one to believe the fits are good.

Using the polynomial fits an offset for Mgb is determined that will put the index on a velocity dispersion scale that is equivalent to the IDS resolution. By definition the following is true.

$$\log I(\sigma_{\text{IDS}}) = \log I(\sigma_{\text{MMT}}) + \log \left(\frac{I(0)}{I(\sigma_{\text{MMT}})} \right) - \log \left(\frac{I(0)}{I(\sigma_{\text{IDS}})} \right) \quad (9.17)$$

$$\delta = \log \left(\frac{I(0)}{I(\sigma_{\text{MMT}})} \right) - \log \left(\frac{I(0)}{I(\sigma_{\text{IDS}})} \right) \quad (9.18)$$

where σ is velocity dispersion, and $I(\sigma)$ is the index value at velocity dispersion σ . The last two terms constitute the offset, δ . A value for each of the terms in the above equation can be estimated. To do so requires an estimate of σ_{IDS} and σ_{MMT} .

A velocity dispersion equivalent to the resolution can be estimated from the FWHM using the following equation.

$$\sigma = \frac{\text{FWHM}}{2.354} \frac{c}{\lambda}$$

where λ is the wavelength of interest and c is the speed of light. For IDS $\lambda = 5200 \text{ \AA}$ and FWHM = 8.2 \AA ([Gon93]). So,

$$\sigma_{\text{IDS}} \approx 201 \text{ km/s}$$

The FWHM of the MMT $2''$ slit is $17.9 \pm 0.5 \text{ \AA}$ as determined by measuring lines in the comparison lamp images. Thus the velocity dispersion for the MMT $2''$ slit at 5200 \AA is

$$\sigma_{\text{MMT}} \approx 438.6 \pm 12.3 \text{ km/s}$$

Now the resolution correction can be calculated. The uncertainty in σ_{MMT} corresponds to a range in $\text{Log}(\sigma_{\text{MMT}})$ of 2.63 to 2.65. Evaluating the polynomial fit for Mgb at these two limits gives 0.12 dex and 0.13 dex respectively. Hence there is a range of .01 dex in $\text{Log}(I(0)/I(\sigma_{\text{MMT}}))$. The error in the resolution correction is dominated by the uncertainty in σ_{MMT} . The error in σ_{IDS} is ignored because it falls on a much shallower part of the curve. Evaluating the fit at the IDS velocity dispersion gives $\text{Log}(I(0)/I(\sigma_{\text{IDS}})) = 0.03$. By Equation 9.18 $\delta = 0.10 \pm 0.01$ dex for Mgb. When the index offset is applied to the index values the errors are added in quadrature.

The second step in the transformation is performed. For the purpose of comparison the Mgb index is measured in 48 uniform apertures in the spectral image of the Lick standard SA103-095. The resolution correction is applied. The average of the corrected values is $3.9 \pm 0.25 \text{ \AA}$. The Lick value of Mgb for SA103-095 is $4.0 \pm 0.2 \text{ \AA}$ [Wor93]. The difference is $0.1 \pm 0.32 \text{ \AA}$. This offset is zero within the errors. The resolution correction is successful. No other corrections are required.

The transformation to the Lick system involves only the resolution correction, a scale factor. The transformation is applied to all Mgb instrumental values. All errors are added in quadrature. Table 9.3 shows the instrumental values of Mgb along side the Lick values for each slit position. The error is the final error estimate for the Lick values. The values are shown for each position along the slit at which Mgb is measured.

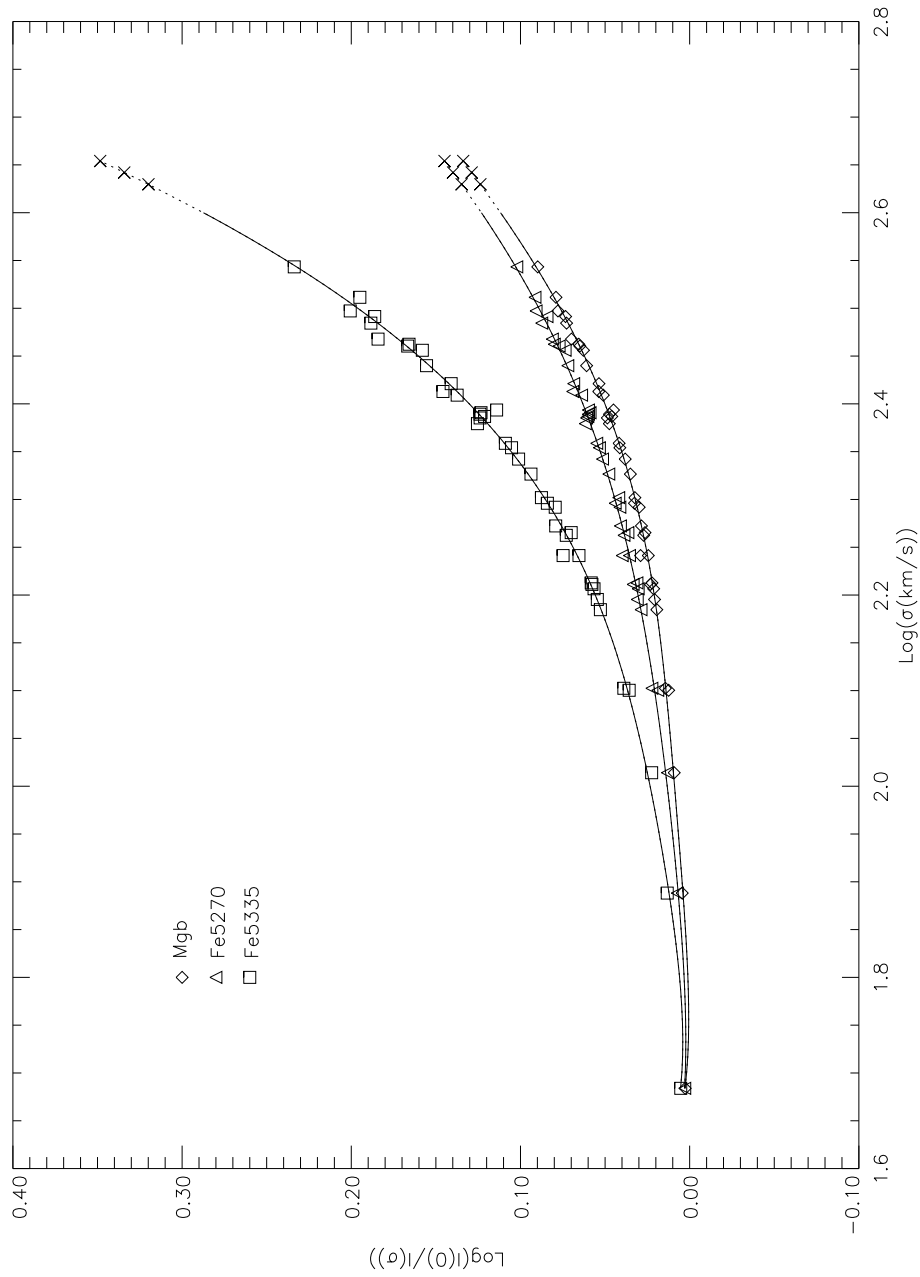


Figure 9.4: Index Values as a Function of Velocity Dispersion: The solid lines are fifth order polynomial fits to the points. The dotted portions are extrapolations of the data using the fits. The points corresponding to the MMT resolution are indicated with X's. Curves for iron lines are shown but not used.

9.4 Mgb Index Profiles

An index profile is generated by plotting the line index value against position along the slit. To determine if the spatial variation seen in the galaxy index profiles is real an index profile for SA103-095 is used. The star was scanned along the slit (Section 2.2). Therefore each point along the slit should have the same Mgb.

The star's Mgb is measured using the same apertures as for the galaxies. Thus differences between the star and galaxy profiles are not due to differences in aperture size or spacing. As seen in Figures 9.5 and 9.6 no significant variation of the star's index with position is seen. For each slit position the galaxy profile is shown on the left and the star profile is shown on the right. Therefore there is no significant variation in the line index along the slit due to the telescope-instrument system. Thus any spatial variation seen in the galaxy index is real.

The outlier seen in the profile of SA103-095 in the upper right panel of the figure is due to imperfect flat-fielding of a spot located just above and to the left of the CCD center. It can be seen in the grey scale of Figure 5.8. The blue side band of the Mgb index falls on this region. Because the measured response over corrects this area the blue flux is higher than it should be causing an artificial increase of $EW(Mgb)$. The galaxy equivalent widths are not affected because the Mgb bands are redshifted and, hence, fall in a different location on the CCD. Also, the area affected is 1-2 pixels in size and, hence, only affects small apertures. This aperture in SA103-095 appears to be the only one affected. In future work this problem will be avoided by masking the affected area.

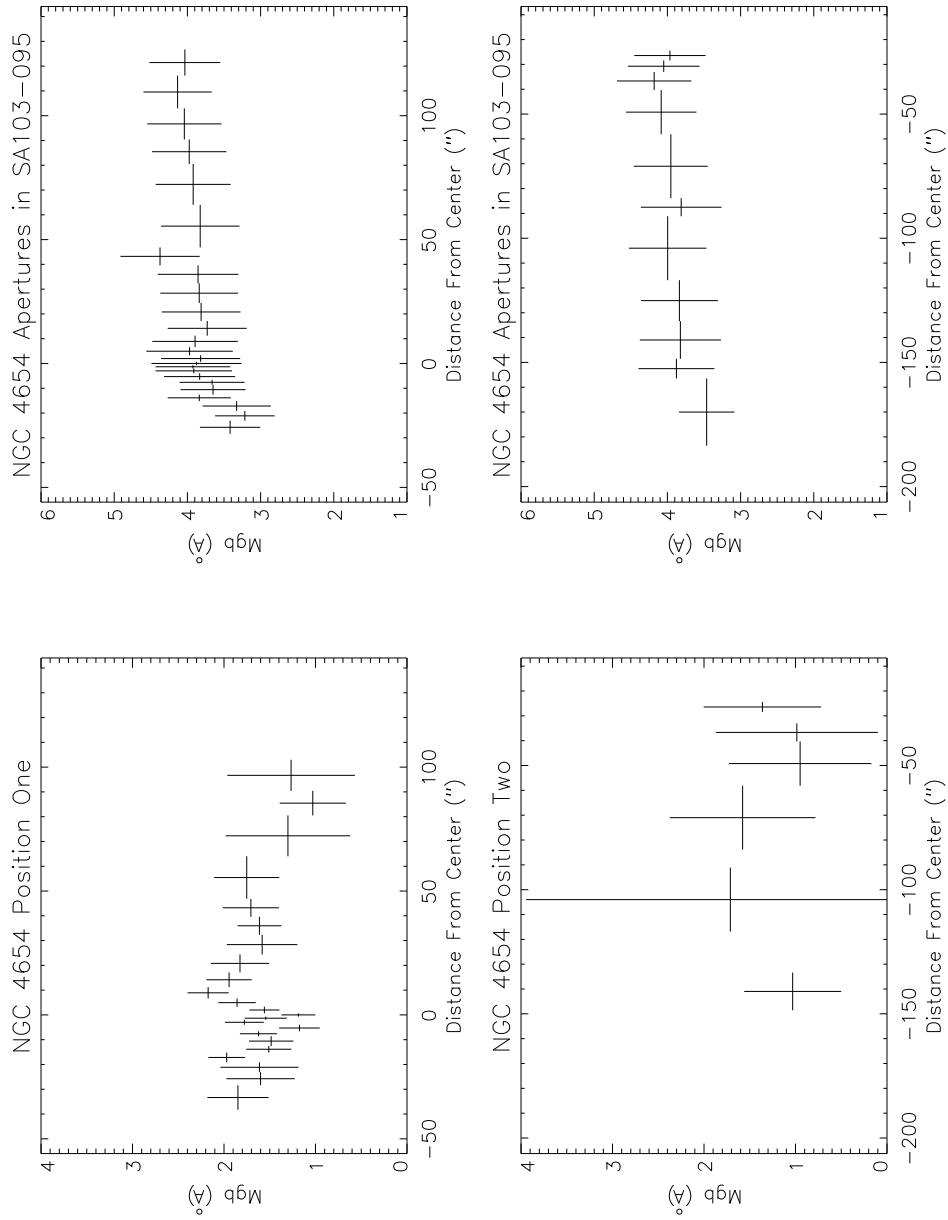


Figure 9.5: Mg b Index Profile for NGC 4654 Positions One and Two: The value of Mg b as a function of position in the galaxy is shown on the left. The value of Mg b along the slit in the star image is shown at right. A significant variation is not seen in the star. Hence the variation in the galaxy is real. The outlier in the profile of SA103-095 in the upper right panel is caused by imperfect flat-fielding of a spot located near the CCD center. Note the galaxy profile is unaffected because Mg b is redshifted to a different location on the detector. See Sections 9.4 and 5.2 for further discussion.

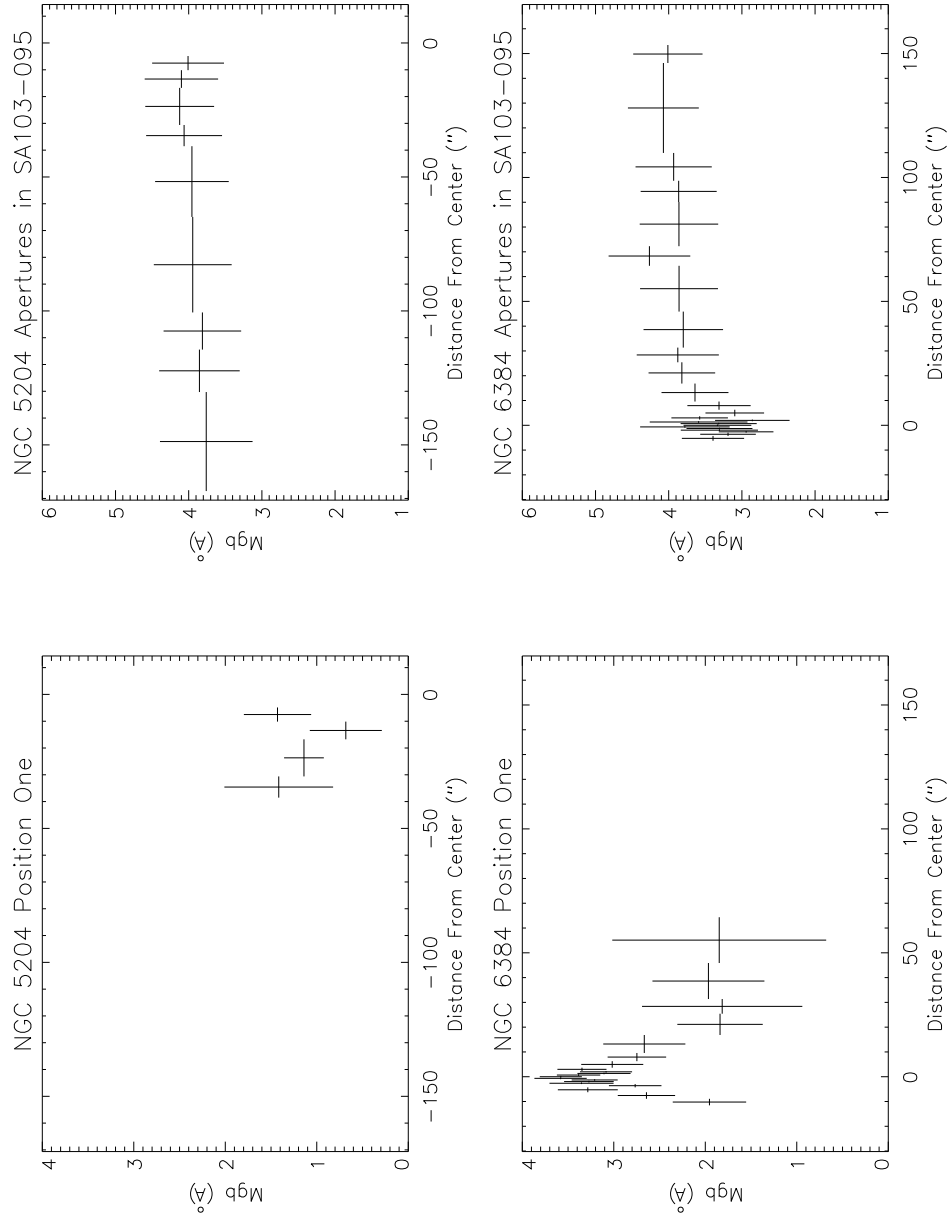


Figure 9.6: Mgb Index Profile for NGC 5204 and NGC 6384 Positions One: The value of Mgb as a function of position in the galaxy is shown on the left. The value of Mgb along the slit in the star image is shown at right. A significant variation is not seen in the star. Hence the variation in the galaxy is real.

9.5 Slit Profile Extraction and Magnitudes

Images taken with different telescopes and instruments do not have the same orientation, resolution, or scale. The orientation of an image will differ because of the telescope mounting, the orientation of the detector relative to the optical axis, the way the image is stored in computer memory, and the number of optical elements in the system. Resolution is determined fundamentally by aperture size or by the longest baseline in the interferometer in a given wavelength band. Because of seeing this fundamental limit is not reached from the ground without adaptive optics. Seeing varies from night to night and location to location. The scale of an image will vary with focal length and detector pixel size. Thus transformations including rotation, translation, and scale must be determined between the longslit, B, and K images. This section explains how the MMT longslit is mapped into the B and K images and addresses the issues of orientation and scale. No attempt is made to correct for seeing or resolution differences.

9.5.1 B Slit Profile Extraction

Recall that the slit position is determined by two points on the finder TV usually the galaxy center and a knot in the galaxy or a field star. This is not accurate enough for comparing positions in the slit with positions in the B image. However, there is a way to ascertain the position of the longslit in the B image. Note that the wavelength range of the spectra include that of the B filter. Thus it is possible to create a B light profile from the spectral image. If the correct profile is extracted from the B image it should closely resemble the profile created from the longslit image. Now it is possible to follow an iterative procedure that extracts the correct profile from the B image.

First the B filter function, [MS63], is used to collapse the longslit image into a one dimensional profile. The filter function is interpolated to match the wavelength spacing in the spectral image. Then the interpolated filter function is multiplied into each column of the spectral image. The product is summed over the wavelength dimension. The result is a one dimensional image of the

galaxy light profile in B. This will be referred to as the B longslit profile. The slit profile extracted from the B image should closely resemble the B longslit profile. By comparing the extracted profile with the B longslit profile the exact position of the slit in the B Image is determined. An iterative procedure that exploits this fact to position the slit in the B image is discussed next.

9.5.2 Iterative Extraction Procedure

An initial guess at the slit position is made interactively. A sample session is shown in Figure 9.7. The slit is positioned by changing its length, width, x position, y position, and position angle. Each adjustment causes a rough slit extraction from the new position to be over plotted on the B longslit profile. After an initial position is settled on it is refined automatically by tweaking the x position, y position, and angle. Generally three steps are made in each parameter for a total of 27 new positions and orientations. Each one is extracted rigorously from the image as defined in the next paragraph.

The longslit aperture is divided into bins in the spatial direction (Section 5.11). The coordinates of the bins are thus known in the spectral image. These coordinates are transformed to the B image. The geometry of the longslit, $2'' \times 3'$, and positions of its bins are converted to pixels using the scale of the image. The software slit is less than a few pixels across. Therefore the extraction must be done rigorously. So, the exact fraction of each B image pixel falling in a bin of the software slit is calculated and the same fraction of the flux in that pixel is added to the bin. The extraction procedure relies on a formula derived from Green's Theorem for the area of an arbitrary polygon [EP82]. A proof is given in Appendix A. Each bin in the software slit overlaps the B image pixels in a set of polygons. Given the geometry of the slit bins and how they overlap the grid of image pixels the polygon vertices are calculated. They are then arranged in counter-clockwise order and their areas determined. The area of each polygon is used to weight the flux in that pixel. The weighted

fluxes are totaled to give the flux in that slit bin:

$$F_{bin} = \sum_{i=1}^n A_{R_i} F_i. \quad (9.19)$$

F_i is the flux in the i th B pixel. A_{R_i} is the area of overlap between a longslit bin and the i th B image pixel.

After each candidate profile has been rigorously extracted it is compared to the B longslit profile. This is done by normalizing the two profiles and plotting them together on the same scale. Sample plots are given in Figure 9.8. From the 27 plots a best is chosen by visual inspection. Then the process is repeated with the new position and smaller step sizes for the three parameters. Again the candidates are plotted. This iterative process continues until it becomes difficult to distinguish between the various candidates. Thus the slit position in the B image is determined. This is done for each slit position.

9.5.3 K Profile Extraction

The iterative extraction procedure cannot be used for the K image because it is not known or expected that the K light profile will match the B profile. Instead a transformation is determined. The transformation takes positions in the B image to the same position in the K image. It is determined from stars and points in the galaxy that are common to both images.

First a scale is determined. A list of positions of objects common to both images is made. The distance between all unique pairs of positions within each image is calculated. Then the ratios, K to B, of these distances between the two images are taken. The average of the ratios is a scale in K relative to B. Using the same set of points a rotation and offset between the two sets are calculated.

The rotation angle is determined by making vectors out of the points (using the first point as the origin). The normalized dot products between the vectors in B to the vectors in K give the cosine of the angle between the two images. The normalized magnitude of the cross products give the sine. The average of the arctangent is used as the rotation angle between B and K.

Table 9.4: B To K Transformation Parameters.

Slit	X (pixels)	Y (pixels)	X Shift (pixels)	Y Shift (pixels)	Scale	Angle ($^{\circ}$)
n4654p1a	242.9	98.4	-215.9	-31.3	0.69738	91.9
n4654p2a	242.9	98.4	-215.9	-31.3	0.69738	91.9
n5204p1a	40.7	37.3	-4.6	148.0	0.69810	94.1
n6384p1a	166.5	128.4	-54.4	87.5	0.69574	91.9

The K coordinates of the points are rotated and scaled. The average shift in x and y is determined between these intermediate K coordinates and the B coordinates. The shifts define the translation between B and K.

The scale, angle, x shift, and y shift are thus determined. Table 9.4 shows the B to K transformation parameters for each slit position. The B slit position is transformed to a K slit position by scaling, rotating, and translating the B slit coordinates into K slit coordinates. Figure 9.9 shows a successful transformation. The X's in the left panel, the B image, and the triangles in the right panel, the K image, show the points used to determine the transformation. The X's in the K image are the positions in B transformed to K. The slit shown in the B image is chosen by the iterative extraction process. The slit in the K image is the transformed position of the slit from the B image. Figures 9.10 and 9.11 show the software slit position in B and K respectively. Within the slit the apertures used for extraction of spectra from the longslit image are shown. In Figure 9.12 the apertures are shown on the B and K profiles. This example is for NGC 4654. Once the profiles have been extracted they are given spatial solutions. A distance in arc seconds from the galaxy center is assigned to each bin in the profile. This will automatically align the B, K, and longslit profiles. Figure 9.13 shows an example of how well the three profiles are aligned for NGC 4654. Interestingly, the K profile does not show the spiral arm as does the B profile. Instead the K profile drops sharply through the region of the arm. This occurs at $35''$ from the center. The K profile is smoother than the B profile because the source of K light is smoother and because of the lower resolution. Note that the spatial information in B-K and E(B-K) will be limited by the resolution of the K image.

9.5.4 Assignment of B and K Magnitudes

Now magnitudes are measured and colors calculated. The longslit aperture boundaries are converted to arc seconds in the B and K extracted profiles. B and K counts in the apertures are summed using partial pixels. Instrumental B and K magnitudes are calculated for each aperture. The photometric solutions determined in Chapters 4 and 6 are applied with one caveat. The B photometric solution involves a $B-R$ color term. $B-R$ is not available for the slit magnitudes. Therefore this term is set to zero. This leads to a small systematic error of at most .1 magnitudes. The color coefficient is 0.09 and $B-R$ would not be more than one magnitude. The error in $B-K$ is dominated by the K zero point and a small shift in $B-K$ to the red will not significantly change the conclusions of this work. Thus B, K, and $B-K$ profiles are obtained for each longslit aperture.

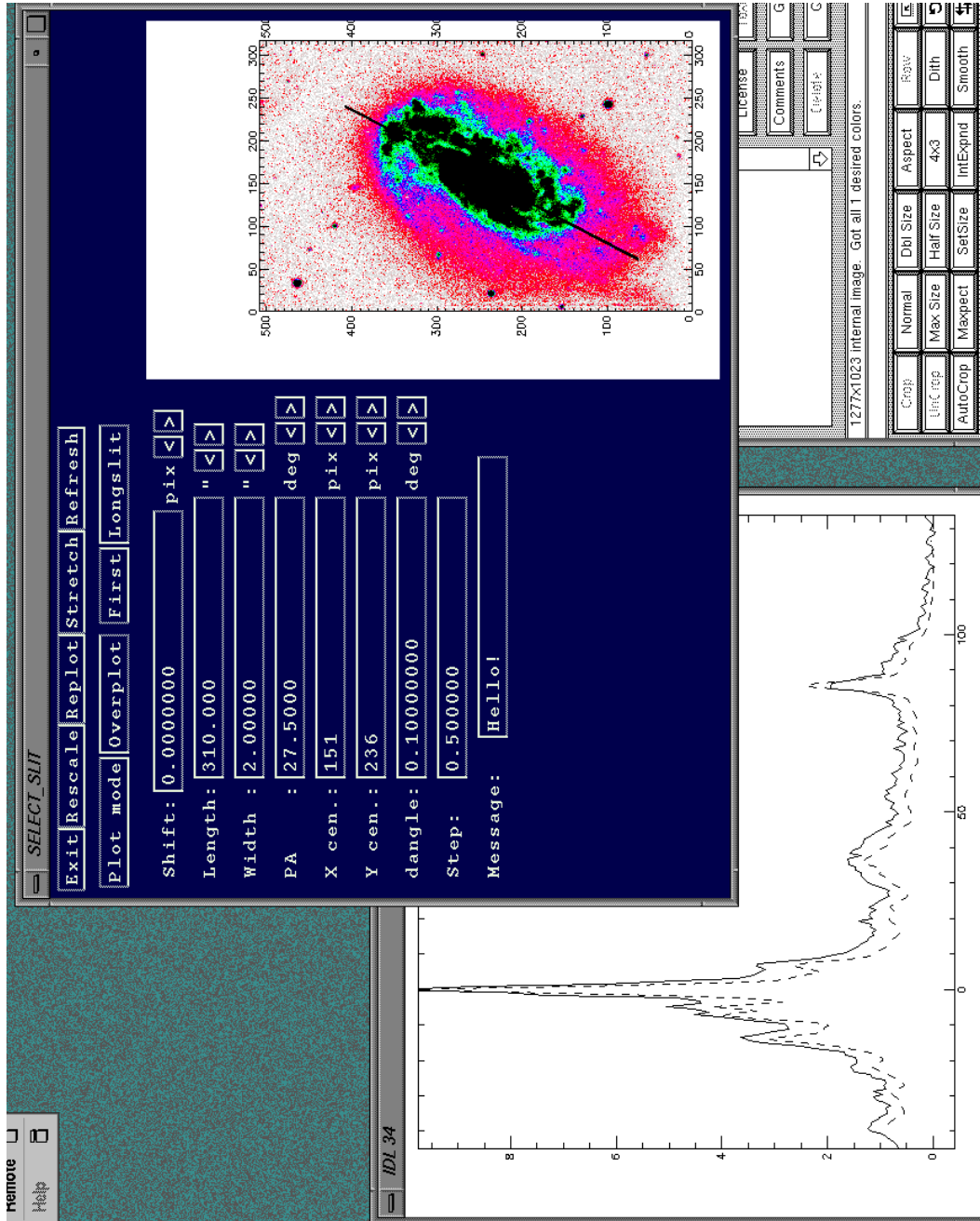


Figure 9.7: Graphical User Interface for Choosing Initial Slit Position: This GUI was developed by the author for the purpose of quickly finding an initial slit position for the iterative extraction technique.

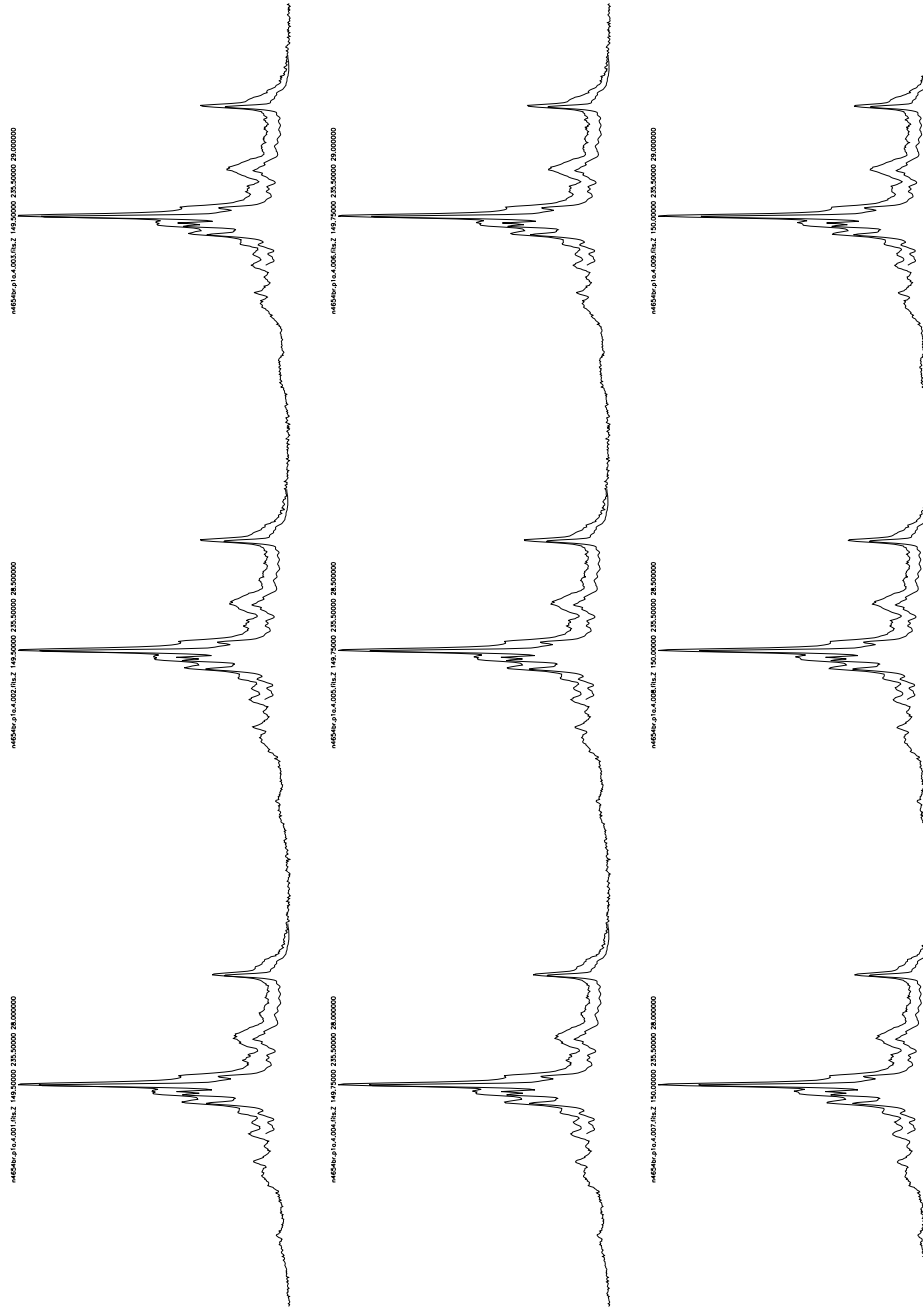


Figure 9.8: Output from Iterative Extraction Procedure for Positioning the Software Slit in B Image: The best match between the B longslit profile and the extracted B profile is chosen by eye. It is input to the next iteration.

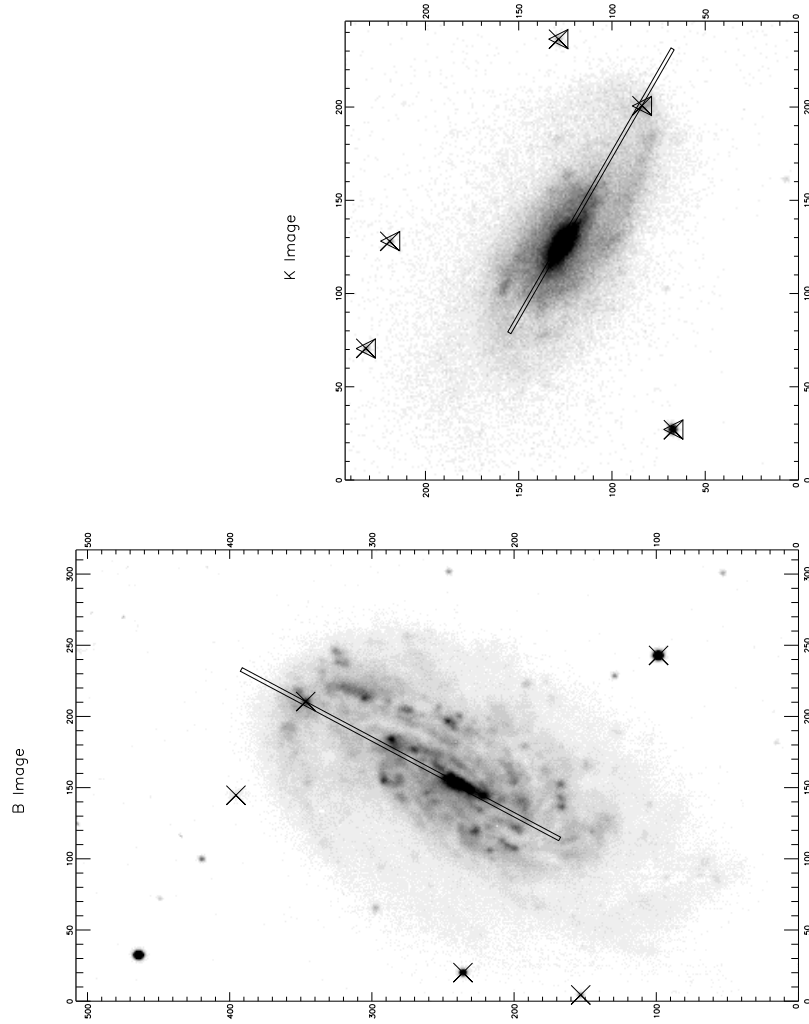


Figure 9.9: B Slit Position Transformed onto K Image: The B image is on the left. K is on the right. The crosses in B and triangles in K mark the objects used to determine the transformation. The crosses in K are the B positions transformed to K. The slit drawn in K is the B slit transformed to K coordinates.

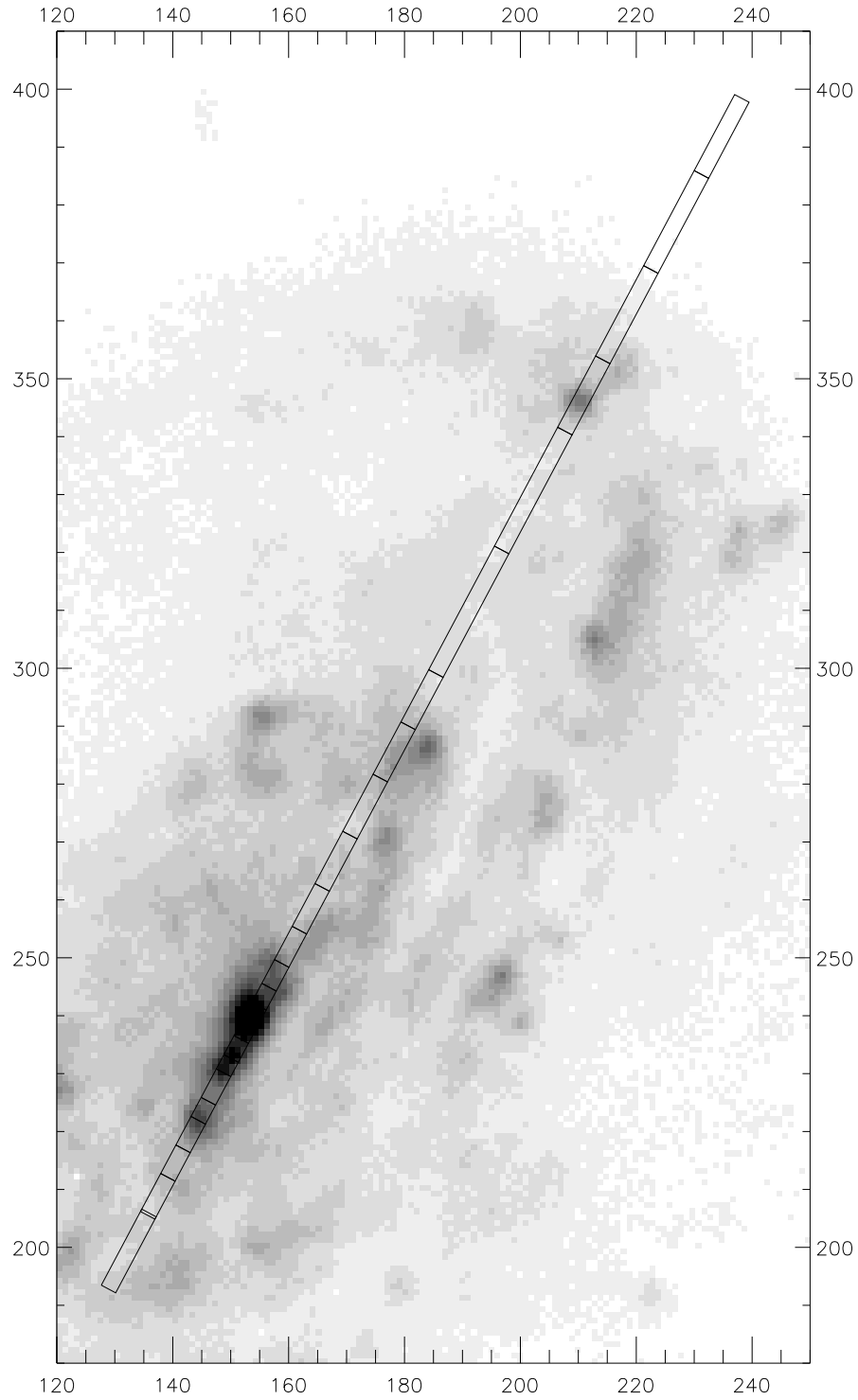


Figure 9.10: Software Slit with Apertures on B Image of NGC 4654: This graphic shows where each spectral aperture falls in the B image. The narrow width of the aperture requires a rigorous extraction procedure when calculating magnitudes. See Section 9.5.2 for full details.

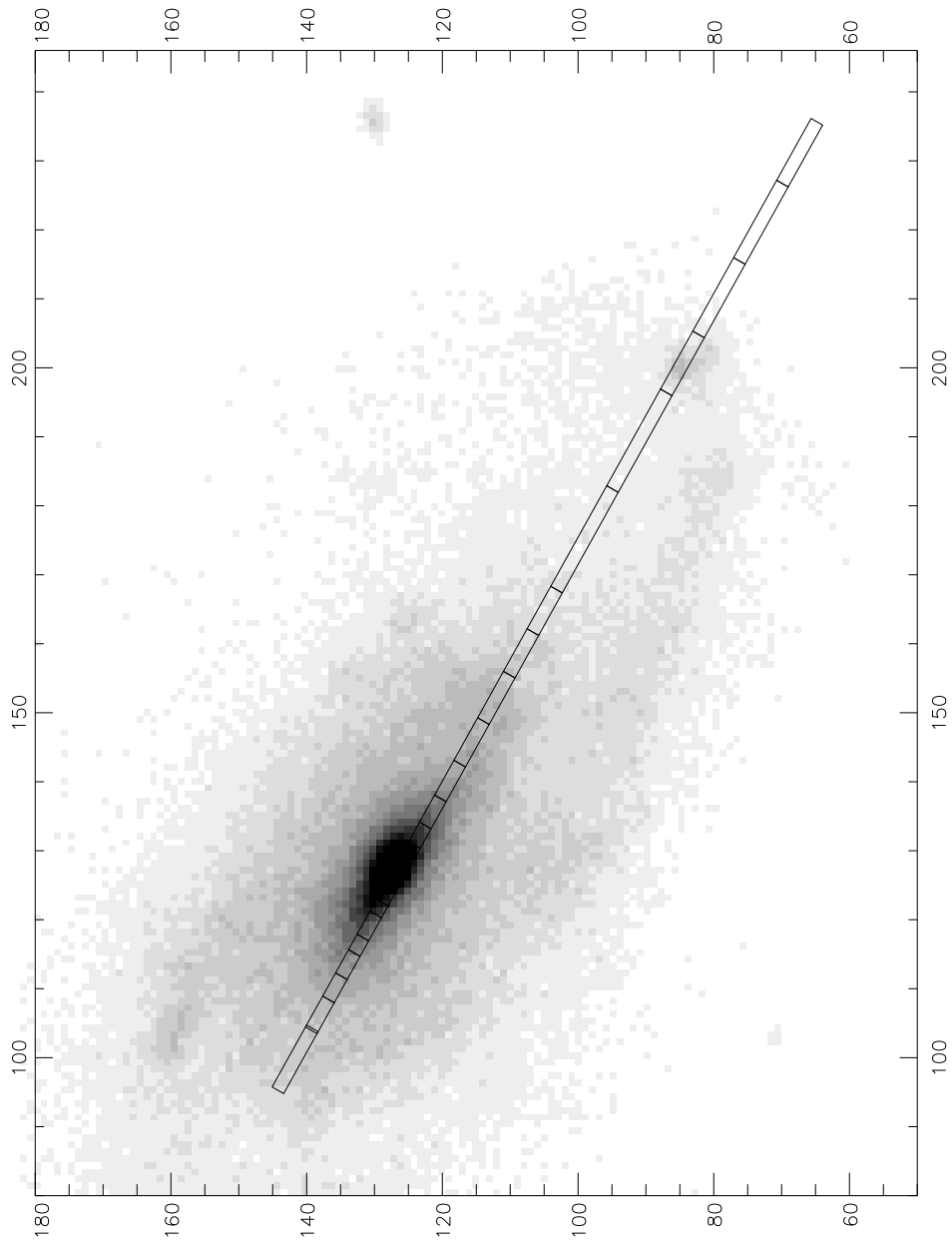


Figure 9.11: Software Slit with Apertures on K Image of NGC 4654: This graphic shows where each spectral aperture falls in the K image. The narrow width of the aperture requires a rigorous extraction procedure when calculating magnitudes. See Section 9.5.2 for full details.

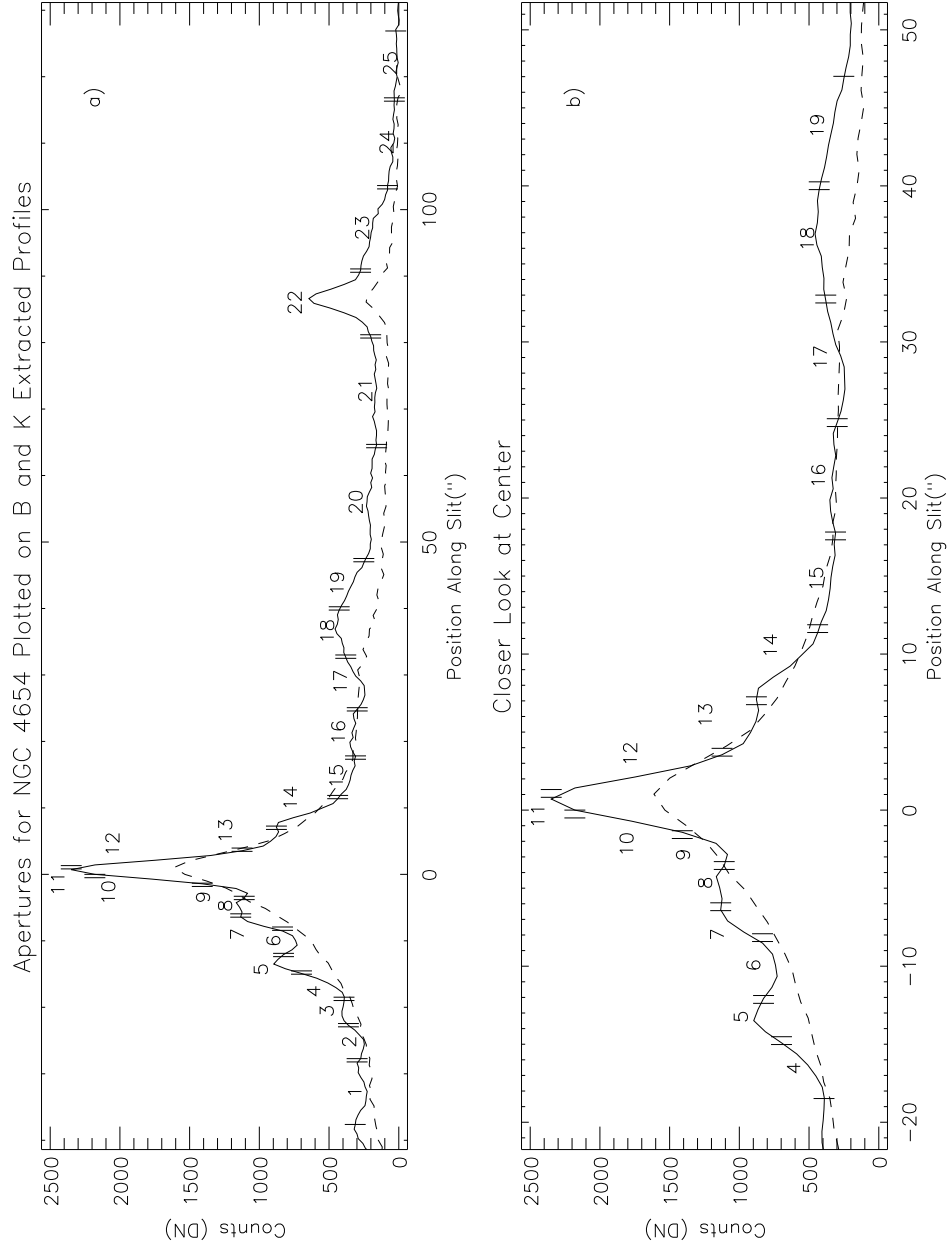


Figure 9.12: Example Longslit Software Apertures Displayed on the Extracted Profiles: a) B and K extracted profiles for NGC 4654. b) Center of the Profiles in a). These correspond to Figures 9.10 and 9.11

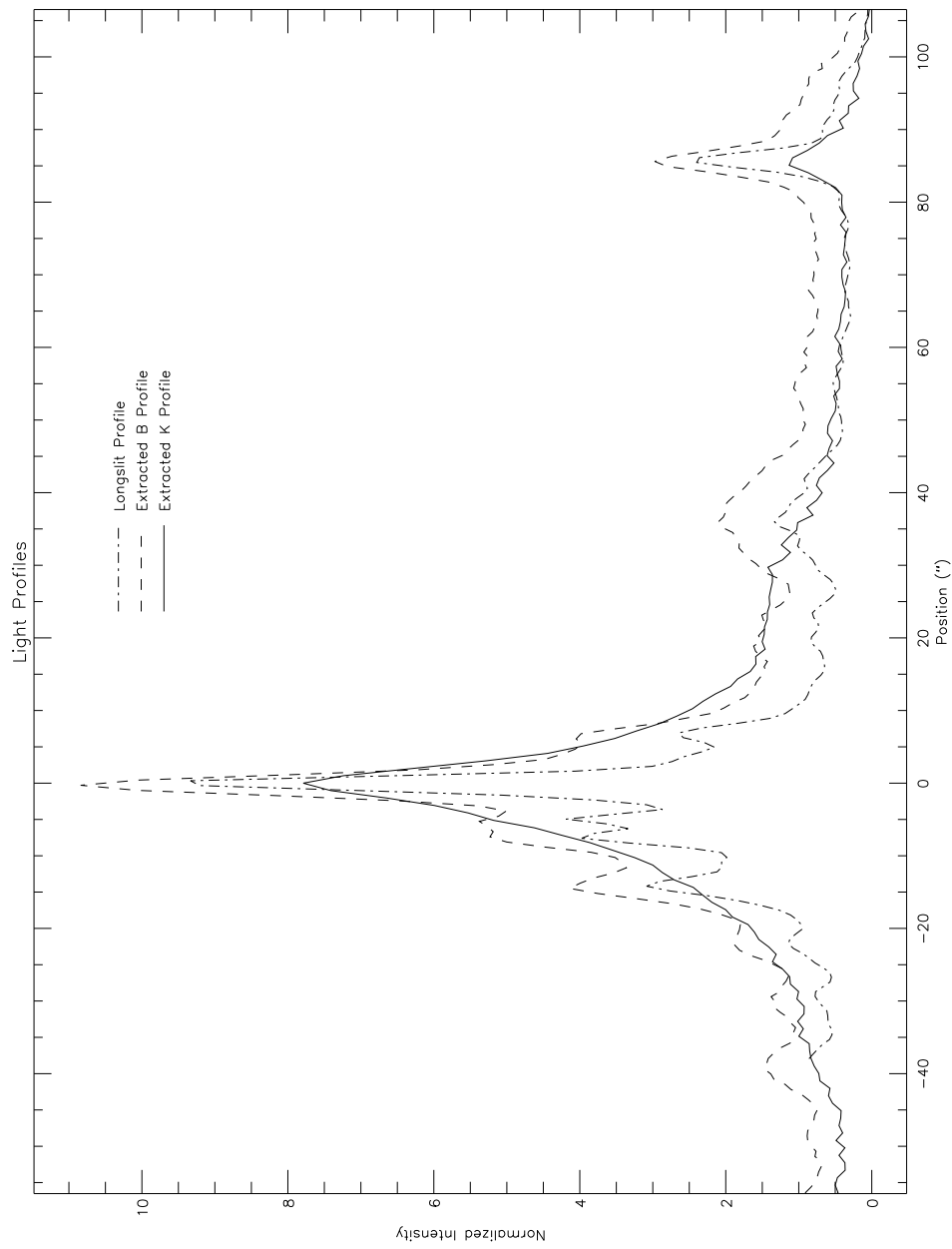


Figure 9.13: The Three Profiles are Aligned in the Spatial Dimension: This shows the B and K profiles aligned and scaled to match the B longslit profile for NGC 4654. Note that the K profile drops sharply through the spiral arm apparent in the B profile starting at 35". Also, the spatial information in $B - K$ and $E(B - K)$ is limit by the K profile.

9.5.5 Galactic Extinction Correction

The magnitudes and colors must be corrected for extinction and reddening due to dust in the Galaxy. Table 2.1 lists the extinction in B for each galaxy. Only the B magnitudes are corrected because the extinction in K is very small. Also the K extinction would have to be determined using a mean extinction curve. The uncertainty in this estimate combined with the error in the K magnitudes overwhelms the correction. Correcting the K magnitudes would simply increase the random error associated with the final color without increasing its accuracy significantly. Thus all the B magnitudes were corrected by the appropriate A_B listed in Table 2.1. The error contributed to the final color is taken as 0.015 as suggested in Burstein and Heiles, [BH84]. This error is added in quadrature with the other errors in B–K. The final B magnitudes and B–K colors with errors are displayed in Table 9.5 for each slit position. The rows in this table match the rows in Table 9.3.

Table 9.5: Observed B and B-K for each Slit Position

NGC 4654 Position One				NGC 4654 Position Two				NGC 5204 Position One				NGC 6384 Position One			
Pos.($''$)	B	Error	B-K	Error	Pos.($''$)	B	Error	B-K	Error	Pos.($''$)	B	Error	B-K	Error	
-32.67	21.36	0.02	4.40	0.17	-34.57	22.38	0.02	4.46	1.47	
-25.08	21.23	0.02	4.58	0.20	-23.68	21.72	0.02	4.14	0.93	
-20.46	20.91	0.02	4.54	0.23	3.55	0.52	-13.45	21.17	0.02	4.04	0.80	
-16.50	20.48	0.02	4.41	0.21	-71.00	23.09	0.02	3.55	0.52	-13.45	21.17	0.02	4.04	0.80	
-13.20	20.10	0.02	4.27	0.23	-49.22	22.83	0.02	3.91	0.33	-7.51	20.88	0.02	4.08	0.67	
-9.90	20.13	0.02	4.55	0.21	-36.68	22.28	0.03	3.95	0.41	
-6.93	19.79	0.02	4.48	0.26	-26.45	21.05	0.02	3.71	0.34	
-4.62	19.79	0.02	4.70	0.24	
-2.31	19.56	0.02	4.69	0.24	
-0.66	19.09	0.02	4.38	0.29	
0.66	19.09	0.02	4.36	0.31	
2.64	19.67	0.02	4.66	0.27	
5.61	20.05	0.02	4.59	0.26	
9.57	20.56	0.02	4.71	0.23	
14.85	21.10	0.02	4.83	0.20	
21.45	21.15	0.02	4.65	0.18	
29.04	21.20	0.02	4.59	0.18	
36.63	20.84	0.02	3.85	0.19	
43.89	21.19	0.02	3.77	0.21	
56.10	21.66	0.02	3.97	0.17	
72.93	21.81	0.02	3.87	0.16	
86.13	20.92	0.02	3.69	0.17	
97.35	21.84	0.02	3.22	0.29	

9.6 Comparing Observations and Models to Constrain Age and Metallicity

Before proceeding with the comparison it is necessary to describe the plotting symbols used to represent the models and data in plots. They are defined in Figure 9.14 which shows the grid of age and metallicity covered by the models in panel a). Each point in this panel represents a stellar population of one age and metallicity. The same IMF is used for the entire grid. The size of the plotting symbol increases with age. The number of vertices in the symbol increases with the metallicity. The age and metallicity represented by a symbol is read from this figure. In panel b) the data plotting symbols are defined. The size of the symbol is proportional to the logarithm of the distance in arc seconds from the center of the galaxy.

At each point in the grid the models predict an $\text{EW}(\text{Mgb})$ and $B-K$. At each point along the slit an $\text{EW}(\text{Mgb})$ and $B-K$ have been measured. It is interesting to examine the model values and measured values of the $\text{EW}(\text{Mgb})$ and $B-K$ color on the same plot as in Figure 9.15 for example. The size of the horizontal error bar on the data points is the size of the error in $B-K$. The size of the vertical error bar is the range in $\text{Log}(\text{EW}(\text{Mgb}))$ due to the error in $\text{EW}(\text{Mgb})$.

Note that the models define a relatively narrow locus in the $\text{Mgb}-B-K$ plane. This locus is highlighted by the shaded region. It includes most of the models and is a clearer representation of the unreddened relationship between $\text{Log}(\text{EW}(\text{Mgb}))$ and $B-K$. In later diagrams only the shaded region is shown for clarity. The models use a Salpeter IMF. Changing the exponent only moves the model locus slightly in the $\text{Mgb}-B-K$ plane. The shape of the relationship does not change significantly. Other IMFs will be used in future work, but it is not expected that the $\text{Mgb}-B-K$ relationship will change significantly. For clarity in many of the plots that follow only the shaded region is shown. The metallicity increases as one moves up this region, and for a given metallicity the age increases as one moves up the locus. However, the models are highly degenerate in this plane. Thus, the observed $\text{EW}(\text{Mgb})$ and $B-K$ with errors overlap multiple populations.

Recall that the Mgb index is not affected by reddening (Section 9.2.4). Therefore, it is not possible to move a point vertically in this diagram by changing the reddening. The reddening vector is horizontal and increases to the right. The vector in the figure represents half a magnitude of reddening.

A plot like this is made for each slit position in the subsample. They are used to discuss the ages and metallicities in the disks in the next chapter. From that discussion it is determined that an estimate of the internal reddening of the disks can be given. This estimate is defined as $E(B-K) \equiv (B-K)_{\text{obs}} - (B-K)_{\text{model}}$. $(B-K)_{\text{obs}}$ and its error are discussed in Section 9.5. The calculation of $E(B-K)$, $(B-K)_{\text{model}}$, and their errors is described in the next section.

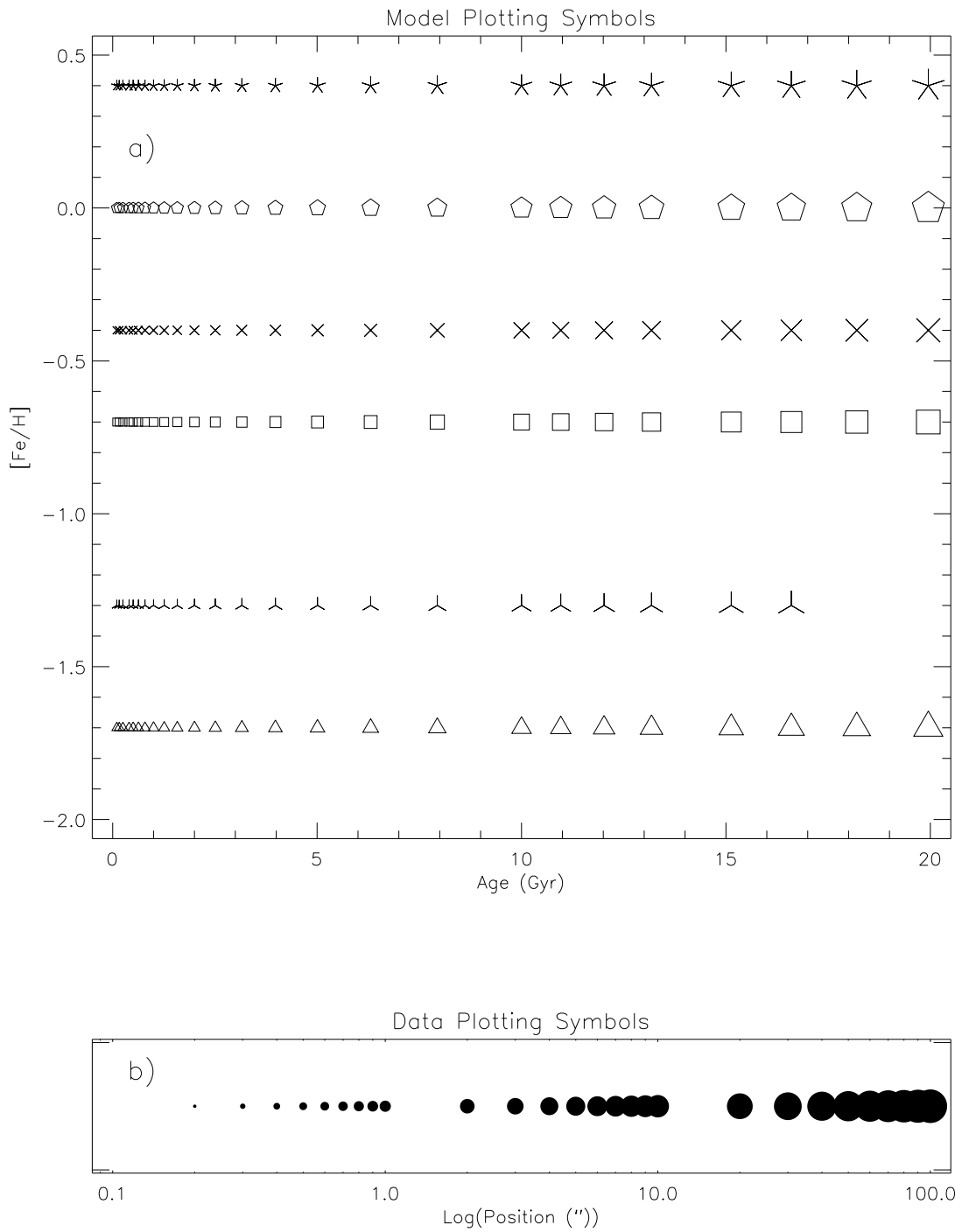


Figure 9.14: Plotting Symbols for Models and Data: a) This is the grid of age and metallicity covered by the models. Each point represents a stellar population of one age and metallicity. The same IMF is used for the entire grid. The number of vertices increases with metallicity. The size of the symbols increases with age. b) Symbols for the data increase in size as distance from galaxy center increases.

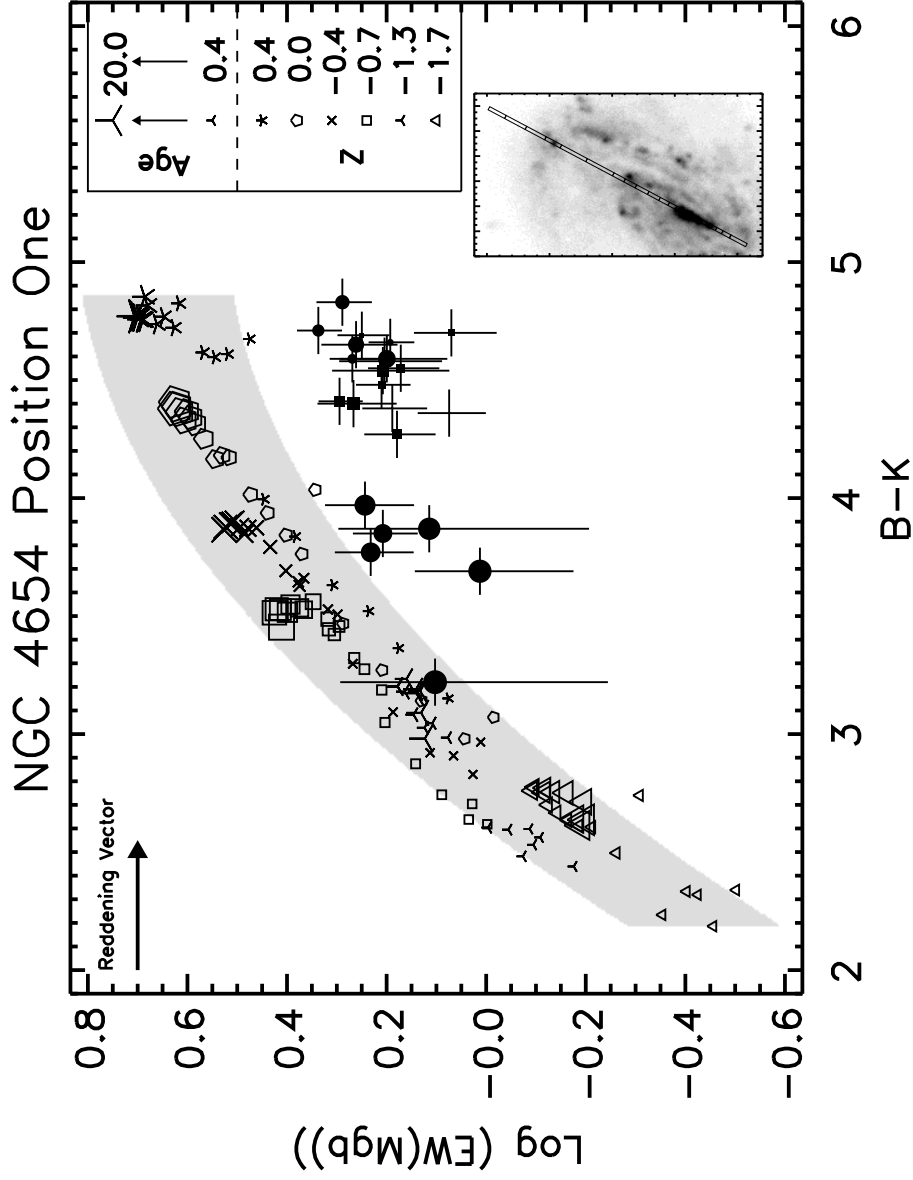


Figure 9.15: Example of Plot used to Analyze Age, Metallicity, and Internal Reddening of a Spiral Disk: The plotting symbols are defined in Figure 9.14. The vector in the upper left represents half a magnitude of reddening. There may be a slight change in population toward but overall the data do not follow the model relationship indicating that the data is reddened. The center is redder than the disk. The data do not match very old metal rich populations or very metal poor populations of any age. They overlap metal poor populations of any age and young metal rich populations. More discussion can be found in Section 10.1.

9.7 Combining Observations and Models to Estimate Internal Reddening

For a given value of $\text{Log}(\text{Mgb})$ there is a range in model color. For each SSP a value of $B-K$ is calculated by interpolating at the observed Mgb . The extrema of the interpolated SSP colors are taken as the range in model color for that value of Mgb . The error in Mgb implies a range in $\text{Log}(\text{Mgb})$. A model range in $B-K$ is determined for the high and low values of $\text{Log}(\text{Mgb})$. The minimum to the maximum of the three ranges is taken as the range in $(B-K)_{\text{model}}$. The middle of this range is quoted as the value of $(B-K)_{\text{model}}$. Half the range is taken as the error in $(B-K)_{\text{model}}$.

Figures 9.16 and 9.17 show an example of the above procedure for calculating $(B-K)_{\text{model}}$. In Figure 9.16 the dot represents the logarithm of the measured Mgb value. The vertical line represents the range in dex due to the error in Mgb . The horizontal dashed lines intersect the model curves at $\text{Log}(\text{Mgb})$ and the minimum and maximum of the range in $\text{Log}(\text{Mgb})$. The bold horizontal lines show the ranges in the model color for these values of $\text{Log}(\text{Mgb})$. The range in $(B-K)_{\text{model}}$ is taken as the minimum to maximum of the three ranges shown. $(B-K)_{\text{model}}$ is taken as the center of this range. The horizontal line in Figure 9.17 represents the reddening, $E(B-K)$. The uncertainty in $E(B-K)$ is the error in $(B-K)_{\text{obs}}$ and the error in $(B-K)_{\text{model}}$ added in quadrature. If the range in $\text{Log}(\text{Mgb})$ extends beyond the model range then that measurement is not used to calculate an effective reddening. This procedure is followed for each bin in every aperture. Results are presented in the next chapter.

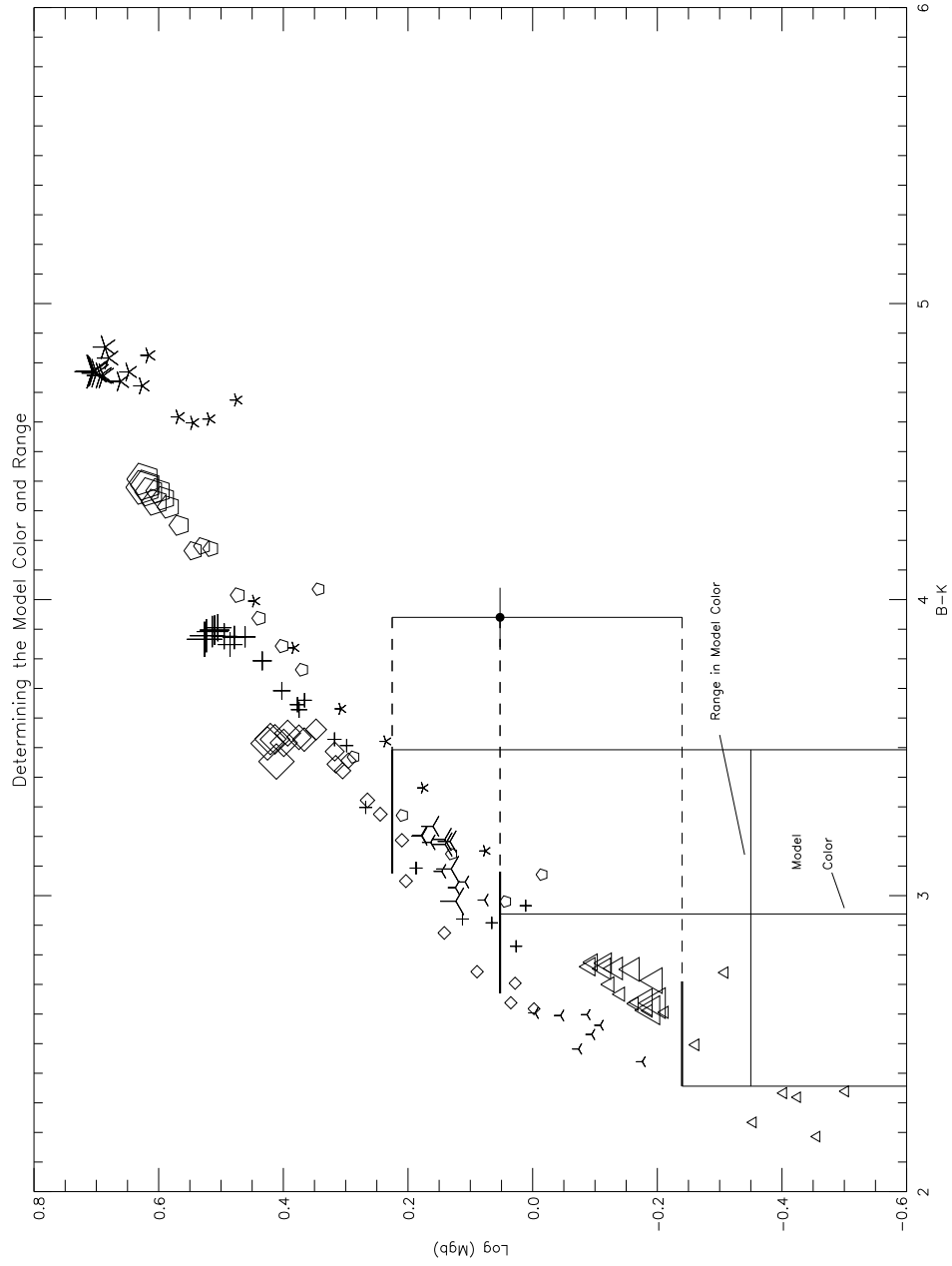


Figure 9.16: Example of How Model Color and Range in Model Color are Determined: This figure shows one observed value of $\text{Log}(\text{Mgb})$ with error bars. The dashed lines show where the observed $\text{Log}(\text{Mgb})$ intersects the models. The bold lines are the range in $(B-K)_{\text{model}}$. The vertical lines show the limits of the range in $(B-K)_{\text{model}}$.

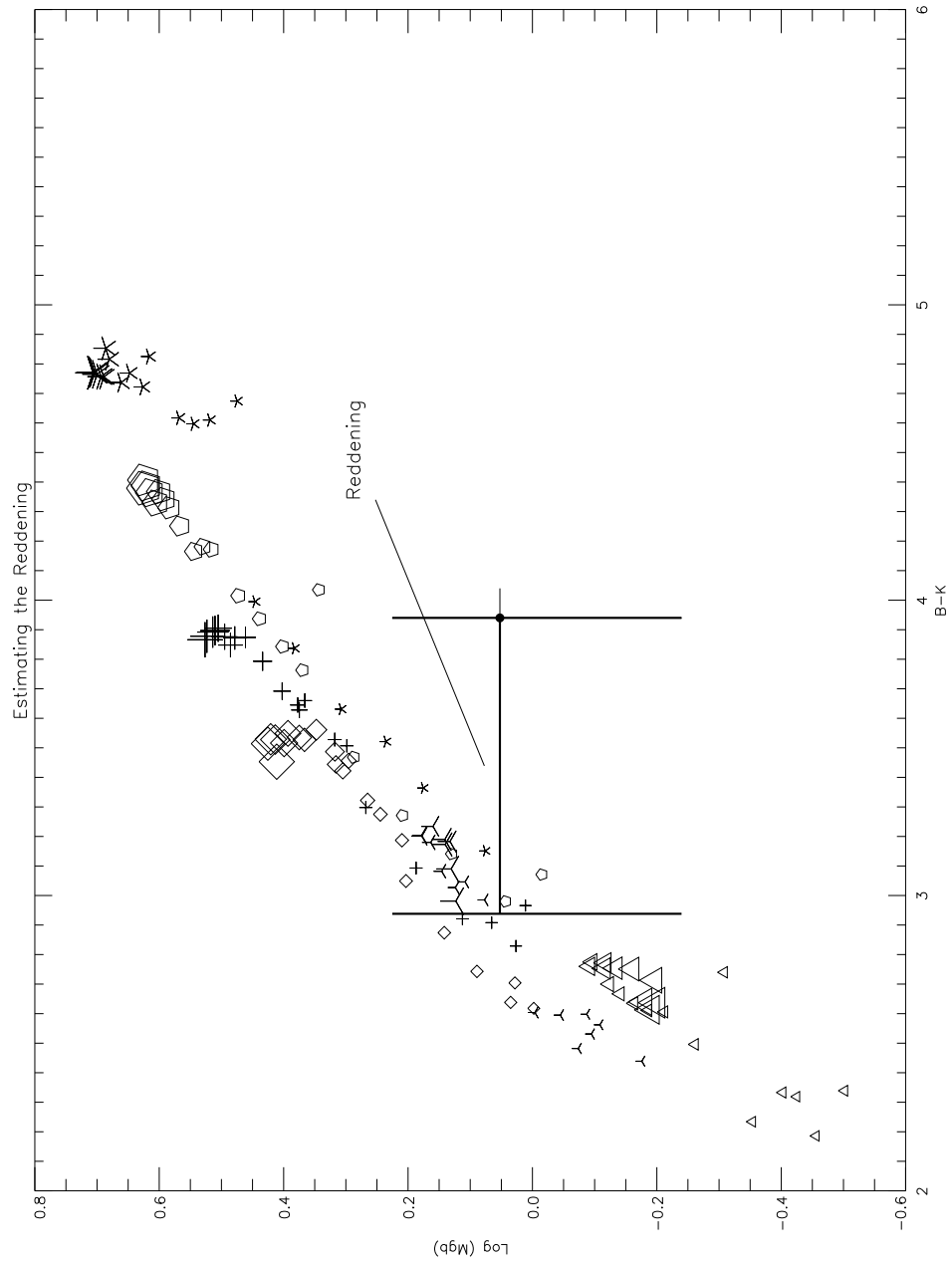


Figure 9.17: Example of How Reddening is Estimated: The length of the horizontal line is the value of $E(B-K)$.

CHAPTER 10

RESULTS AND CONCLUSIONS

This chapter begins by analyzing the Mgb and B–K profiles and the $\text{Log}(\text{EW}(\text{Mgb}))$ versus B–K plots. Then summary plots are introduced and used to discuss population constraints and internal reddening. The results of the processes described in Chapter 9 are in the summary plots. Each galaxy slit position is discussed. Conclusions are drawn and future work is itemized.

10.1 Results

10.1.1 Color Gradients

The cause of color gradients within the subsample galaxies is now discussed. First the Mgb and B–K profiles are shown and discussed for each slit position. Then the observed relationship between the Mgb and B–K is examined for NGC 4654 position one and NGC 6384.

In Figure 10.1 the Mgb profile is shown in the upper panel and B–K in the lower panel. The B longslit profile (Section 9.5.1) is inserted in the bottom panel for reference. The Mgb profile appears to be approximately flat indicating that the stellar population is not changing. The B–K profile obviously becomes suddenly bluer at the location of the spiral arm near $35''$ from the center. Inside the arm and outside the arm B–K is approximately constant. Since the population is constant it cannot be the cause of the change in B–K. The most likely cause is a change in the amount of reddening due to dust.

NGC 6384 position one provides a very different example. The profiles are shown in Figure 10.2. In the inner parts of this galaxy Mgb and B–K appear to change together implying that a change in population causes the change in B–K. The color becomes redder towards the center. In its outer disk Mgb is constant while B–K becomes bluer as the distance from the center increases. Therefore,

this color change must be due to a decrease in the amount of reddening.

The signal in the K image of NGC 5204 is weak, and the profiles yield only three good measurements. They are shown in Figure 10.3. No significant gradient in either Mgb or $B-K$ is measured. NGC 4654 position two suffered similar problems. In addition the slit position was not well determined because the galaxy center was not in the slit. So, as seen in Figure 10.4, there was only one point available for performing the iterative extraction technique. These profiles yield only two measurements. Therefore, NGC 4654 position one and NGC 6384 will be the focus of the remainder of this chapter.

To determine the observed relationship between Mgb and $B-K$ the data are plotted in the Mgb- $B-K$ plane as in Figure 10.5. The size of the plotting symbol increases with distance from center of the galaxy. The reddening vector is horizontal and increases to the right. The shaded region represents the model relationship between Mgb and $B-K$ as discussed in Section 9.6. The two clusters of points are separated by the spiral arm as discussed above. In this plot there is a small spread in $\text{Log}(\text{EW}(\text{Mgb}))$ while $B-K$ ranges over two magnitudes. Since $\text{EW}(\text{Mgb})$ measures the population and is independent of reddening and since the data do not follow the unreddened model relationship the previous result, that the population remains constant while $B-K$ depends on changes in reddening, is confirmed. Within each cluster of points the color is constant, but between the two clusters the color differs. The inner group is redder than the outer group.

The same plot for NGC 6384 is shown in Figure 10.6. Clearly, in the inner parts of this galaxy Mgb and $B-K$ are related. This implies that the color becomes redder toward the center because of changes in the population. However, some part of this change could be due to reddening i.e. reddening could change the slope of the relationship between Mgb and $B-K$. Yet, the data follow the model relationship as represented by the shaded region, although they are shifted to the right a small amount. This indicates that the inner regions suffer a constant reddening, if any, and that the changes in color are due solely to the population becoming older and/or more metal rich. Just

the opposite happens in the outer parts of this galaxy. Here the data obviously do not follow the model relationship. Mgb remains constant while $B-K$ becomes bluer moving outward in the disk. As the models represent the unreddened relationship between Mgb and $B-K$ this change in color must be due to a decrease in reddening moving outward in the disk.

All the data for the four slit positions is shown in Figure 10.7. This is the same diagram as above except different slit positions are represented by different plotting symbols, and the error bars have been removed for clarity. The data from NGC 4654 position two and NGC 5204 fall in the same region as the data for NGC 4654 position one. The outer regions of NGC 6384 also fall there. Only the inner regions of NGC 6384 stand out because they follow the model relationship and have significantly stronger Mgb. Its populations are older and/or more metal rich than the others. This is the only field galaxy of the three. Perhaps it is different because of its different environment. Furthermore, recall that these three galaxies were selected by their $B_T-H_{0.5}$ colors. NGC 6384 is the reddest of the three with $B_T-H_{0.5} = 2.37$ while NGC 5204 is the bluest at 1.17. NGC 4654 is in the middle at 2.01. Although NGC 5204 and NGC 4654 have the larger difference in $B_T-H_{0.5}$ they have similar internal character. NGC 6384 has a very different internal character but is closer to NGC 4654 in $B_T-H_{0.5}$ than NGC 5204. Thus, it is not clear what the global color indicates.

If the color gradient in NGC 4654 is due to reddening then it may also be correlated with the location of dust lanes. However, in Figure 10.8 this does not appear to be the case. The left panel in this figure shows where the slit apertures are located in the B image. The dust lanes are assumed to be the fainter parts of the disk. The right panel in this figure shows the slit apertures again with each aperture labeled with its Mgb and $B-K$ values. One arbitrarily chosen contour from the B image is also shown for reference. A similar diagram is shown for NGC 6384 in Figure 10.9 except the B image is in the top panel and the Mgb and $B-K$ values in the lower panel. Also in the lower panel only the average values are shown for the very center of NGC 6384 because of crowding. A change in reddening occurs in the outer parts of this galaxy. Comparing the two panels in both figures, it

does not appear that the variations in $B-K$ match the apparent dust lanes in the B images. One possible explanation is that the dust causing the reddening in these galaxies is smoothly distributed and the effect of the non-uniform distribution of dust is not measured. Recall however that the apertures used in the slit were not chosen to match the dust lanes. The relatively large apertures may average out the effects of clumped dust. Another possibility is that the fainter parts of the disk are faint because of a lack of star formation not because of an increase in the amount of dust.

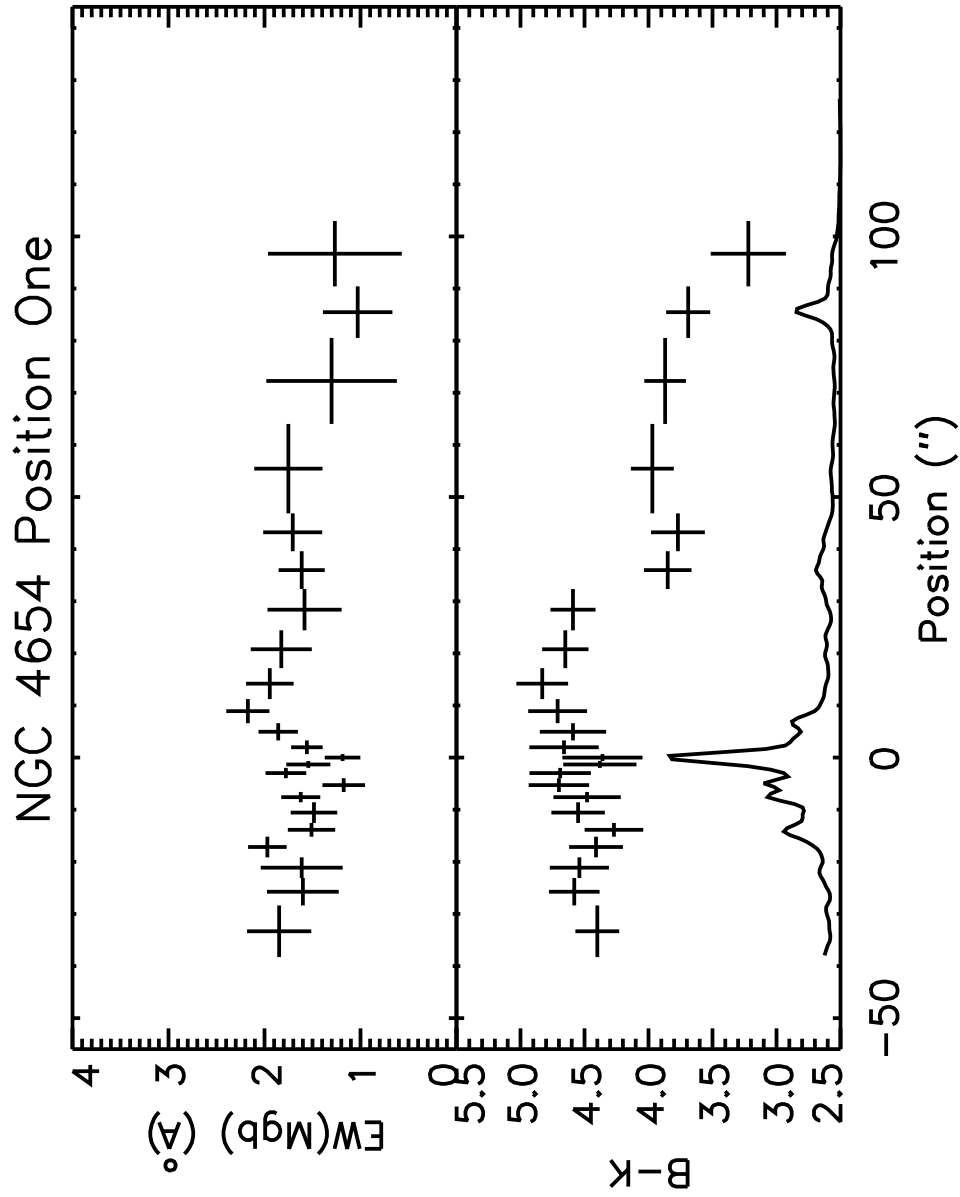


Figure 10.1: NGC 4654 Position One Mgb and B-K Profiles: The Mgb profile is flat while B-K suffers a step change at the position of the spiral arm (35"). This implies the change in color is due to a change in reddening not population.

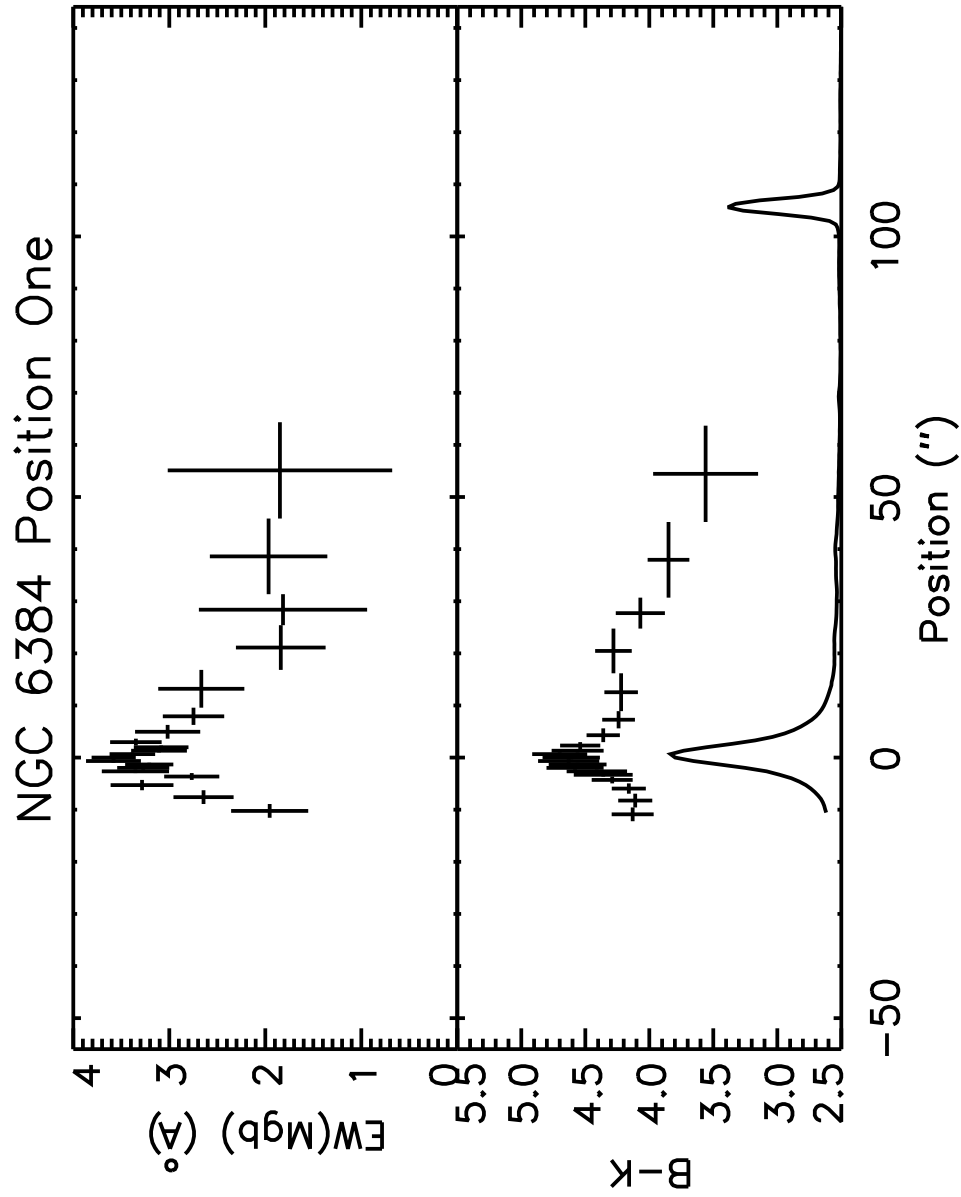


Figure 10.2: NGC 6384 Position One Mgb and B-K Profiles: Mgb and B-K change together in the inner parts of this galaxy. This implies the change in color is due to a change in population. In the outer parts Mgb remains constant as B-K becomes bluer moving outward. This implies the change in color is due to a decrease in reddening.

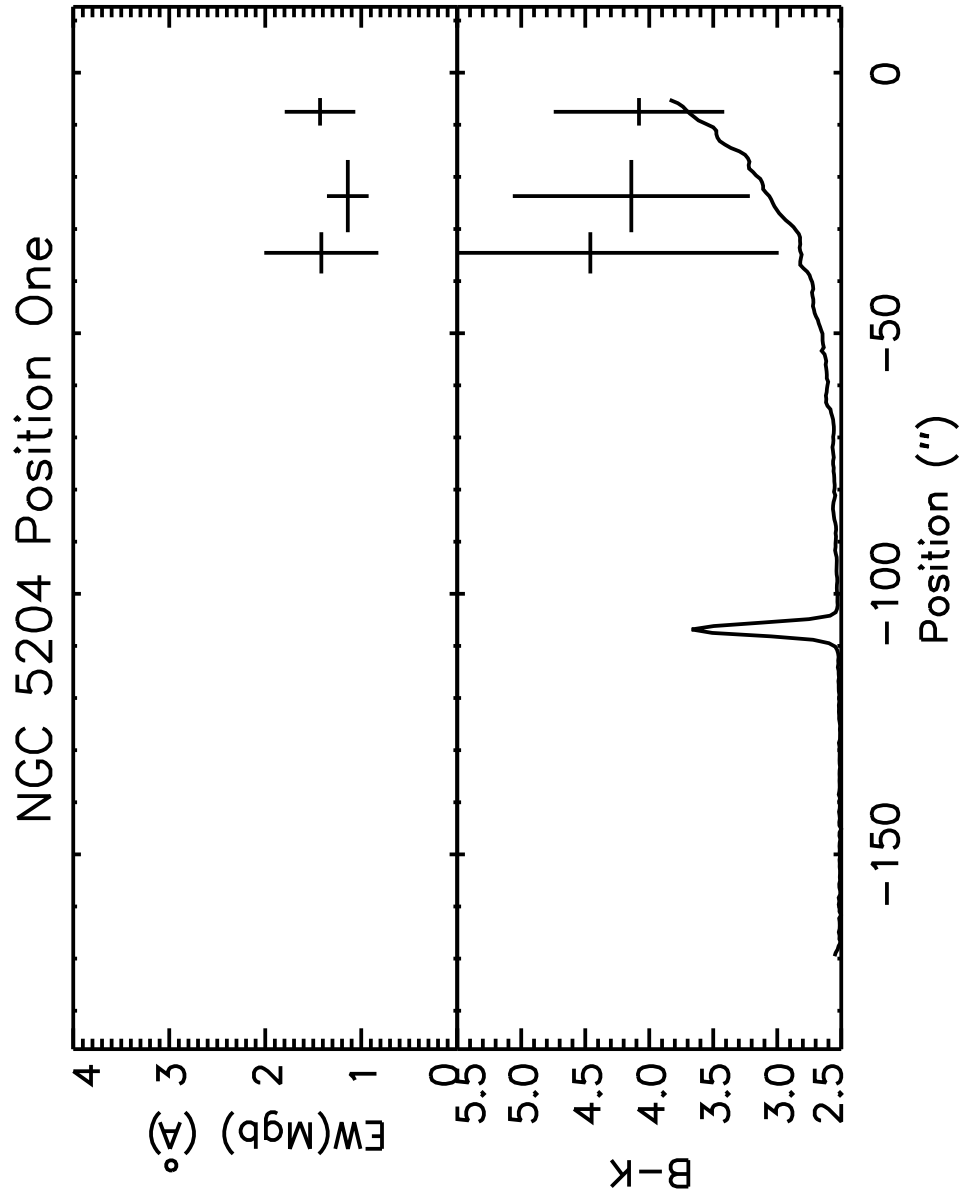


Figure 10.3: NGC 5204 Position One Mgb and B – K Profiles: Due to the weak signal in K only three points are measured in these profiles. No gradients are detected.

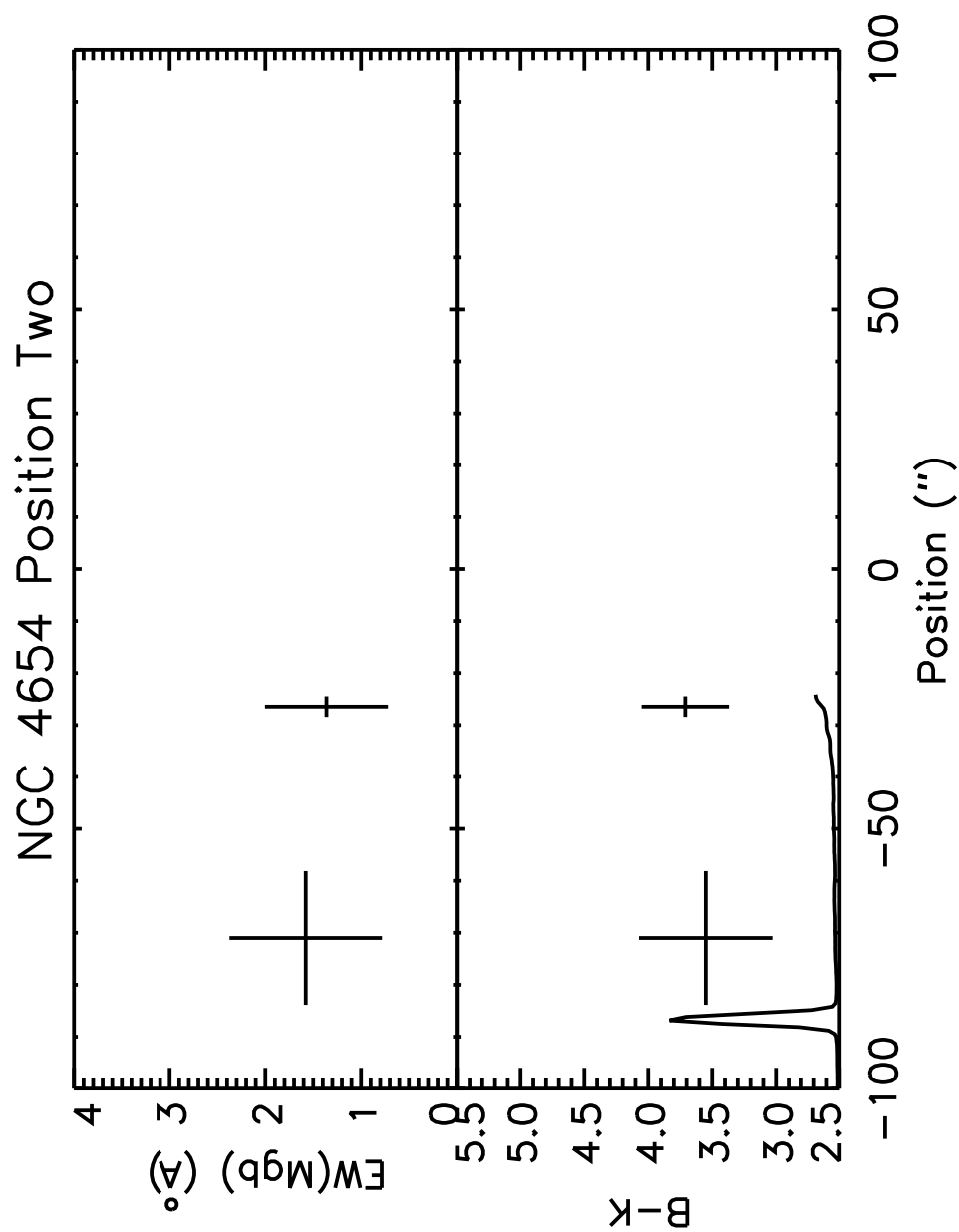


Figure 10.4: NGC 4654 Position Two MgB and B – K Profiles: Due to low signal only two points are measured in these profiles. They are in agreement with the measurements in position one.

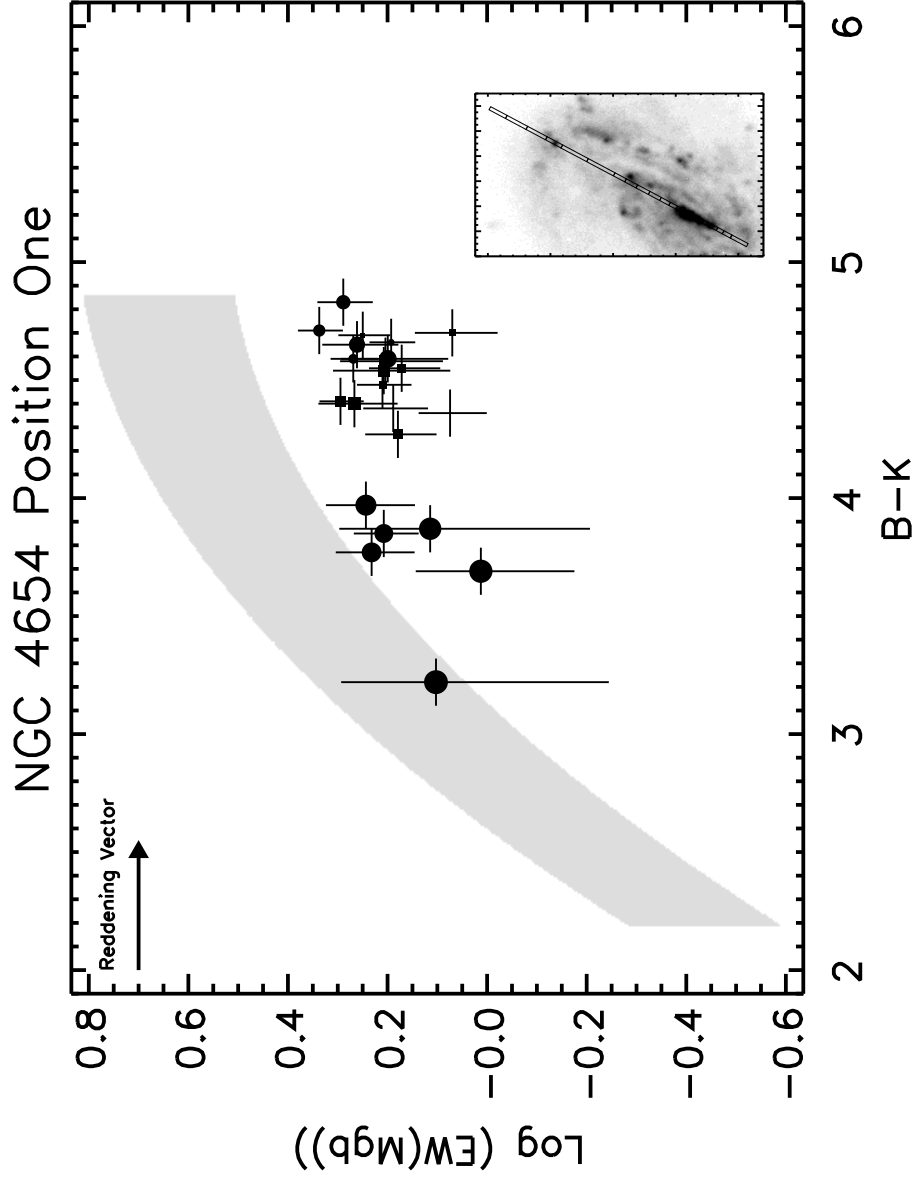


Figure 10.5: Observed Relationship between Mgb and B-K in NGC 4654 Position One: The plotting symbols become larger as distance from center increases. The shaded region represents the unreddened model relationship between Mgb and B-K. The data clearly do not follow this relationship. Mgb remains constant while B-K ranges over 2 magnitudes. This implies the change in color is due to a change in reddening. See Section 10.1.1 for further discussion.

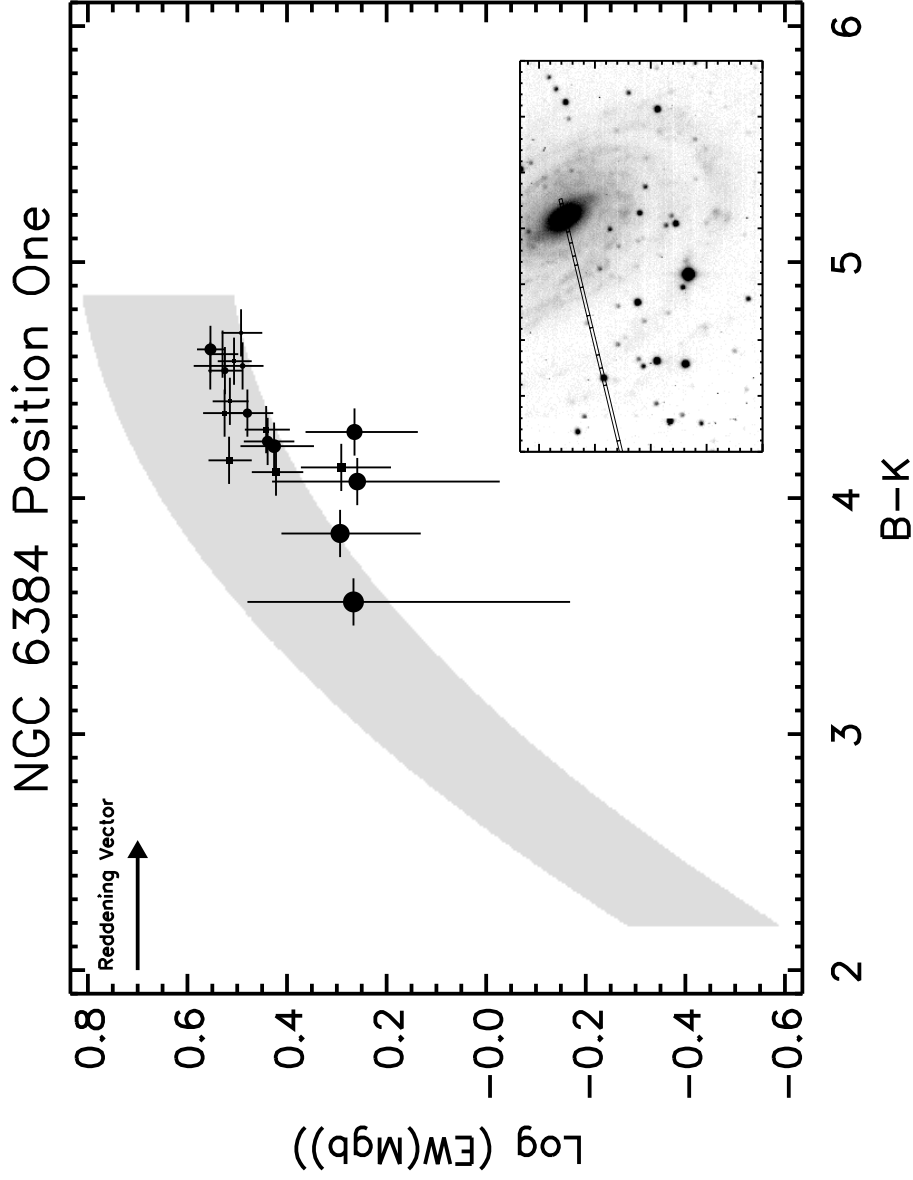


Figure 10.6: Observed Relationship between Mgb and $B-K$ in NGC 6384 Position One: The plotting symbols become larger as distance from center increases. The shaded region represents the unreddened model relationship between Mgb and $B-K$. The data from the inner regions follow the model relationship closely. Although they may suffer a constant reddening, the change in color is due to change in population. It becomes redder toward the center as the population becomes older and/or more metal rich. The outer regions do not follow the model relationship. Hence the change in color is due to a change in reddening. The reddening decreases with radius.

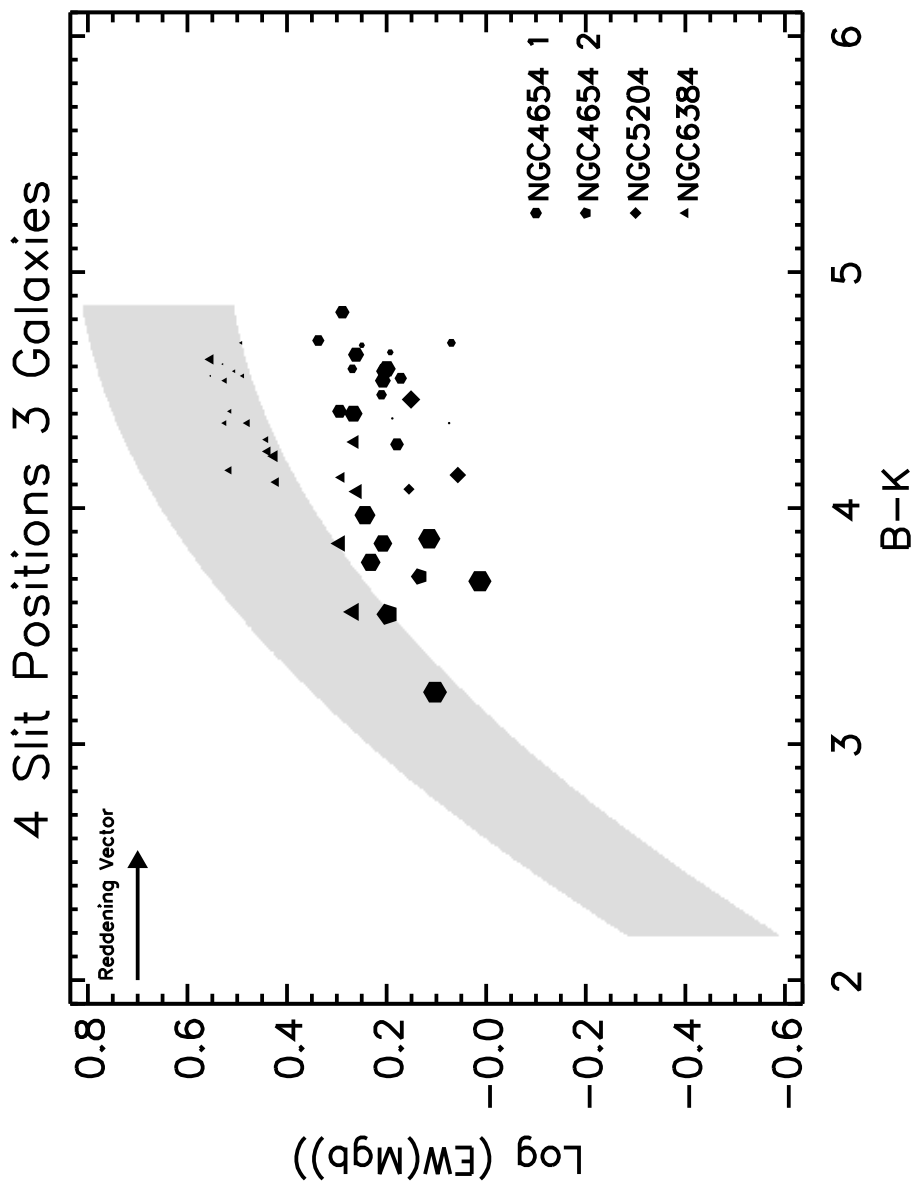


Figure 10.7: Four Slit Positions in Three Galaxies: The plotting symbols become larger as distance from center increases. The shaded region represents the unreddened model relationship between Mgb and B-K. Different slit positions are represented by different plotting symbols. The data from NGC 4654 position two and NGC 5204 fall in the same region as the data for NGC 4654 position 1. The outer regions of NGC 6384 also fall there. Only the inner regions of NGC 6384 stand out because they follow the model relationship and have significantly stronger Mgb. This is the only field galaxy of the three. Perhaps it is different because of its different environment.

Figure 10.8: Apparent Dust Distribution, Mgb, and B-K in NGC 4654: a) This panel shows a grey scale of the B image with the software apertures. b) This panel shows the same region of the image with the same apertures. There is one arbitrary contour drawn from the B image for reference. Each aperture is labeled with its Mgb value and B-K. The changes in Mgb and B-K are not correlated with the apparent dust lanes. The changes in Mgb and B-K are smoother.

NGC6384

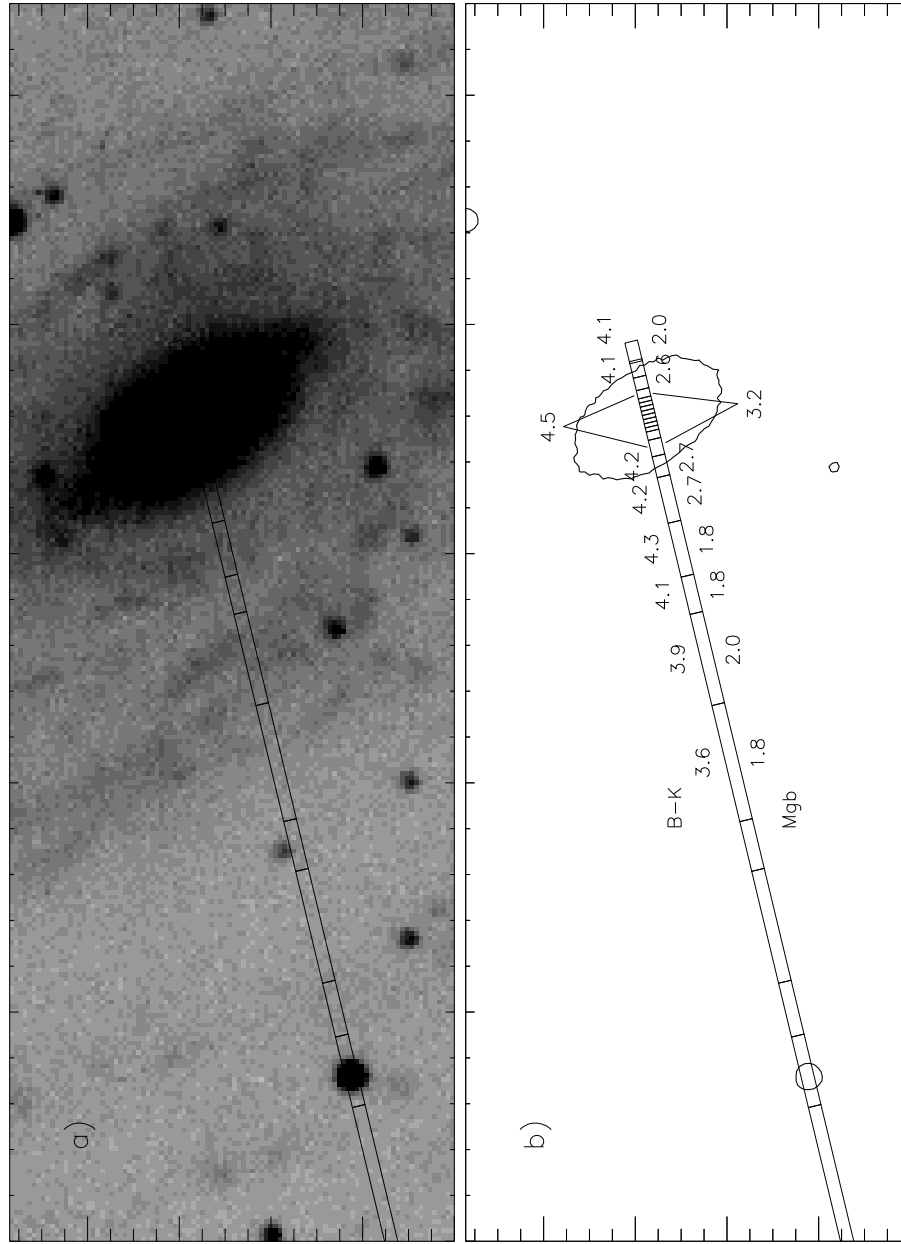


Figure 10.9: Apparent Dust Distribution, Mgb, and B-K in NGC 6384: a) This panel shows a grey scale of the B image with the software apertures. b) This panel shows the same region of the image with the same apertures. There is one arbitrary contour drawn from the B image for reference. Each aperture is labeled with its Mgb value and B-K. In the center of the galaxy the average Mgb and B-K are shown. The changes in Mgb and B-K are not correlated with the apparent dust lanes. The changes in Mgb and B-K are smoother.

10.1.2 Constraints on Stellar Population and Internal Reddening

A summary figure is created for each slit position. The summary figure contains the following information. In panel a) the B image is displayed as a grey scale. The scale is chosen to show the disk of the galaxy. The contours are from the K image and are chosen arbitrarily to match the grey scale. The location of the extracted slit is shown as well. The purpose of this panel is to show that the B and K images are aligned, that the extracted slit is properly located, and to serve as a visual reference when examining the other panels. Panel b) of the summary figure shows the three profiles. The vertical scale is arbitrary. The purpose of this plot is to show that the profiles were properly extracted and aligned and to compare the B and K profiles. Panel c) shows all models and data in the $\text{Log}(\text{Mgb})-(\text{B}-\text{K})$ plane. The plotting symbols are defined in Figure 9.14. This is the same figure as in the previous section but without the shaded region. As age increases the plotting symbol size increases. As the metallicity increases the plotting symbol gains more vertices. Note that the models are highly degenerate in this plane forming a well defined locus. However, it is still possible to distinguish extremes in age and metallicity. Panel d) gives the results of the procedure described in Section 9.6 for combining the models and the observations to estimate the internal reddening along the slit. The horizontal axis is position along the slit. The points are estimates of $E(\text{B}-\text{K})$ for each aperture in the slit.

Examine panel c) for each slit position. Notice that for all slit positions the observations fall to the red side of the models. It is argued above that the discrepancy between $(\text{B}-\text{K})_{\text{model}}$ and $(\text{B}-\text{K})_{\text{obs}}$ is due to the internal reddening of the galaxy. In further support of this argument note that the models cover all ages and metallicities. Thus, there is no missing simple stellar population (SSP) to account for this shift. Second a population made with a combination of SSPs will fall on the same locus in the $\text{Log}(\text{Mgb})-(\text{B}-\text{K})$ plane [O'C82, FTGW94]. So a combination of ages or metallicities will not account for this shift. The later stages of stellar evolution not included in these models are not likely to produce populations with such red colors for a given line index. Also it is not

expected that changing the IMF will change significantly the relationship between Mgb and B-K. Given that the models work well for ellipticals [Gon93, CWB96, TFWG00] which have little or no dust it is concluded that $(B-K)_{\text{model}}$ is too blue because dust is neglected. So if the model colors give the correct intrinsic color for the populations and the line index is unaffected by reddening then the difference between the observed and model colors is due to the internal reddening of these spirals. It is this line of reasoning that supports the definition of $E(B-K)$ as $(B-K)_{\text{obs}} - (B-K)_{\text{model}}$ and the procedure given in Section 9.6.

Figure 10.10 is the summary plot for NGC 4654 at slit position one. Panel b) shows for this slit position in this galaxy that the K profile is significantly different from the B profile. The smoothness of the K profile relative to the B profile is due to the intrinsic smoothness of the K light distribution and the lower resolution of the K image. The inner spiral arm in the B profile is not evident in the K profile. Instead there is a significant drop in K at the location of the arm in B. This difference is seen in the bottom panels as well.

Constraints are placed on the age and metallicity of the stars contributing to the integrated light of NGC 4654 at this slit position. The horizontal shift is due only to internal reddening. Ignore it and consider only how the observed $\text{Log}(\text{Mgb})$ overlaps the models. It is seen that the overlap ranges from about -0.1 dex to 0.4 dex. Because of the degeneracy of the models it is easier to start with populations that do *not* contribute to the integrated light. Above 0.4 are found the old metal rich populations. These are older than 5 Gyr with $[\text{Fe}/\text{H}]$ from solar to 0.4. At the opposite extreme below -0.1 are the very metal poor populations ($[\text{Fe}/\text{H}] < -1.5$) of all ages. These do not appear to contribute to the integrated light of NGC 4654 at this slit position. However, without applying a population fitting technique a confidence limit cannot be assigned to this inference. Also, just because a population is not detected in the integrated light does not mean that it does not exist in the galaxy observed.

The data overlap the remaining populations. These include the metal poor populations ($[\text{Fe}/\text{H}] \approx$

-1.3) of all ages, intermediate metallicity populations ($-1.3 < [\text{Fe}/\text{H}] < -0.7$) of young and intermediate age (< 8 Gyr), and the metal rich (solar to 0.4) and very young (< 1 Gyr) populations. A single line index and single color can not be used to determine which of these populations dominates the integrated light. Any one of these or a mixture of them can reproduce the observed values of Mgb.

There appears to be the slightest of gradients in Mgb along the slit. It is perhaps 0.1 dex larger for the inner points than the outer most points. The gap in $(B-K)_{\text{obs}}$ that occurs near 4.1 coincides with the spiral arm and drop in the K profile. It does not coincide with the change in Mgb.

Inspection of panel d) reveals a significant change in the reddening. The inner parts of the galaxy suffer more reddening than the outer parts. From the figure the center is about 1.3 magnitudes redder than the models. In the outer disk it is roughly 0.5 magnitudes redder than the models. The change of 0.8 magnitudes occurs abruptly at the inner spiral arm. $E(B-K)$ is approximately constant on either side of the arm. The outer most point does not suffer any reddening.

NGC 4654 is a member of the Virgo cluster. It is interacting with the intragalactic medium [PM95]. Perhaps this accounts for the interesting reddening profile. However, the 160 micron and 360 micron maps of [SDH⁺89] are smooth out to just over one arc minute.

Figure 10.11 shows the summary plot for the second slit position in NGC 4654. This spectrum yielded fewer good measurements than in position one. The points it did yield have a much larger uncertainty. The results are very similar to the those for the first slit position. In panel c) it is seen that the observed Mgb overlaps the models in the same general region. Thus no very old metal rich or very metal poor populations contribute to the integrated light. It comes from the population or mixture of populations of metal poor stars of all ages and younger to intermediate age populations of all metallicities. There is a spread in the estimated internal reddening that supports the variation seen in the first slit position. The amount of reddening is the same as in position one.

Figure 10.12 is the summary figure for NGC 5204. This galaxy has a significantly lower surface brightness than the other two. Thus the spectroscopy yielded only four reasonable measurements of

Mgb. These four points overlap the models in the same region as in NGC 4654 with the uncertainty in one measurement reaching down to the old very metal poor population. The observed colors are about 1 magnitude redder than the model colors. No gradient is detected along the slit.

The internal reddening of NGC 5204 has been estimated by [FP83]. In order to match the IUE spectrum of NGC 5204 with OB stars they required an $E(B-V)$ between 0.1 and 0.2. This corresponds to an $E(B-K)$ of between 0.4 and 0.75 using the extinction curve of [SM79]. This is in agreement, within the uncertainties, with the value derived in this work.

Figure 10.13 is the summary figure for NGC 6384. This galaxy is different from NGC 4654 and NGC 5204 in that the populations contributing to the integrated light are more metal rich and older. In addition the populations vary within the galaxy. The observed $\text{Log}(\text{Mgb})$ ranges from 0.25 dex to 0.55 dex. Five of the data points from the outer part of NGC 6384 overlap the models that are metal poor (between $[\text{Fe}/\text{H}] \approx -0.7$ and -0.4) and younger to intermediate age and that are solar and above in $[\text{Fe}/\text{H}]$ but very young. Examining the inner disk of the galaxy the data overlap populations that are more metal rich (> -0.8 or -0.5) and older (> 5 Gyr) and that are more metal rich (up to solar) and young (< 5 Gyr). This trend continues to the center of galaxy with the very old and metal poor (≈ -0.4) populations and the solar metallicity old populations (≈ 10 Gyr). Note that metal rich (≈ 0.4) populations > 5 Gyr old are still excluded as are the very old solar populations. Thus it appears that the populations contributing to the integrated light of NGC 6384 at this slit position vary. They are younger and more metal poor in the outer portions of the disk tending to be older and more metal rich towards the center. Not being able to determine which populations are dominating at a give $\text{Log}(\text{Mgb})$ it is not possible to make a quantitative evaluation of the gradient.

Again data points are shifted to the red from the model locus in panel c). In this case the shift is significantly less than in NGC 4654 and NGC 5204. Indeed the observations of the center of NGC 6384 fall on top of the young solar metallicity points in the $\text{Log}(\text{Mgb})$ - $B-K$ plane. Thus for the center the results are ambiguous. There may or may not be significant internal reddening of the

center of NGC 6384. For the rest of the disk there is a definite shift of $(B-K)_{\text{obs}}$ relative to the models. For the inner disk it is constant at ≈ 0.5 magnitudes. For the outer disk there is a jump in $E(B-K)$ to ≈ 1 . It then decreases to zero in a linear fashion over $50''$.

This result is in agreement with [PLP⁺92, PBCV92] who examined color index profiles to conclude that the stellar populations of NGC 6384 become older and more metal-rich towards the nucleus. Although they did not find a gradient in the disk, [PLP⁺92] did comment that the disk of NGC 6384 is reddened by dust. Their conclusion that the overall extinction of NGC 6384 is not significant is in agreement with the result found here that it falls much closer to the model locus than do NGC 4654 and NGC 5204. NGC 6384 was in the sample of [CSZ⁺] who used HST optical-near-infrared colors to determine that the nuclei of exponential bulges contain young (≈ 1 Gyr) unobscured populations. Young populations in the center of NGC 6384 are not ruled out in this work. This is not in conflict with the [CSZ⁺] result.

Tully and Fisher, [TF77], discovered a well defined relationship between spiral galaxies' absolute magnitudes and HI velocity dispersions, which they introduced as a new method for determining distances. In addition, the Tully-Fisher relation is the edge on projection of the Fundamental Plane of galaxies into the luminosity-velocity dispersion plane [DD87, BBFN97]. Understanding why some galaxies fall above or below the Fundamental Plane, i.e. have large Tully-Fisher residuals, will not only improve distance determinations but will shed light on the connection between the internal and global properties of galaxies. The Tully-Fisher residuals, kindly provided by David Burstein, for NGC 4654, NGC 5204, and NGC 6384 are -0.004, 0.050, and -0.281 respectively. NGC 6384 has a significant residual and is also the only one of the three to show a significant radial gradient in stellar population. It also has the smallest central internal reddening estimate but the larger reddening gradient in the outer disk. NGC 4654 has a constant reddening in the outer disk. A gradient in NGC 5204 is not detected. However, no conclusion can be drawn at this time because it is known that the NGC 4654 and NGC 5204 residuals are small because they have small peculiar velocities.

NGC 5204 and NGC 4654 are cluster galaxies while NGC 6384 is in the field. NGC 4654 belongs to Virgo and interacts with the intragalactic medium [PM95]. NGC 5204 is a member of the M101 group and has a very warped disk [SCD96]. Perhaps the differences in the internal properties of NGC 4654 and NGC 6384 are accounted for by their different environments.

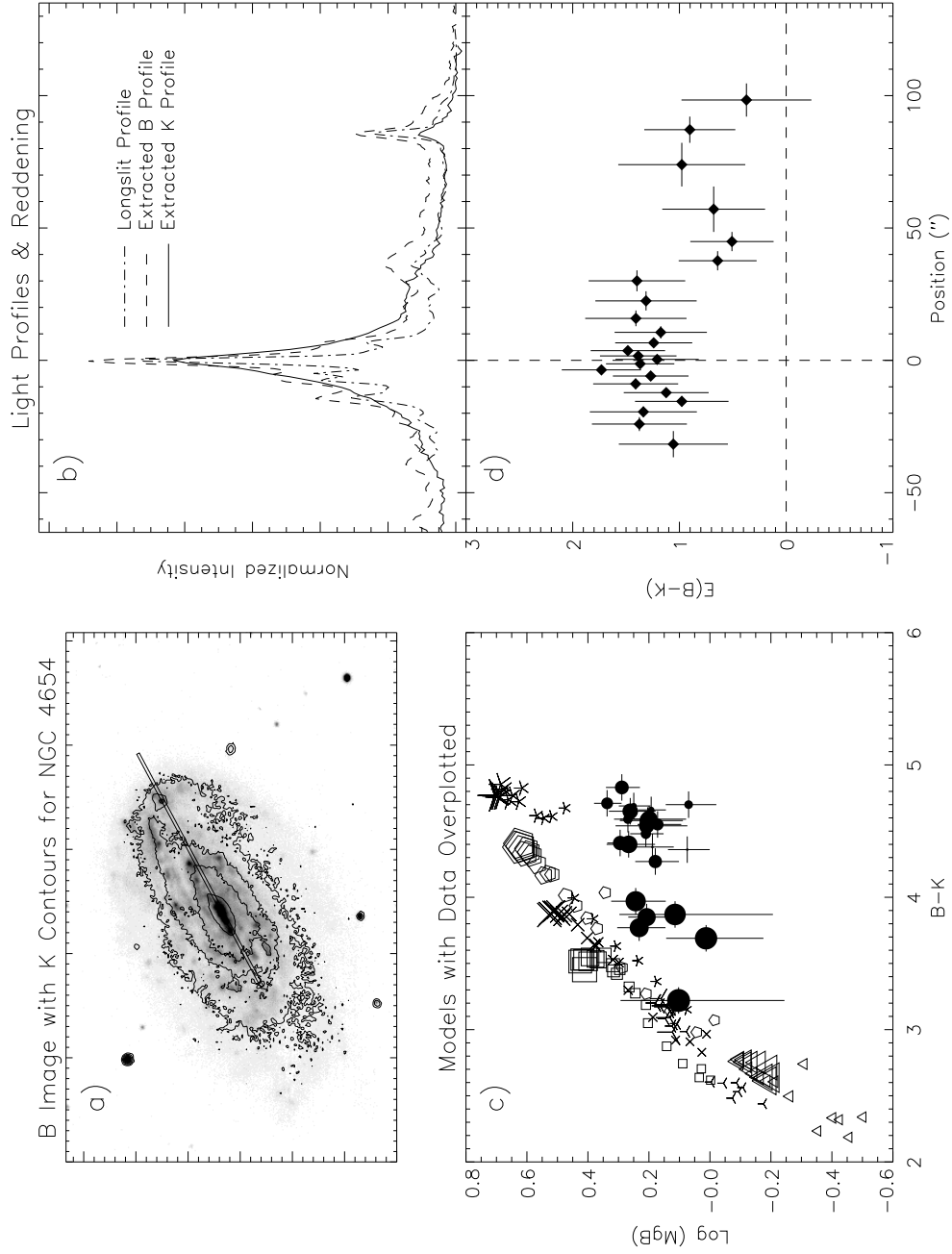


Figure 10.10: Summary Figure for NGC 4654 Position One: a) The slit position. B image with K contours b) B & K extracted profiles aligned with B longslit profile c) Models represented by lines with symbols, including all ages & metallicities. Data represented by filled symbols with error bars. d) Reddening decreases outward. Marginal population gradient. See text for detailed discussion.

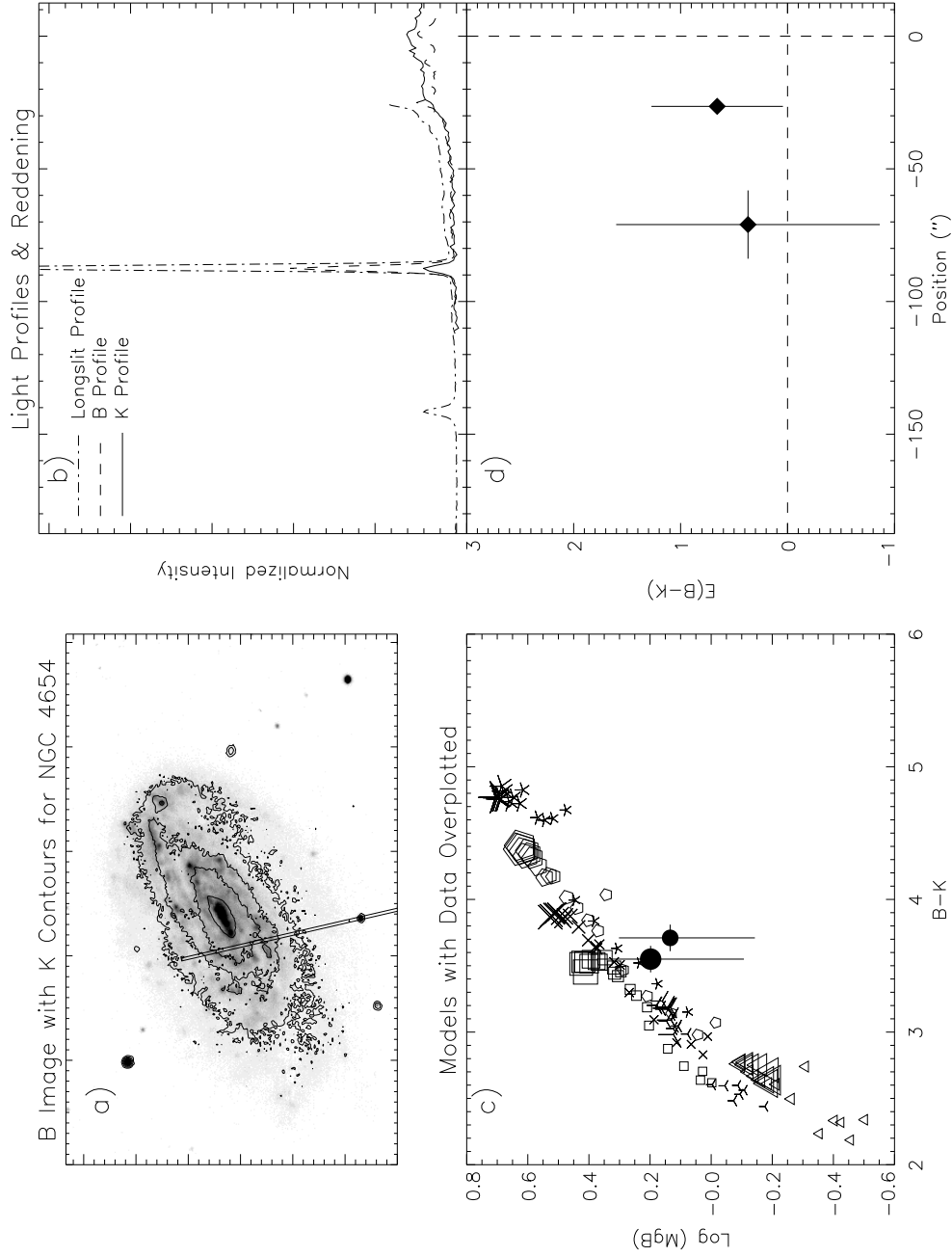


Figure 10.11: Summary Figure for NGC 4654 Position Two: a) The slit position. B image with K contours b) B & K extracted profiles aligned with B longslit profile c) Models represented by lines with symbols, including all ages & metallicities. Data represented by filled symbols with error bars. d) Reddening constant within errors. Two points not shown were excluded because their $\text{Log}(\text{Mgb})$ errors extended beyond the models.

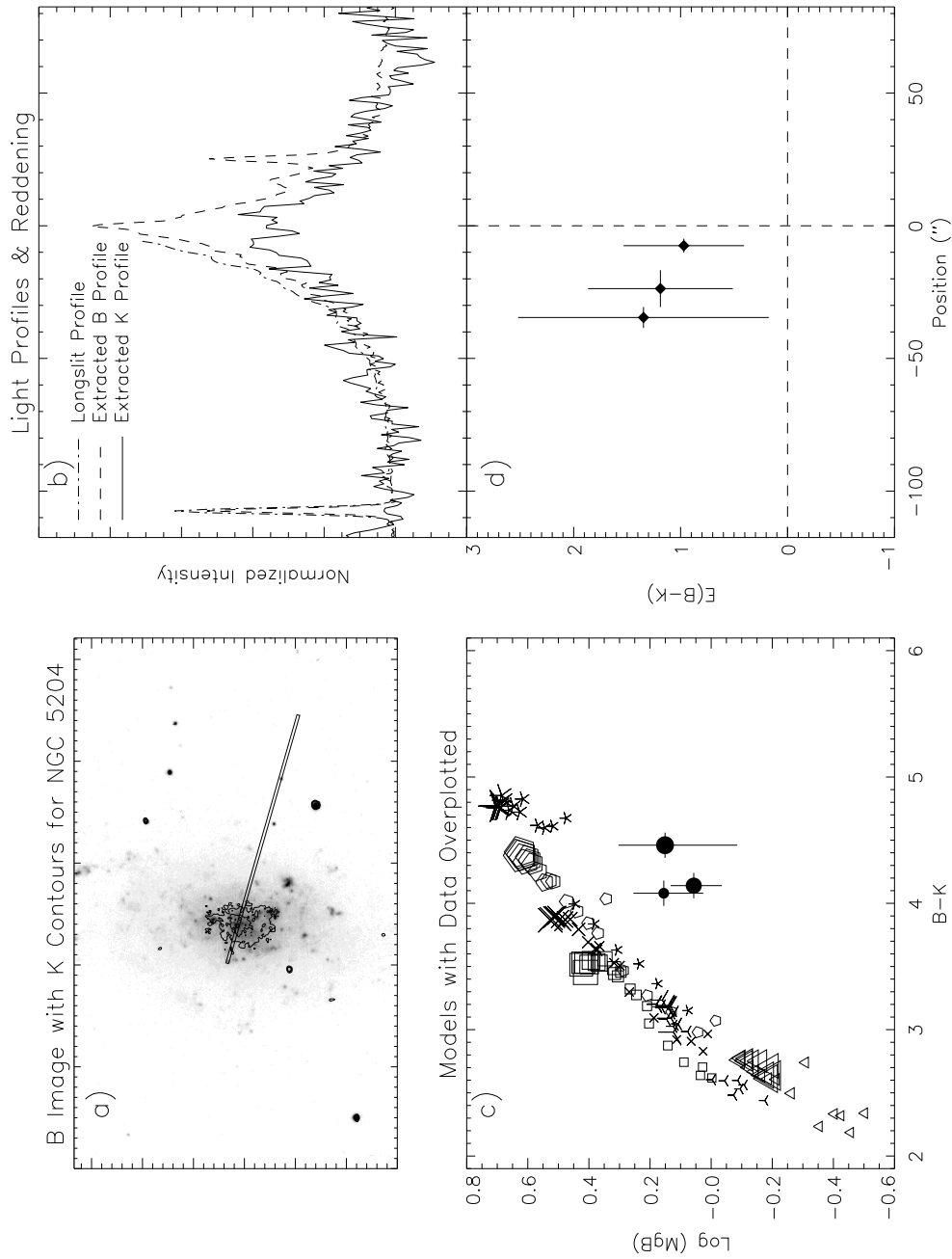


Figure 10.12: Summary Figure for NGC 5204 Position One: a) The slit position. B image with K contours b) B & K extracted profiles aligned with B longslit profile c) Models represented by lines with symbols, including all ages & metallicities. Data represented by filled symbols with error bars. d) No reddening or population gradient. Two points not shown were excluded because their $\text{Log}(\text{MgB})$ errors extended beyond the models.

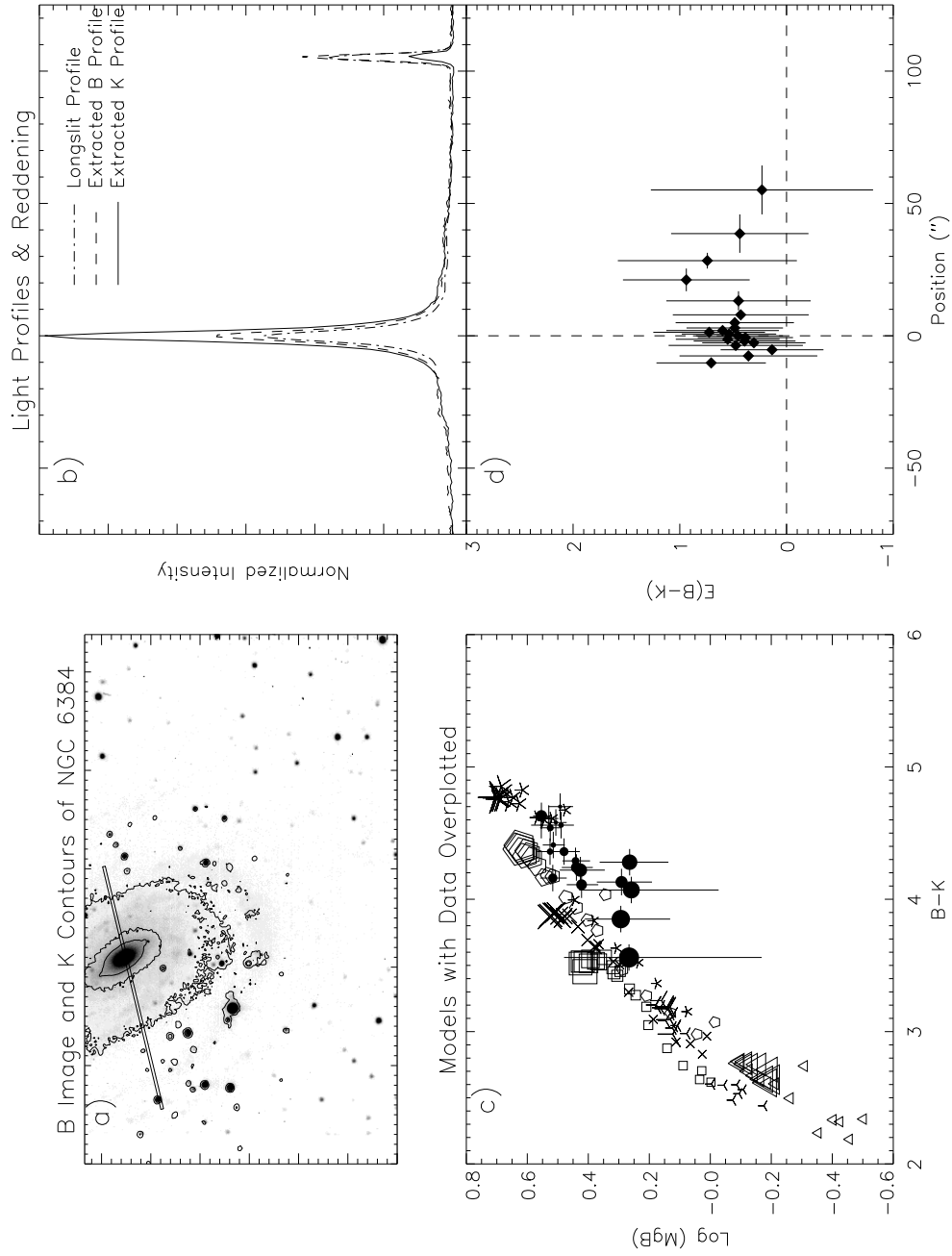


Figure 10.13: Summary Figure for NGC 6384 Position One: a) The slit position. B image with K contours b) B & K extracted profiles aligned with B longslit profile c) Models represented by lines with symbols, including all ages & metallicities. Data represented by filled symbols with error bars. d) Reddening constant with in errors. Color gradient due to change in stellar population. See text for detailed discussion.

10.2 Conclusions

Ten spiral galaxies have been observed in B, V, R, I, J, H, and K. Spectral images have been collected at two position angles and two resolutions in each galaxy. The inter-arm regions of their disks have been detected in all bands and the spectroscopy. The data processing of the data has been described. The calibration of a subset of the data has been documented. The data are unique because of the combination of spectroscopy and broad band imaging. Seldom is such a data set possible to obtain. The images are ready for exploitation and are the starting point for many possible investigations. An example of one such investigation is given.

Color gradients can be caused by changes in stellar population *or* changes in reddening. Gradients in B–K and Mgb have been measured in four slit positions in three galaxies. All are reddened by dust. Color gradients are detected in two of the galaxies. The field galaxy, NGC 6384, suffered the least reddening. It had a color gradient due to population changes, becoming older and/or more metal rich toward the center. In its outer disk, the color becomes bluer outward because of a decrease in the reddening. The two cluster galaxies have more reddening. One, NGC 4654, has a color gradient due mostly to an increase in reddening toward its center. These conclusions are confirmed by comparing the data to the unreddened relationship between Mgb and B–K provided by stellar population synthesis models. Thus, the field galaxy and cluster galaxy become redder in their centers for different reasons. The shape of their color profiles are also different. The cluster galaxy's B–K profile is like a step function with the transition from the red inner region to the bluer outer region marked by a spiral arm. The field galaxy's B–K profile is smoother although it too has a transition from the inner regions where the populations are changing to the outer regions where the reddening is changing. The transition may coincide with the bulge to disk transition.

The two cluster galaxies are disturbed by interactions with their environment. These two are more similar in their populations and reddening than the third galaxy which is in the field. But, they differ more in $B_T - H_{-0.5}$ than the field galaxy and the redder of the two cluster galaxies. Hence, it

is likely the environment is dominating the internal character of these galaxies and that the global color does not correlate with internal character.

By visual inspection, the color gradients are smoother than the appearance of dust lanes in the B images. There are several possible explanations. The dust causing the reddening in these galaxies is smoothly distributed, the effect of the non-uniform distribution of dust is not measured, the relatively large apertures may average out the effects of clumped dust, or the fainter parts of the disk are faint because of a lack of star formation not because of an increase in the amount of dust.

Constraints were placed on the ages and metallicities of the stars contributing to the integrated light of three spiral disks. One color, $B-K$, and one spectral index, Mgb , have been compared to the models. In no case was there a very metal rich very old population detected in the integrated light. All three cases overlapped with young models (< 5 Gyr) of all metallicities. Two of the galaxies overlapped with very metal poor older populations. One field galaxy, NGC 6384, showed evidence of a change in population with position. Its stellar populations appear to become more metal rich (up to solar) and/or older towards its center. This agreed with a previous investigation of its stellar populations. The range of populations is rather broad and cannot be understood in terms of single age or metallicity.

For three of the galaxies studied so far the stellar population models predict colors that are too blue for a given value of Mgb line strength. This cannot be explained by any mixture of the simple stellar population models. The next most likely explanation is the reddening effect of the ISM of the galaxies. Given that the models work well for ellipticals [Gon93, CWB96, TFWG00] which have little or no dust it may be concluded that the models are too blue for the spirals because they neglect dust. If the model colors are correct for unreddened populations then the difference between the observed and model colors is due to internal reddening. This leads to a technique for estimating $E(B-K)$. In these cases the estimated value of $E(B-K)$ ranges from .5 to 1 magnitudes. If a screen model obeying the [SM79] extinction curve with $R_V = 3$ is assumed, then this corresponds to a

visual extinction of 0.4 to 0.8 magnitudes. In two cases there is evidence of a decrease in reddening outward from the galaxy center. One case was closer to the models than the other two. The results agreed with previous determinations of internal reddening for two of the galaxies. No previous determination was found for the third galaxy. The technique works and will enable the separation of reddening from age and metallicity effects in future work. Thus, it will be possible to correctly interpret the colors of the unresolved disks of spiral galaxies. This is critical to understanding the stellar content of spiral galaxies and hence their evolution and the evolution of galaxies in general.

A comparison was made between the Tully-Fisher residuals, internal reddening estimate, and population constraints of the three galaxies studied. Results are inconclusive because of the small peculiar velocities of the two cluster galaxies.

10.3 Future Work

The conclusions made here are more qualitative than quantitative because of the large uncertainty in the measured line strength and colors. This situation will improve with the analysis of the remaining sixteen slit positions and seven galaxies. The problem of emission in the spectra will be addressed as well. The other available colors will be used to estimate the wavelength dependence of the internal reddening and to determine how it varies within a galaxy and from galaxy to galaxy. Comparisons will be made between these galaxies and the Galaxy. Other line indices will be measured to confirm the reddening estimates and to help distinguish between changes in age and metallicity. Different IMFs will be used in the population synthesis to confirm the expectation that the unreddened relationship between Mgb and B–K will not change significantly. In addition, reddening independent quantities other than line indices will be investigated. Chemical evolution models will be used to constrain the star formation history of each galaxy as a function position and to look for trends between internal and global properties.

The calibrated data presented here have many uses including but not limited to the study of

surface brightness and color distributions, chemical compositions, bulge-disk decomposition, galaxy chemical evolution models, dust models, the Tully-Fisher relation, and stellar population.

Analysis of the emission line spectra using CLOUDY, [FT81], will help separate the star forming population from the older underlining population, estimate the star formation rate, and give an independent reddening estimate. This feeds back into the population synthesis which can be refined, [FRV97]. It can also constrain a multi-zone chemical evolution model, [AY86, SGBD98]. By constraining the models physical limits can be put on the evolution of disks.

In addition, two-dimensional surface fitting will be used to get a bulge-disk decomposition and put limits on the disk scale height and dust distribution, [Byu92, Hui94, Dwe98]. This also constrains the multi-zone chemical evolution model. It will be possible to test models which incorporate both dynamical and chemical evolution with this data set.

Once these spirals are well characterized many questions will be addressed. What relationships are there between colors and line-strengths within a galaxy and from galaxy to galaxy? Are these relationships related to global properties of the galaxies? Do differences among stellar populations affect scatter in the Tully-Fisher relation? What might result if two of these spirals were merged? Can the stellar populations of spiral disks be related in a coherent manner to the stellar populations of elliptical galaxies? This might be accomplished by comparing colors and line indices and model results of spirals and ellipticals. Does reddening correlate with age, metallicity, or global properties of the galaxies? How does it compare to the reddening in the Galaxy? Can the properties of Galactic dust reproduce the reddening seen in these galaxies? The usefulness of this data set is far from depleted. There are many paths of inquiry to follow.

REFERENCES

- [Aar77] M. Aaronson. *Infrared Observations of Galaxies*. Ph.D. Thesis, Harvard University, Cambridge, 1977.
- [AMH82] Marc Aaronson, Jeremy Mould, and John Huchra. A Distance Scale from the Infrared Magnitude/HI Velocity-Width Relation. I. The Calibration. *The Astrophysical Journal Supplement Series*, 50(2):241–262, October 1982.
- [AY86] N. Arimoto and Y. Yoshii. Photometric and Chemical Evolution of Galaxies Based on an Evolutionary Method of Population Synthesis. *Astronomy and Astrophysics*, 164:260–273, August 1986.
- [Baa44] W. Baade. The Resolution of Messier 32, NGC 205, and the Central Region of the Andromeda Nebula. *The Astrophysical Journal*, 100(2):137–146, April 1944.
- [BBB⁺88] David Burstein, F. Bertola, L. M. Buson, S. M. Faber, and Tod R. Lauer. The Far-Ultraviolet Spectra of Early-Type Galaxies. *The Astrophysical Journal*, 328:440–462, May 1988.
- [BBFN97] David Burstein, Ralf Bender, S. Faber, and R. Nolthenius. Global Relationships Among the Physical Properties of Stellar Systems. *The Astronomical Journal*, 114(4):1365–1392, November 1997.
- [BC93] Gustavo Bruzual and Stéphane Charlot. Spectral Evolution of Stellar Populations using Isochrone Synthesis. *The Astrophysical Journal*, 405(2):538–553, March 1993.
- [BCF94] Alessandro Bressan, Cesare Chiosi, and Franco Fagotto. Spectrophotometric Evolution of Elliptical Galaxies. I. Ultraviolet Excess and Color-Magnitude-Redshift Relations. *The Astrophysical Journal Supplement Series*, 94(1):63–115, September 1994.
- [BdJ00] Eric F. Bell and Roelof S. de Jong. The Stellar Populations of Spiral Galaxies. *Monthly Notices of the Astronomical Society*, 312:497–520, March 2000.
- [BEMM92] B. Barbuy, M. Erdelyi-Mendes, and A. Milone. Synthetic Mg₁, Mg₂, and Mgb Indices: Relative Intensities of Molecular Bands as a Function of Stellar Parameters. *Astronomy and Astrophysics Supplement Series*, 93(2):235–246, 1992.
- [Bet39] Hans Bethe. Energy Production in Stars. *Physical Review*, 55:434–456, March 1939.
- [BFGK84] D. Burstein, S. M. Faber, C. M. Gaskell, and N. Krumm. Old Stellar Populations. I. A Spectroscopic Comparison of Galactic Globular Clusters, M31 Globular Clusters, and Elliptical Galaxies. *The Astrophysical Journal*, 287:586–609, December 1984.
- [BH84] D. Burstein and C. Heiles. Reddening Estimates for Galaxies in the Second Reference Catalog and the Uppsala General Catalog. *The Astrophysical Journal Supplement Series*, 54:33–79, January 1984.
- [Bla65] A. Blaauw. The Concept of Stellar Populations. In A. Blaauw and Maarten Schmidt, editors, *Galactic Structure*, volume 9 of *Stars and Stellar Systems*, pages 435–453, Chicago, 1965. University of Chicago Press.
- [Bru95] Gustavo A. Bruzual. Radiative Transfer Models. In Jonathan I. Davies and David Burstein, editors, *The Opacity of Spiral Disks*, volume 469 of *Series C: Mathematical and Physical Sciences*, pages 33–41, Dordrecht, 1995. Kluwer Academic Publishers.

- [Bur79] D. Burstein. The Absorption-Line Strengths of Elliptical and S0 Galaxies. *The Astrophysical Journal*, 232:74–83, August 1979.
- [Buz89] Alberto Buzzoni. Evolutionary Population Synthesis in Stellar Systems I. A Global Approach. *The Astrophysical Journal Supplement Series*, 71:817–869, December 1989.
- [Byu92] Yong-Ik Byun. *Dust Opacity and Structure of Spiral Galaxies*. Ph.D. Thesis, The Australian National University, 1992.
- [CF00] Stéphane Charlot and S. Micalle Fall. A Simple Model for the Absorption of Starlight by Dust in Galaxies. *The Astrophysical Journal*, 539:718–731, August 2000.
- [CSFvA98] Gertrud Contardo, Matthias Steinmetz, and Uta Fritze-von Alvensleben. Photometric Evolution of Galaxies in Cosmological Scenarios. *The Astrophysical Journal*, 507:497–506, November 1998.
- [CSZ⁺] C. Marcella Carollo, Massimo Stiavelli, P. Tim De Zeeuw, Marc Seigar, and Herwig Dejonghe. *Hubble Space Telescope* Optical-Near-Infrared Colors of Nearby $R^{1/4}$ and Exponential Bulges.
- [CWB96] Stéphane Charlot, Guy Worthey, and Alessandro Bressan. Uncertainties in the Modeling of Old Stellar Populations. *The Astrophysical Journal*, 457:625–644, February 1996.
- [DD87] S. Djorgovski and Marc Davis. Fundamental Properties of Elliptical Galaxies. *The Astrophysical Journal*, 313:59–68, February 1987.
- [Dee60] T. J. Deeming. The Magnesium b Lines in Late-Type Stars. *Monthly Notices of the Astronomical Society*, 121:52–66, February 1960.
- [dVdVC⁺91] G. de Vaucouleurs, A. de Vaucouleurs, H. Corwin, Jr., R. Buta, G. Paturel, and P. Fouque. *Third Reference Catalogue of Bright Galaxies*, volume I-III. Springer-Verlag, New York, 1991.
- [Dwe98] Eli Dwek. The Evolution of the Elemental Abundances in the Gas and Dust Phases of the Galaxy. *The Astrophysical Journal*, 501:643–665, 1998.
- [EFMN82] J. H. Elias, J. A. Frogel, K. Matthews, and G. Neugebauer. Infrared Standard Stars. *The Astronomical Journal*, 87(7):1029–1034, July 1982.
- [ELBS62] O. J. Eggen, D. Lynden-Bell, and A. R. Sandage. Evidence from the Motions of Old Stars that the Galaxy Collapsed. *The Astrophysical Journal*, 136:748–766, November 1962.
- [EP82] C. H. Edwards and D. E. Penny. *Calculus and Analytic Geometry*. Prentice-Hall, Inc., 1982.
- [Fab72] S. M. Faber. Quadratic Programming Applied to the Problem of Galaxy Population Synthesis. *Astronomy and Astrophysics*, 20:361–374, September 1972.
- [Fab73] S. M. Faber. Variations in Spectral-Energy Distributions and Absorption-Line Strengths among Elliptical Galaxies. *The Astrophysical Journal*, 179(3):731–754, February 1973.

- [Fer92] Federico Ferrini. Evolution of Spiral Galaxies. I. Halo-Disk Connection for the Evolution of the Solar Neighborhood. *The Astrophysical Journal*, 387:138–151, March 1992.
- [FP83] G. Fabbiano and N. Panagia. X-Ray and Ultraviolet Observations of Extragalactic HII Regions. *The Astrophysical Journal*, 266:568–575, March 1983.
- [Fro85] J. A. Frogel. The Stellar Content of the Nuclei of Late-Type Spiral Galaxies. *The Astrophysical Journal*, 298(2):528–543, November 1985.
- [Fro88] Jay. A. Frogel. The Galactic Nuclear Bulge and the Stellar Content of Spheroidal Systems. *Annual Review of Astronomy & Astrophysics*, 26:51–92, 1988.
- [FRV97] Michel Fioc and Brigitte Rocca-Volmerange. PEGASE: A UV to NIR Spectral Evolution Model of Galaxies. *Astronomy and Astrophysics*, 326:950–962, October 1997.
- [FT81] G. J. Ferland and J. W. Truran. An X-Ray Model for the Nebula of Nova DQ Herculis 1934. *The Astrophysical Journal*, 244:1022–1032, March 1981.
- [FTGW94] S. M. Faber, S. C. Trager, J. J. González, and Guy Worthey. The Stellar Ages of Elliptical Galaxies. In P.C. Van der Kruit and G. Gilmore, editors, *Stellar Populations*, number 164 in IAU Symposium, pages 21–30, Dordrecht, 1994. International Astronomical Union, Kluwer Academic Publishers.
- [Gam38] G. Gamow. Nuclear Energy Sources and Stellar Evolution. *Physical Review*, 53:595–604, April 1938.
- [Gil92] Ronald L. Gilliland. Details of Noise Sources and Reduction Processes. In Steve Howell, editor, *Astronomical CCD Observing and Reduction Techniques*, volume 23 of *ASP Conference Series*, pages 68–89, San Francisco, 1992. Astronomical Society of the Pacific, BookCrafters, Inc.
- [Gon93] J. J. González. *Line-Strength Gradients and Kinematic Profiles in Elliptical Galaxies*. Ph.D. Thesis, University of California, Santa Cruz, 1993.
- [Gre89a] Michael D. Gregg. Differential Population Synthesis of S0 Galaxies I. Methods and Results. *The Astrophysical Journal*, 337:45–65, February 1989.
- [Gre89b] Michael D. Gregg. Differential Population Synthesis of S0 Galaxies I. The Data. *The Astrophysical Journal Supplement Series*, 69:217–232, February 1989.
- [Hod89] Paul Hodge. Populations in Local Group Galaxies. *Annual Review of Astronomy & Astrophysics*, 27:139–159, 1989.
- [How92] Steve Howell. Introduction to Differential Time-Series Astronomical Photometry Using Charged-Coupled Devices. In Steve Howell, editor, *Astronomical CCD Observing and Reduction Techniques*, volume 23 of *ASP Conference Series*, pages 105–128, San Francisco, 1992. Astronomical Society of the Pacific, BookCrafters, Inc.
- [HS55] Fred Hoyle and Martin Schwarzschild. The Evolution of Type II Stars. *The Astrophysical Journal*, 2:1–40, June 1955.
- [Hui94] J. Edwin Huizinga. *Extinction Studies of Spiral Galaxies*. Ph.D. Thesis, Groningen University, 1994.

- [Jav93] Javier Gorgas and S. M. Faber and David Burstein and J. Jesús Gonzalez and Stéphane Courteau and Charles Prosser. Old Stellar Populations. IV. Empirical Fitting Functions for Features in Spectra of G and K Stars. *The Astrophysical Journal Supplement Series*, 86:153–198, May 1993.
- [JCC⁺00] T. H. Jarrett, T. Chester, R. Cutri, S. Schneider, M. Skrutskie, and J. P. Huchra. 2MASS Extended Source Catalog: Overview and Algorithms. *The Astronomical Journal*, 119:2498–2531, May 200.
- [JE92] James Janesick and Tom Elliott. History and Advancements of Large Area Array Scientific CCD Images. In Steve Howell, editor, *Astronomical CCD Observing and Reduction Techniques*, volume 23 of *ASP Conference Series*, pages 1–67, San Francisco, 1992. Astronomical Society of the Pacific, BookCrafters, Inc.
- [Joy92] Richard R. Joyce. Observing with Infrared Arrays. In Steve Howell, editor, *Astronomical CCD Observing and Reduction Techniques*, volume 23 of *ASP Conference Series*, pages 258–284, San Francisco, 1992. Astronomical Society of the Pacific, BookCrafters, Inc.
- [Ken98] Robert C. Kennicutt, Jr. Star Formation in Galaxies Along the Hubble Sequence. *Annual Review of Astronomy & Astrophysics*, 36:189–231, 1998.
- [Kin71] Ivan R. King. Stellar Populations in Galaxies. *Publications of the Astronomical Society of the Pacific*, 83(494):377–400, August 1971.
- [KK53] Philip C. Keenan and Geoffrey Keller. Star Formation in Galaxies Along the Hubble Sequence. *The Astrophysical Journal*, 117(2):241–255, March 1953.
- [L⁺96] Claus Leitherer et al. A Data Base for Galaxy Evolution Modeling. *Publications of the Astronomical Society of the Pacific*, 108:996–1017, November 1996.
- [Lan73] A. Landolt. UBV Photoelectric Sequences in the Celestial Equatorial Selected Areas 92–115. *The Astronomical Journal*, 78:959–1021, November 1973.
- [Lan92] A. Landolt. UBVR Photometric Standard Stars in the Magnitude Range 11.5–16.0 Around the Celestial Equator. *The Astronomical Journal*, 104(1):340–371, 436–491, July 1992.
- [Las70] Barry M. Lasker. On the Homogeneity of the Spectral-Energy Distribution among Giant E and S0 Galaxies and Other Results. *The Astronomical Journal*, 75(1):21–33, February 1970.
- [Lin25a] Bertil Lindblad. On the Cause of Star-streaming. *The Astrophysical Journal*, 191:191–197, 1925.
- [Lin25b] Bertil Lindblad. Star-streaming and the Structure of the Stellar System. *Arkiv för Matematik, Astronomi, och Fysik*, 19A(27), 1925.
- [Lup93] Robert Lupton. *Statistics in Theory and Practice*. Princeton, Princeton, New Jersey, 1993.
- [LVPB01] S. Lourenso, A. Vazdekis, R. F. Peletier, and J. E. Beckman. The Stellar Populations of the Bars of Barred Spirals Through Evolutionary Synthesis: First Results. *The Astrophysics and Space Science*, 276:651–658, 2001.

- [May46] N. U. Mayall. The Radial Velocities of Fifty Globular Star Clusters. *The Astrophysical Journal*, 104:290–323, September 1946.
- [MB81] Dimitri Mihalas and James Binney. *Galactic Astronomy*. W. H. Freeman and Company, 1981.
- [Mor56] W. W. Morgan. The Integrated Spectral Types of Globular Clusters. *Publications of the Astronomical Society of the Pacific*, 68(405):509–516, December 1956.
- [Mor59] W. W. Morgan. The Integrated Spectra of Globular Clusters. *The Astronomical Journal*, 64(1275):432–436, December 1959.
- [Mou78] J. R. Mould. The Mg Index in Old Galaxy Populations: A Theoretical Approach. *The Astrophysical Journal*, 220:434–441, March 1978.
- [Mou82] J. R. Mould. Stellar Populations in the Galaxy. *Annual Review of Astronomy & Astrophysics*, 20:91–115, 1982.
- [Mou94] Jeremy Mould. Conference Summary. In P. C. van der Kruit and G. Gilmore, editors, *Stellar Populations*, number 164 in IAU Symposium Series, pages 349–355, Dordrecht, 1994. International Astronomical Union, Kluwer Academic Publishers.
- [MS63] T. A. Matthews and A. R. Sandage. Optical Identification of 3C 48, 3C 196 and 3C 286 with Stellar Objects. *The Astrophysical Journal*, 138(1):30–56, July 1963.
- [MvdB68] Robert D. McClure and Sidney van den Bergh. Five-Color Intermediate-Band Photometry of Stars, Clusters, and Galaxies. *The Astronomical Journal*, 73(5):313–337, June 1968.
- [O’C82] Robert W. O’Connell. Metallicity Versus Age in Spiral Nuclei. *The Astrophysical Journal*, 257(10):89–93, June 1982.
- [O’C86] Robert W. O’Connell. Population Synthesis in Early Type Galaxies. In Alvio Renzini and Monica Tosi, editors, *Stellar Populations*, number 1 in Space Telescope Science Institute Symposium Series, pages 167–189, Cambridge, 1986. Space Telescope Science Institute, Cambridge University Press.
- [Oke74] J. B. Oke. The Absolute Energy Distribution for White Dwarfs. *The Astrophysical Journal Supplement Series*, 27(263):21–36, February 1974.
- [Oor28] Jan Hendrik Oort. Dynamics of the Galactic System in the Vicinity of the Sun. *Bulletin of the Astronomical Institute of the Netherlands*, 4(159):269–284, November 1928.
- [Ost94] Donald E. Osterbrock. Walter Baade’s Discovery of the Two Stellar Populations. In P.C. Van der Kruit and G. Gilmore, editors, *Stellar Populations*, number 164 in IAU Symposium, pages 21–30, Dordrecht, 1994. International Astronomical Union, Kluwer Academic Publishers.
- [PBCV92] M. Prieto, J. E. Beckman, J. Cepa, and A. M. Varela. Multiband Analysis of the Surface Brightness Distributions of Sb and Sc Spirals CCD Images. II. Bulge-Disc Decomposition. *Astronomy & Astrophysics Supplement Series*, 257:85–96, April 1992.
- [Pic85] A. J. Pickles. Differential Population Synthesis of Early-type Galaxies. III. Synthesis Results. *The Astrophysical Journal*, 296:340–369, September 1985.

- [PLP⁺92] M. Prieto, D. P. T. Longley, E. Perez, J. E. Beckman, A. M. Varela, and J. Cepa. Multiband Analysis of the Surface Brightness Distributions of Sb and Sc Spirals CCD Images. I. Observations. *Astronomy & Astrophysics Supplement Series*, 93:557–585, June 1992.
- [PM95] Bikram Phookun and Lee G. Mundy. NGC 4654: A Virgo Cluster Spiral Interaction with the Intracluster Medium. *The Astrophysical Journal*, 453:154–161, November 1995.
- [RB86] Alvio Renzini and Alberto Buzzoni. Global Properties of Stellar Populations and the Spectral Evolution of Galaxies. In Cesare Chiosi and Alvio Renzini, editors, *Spectral Evolution of Galaxies*, volume 122 of *Astrophysics and Space Science Library*, pages 195–231, Dordrecht, 1986. Astrophysics and Space Science Library, D. Reidel Publishing Company.
- [Rob63] Mortan S. Roberts. The Content of Galaxies: Stars and Gas. *Annual Review of Astronomy & Astrophysics*, 1:149–178, 1963.
- [Rom50] Nancy Roman. A Correlation Between the Spectroscopic and Dynamical Characteristics of the Late F- and Early G-Type Stars. *The Astrophysical Journal*, 112:554–558, November 1950.
- [Rus48] Henry Norris Russell. On the Distribution of Absolute Magnitude in Populations I and II. *Publications of the Astronomical Society of the Pacific*, 60(354):202–204, June 1948.
- [San86] Allan R. Sandage. The Population Concept, Globular Clusters, Subdwarfs, Ages, and the Collapse of the Galaxy. *Annual Review of Astronomy & Astrophysics*, 24:421–458, 1986.
- [ŠC42] M. Ščönberg and S. Chandrasekhar. On the Evolution of the Main-Sequence Stars. *The Astrophysical Journal*, 96(2):161–172, September 1942.
- [SCD96] Vincent Sicotte, Claude Carignan, and Danial Durand. NGC 5204: A Strongly Warped Magellanic Spiral. I. Light Distribution and HII Kinematics. *The Astronomical Journal*, 112(4):1423–1428, October 1996.
- [Sch99] J. Scheiner. On the Spectrum of the Great Nebula in Andromeda. *The Astrophysical Journal*, 9:149–150, March 1899.
- [Sch63] Maarten Schmidt. The Rate of Star Formation. II. The Rate of Formation of Stars of Different Mass. *The Astrophysical Journal*, 137:758–769, April 1963.
- [SDH⁺89] A. A. Stark, J. A. Davidson, D. A. Harper, R. Pernic, R. Loewenstein, S. Platt, G. Engargiola, and S. Casey. Far-Infrared and Submillimeter Photometric Mapping of Spiral Galaxies in the Virgo Cluster. *The Astrophysical Journal*, 337:650–657, February 1989.
- [Sea86] Leonard Searle. Introduction and Overview. In Alvio Renzini and Monica Tosi, editors, *Stellar Populations*, number 1 in Space Telescope Science Institute Symposium Series, pages 3–7, Cambridge, 1986. Space Telescope Science Institute, Cambridge University Press.

- [SGBD98] Laura Silva, Gian Luigi Granato, Alessandro Bressan, and Luigi Danese. Modeling the Effects of Dust on Galactic Spectral Energy Distributions from the Ultraviolet to the Millimeter Band. *The Astrophysical Journal*, 509:103–117, December 1998.
- [Sil91] D. R. Silva. *Empirical Population Synthesis: New Directions*. Ph.D. Thesis, University of Michigan, Ann Arbor, 1991.
- [SM79] B. D. Savage and J. S. Mathis. Observed Properties of Interstellar Dust. *Annual Review of Astronomy & Astrophysics*, 17:73–111, 1979.
- [SMR⁺95] Luigi Spinoglio, Matthew A. Malkan, Brian Rush, Luis Carrasco, and Elsa Recillas-Cruz. Multiwavelength Energy Distributions and Bolometric Luminosities of the 12 Micron Galaxy Sample. *The Astrophysical Journal*, 453:616–633, November 1995.
- [ST69] H. Spinrad and B. J. Taylor. Scanner Abundance Studies. I. An Investigation of Supermetallicity in Late-Type Evolved Stars. *The Astrophysical Journal*, 157(3):1279–1340, September 1969.
- [Sto77] R. P. S. Stone. Spectral Energy Distributions of Standard Stars of Intermediate Brightness. II. *The Astrophysical Journal*, 218(3):767–769, December 1977.
- [Str24] Gustaf Strömberg. The Asymmetry in Stellar Motions and the Existence of a Velocity-Restriction in Space. *The Astrophysical Journal*, 56:228–251, May 1924.
- [Str25] Gustaf Strömberg. The Asymmetry in Stellar Motions as Determined from Radial Velocities. *The Astrophysical Journal*, 56:363–388, June 1925.
- [Str77] K. M. Strom. *Standard Stars for IIDS Observations*. Kitt Peak National Observatory, September 1977. Memorandum.
- [TB95] Giuseppe Tormen and David Burstein. Recalibration of the $H_{-0.5}$ Magnitudes of Spiral Galaxies. *The Astrophysical Journal Supplement Series*, 96(1):123–157, January 1995.
- [TF77] R. B. Tully and J. R. Fisher. A New Method of Determining Distances to Galaxies. *Astronomy and Astrophysics*, 54(3):661–673, February 1977.
- [TFWG00] S. C. Trager, S. M. Faber, Guy Worthey, and J. J. González. The Stellar Population Histories of Early-Type Galaxies. II. Controlling Parameters of the Stellar Populations. *The Astronomical Journal*, 120:165–188, June 2000.
- [Tin80] Beatrice M. Tinsley. Evolution of the Stars and Gas in Galaxies. *Fundamentals of Cosmic Physics*, 5(4):287–388, 1980.
- [TT72] Alar Toomre and Juri Toomre. Galactic Bridges and Tails. *The Astrophysical Journal*, 178:623–666, December 1972.
- [Tur76] Barry E. Turnrose. The Stellar Content of the Nuclear Regions of Sc Galaxies. *The Astrophysical Journal*, 210:33–57, November 1976.
- [vdB75] Sidney van den Bergh. Stellar Populations in Galaxies. *Annual Review of Astronomy & Astrophysics*, 13:217–255, 1975.
- [vW38] Carl Friedrich Freiherr von Weizsäcker. Über Elementumwandlungen im Innern der Sterne. II. *Physik Zeitschrift*, 39:633–646, 1938.

- [WFGB94] G. Worthey, S. M. Faber, J. J. González, and D. Burstein. Old Stellar Populations. V. Absorption Feature Indices for the Complete Lick/IDS Sample of Stars. *The Astrophysical Journal Supplement Series*, 94(2):687–722, October 1994.
- [Whi35] Fred Lawrence Whipple. The Colors and Spectra of External Galaxies. *Harvard College Observatory Circular*, 404:1–21, 1935.
- [Woo66] David B. Wood. Multicolor Photoelectric Photometry of Galaxies. *The Astrophysical Journal*, 145:36–56, June 1966.
- [Wor93] G. Worthey. *The Controlling Parameters of the Integrated Flux of a Stellar Population*. Ph.D. Thesis, University of California, Santa Cruz, 1993.
- [Wor94] G. Worthey. Comprehensive Stellar Population Models and the Disentanglement of Age and Metallicity Effects. *The Astrophysical Journal Supplement Series*, 95(1):107–149, November 1994.

APPENDIX A

AREA OF A POLYGON

Here is a proof of the formula for the area of an n-sided polygon.

$$A = \frac{1}{2} \sum_{i=1}^{n-1} (x_i y_{i+1} - x_{i+1} y_i) + \frac{1}{2} (x_n y_1 - x_1 y_n). \quad (\text{A.1})$$

It is straight forward to show this. Start with Green's Theorem:

$$\oint_C (Pdx + Qdy) = \iint_R \left(\frac{\partial Q}{\partial x} - \frac{\partial P}{\partial y} \right) dA \quad (\text{A.2})$$

Now let

$$Q = x \quad (\text{A.3})$$

$$P = -y. \quad (\text{A.4})$$

Then

$$\oint_C (-ydx + xdy) = 2 \iint_R dA. \quad (\text{A.5})$$

Now consider the right triangle in Figure A.1. Its area is given by

$$\oint_{-CC_1C_2} (-ydx + xdy) = 2A_R. \quad (\text{A.6})$$

The area of the triangle is known, $A_R = \frac{1}{2}(x_2 - x_1)(y_2 - y_1)$, and the line integral from (x_2, y_2) to (x_1, y_1) becomes

$$\oint_{-C} (-ydx + xdy) = (x_2 - x_1)(y_2 - y_1) - \oint_{C_1C_2} (-ydx + xdy). \quad (\text{A.7})$$

Doing the integrals over C_1 and C_2 we have

$$\oint_{-C} (-ydx + xdy) = (x_2 - x_1)(y_2 - y_1) + \int_{x_1}^{x_2} y_1 dx - \int_{y_1}^{y_2} x_1 dy \quad (\text{A.8})$$

$$\oint_{-C} (-ydx + xdy) = y_1 x_2 - x_1 y_2. \quad (\text{A.9})$$

Since

$$\oint_{-C} (-ydx + xdy) = - \oint_C (-ydx + xdy) \quad (\text{A.10})$$

we can write

$$\oint_C (-ydx + xdy) = (x_1 y_2 - y_1 x_2). \quad (\text{A.11})$$

Now we can generalize to an n-side polygon as in Figure A.2. The line integral over the circumference of the polygon is the sum of the line integrals over each side.

$$\oint_C (-ydx + xdy) = \sum_{i=1}^n \int_{C_i} (-ydx + xdy) \quad (\text{A.12})$$

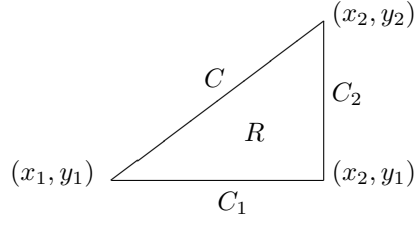


Figure A.1: Right Triangle used in Proof.

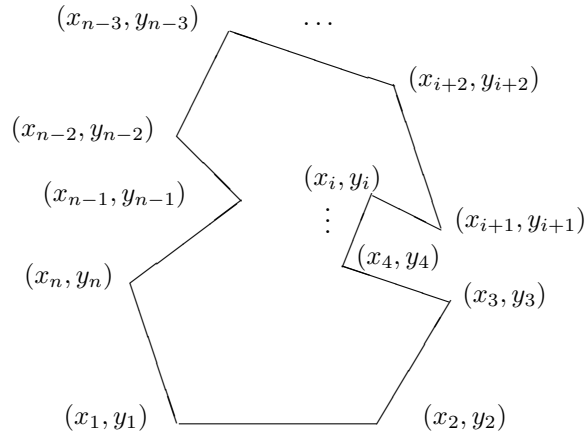


Figure A.2: Example of N-sided Polygon used in Proof.

Using equation A.11 we have

$$\int_{C_i} (-ydx + xdy) = \frac{1}{2}(x_i y_{i+1} - y_i x_{i+1}) \quad (\text{A.13})$$

$$\int_{C_n} (-ydx + xdy) = \frac{1}{2}(x_n y_1 - y_n x_1). \quad (\text{A.14})$$

Therefore,

$$A_R = \frac{1}{2} \sum_{i=1}^{n-1} (x_i y_{i+1} - y_i x_{i+1}) + \frac{1}{2} (x_n y_1 - y_n x_1). \quad (\text{A.15})$$